Università degli studi di Napoli Federico II

Scuola Politecnica e delle Scienze di Base

Dottorato di Ricerca in Ingegneria Industriale

XXXIV ciclo

Doctoral thesis

Experimental and numerical analysis about new control, layout and low-GWP refrigerant options for the commercial refrigeration

Coordinator of PhD course
Prof. Michele Grassi

Supervisor
Prof. Alfonso William Mauro

Company co-supervisor
Katsuki Mochizuki
Zanotti S.p.A. Daikin group

Candidate
Biagio Citarella

Index

Nomenclature

Roman	
A	Area [m^{-2}]
a	Coefficient a
b	Coefficient b
C	Cost [€]
c	Coefficient c
CC	Displacement [m^3]
c_p	Specific heat [$kJ\ kg^{-1}\ K^{-1}$]
CR	capacity ratio [-]
d	Coefficient d
D	Diameter [m]
f_{R290}	Correction factor for propane
h	Heat transfer coefficient [$W\ m^{-2}\ K^{-1}$]
H	Height [m] or heater in CO_2 condesing unit activity
hh	Operational hours [$h\ years^{-1}$]
i	Specific enthalpy [$kJ\ kg^{-1}$]
k	Thermal conductivity [$W\ m^{-1}\ K^{-1}$]
L	Length [m]
m	Mass [kg]
m	mass [kg]
N	Number (of)
n	Compressor speed [rpm] or [rps]
$N_{duty\text{-}cycle}$	number of duty cycles [-]
P	Pitch [m]
$\bar{P}$	Average electric power
p	pressure [Pa] for air or [bar] for refrigerant
p_t	total (atmospheric) pressure [kPa]
p_{vs}	saturated vapor pressure [kPa]
R	Thermal resistance [$K\ W^{-1}$]
s	Specific entropy [$kJ\ kg^{-1}\ K^{-1}$]
T	Temperature [K] or [°C]

t	Thickness [m]
UA	Thermal conductance [W K^{-1}]
V	Volume [m^3]
w	Velocity [m s^{-1}]
W	Width [m]
x	Vapor quality [-]
yy	Lifetime [years]
$\dot{L}$	Electric power consumption [W]
$\dot{m}$	Mass flow rate [kg s^{-1}]
$\dot{Q}$	Heat rate [W]
$\dot{V}$	Volumetric flow rate [m^3 s^{-1}]

Subscripts	
1	Compressor inlet
2	Compressor outlet = condenser inlet
3	Condenser outlet
1h	hourly
1p	Single-phase
2p	Two-phase
a	air
A	Valve A in CO_2 condensing unit
acc	accumulation
air	Air
al	Aluminium
amb	Ambient
anc	Ancillaries
avg	average
B	Valve B in CO_2 condensing unit
bot	Bottom compressor case
bubble	Bubble point
C	Valve C in CO_2 condensing unit
c	Cold room
cal box	calibrated box
circ	Heat exchanger circuit

co	Condenser
comp	compressor
cond	Condensing
cor	Corrected value according to EN13215:2016
cover	External unit cover
cp	Compressor
cr	Cold room
cu	Copper
def	defrost
des	Desuperheating
dew	Dew point
dm	Demand
e	External
el	Elementary part, Electrical (CO_2 condensing unit activity)
en	Energy
ev	Evaporator
evap	Evaporating
fan	fan
fin	fins
free-flow	Free flow
gc	Gascooler
h	Heater
in	Internal, inlet
int	Intermediate
is	Isentropic
liq	Liquid
man	Manufacturing
max	Maximum value
met	Metal cover
mid	Mid point value in two phase region
MT	Medium temperature refrigeration condition (T_{ev}= - 10°C)
opt	optimum
out	outlet
panel	Metal panel
r	Heat exchanger row
rec	Receiver

ref	refrigerant , Reference value (CO_2 condensing unit activity)
run	Running
sat	saturation
sc	Subcooling
set-up	Set-up
sh	Superheating
solenoid	Solenoid
spare	Metal spare
steel	Galvanized steel
suc	Suction
t	Tubes
top	Top compressor case
tot	Total
tp	Two phase
u	Unit
v	Volumetric
w	water
win	Compressor electrical windings
ZX	thermocouple position on 3 × 2 grid on the evaporator

Greek symbols	
α	Void fraction [-]
β	Pressure ratio
Δ	Variation, difference [-]
ε	Error threshold
η	Efficiency [-]
θ	Time [min]
ρ	Density [kg m^{-3}]
$\tau_{on\ comp}$	On time for compressor [min]
ϕ	Relative humidity [%]
ω	Specific humidity [$g_w\ kg_a^{-1}$]

Acronyms	
AC	Air conditioning
AE	Annual energy consumption [kWh a^{-1}]
ALR	Annual leakage ratio [% of refrigerant charge]
BB	Basic booster
BV	Ball valve
COP	Coefficient of Performance
CR	COP penalizing factor with on/off operation
DSH	De-superheater
EEI	Energy efficiency index
EEV	Electronic expansion valve
EF	Carbon dioxide emission factor [$kgCO_{2eq}$ kWh^{-1}]
EOL	End of life emission [% of refrigerant charge]
EV	Evaporator
FGV	Flash gas valve
GC	Gascooler
GWP	Global Warming Potential
HFC	Hydro-fluoro-carbon
HFO	Hydro-fluoro-olefin
HPV	High pressure valve
IC	Intercooler
IHX	Internal heat exchanger
INV	Inverter
LEJ	Liquid ejector
MEJ	Multi-phase ejector liquid + vapour
MS	Mechanical subcooler
PC	Parallel compression
REC	Receiver
SAE	Standard annual energy consumption [kWh a^{-1}]
SEPR	Seasonal Energy Performance Ratio
TEWI	Total Equivalent Warming Impact
VCE	Volumetric cooling effect [kJ m^{-3}]

CO_2 condensing unit thermodynamic cycle	
1	Evaporator outlet / Condensing unit inlet
2	First stage compressor suction
3	First stage compressor discharge
4	Outlet intercooler
5	Second stage compressor suction
6	Second stage compressor discharge
7	Gascooler outlet
8	High pressure valve outlet
9	Liquid outlet receiver
10	Inlet evaporator
11	Vapour outler receiver
12	Flash gas valve outlet

Acknowledgement

This PhD thesis and research activity is funded by Zanotti S.p.A. member of Daikin group. The same company has also financially supported my stay abroad at Daikin Europe in Oostende, Belgium from 3rd to 21st January 2022, to collaborate with their testing activities. For those reasons Zanotti S.p.A. is kindly acknowledged.

Introduction

This PhD activity has been funded by Zanotti S.p.A that has made available its facility to carry out the research activity.

Context

Nowadays cold chain ensures the need to make available food far from harvesting points, farms or sea or in different times of the year from the harvesting period, seeking for the maintenance of good quality, organoleptic properties and nutrients. Commercial refrigeration is one of the intermediate steps of the cold chain, where the fresh or frozen food is stored and displayed to be bought in markets, grocery stores and supermarkets. Depending on the size of displayed area, commercial refrigeration appliances are capable to cover a wide range of cooling capacities from 500 W to above 100 kW with different plant architectures. Roughly 90 million of commercial refrigeration appliances are estimated by IIR (2015) in 2015, and the future market trend proves that this number is expected to increase with a huge impact in energy consumption and greenhouse gases emissions. These latter are caused either by refrigerant emission (direct emissions) and using fossil fuels to produce the electric energy (indirect emissions) that power the systems. The use of low – GWP refrigerants and the increase of efficiency of refrigeration units can help to reduce both. Montreal Protocol, through Kigali Amendment, has the aim to reduce the greenhouse gases emissions up to 20% in 2045 and 15% in 2036 for Art. 5 and no – Art. 5 parties respectively in the World. In Europe, F-Gas regulation (European Parliament, 2014) establishes the rules for the phase-down schedule of HFC production and consumption and GWP thresholds of used refrigerants based on the specific application with the aim to reach 30% of HFC in 2030 compared to the one of 2015. In addition, the efficiency of commercial refrigeration products must fulfil the requirements of Ecodesign (European Parliament, 2009) that imposes minimum threshold values for efficiency indexes (COP, SEPR, EEI) with respect to the specific application. In this framework, the interest of the scientific and technical community on new low – GWP refrigerants and innovative solutions to reduce the energy consumption of the refrigeration systems is high. Among the new refrigerants, natural ones, such as carbon dioxide and propane, and low – GWP blends are soaring interest from the last 20 years; instead, a better defrost control logic with adaptation of defrost launch time basing on operating conditions, can reduce the energetic impact avoiding unnecessary defrost cycles with beneficial effects on temperature control and running cost reduction. In fact, the running costs related to defrost purposes have huge impact on the total, Datta et al. (1997) estimated that the extra costs related to the energy consumption of defrost phase for a retail food store is around 500000£ in the hypotheses of 30000 display cabinets with time interval electric defrost system occurring every 6 hours. The work reported in this thesis is aligned with the abovementioned framework and goals.

Organization of the thesis

The entire work is divided in two parts, a first one dealing with the research activity of low – GWP refrigerants in commercial refrigeration applications with experimental and theoretical approaches. The second part copes with the development of a new method to evaluate the optimal defrost start time aiming the minimization of total absorbed electric energy and compressor duty cycle preserving its lifespan. More in detail, the thesis is composed by 6 chapters:

- In Chapter 1 a brief overview of commercial refrigeration sector is presented with the explanation of operating temperature levels, kind of appliances with their cooling capacity, refrigerant charge ranges and plant layouts.

- In Chapter 2, is shown an overview of commercial refrigeration market share status, with the number of installed units worldwide divided by equipment kind. Furthermore, future market trends, with projections of energetic and environmental impact in terms of greenhouse gases emission are presented, with the description of the major provisions adopted worldwide (Montreal Protocol and its Kigali Amendment) and in Europe (F-Gas regulation 517/2014, Ecodesign Directive 2009/125/EC and its regulations).

- In Chapter 3, a state of the art of research about low – GWP refrigerants in commercial refrigeration systems is presented. The chapter is divided in two parts: the first is focused on low – GWP blends and hydrocarbons, mostly used in small appliances, presenting works that focus the attention on new molecules (starting from 100 million of substances up less than 65) and model development and improvement to evaluate thermophysical properties of these substances. The second part of chapter 3 is focused on carbon dioxide as refrigerant, with theoretical analyses and comparison of different configurations of supermarket booster refrigeration systems in different climates or with other plant layouts (e.g., cascade refrigeration systems) and alternative refrigerants. Moreover, experimental works about field tests of centralized units or laboratory tests on small scale prototypes are also analysed.

- In Chapter 4, the research work about low – GWP refrigerants is presented in two steps. The first one deals with a multi criteria thermo-economic optimization and environmental analysis of R404A replacements, R452A, R449A, R454C, R455A and propane in a 2.5 kW positive monoblock commercial refrigeration unit for small walk-in cold rooms. More than 100k combinations are simulated for each refrigerant, varying the heat exchanger geometry and the temperature differences between air and refrigerant and constrained with technical limits on refrigerant compressor discharge temperature, air and refrigerant side pressure drop in the heat exchangers, refrigerant charge and real dimension limits. A Pareto front is evaluated in terms of set-up costs versus COP and an optimal configuration is found. Finally, an environmental analysis with TEWI evaluation is carried out also using the total costs (sum of set-up and running costs). The second part of the Chapter is focused on an experimental campaign of a small-scale condensing unit using CO_2 as refrigerant; the most key innovative features of the prototype are the presence of hermetic inverter driven two-stage rotary compressor, the intercooler between the first and second stage and the flash gas injection valve from the receiver. 14 tests are carried out to evaluate the influence of ambient and evaporating temperatures on performances, the effect of intercooler operation, and the effect of flash gas injection cooling effects. Finally, also the SEPR is evaluated and compared with another R449A unit equipped with semi hermetic reciprocating compressor with fixed speed.

The last two chapters deal with the optimization of the defrosting phase that is always needed in case of low-medium temperature appliances:

- In Chapter 5, a state of the art about frost formation phenomena (in flat plates and heat exchanger coils) and defrost control logic optimization is reported. Experimental works related on the effect of heat exchanger geometry and boundary conditions on frost formation rate and performances degradation are then reviewed for both fin and coil and microchannel heat exchangers. In addition, entire systems are studied with experimental and modelling approaches, with the evaluation of the impact of frost formation on performances. Finally, works about defrost control logic optimization using commercial systems or innovative approaches (e.g., neural network) are reviewed.

- Chapter 6 presents and proposes a new method to evaluate the optimal defrost start time at each operating condition. The activity is composed by two phases, in the first one the experimental campaign on a positive 1.1 kW monoblock commercial refrigeration unit is presented with tests at different combinations of calibrated box temperature and relative humidity. Tests in which the unit is left in operation up to the complete blockage of the evaporator air flow path due to frost formation are performed, useful for the definition of a novel data reduction to obtain the optimal defrost start time in phase two. The main objectives of the optimization are the total energy consumption and on / off compressor cycle minimization limiting, at the same time, the CR index (capacity ratio) below a maximum threshold in order to ensure that the refrigerator has enough cooling capacity to cope with additional extra load due to high food transpiration and / or door openings.

Chapter 1 – Commercial refrigeration equipment overview

In this chapter an overview of commercial refrigeration sector is reported with the description of the appliances, their layout, the cooling capacity and the refrigerant charge ranges and operating temperature levels.

Commercial refrigeration appliances are used in market, supermarket, grocery stores and restaurants to display and sell fresh and frozen food to the final customer. Therefore, commercial refrigeration sector together with industrial and transport refrigeration ones constitute one of the last steps of the cold chain before domestic refrigeration. The fresh food is typically stored at temperatures between +2°C to +4°C, frozen food between -18°C and -20°C. The two temperature ranges define the medium temperature refrigeration condition (MT, evaporating temperature = -10°C) and low temperature refrigeration condition (LT, evaporating temperature = -35°C).
The commercial refrigeration systems are divided in three classes depending on cooling capacity and installation (for instance if a machinery room is required, if the components are far from each other or they are in the same enclosure):

1) Stand-alone and monoblock refrigeration systems
2) Condensing units
3) Centralized systems

In Table 1.1 a summary of cooling capacity and refrigerant charge ranges are listed according to EPA (2016), except for monoblock refrigeration units. A deeper description of each system type will be presented in the next paragraphs.

Table 1.1 – Cooling capacity and refrigerant charge ranges of commercial refrigeration equipment

Equipment	**Cooling capacity range [kW]**	**Refrigerant charge range [kg]**
Stand-alone	0.1 – 1	0.1 – 2
Monoblock refrigeration systems	0.5 – 5	0.1 – 3
Condensing units	0.1 – 20	1 – 20
Centralized systems	40 – above 200	20 – 3000

1.1 Stand-alone and monoblock refrigeration systems

Stand-alone commercial refrigeration units are constituted mainly by a single-stage cycle whose components are included in the same enclosure together with the refrigerated cabinet, except for monoblock refrigeration units that serve external cold rooms where they are mounted on the wall or on the ceiling. Typically, these units can be either air or water cooled, and are equipped with hermetic reciprocating compressors, capillary tube or thermostatic expansion valve and fin and coil heat exchangers and in some cases also with internal heat exchanger as shown in Figure 1.1. The cooling capacity ranges from 100 W to a maximum of 5 kW with refrigerant charges from 100 g to 3 kg. In smaller appliances with refrigerant charge below 150 g A3 refrigerants can be used. For larger appliances, instead, A1 and A2L refrigerants generally are used with refrigerant charge limitation according to EN378-1:2016 (CEN, 2016). Beverage coolers, horizontal and vertical display cabinets, ice-cream freezers, vending machines, ice makers are example of stand-alone commercial refrigeration units, and they are shown in Figure 1.2.

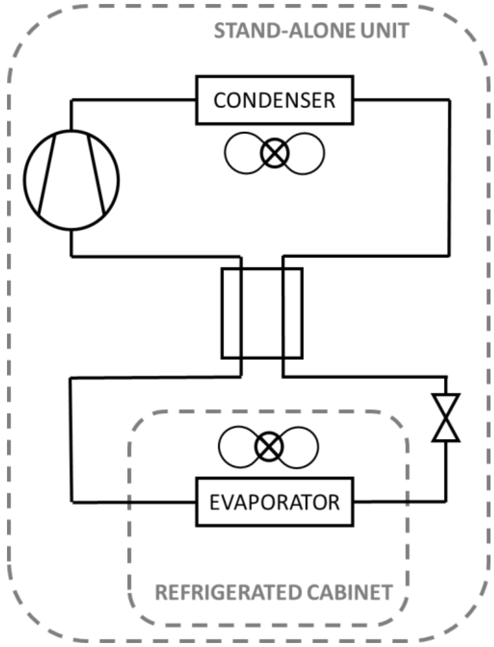

Figure 1.1 – Refrigeration schematic layout

(a)

(b)

(d)

(c)

(e)

Figure 1.2 – Vending machine (a), beverage cooler (b), vertical display cabinet (c) horizontal display cabinet (d) and monoblock refrigeration unit (e)

1.2 Condensing unit systems

Condensing unit systems are equipped mainly by one or more compressors, a condenser and a liquid receiver. They are connected to remote evaporators in cold rooms or remote display cabinets by means of liquid and suction lines having lengths of around tens of meters and height differences that can reach also 10 m between the condensing unit and the remote evaporators / display cabinets. Depending on the site layout, the condensing unit can be installed below or above the evaporators and the connections are made directly on the installation site. The cooling capacity ranges from 100 W to 20 kW with refrigerant charges varying from 1 kg to 20 kg. A refrigeration schematic layout and a simplified installation schemes of condensing units are shown in Figure 1.3.

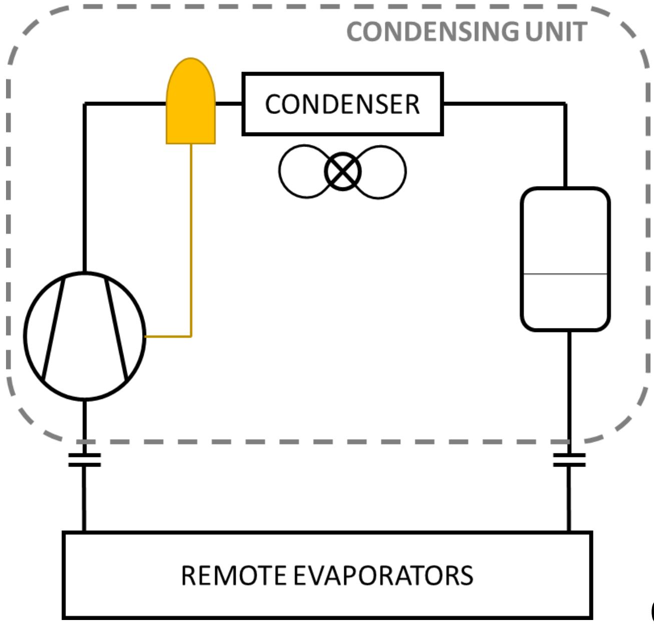

(a)

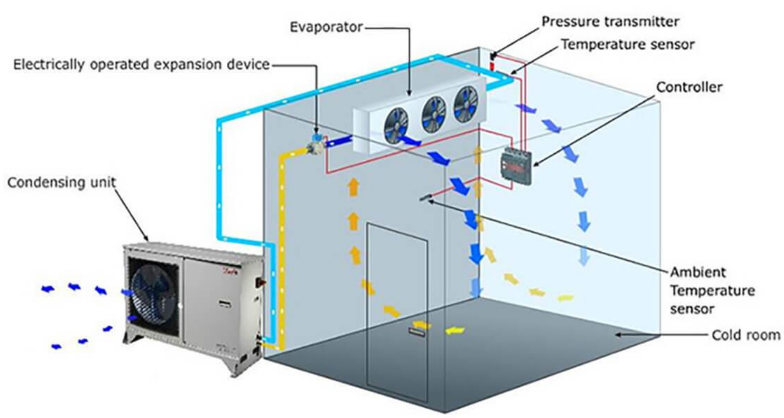

(b)

Figure 1.3 – Refrigeration schematic layout (a), simplified installation scheme (b)

Typically, these units are equipped with semi-hermetic reciprocating or, in newer units, hermetic rotative compressors with fixed or variable speed, variable or fixed speed condenser fans and fin and coil heat exchanger as condenser and a liquid receiver. Compressor oil return management plays an important role in these particular applications due to the lengths of the connection lines. For this reason, an oil separator on the discharge line is always present and traps from evaporator must be also provided to ensure the return of the remaining amount of oil not originally trapped in the separator.

1.3 Centralized systems

Supermarket centralized systems have a cooling capacity between 40 kW to more than 200 kW, depending on the operating temperature ranges (MT or LT). The refrigerant charge goes from 20 kg to 3 tons. The centralized systems can be air cooler, or water cooled, with this latter that rejects heat to the surrounding air or to the ground. Three different architectures are defined:

1) Direct expansion systems
2) Indirect expansion systems
3) Cascade systems

In the direct expansion systems two compressor racks MT and LT, are connected respectively to MT and LT remote display cabinets as shown in Figure 1.4, where a schematic layout of direct expansion supermarket system is represented.
The compressor racks are installed in a machinery room, instead the remote condenser outside the store generally on the rooftop, by means a liquid manifold the refrigerant is distributed to the display cabinets in the sales area and then collected in the suction manifold before entering the compressors. The distance among the components can be roughly 100 m with height differences of maximum 20 m.
Due to the huge amount of refrigerant in the plant, only A1 ASHRAE class refrigerants can be used, such as R404A, R134a and CO_2 in transcritical booster refrigeration system whose schematic layout is shown in Figure 1.5.

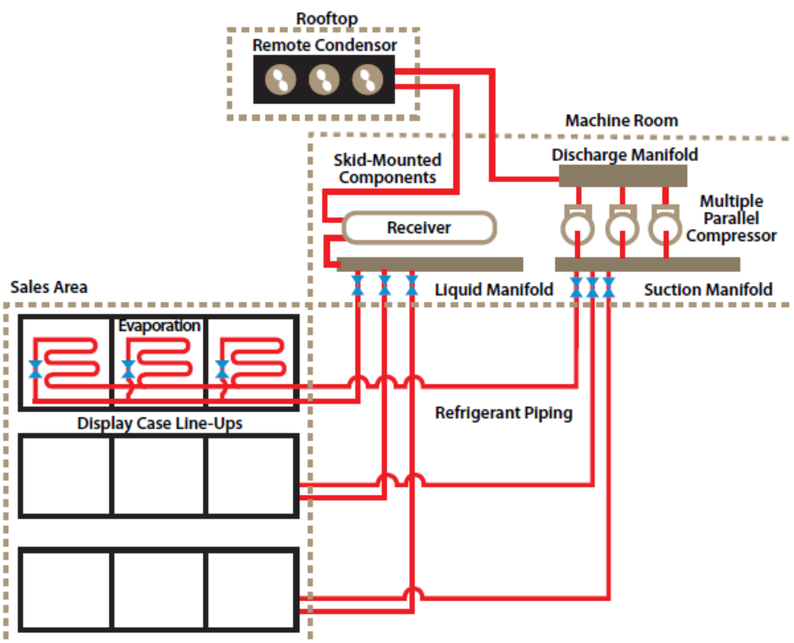

Figure 1.4 – Direct expansion supermarket refrigeration system schematic layout

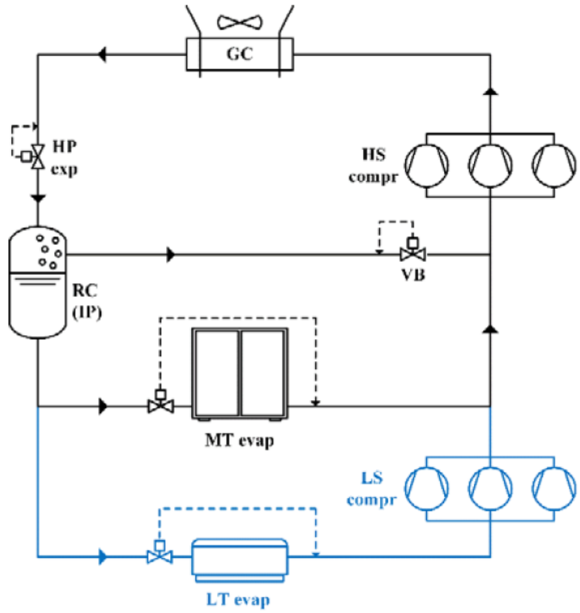

Figure 1.5 – Transcritical booster refrigeration system schematic layout (Gullo et al., 2017)

In this configuration, the refrigerant coming from LT evaporators enters in LT compressor (LS in Figure 1.5) and then it is compressed up to MT evaporating pressure. The two flows from MT evaporators and LT compressor mix each other and then with the flash vapour coming from receiver back pressure valve. Subsequently, the flow enters in MT compressors (HS in Figure 1.5) and then goes into the gascooler in which the pressure is regulated by the back pressure valve HP (more details about gascooler pressure regulation are given in Chapter 3). Finally, the refrigerant is collected in the liquid receiver.
In the indirect expansion system, the refrigerant cools a secondary fluid, generally water-glycol mixture (brine) or liquid carbon dioxide that absorbs heat from the food. A schematic representation of the plant is shown in Figure 1.6.

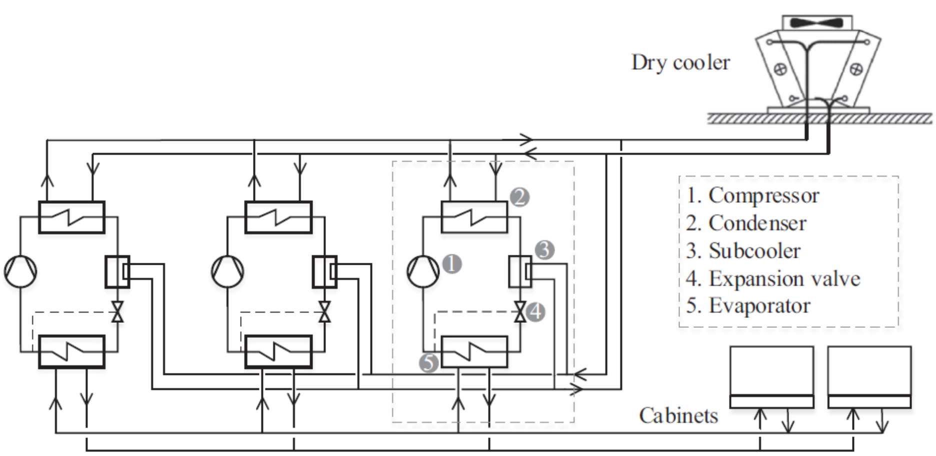

Figure 1.6 - Indirect expansion supermarket refrigeration system schematic layout (Makhnatch et al. 2017)

In this configuration, all the refrigerant containing parts (compressor, condenser, evaporator and expansion valve) are installed in the machinery room with the possibility to use also A2L, A3 or B classified refrigerants according to ASHRAE safety standard, thanks to lower refrigerant charge compared to a direct expansion system and the restricted access inside a machinery room. Instead, the lines with the secondary fluid at evaporator and condenser side (in case of water-cooled systems) could have length around 100 m.
Cascade refrigeration systems are constituted by two refrigerant loops operating at MT and LT conditions. The two loops are connected thermally by means of heat exchangers operating as an evaporator for MT cycle and condenser for LT one. As for the centralized direct expansion systems, the refrigerants that can be employed should have A1 ASHRAE classification since the evaporators are located in the occupied space; the MT refrigeration loop usually is charged with HFC A1 refrigerants, and the LT one can work with CO_2 in subcritical condition. A schematic layout is shown in Figure 1.7. A real image of the main components of supermarket systems is shown in Figure 1.8

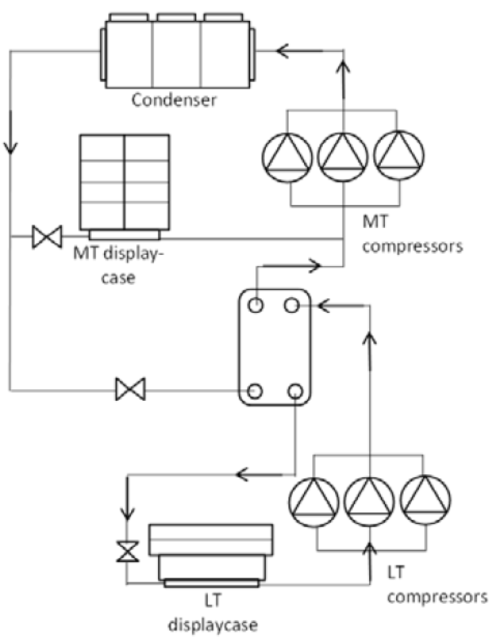

Figure 1.7 – Cascade supermarket refrigeration system schematic layout

(a)

(b)


(c)


(d)

Figure 1.8 – Remote condenser (a), compressor rack (b), horizontal display cabinet (c), vertical display cabinet (d)

Chapter 2 – Energetic and environmental impact of commercial refrigeration and actions for its reduction

In this chapter 2, the actual energetic and environmental impact of commercial refrigeration appliances is presented. Firstly, the actual status of market share, number of installed units is given to the reader to understand the energetic and the environmental impact of the sector. Furthermore, future projections of sold units and greenhouse gases emissions in the "business as usual" and "mitigation" scenarios will be mentioned to highlight the necessity to take countermeasures to reduce them. In the second part of the chapter, the major provisions and agreements to reduce energetic impact and greenhouse gases emissions emended in worldwide and European countries will be presented with their possible impact on commercial refrigeration sector.

2.1 Market status for the commercial refrigeration sector

According to reports of IIR "The Role of Refrigeration in the Global Economy" (2015), roughly 90 million of commercial refrigeration appliances are installed worldwide; Clodic et al. in the report "Alternatives to high GWP HFCs in refrigeration and air-conditioning application" (2014) give an indication of installed units divided by equipment kind as listed in Table 2.1 reporting also the average lifetime.

Table 2.1 – Estimated installed units worldwide divided by commercial refrigeration equipment in 2012 (Clodic et al., 2014)

Equipment	***Average lifetime in years***	***Estimated installed units***
Centralized systems	10	300.000
Condensing units	12	35.000.000
Stand-alone	7	55.000.000

The number of installed units is expected to increase with the growth of worldwide population, higher food demand and the necessity to reduce post-harvest losses (one quarter of the total according to IIR, 2009). In fact, Persistence Market Research (2014) estimated a growth of frozen food market of 30% in 2020, based on 2014 data.

A European Union study (2014) estimated commercial refrigeration market trend in EU28 until 2030, forecasting an increase up to 28% on total stock of appliances as shown in Figure 2.1 than the values of 2004.

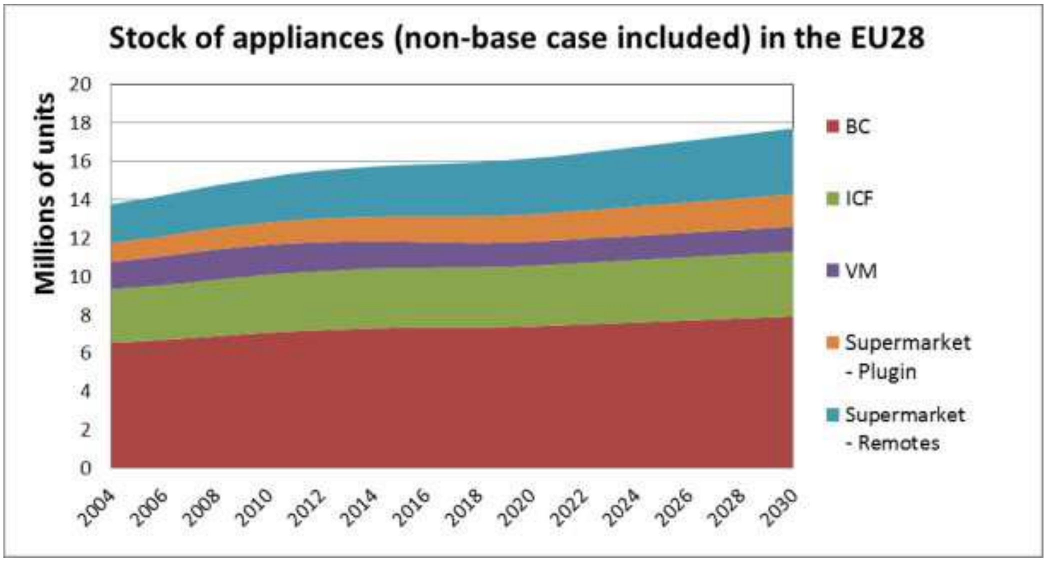

Figure 2.1 – Prediction of stock of commercial refrigeration appliances in EU28 divided by equipment kind (European Commission, 2014)

2.2 Energy and environmental impact

Commercial refrigeration plants must operate continuously during the year in the whole lifetime to ensure food temperature and quality, and for this reason a non-negligible part of electric energy produced worldwide is required to operate them. The IIR (2015) estimated that 17% of total worldwide produced electricity is required for commercial refrigerators. According to a report of UNEP (2002), around 65% of a supermarket energy demand is covered for refrigeration purposes with a centralized system. The energy demand reflects on indirect greenhouses gases emissions related to the electricity production from fossil fuels that depends on the source mix of each country and by the efficiency of the refrigeration system. The increase of installed refrigeration plants worldwide will increase the energy demand.

The refrigerants widely used in commercial refrigeration applications are R404A, R134a and R507A (like R404A but less used) which have very high GWP values determining also a huge direct environmental impact related to refrigerant leakages from the plant during commissioning, operation, maintenance and dismission phases. The leakage ratio ranges between values lower than 1% to 35% depending on the application; according to EPA (2016). In stand-alone hermetically sealed equipment, the leakage ratio is below 1%; for remote condensing units it ranges instead from 5% to 20%; finally, in multiplex centralized systems it is between 10% and 35%. Clodic et al. (2014) estimated the total refrigerant amount in tons present in EU and its value expressed in equivalent tons of carbon dioxide as listed in Table 2.2.

Table 2.2 – Total refrigerant amount and their equivalent carbon dioxide amount in EU in 2012 (Clodic et al., 2014)

Refrigerant	**Total amount in 2012 in EU [tons]**	**GWP**	**Equivalent carbon dioxide amount in millions of tons [MteqCO2]**
R404A	250000	3922	980.5
R507A	33000	3300	108.9
R134a	1200000	1300	1560

R134a amount is not related only to commercial refrigeration appliances since it is used also in domestic refrigeration and automotive air conditioners until 2012.
The increase of commercial refrigeration installations as presented in paragraph 2.1 could reflect in a dramatic increase of HFC consumption as predicted by Zeiger (2015). Based on its actual installations number, future market trends, import and export, initial refrigerant charge and lifetime of refrigeration and air conditioning units, a prediction of HFC and HCFC consumption is carried out in the case of business-as-usual scenario until 2030. The results of the evaluation are shown in Figure 2.2 with the total emissions on the left and the emissions divided for each sector on the right.

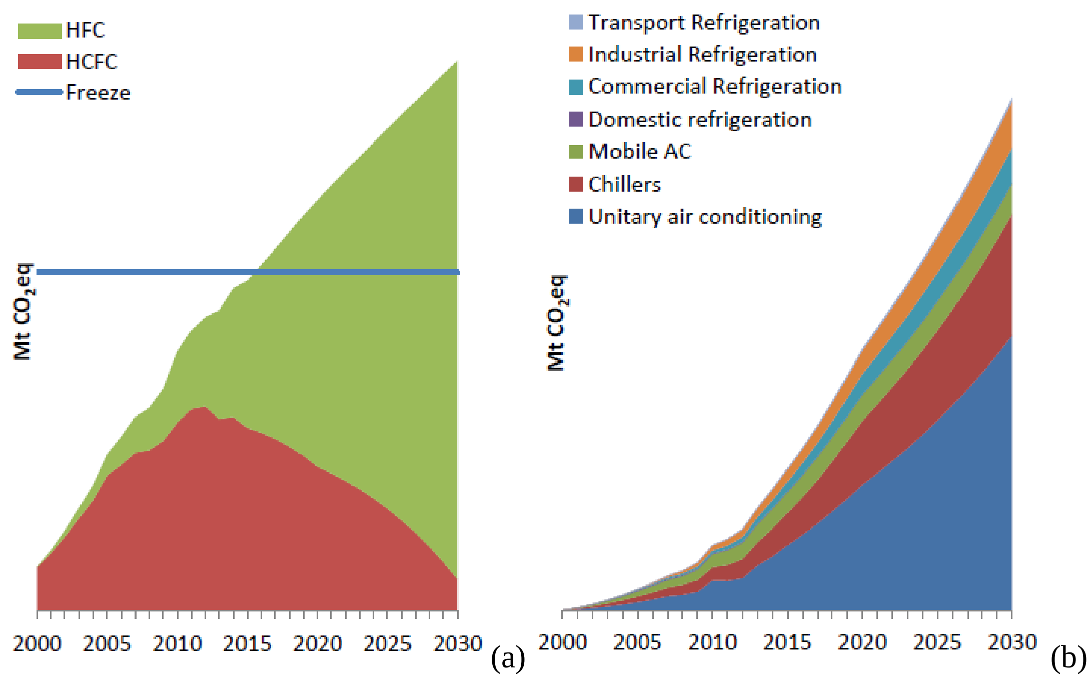

Figure 2.2 – Total HFC and HCFC consumption (a) and divided for each sector (b) in business-as-usual scenario (Zeiger, 2015)

In Figure 2.2a the reduction of HCFC consumption is related mainly on the provision of Montreal Protocol. Instead, the HFC ones are related to the increase of number of installation and the lack of provision to abate them. The horizontal line is referred to the consumption freeze of total HFC amount proposed in EU. In this scenario it is not possible comply with the limit imposed, since the trend

overcomes the freeze level. In Figure 2.2b it is shown that commercial refrigeration sector is the fourth major consumer of HFC refrigerants after unitary and mobile air conditioning units and chillers.
Furthermore, the case of intervention (called in the work "Mitigation Scenario") is also analysed and shown in Figure 2.3. In this scenario, provisions like the shift from high – GWP to low – GWP refrigerants, the increase of system efficiency and the increase of the use of renewable sources to produce electric energy are considered. In Figure 2.3a, the total amount of HFC trend reaches a peak in 2014, after it decrease due to European F-Gas regulation entering in force. In Figure 2.3b, the commercial refrigeration sector is still the fourth major consumer of HFCs.
Environmental Protection Agency (EPA, 2016) estimated a 26% of contribution of commercial refrigeration sector in global HFC emissions in 2020. Moreover, a quadruplication of global HFC emissions until 2030 is expected. The actual trends and their projections highlight the importance of take provisions in worldwide and local (European) scale to reduce the direct impact of refrigeration and air conditioning units.

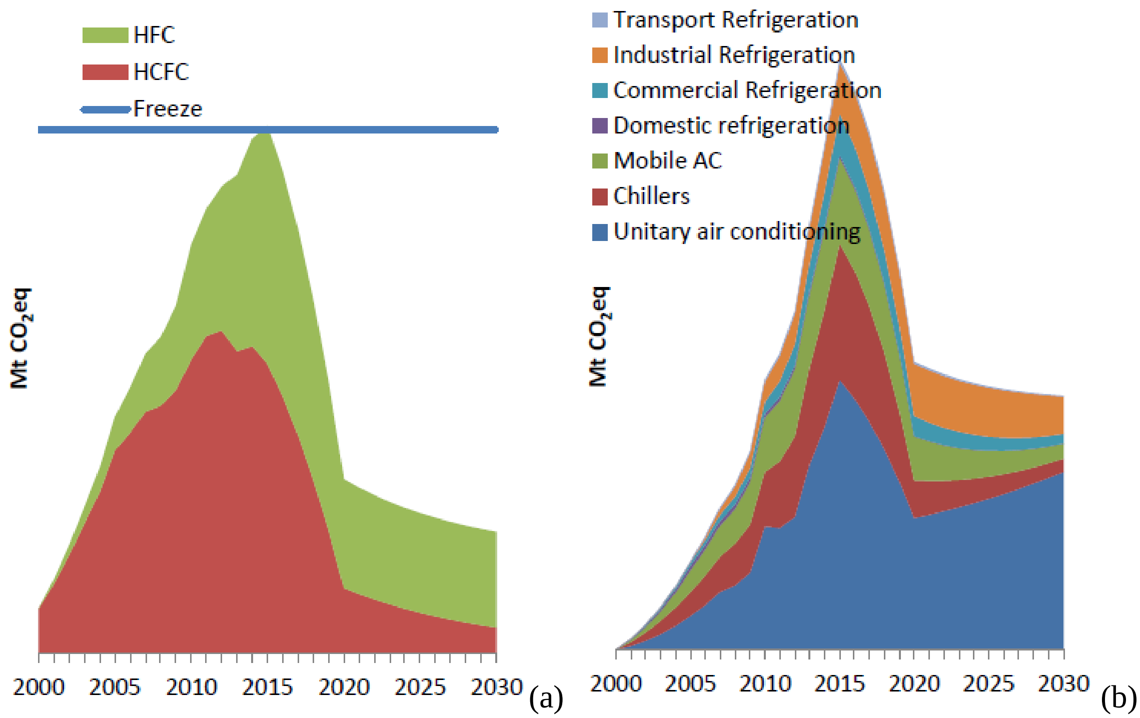

Figure 2.3 - Total HFC and HCFC consumption (a) and divided for each sector (b) in mitigation scenario (Zeiger, 2015)

2.3 Measures to limit the greenhouse gases emissions worldwide and in Europe

The Montreal Protocol (1987) has been ratified by 197 nations to reduce the CFCs and HCFCs substances and related emissions dangerous for the ozone layer, introducing the HFCs. These latter, instead, are dangerous for the global warming and thanks to the Kigali Amendment (entered in force in January 2019) the reduction of these substances is introduced as a further provision of Montreal Protocol. Different reduction schedules, starting from January 1989, are defined based on no - Art. 5 (developed) or Art. 5

(developing) countries for each substance class. In Table 2.3 the deadline to stop the production and consumption of CFC, Halon, HCFC and HFC is reported for no – Art.5 and Art. 5 parties.
According to Kigali Amendment, the HFCs phase-down starts in 2019 for no – Art. 5 countries, instead, it starts in 2024 for Art. 5 ones as shown in Figure 2.4.

Table 2.3 – Deadline for the production and consumption of CFC, Halon, HCFC and HFC substances for no – Art. 5 and Art. 5 of Montreal Protocol

Substances	**no – Art. 5**	**Art. 5**
CFC	1st January 1996	1st January 2010
Halon	1st January 1994	1st January 2010
HCFC	1st January 2020	1st January 2030
HFC	1st January 2019 (first reduction step)	1st January 2024 (first reduction step)

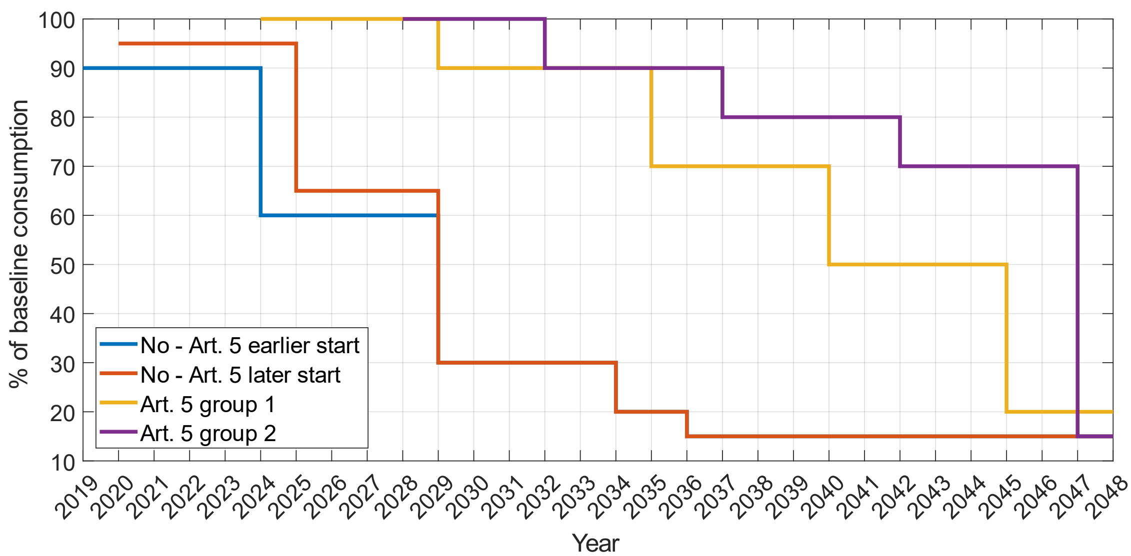

Figure 2.4 – Phase – down schedule of HFCs according to Kigali Amendment

For no – Art. 5 parties the aim is to reduce the consumption of HFCs of 15% until 2036. Instead, the Art. 5 parties are divided in two groups with the objective to reach 20% until 2045 and 15% until 2047 than the initial level for group 1 and 2, respectively.
In the framework of the Montreal Protocol, in the European Union the HFC emissions are regulated by the Paris Agreement (Council Decision (EU) 2016/1841) with the aim to limit the temperature rise below 2°C than pre-industrial time. In 2021 the COP26 renewed the objective of carbon neutrality until 2050 and the reduction of limit on Earth temperature rise to 1.5°C.

2.3.1 *Reduction of direct emissions in Europe: F-Gas regulation (517/2014)*

In European Union, the production and consumption of HFC substances is regulated by the F-Gas regulation (517/2014), entered in force in 2015. The regulation establishes the phase-down schedule of HFC substances, expressed in terms of percentage difference of actual equivalent tonnes of carbon dioxide than a reference value, by means of a quota system institution that the refrigerant manufacturers and distribution channels must follow. The reference value is referred to the manufactured, imported, and commercialized level between 2009 – 2012, and a reduction of 89% must be achieved by all European countries until 2030. The phase-down schedule is shown in Figure 2.5.
The F-Gas regulation imposes also limits on GWP value for the substances that must be used depending on the application and the starting day of the prohibition. In Table 2.4, the dates of prohibitions are reported regarding commercial refrigeration appliances.

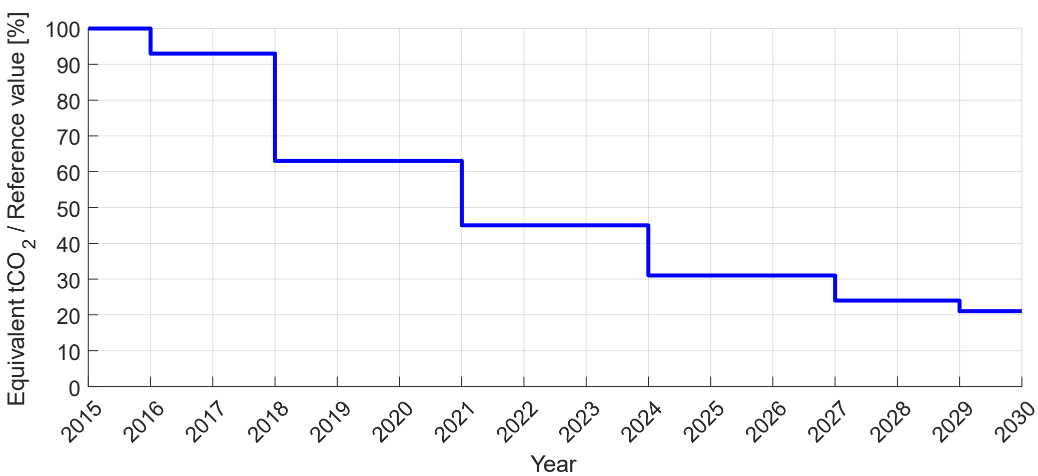

Figure 2.5 – Phase – down schedule of HFCs according to F-Gas regulation (517/2014)

Table 2.4 – Date of prohibition of HFCs usage basing on GWP value for commercial refrigeration appliances according to F-Gas regulation

<table>
<tr><th colspan="2">Equipment</th><th>Date of prohibition</th></tr>
<tr><td rowspan="2">Refrigerators and freezers for commercial use (hermetically sealed equipment)</td><td>That contain HFCs with GWP of 2500 or more</td><td>1 January 2020</td></tr>
<tr><td>That contain HFCs with GWP of 150 or more</td><td>1 January 2022</td></tr>
<tr><td colspan="2">Stationary refrigeration equipment, that contains, or whose functioning relies upon, HFCs with GWP of 2500 or more except equipment intended for application designed to cool products to temperatures below -50°C</td><td>1 January 2020</td></tr>
<tr><td colspan="2">Multipack centralized refrigeration systems for commercial use with a rated capacity of 40 kW or more that contain, or whose functioning relies upon, fluorinated greenhouse gases with GWP of 150 or more, except in the primary refrigerant circuit of cascade systems where fluorinated greenhouse gases with a GWP of less than 1500 may be used</td><td>1 January 2022</td></tr>
</table>

According to Table 2.4 and the GWP value of the widely used refrigerants listed in Table 2.2, it can be concluded that R404A and R134a will be forbidden in new stand-alone commercial refrigeration units (hermetically sealed systems) after 2020 and 2022 respectively. The R404A is banned also in higher capacity condensing units after January 2020. Finally, R404A is forbidden also in direct or indirect expansion centralized supermarket refrigeration systems after 1st January 2022, with an exception for cascade systems whose primary circuit can be still charged with R134a. Alternative refrigerants to R404A and R134a have been identified and they are listed in Table 2.5 with their value of GWP and ASHRAE safety class.

Table 2.5 – Alternative refrigerants for commercial refrigeration appliances with GWP and ASHRAE safety classification

Refrigerant	**GWP**	**Ashrae safety class**
R452A	2140	A1
R407H	1495	A1
R449A	1397	A1
R448A	1387	A1
R454C	148	A2L
R455A	145	A2L
R1234ze	7	A2L
R290	3	A3
R744	1	A1
R1234yf	0	A2L

In the Table 2.5 mid and long – term scenario refrigerants are listed. One point worth noting is that there is not a single replacement, due to different thermodynamic characteristics (the new blends are characterized by a not negligible glide as R404A in two phase region), flammability issues (some of them are classified as A2L and A3) for which countermeasure should be taken. R452A, R448A, R449A and R407H, can be used as R404A drop-ins since they are classified as A1 and have similar thermodynamic properties and minor modifications to the plant are required to adapt the new refrigerants in hermetically sealed plants until 2022. R455A, R454C and R290 are considered long-term replacement of R404A thanks to their low GWP value. For these refrigerants, a system re-design is needed to ensure good performances and safety operation especially against flammability issues; the same comments can be extended also for R134a replacements HFOs R1234ze and R1234yf. A technical constraint to be considered in the design phase is the refrigerant charge limit based on plant ubication class, access category and refrigerant ASHRAE class according to EN378-1:2016 (CEN, 2016).
It is then possible to build a refrigerant versus equipment matrix as shown in Table 2.6. It is important to underline that the projections presented in Table 2.6 are based only on the limits of GWP according to F-Gas regulation and charge limitation, without considering the actual market trends and other technical aspects.

Table 2.6 – Future projection for mid- and long-term scenarios replacements basing on F-Gas regulation and EN378-1:2016 refrigerant charge limits

Equipment	**R452A**	**R407H**	**R449A**	**R448A**	**R134a**	**R454C**	**R455A**	**R1234ze**	**R1234yf**	**R290**	**R744**
Stand-alone	M-T	M-T	M-T	M-T	M-T*	L-T	L-T	L-T*	L-T*	L-T	×
Condensing units	L-T	L-T	L-T	L-T	×	L-T	L-T	×	×	×	L-T
Centralized direct expansion systems (above 40 kW)	M-T	M-T	M-T	M-T	M-T	×	×	×	×	×	L-T
Centralized indirect expansion systems (above 40 kW)	M-T	M-T	M-T	M-T	M-T*	L-T	L-T	L-T*	L-T*	×	L-T
Cascade refrigeration systems	M-T	M-T	M-T	M-T	L-T*	L-T	L-T	L-T*	L-T*	×	L-T**
M-T = mid-term scenario L-T = long-term scenario × = not used											
* Only medium temperature refrigeration condition or primary circuit in case of cascade systems											
** Only in secondary refrigeration loop											

An implication of F-Gas regulation is the increase of high-GWP refrigerant prices due to production reduction and increase of stocks in warehouses as shown in Figure 2.6.
R404A and R134a prices are increased up to 10 times in 2017 and 8 times in 2018 than the 2014 levels, respectively. In fact, since HFC quotas are expressed in amount of equivalent carbon dioxide tonnes that are directly proportional to GWP value and to the weight of the substance, to maintain similar incomes before F-Gas regulation levels, the stakeholders should increase the price of residual stocks of high - GWP refrigerants and at the same time shifting on the low - GWP ones.

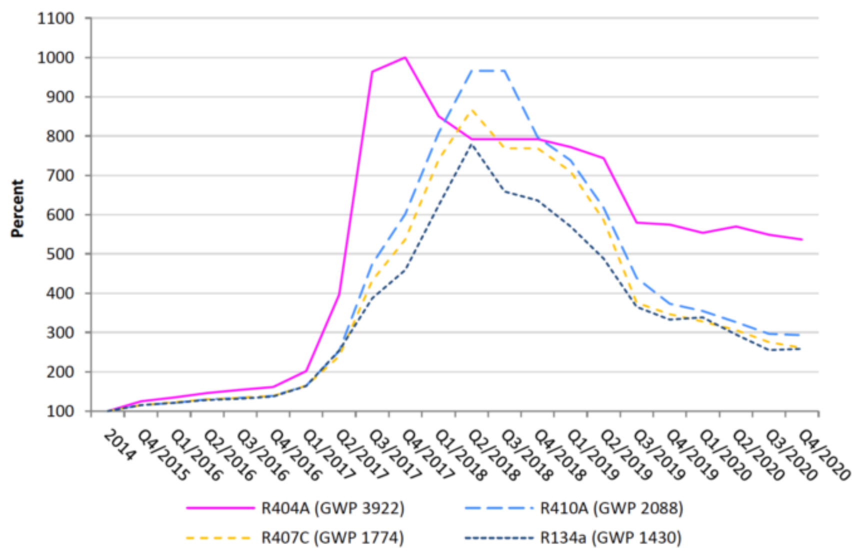

Figure 2.6 – Refrigerant prices trends from 2014 to 2020
(https://www.zerosottozero.it/2021/04/16/europa-hfc-prezzi-stabili-ma-leggero-aumento-della-domanda-nel-quarto-trimestre-2020/)

2.3.2 Reduction of energetic impact and indirect emissions in Europe: Ecodesign directive 2009/125/EC and energy labelling regulation (EU) 2017/1369

A countermeasure to reduce the indirect emissions is to cover the energy demand with higher rate of renewable sources. But since this provision does not depend by the refrigeration system is beyond to the scope of the thesis.
To reduce the energy demand and consequently the indirect emissions of commercial refrigeration systems, the efficiency of components and of the whole system must be improved with a proper design. The most used indexes to measure the energy performance of a refrigerator basing on the application and capacity range are COP, SEPR and EEI. They are defined as follow:

$$COP = \dot{Q}_{ev}\,\dot{L}_{el}^{-1} \qquad \text{Eq. 2.1}$$

$$SEPR = \sum_{j=1}^{nbin}\left(\dot{Q}_{dm,j} d_j\right)\left\{\sum_{j=1}^{nbin}\left[\dot{Q}_{dm,j} d_j \left(COP_j\right)^{-1}\right]\right\}^{-1} \qquad \text{Eq. 2.2}$$

$$EEI = AE\ SAE^{-1} \qquad \text{Eq. 2.3}$$

In the Eq. 2.1 $\dot{Q}_{ev}$ and $\dot{L}_{el}$ are respectively the cooling capacity and the power absorbed by the unit expressed in [W], instead, the seasonal energy performance ratio is calculated by means Eq. 2.2 using bin method dividing the user yearly energy demand ($\dot{Q}_{dm,j} d_j$) [kWh] with the electric energy absorbed by the unit ($\dot{Q}_{dm,j} d_j \left(COP_j\right)^{-1}$) [kWh], according to EN13215:2016 (CEN, 2016) standard. Finally, EEI is calculated with Eq. 2.3 where AE and SAE are the annual energy consumption and standard annual energy consumption [kWh/a] as defined in 2017/1369 EU regulation (European Commission, 2017).

In Europe, Ecodesign directive 2009/125/EC (European Parliament, 2009) establishes the criteria of environmentally sustainable requirements for energy-related products. By means of the executive regulation 2015/1095 (European Commission, 2015), minimum energy efficiency thresholds are imposed on professional refrigerated storage cabinets, blast cabinets, condensing units and process chillers to be sold in European Union. Referring to the condensing units, COP and SEPR threshold values are imposed depending on declared operating range, MT or LT refrigeration condition, and on the rated cooling capacity as shown in Figure 2.7. The values reported are valid from 1st July 2018 and, if the unit is charged with a refrigerant having GWP lower than 150, the value is reduced of 10%.

Operating temperature	Rated capacity P_A	Applicable ratio	Value
Medium	0,2 kW≤ P_A ≤ 1kW	COP	1,40
	1 kW< P_A ≤ 5 kW	COP	1,60
	5 kW < P_A ≤ 20 kW	SEPR	2,55
	20 kW < P_A ≤ 50 kW	SEPR	2,65
Low	0,1 kW≤ P_A ≤ 0,4 kW	COP	0,80
	0,4 kW< P_A ≤ 2 kW	COP	0,95
	2 kW < P_A ≤ 8 kW	SEPR	1,60
	8 kW < P_A ≤ 20 kW	SEPR	1,70

Figure 2.7 – COP and SEPR threshold values for condensing units in force by 1st July 2018 according to regulation 2015/1095 (European Commission, 2015)

The maximum value of EEI is imposed to direct sales refrigerators, belonging to stand-alone commercial refrigeration unit category, with the regulation 2019/2024 (European Commission, 2019) entered in force on 1st March 2021. The thresholds are shown in Figure 2.8, and they are referred to two periods: the first from the 1st March 2021 (Figure 2.8a) and the second from 1st September 2023 (Figure 2.8b) with new values.

	EEI
Ice-cream freezers	80
All other refrigerating appliances with a direct sales function	100

(a)

	EEI
Ice-cream freezers	50
All other refrigerating appliances with a direct sales function, except refrigerated drum vending machines	80

(b)

Figure 2.8 – Maximum values of EEI imposed to direct sales refrigerators and ice-cream freezers starting from 1st March 2021 (a) and from 1st September 2023 (b) according to regulation 2019/2024 (European Commission, 2019)

The regulation 2017/1369 (European Commission, 2017), instead, establishes the criteria of energy efficiency classification and labelling; its executive regulation 2019/2018 (European Commission, 2019) is referred to refrigerating appliances having a direct sales function. These rules are applied to stand-alone commercial refrigeration units such as vending machines, vertical and horizontal display cabinets, beverage coolers and ice-cream freezers. The remote evaporators and monoblock refrigeration units are excluded. The energy efficiency classification according to regulation 2019/2018 (European Commission, 2019) is shown in Figure 2.9 where the class is associated with the EEI (energy efficiency index) range.
The regulation establishes the criteria for the label design to be applied on the unit, as shown in Figure 2.10a, 2.10b and 2.10c for direct sales refrigerators, beverage coolers and ice-cream freezers respectively.

Energy Efficiency Class	EEI
A	$EEI < 10$
B	$10 \leq EEI < 20$
C	$20 \leq EEI < 35$
D	$35 \leq EEI < 50$
E	$50 \leq EEI < 65$
F	$65 \leq EEI < 80$
G	$EEI \geq 80$

Figure 2.9 – Energy efficiency classification according to regulation 2019/2018 of European Commission

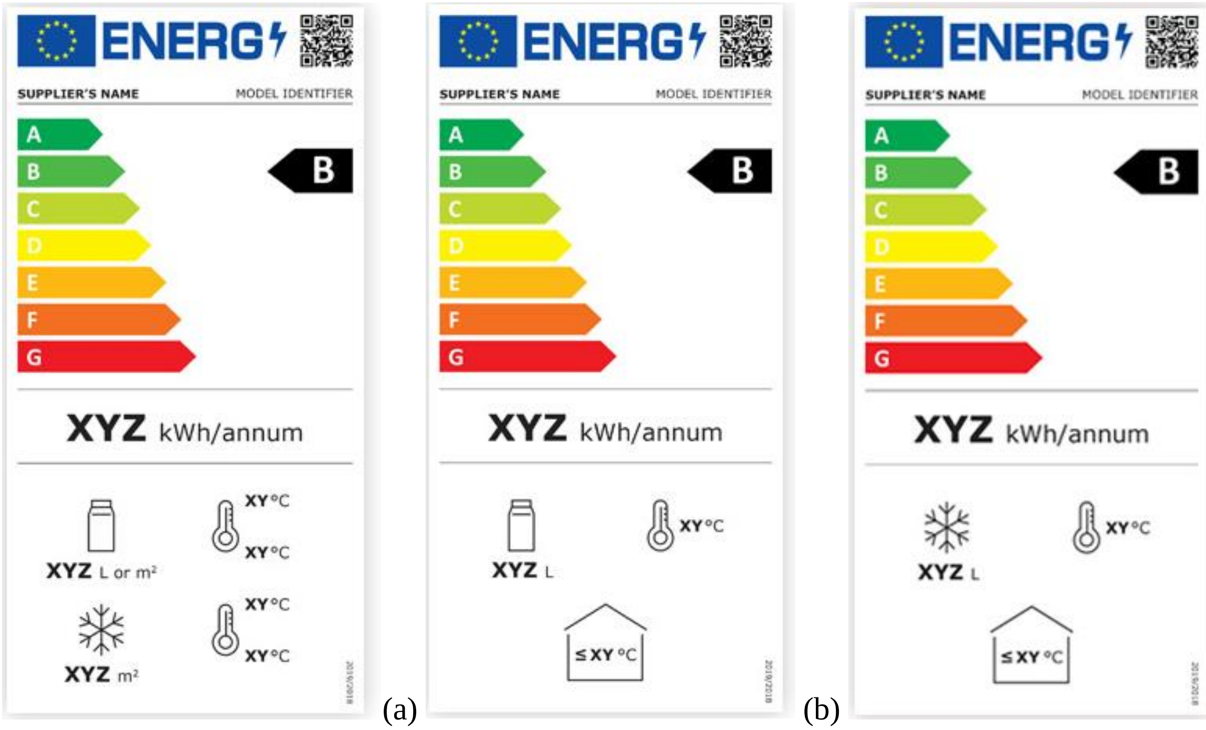

(a) (b) (c)

Figure 2.10 – Energy labels for direct sales refrigerators (a), beverage coolers (b) and ice-cream freezers (c) according to regulation 2019/2018 of European Commission

Chapter 3 – State of the art on low – GWP refrigerants in commercial refrigeration systems

In this chapter a state of the art on low – GWP refrigerants in the commercial refrigeration sector is presented. The chapter is divided in two parts: in the first one, studies about low – GWP blends and hydrocarbons, mostly used in small commercial refrigeration appliances, are reviewed including also works containing environmental impact studies. In the second part, the state of the art on the use of carbon dioxide as refrigerant is presented, mostly regarding energy and environmental assessment of supermarket refrigeration systems with modelling approaches and others relating on experimental activities on field tests or laboratory test benches in case of small cooling capacity appliances.

3.1 Low – GWP blends and hydrocarbons

3.1.1 Theoretical thermodynamic comparison studies

In the last decade, especially in Europe, a refrigerant shift in small commercial refrigeration appliances is occurring due to the limits imposed by F-Gas regulation as discussed in Chapter 2. The research of new blends starts from molecule composition investigation and the development of models to evaluate thermophysical properties. A first study relying on the development of thermodynamic models to evaluate the properties of alternative refrigerants used in refrigeration and air conditioning sector is carried out by McLinden et al. (1997). The authors developed models to be applied on both pure and refrigerant mixtures by means of the use of mixing parameters added to the equation of state. The authors obtained high grade of accuracy assessing their developed method with Helmotz energy mixture model of Lemmon and Jacobsen.

Domanski et al. (2013) carried out a thermodynamic study of different substances starting from a database of 100 million; then the database is further reduced to 1200 and finally to less than 65, after the screening and the application of constraints on thermodynamic characteristics, toxicity, flammability, and chemical stability of the molecule inside the plant and in the atmosphere. This latter characteristic affects the GWP value. A fair comparison is carried out by considering a theorical thermodynamic cycle, of different system architectures, with the definition of Pareto front between the reciprocals of volumetric cooling effect Q_{vol} (1 Q_{vol}^{-1}) and COP (1 COP^{-1}) as shown in Figure 3.1 where each refrigerant is represented with scatters.

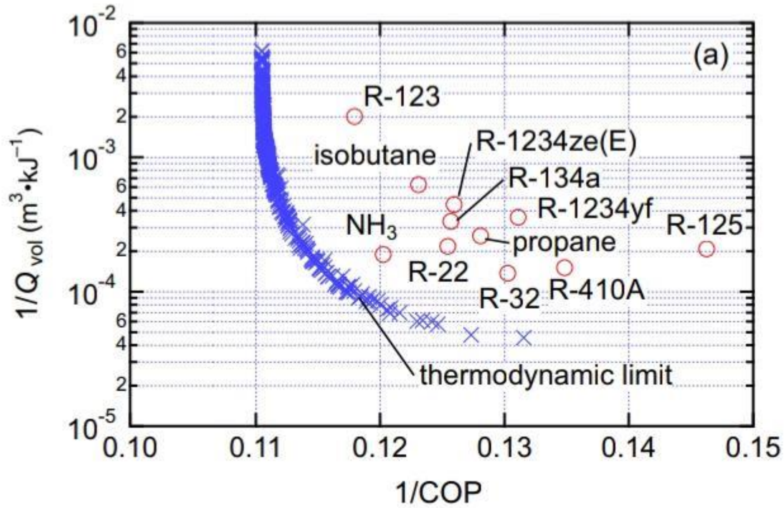

Figure 3.1 – Pareto front (x) and defined substances (o) as a function of reciprocal volumetric cooling effect and COP at T_{evap} = - 10°C and T_{cond} = 40°C (Domanski et al., 2013)

A trade-off is found between the volumetric cooling effect and COP: a high value of this latter is found in refrigerants with high critical temperature, but lower volumetric cooling effect has been found. From the screening process emerged that only a small number of substances can be suitable, and they are blends of R134a, R32, R125 and R143a or natural refrigerants such as hydro-fluoro-olefins, hydrocarbons (propane, iso-butane), ammonia and carbon dioxide. The authors stated that, due to high taxation in EU, the costs of high – GWP HFCs is increasing, advantaging the low – GWP ones. It is found that the optimal low – GWP refrigerant is not the same for all applications, but it should be selected considering several trade-offs between thermodynamic characteristic, safety (toxicity and flammability) and environmental impact.

These results are extended in Domanski et al. (2017) where the same refrigerants are compared with the reference refrigerants R410A and R404A, in air conditioning and refrigeration operating conditions respectively. Three refrigerant circuit diagrams are considered with the assumptions of finite temperature difference between air and refrigerant in heat exchangers, isentropic efficiency equal to 70% and pressure drops inside the heat exchangers. The simulated reverse vapour cycle diagrams are shown in Figure 3.2.

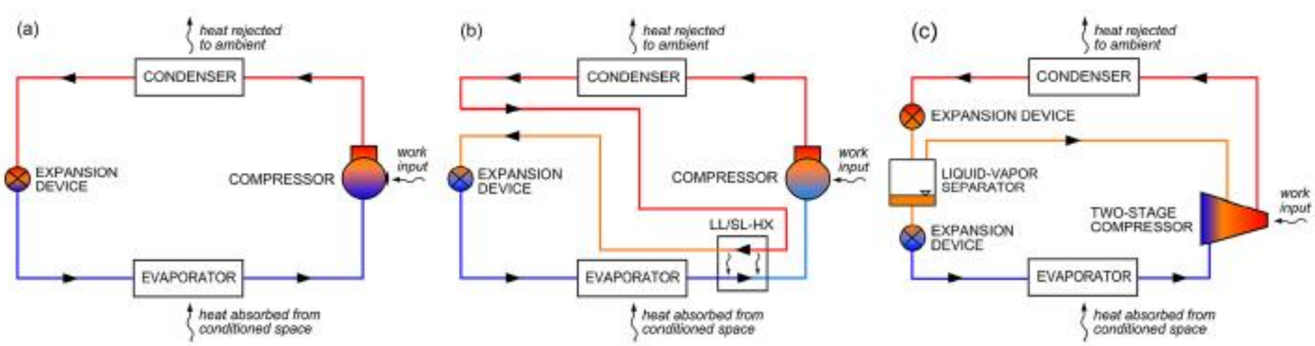

Figure 3.2 – Simulated reverse vapour diagram cycles, basic cycle (a), cycle with liquid line / suction line heat exchanger (LL/SL) (b), two – stage economizer cycle (c) from Domanski et al. (2017)

The results are presented in terms of dimensionless COP and volumetric efficiency referred to R410A and R404A. Firstly, the results between ideal and real thermodynamic cycle are compared. Then, the effects of the different plant schemes on performances and the difference of refrigerants basing on their own thermodynamic characteristics are compared. Considering the case of refrigeration operating conditions with R404A, the differences between basic cycle and two – stage economizer cycle are illustrated as shown in Figure 3.3.

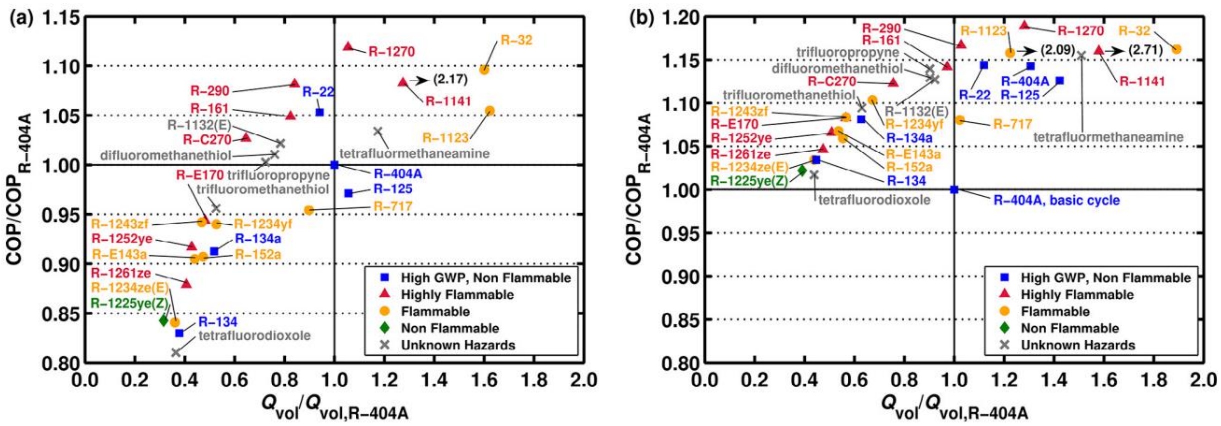

Figure 3.3 – Dimensionless results (referred to R404A) of simulations in refrigeration operating condition of screened substances for basic refrigeration cycle (a) and two-stage economizer cycle (b) (Domanski et al., 2017)

In Figure 3.3b the COP values are higher than the ones in Figure 3.3a thanks to the advantage of the two-stage economizer refrigeration cycle than the basic one. Most of the evaluated substances have lower COP value than R404A in the basic cycle, while the opposite situation occurs with two-stage refrigeration cycles. Moreover, most of the low – GWP substances are flammable or highly flammable, since these two characteristics are related one to each other. In fact, higher number of halogenated groups (fluorine, chlorine and bromine) increase the chemical stability of the molecule with a reduction of flammability as shown in Figure 3.4. Moreover, higher molecule stability leads higher GWP value. A double bond between the carbon atoms helps to reduce the GWP, but at the same time it increases the flammability.

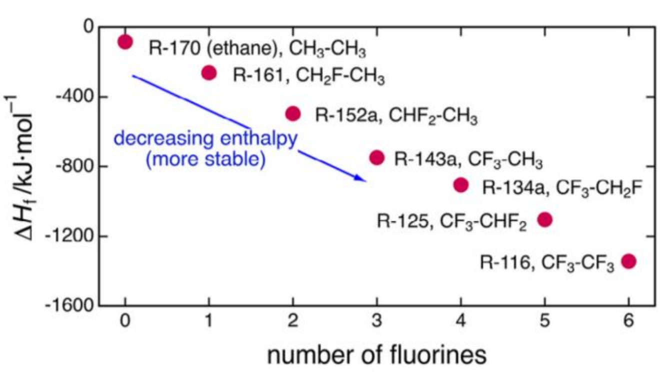

Figure 3.4 – Heat of formation and number of fluorines for different two carbons HFC substances (Domanski et al., 2017)

Heredia-Aricapa et al. (2019), reviewed the possible low – GWP mixtures replacement of R134a, R404A and R410A in refrigeration and air conditioning appliances. The results of thermodynamic analysis are reported in Figure 3.5a, 3.5b and 3.5c, respectively, for R134a, R404A and R410A replacements, where pressure – enthalpy diagrams are shown. The main hypotheses are isentropic compression, no pressure drops in heat exchangers and isenthalpic expansion process.

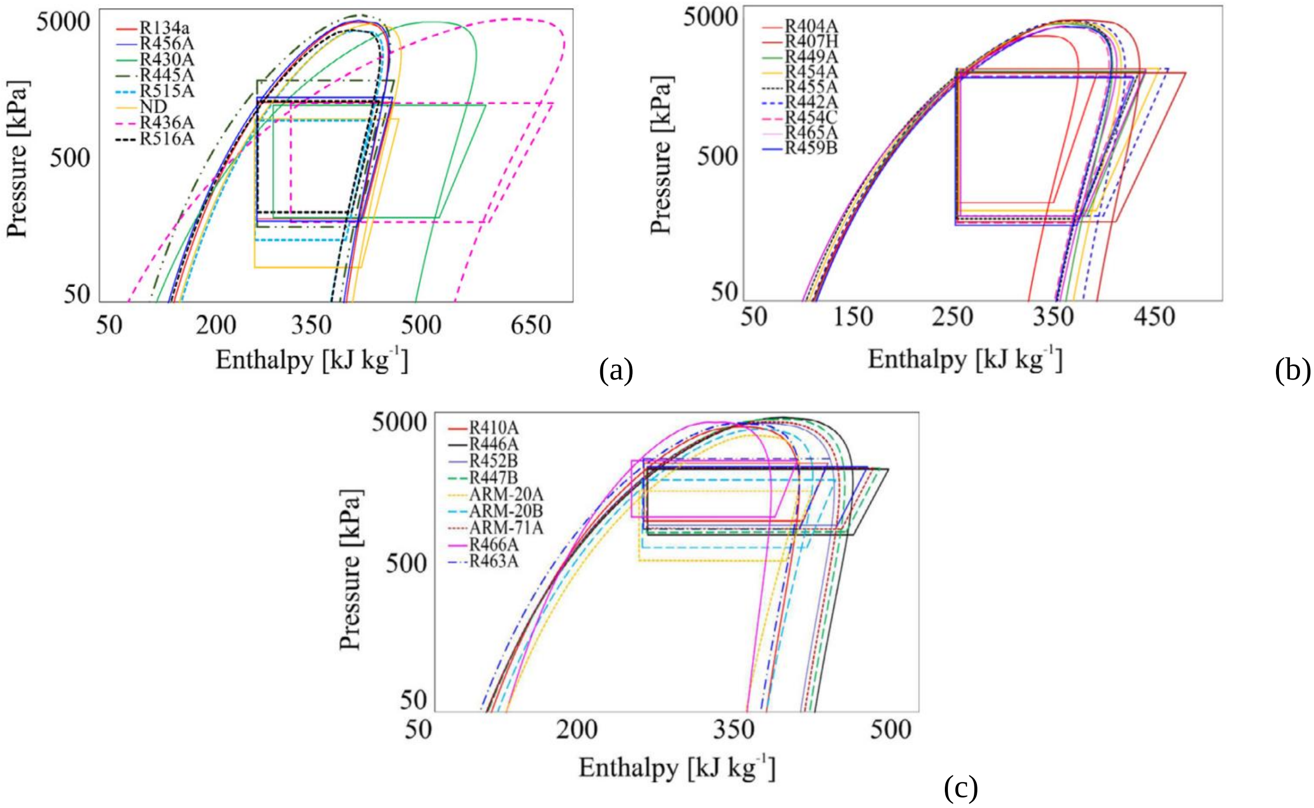

Figure 3.5 – Pressure – enthalpy thermodynamic cycle of R134a (a), R404A (b) and R410A (c) low – GWP mixtures replacements (Heredia-Aricapa et al., 2019)

For R134a replacements, little differences have been found in saturation curves except for R430A and R436A which have higher latent heat. In Figure 3.5b, instead, the replacements have a wider saturation curve width than R404A. Finally, R410A is in the middle in terms of latent heat. Furthermore, the COP of the thermodynamic cycles is evaluated and reported in Figure 3.6. Each refrigerant is indicated by each bar where GWP value and ASHRAE safety classification index are reported. From Figure 3.6, the low – GWP mixtures having the highest COP value are R430A, R407H and R466A that are the replacement of R134a, R404A and R410A respectively. R430A and R407H have GWP value of 110 and 1378 meaning that the first can be used as long alternative refrigerant (after 2022) and the second as only mid-term (until 2022) replacement according to F-Gas regulation in hermetically sealed commercial refrigeration appliances. R466A GWP value is equal to 696, below of value limit of 750 for split type air conditioners. In terms of ASHRAE safety class index, the R430A is A3, R407H is A1 and R466A is A2L. Other R134a good low – GWP mixtures replacements are R515A and R516A with the last being A2L and that can be considered a long – term alternative thanks to its GWP = 95. R459B is another feasible R404A long term alternative since it has the second highest COP value, it is A2 class and has a

GWP = 143. Finally, ARM-20A can be another long-term alternative to R410A with its GWP = 139 and the lower flammability (A2L, ASHRAE class).

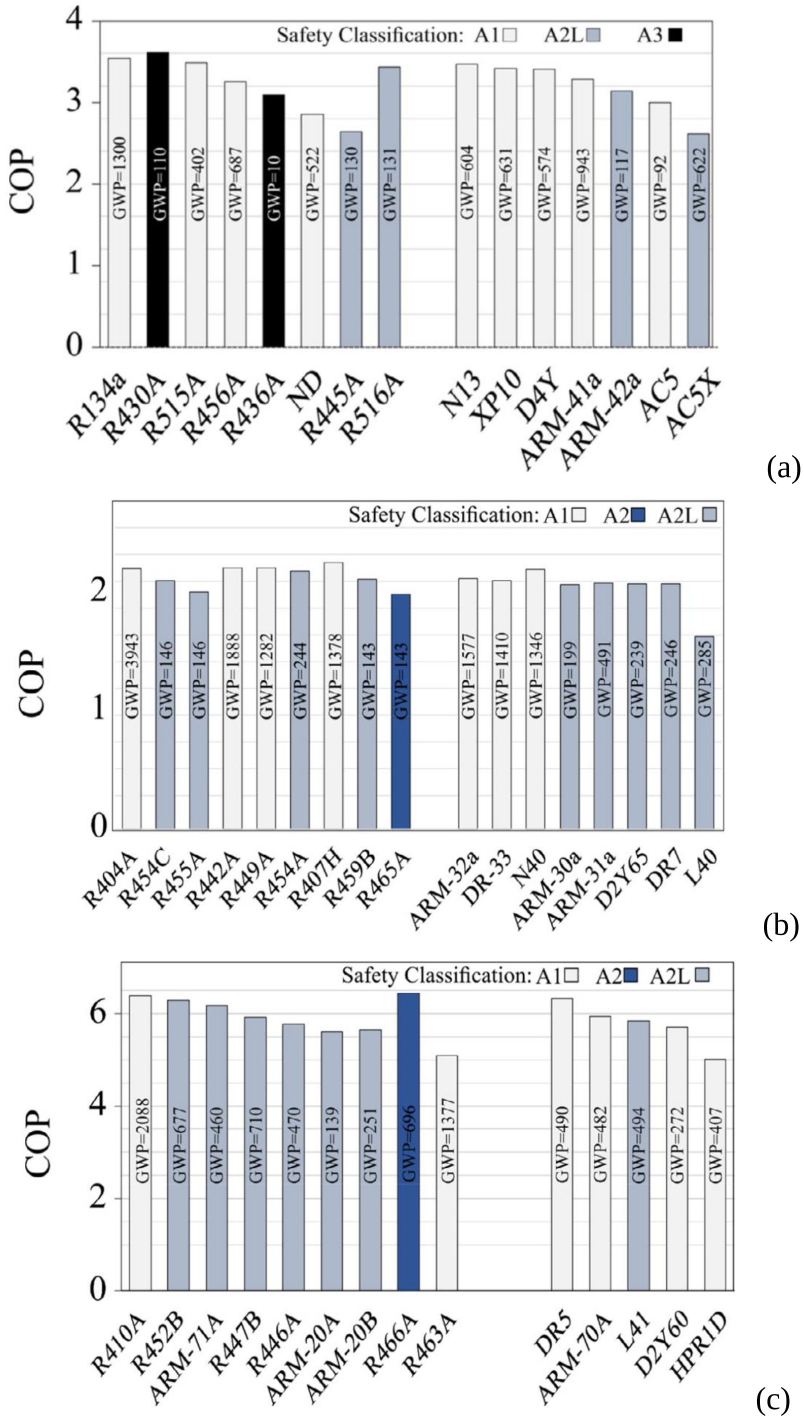

Figure 3.6 – COP, GWP and Ashrae safety classification index for each low – GWP mixture replacement of R134a (a), R404A (b) and R410A (c) (Heredia-Aricapa et al., 2019)

3.1.2 Experimental studies

Also, experimental assessments are carried out to compare the different low – GWP replacements with the reference fluids. Mota-Babiloni et al. (2018), analysed experimentally the two blends R454C and R455A as R404A replacement in a one-stage vapour compression cycle test bench with internal heat exchanger (IHX) shown in Figure 3.7.

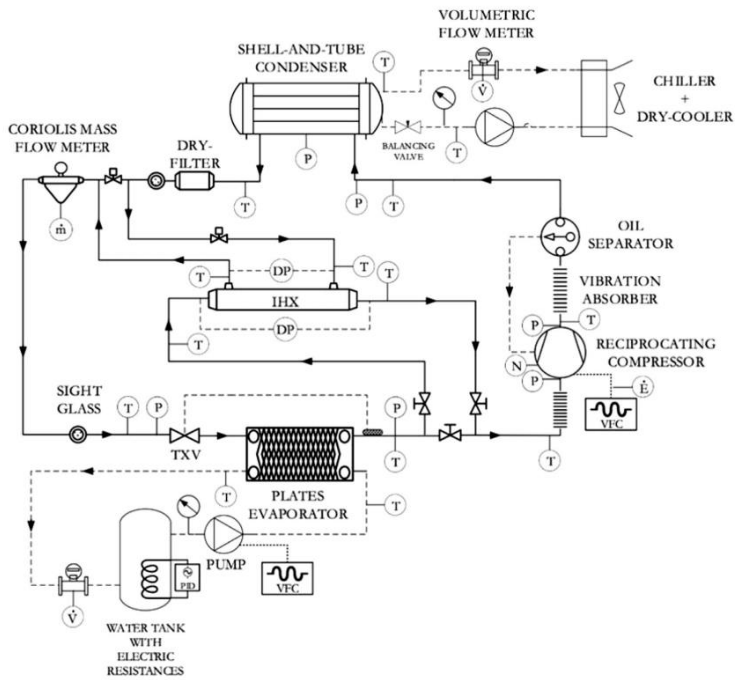

Figure 3.7 – Experimental test bench used in Mota-Babiloni et al. (2018)

Tests at different condensing and evaporating temperatures representing the medium temperature and low temperature refrigeration conditions are carried out. From the results emerged that R454C and R455A have COP 15% and 10% higher than the one of R404A. Conversely, the cooling capacity difference is within the measurement uncertainty. Even if the presence of a IHX is beneficial for system performances, the authors stated that the new mixtures can be used in the same plant without it, since only 4% COP improvement is measured, with the compressor discharge temperatures are close to the operational limit value. The discharge temperatures, cooling capacity and coefficient of performance are shown in Figure 3.8 as a function of evaporating temperatures.

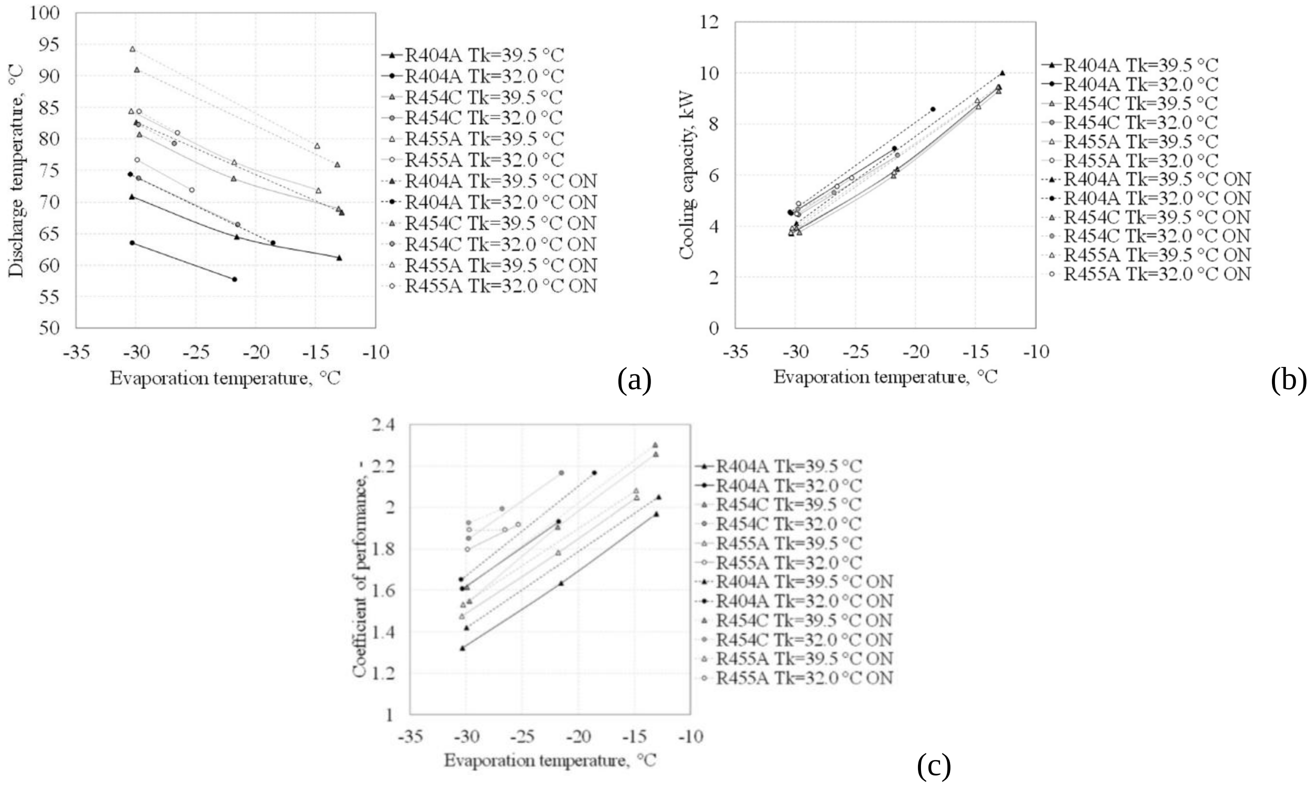

Figure 3.8 – Measured discharge temperature (a), cooling capacity (b) and coefficient of performance (c) as a function of evaporating temperature for all tested refrigerants (Mota-Babiloni et al., 2018)

Among the R404A alternatives studied by Heredia-Aricapa et al. (2019), R407H is analysed experimentally by Tammaro et al. (2018) in which the authors carried out an experimental campaign on a walk-in monoblock refrigeration unit. A soft optimization of a walk-in monoblock refrigeration unit is performed in terms of capillary length tube and refrigerant charge with R407H and R452A using similar approach of Pisano et al. (2014). The results have been compared to the ones of R404A in standard configuration. The cooling capacity with R407H is slightly lower than that of R404A. Instead, it has higher coefficient of performance with a 60% longer capillary and 17% less refrigerant charge with benefits in running and set-up costs. Finally, the coefficient of performance of R407H in the optimized configuration is found to be 4% higher than the one of R452A tested with the same configuration of refrigerant charge and capillary length tube of R404A. A summary of the results is reported in Table 3.1, where each configuration is indicated in terms of dimensionless refrigerant charge and capillary length tube (referred to the one with R404A), and the results of average values of evaporating and condensing temperatures, evaporator superheat, condenser subcooling, compressor discharge temperature and dimensionless cooling capacity and COP (referred to R404A) are reported.

Table 3.1 – Results of comparison among analysed blend in the optimal configuration (Tammaro et al., 2018)

Fluid	Capillary L (norm.)	Charge (norm.)	$T_{ev,mid}$	$T_{co,mid}$	SH_s	SC	$T_{discharge}$	$Q_{ev,\ norm}$	COP
	-	-	*[°C]*	*[°C]*	*[K]*	*[K]*	*[°C]*	-	-
R404A	1	1	-13	45.9	17.2	3	82.9	1	1
R407H	1.6	0.83	-12.2	45.4	14.1	3.7	110.2	0.95	1.08
R452A	1	1	-12.7	47.7	14	3.2	87.2	0.94	1.04

R407H is studied also by Llopis et al. (2017), considering a direct expansion commercial refrigeration system (composed by compressor-condenser-receiver unit connected to a commercial horizontal island display cabinet for frozen product) by means of experimental campaign carried out in a climatic chamber. Tests with -20°C product temperatures and three values of ambient temperature 25°C, 35°C and 45°C with mixtures of R404A and R407H are carried out. 0%, 10%, 20%, 30% and 100% are considered as R407H weight percentages being R404A its complement. From the experimental campaign it emerged that the increasing of R407H percentage causes an increase of COP, compressor discharge temperature and cooling capacity as shown in Figure 3.9 where 100% of R404A and 100% of R407H are compared for different values of condensing temperatures.

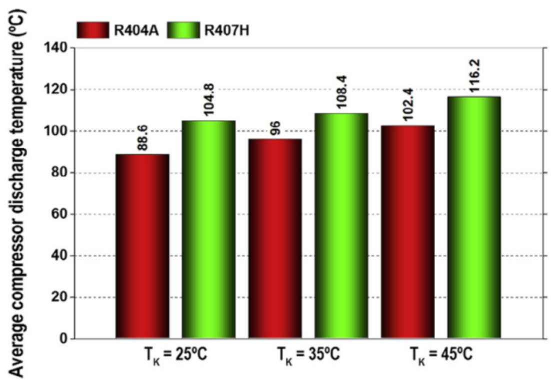

(a)

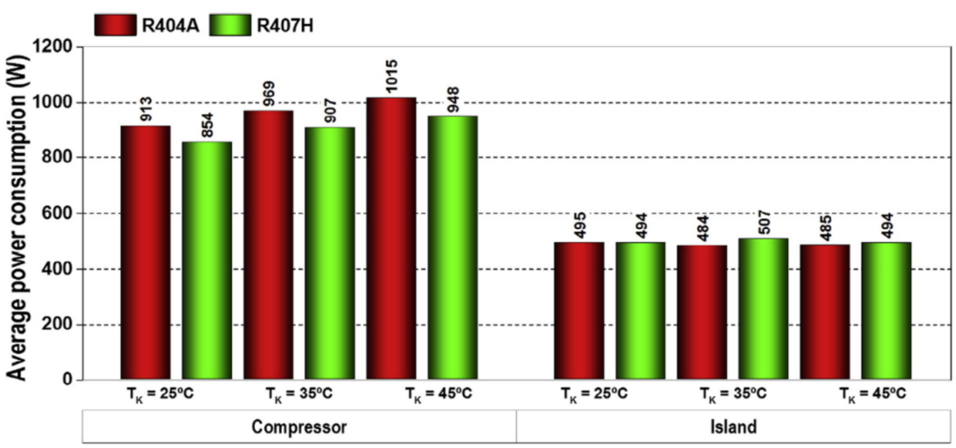

(b)

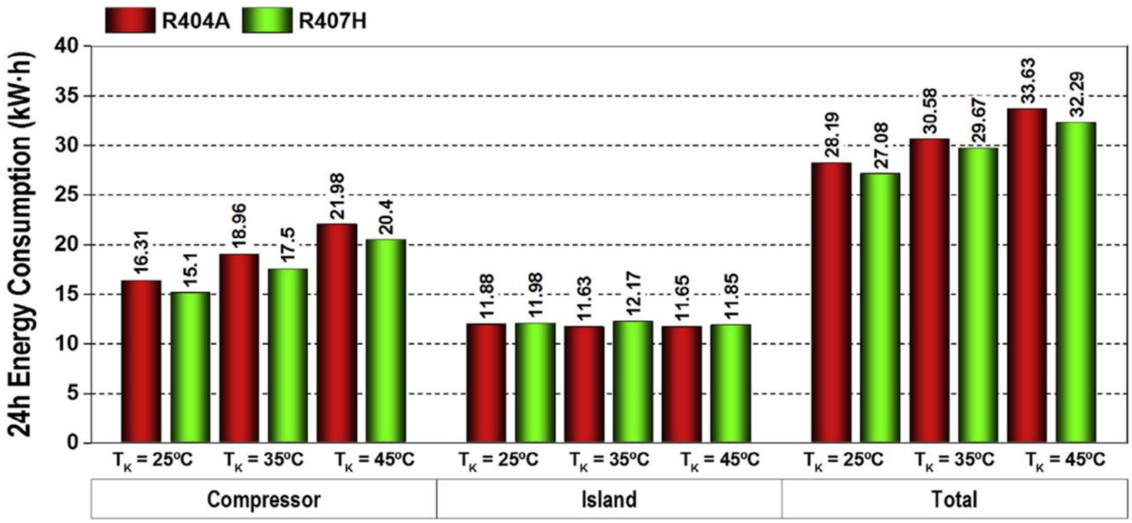

(c)

Figure 3.9 – Average compressor discharge temperature (a), average power consumption (b), 24h Energy Consumption (c) as a function of condensing temperatures (Llopis et al., 2017)

Sethi et al. (2016) studied two alternative mixtures to R404A, the R448A and R455A in three different commercial refrigeration applications. The first is a 560W self-contained refrigerator, shown in Figure 3.10a, where experimental and modelling approach is used to compare the thermodynamic cycle and performances of the three refrigerants. Up to 6% reduction of power consumption is measured with the new blends, with similar value of cooling capacity, resulting in a better efficiency. A similar approach is used for a condensing unit (its diagram is shown in Figure 3.9b) for walk-in cold rooms with the blends R404A and R448A. From the analysis, higher cooling capacity is found with R448A, resulting in up to 10% higher efficiency.

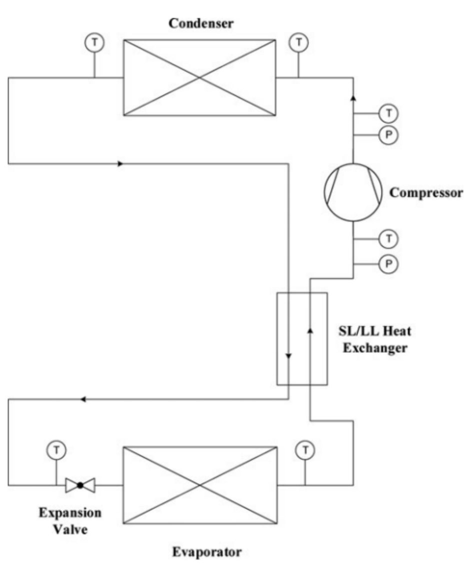

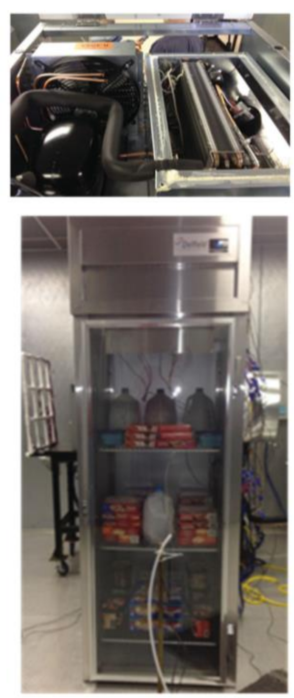

(a)

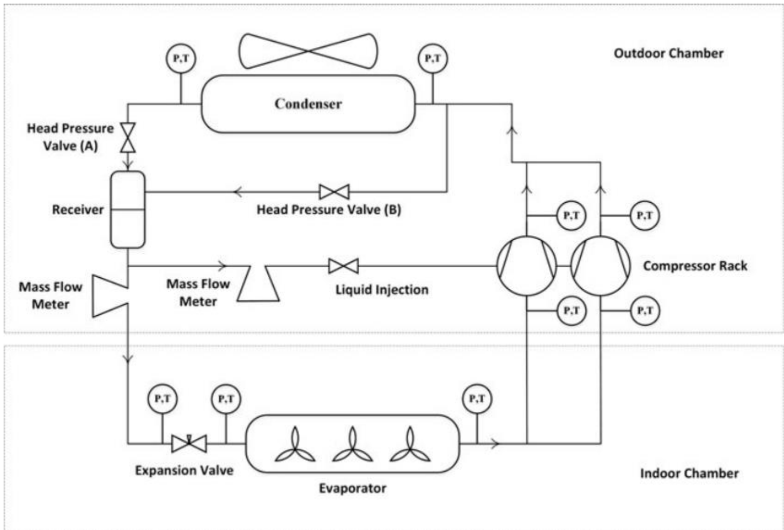

(b)

Figure 3.10 – Self-contained refrigeration system (a), condensing unit for walk-in freezer (b) analysed in Sethi et al. (2016)

The mixtures for R404A replacement, namely R454C, R459B, R457A and R455A, are analysed by Llopis et al. (2019), in a stand-alone commercial refrigeration system for fresh product compliant to ISO 23953-2. The experimental test bench used in the work is shown in Figure 3.11.

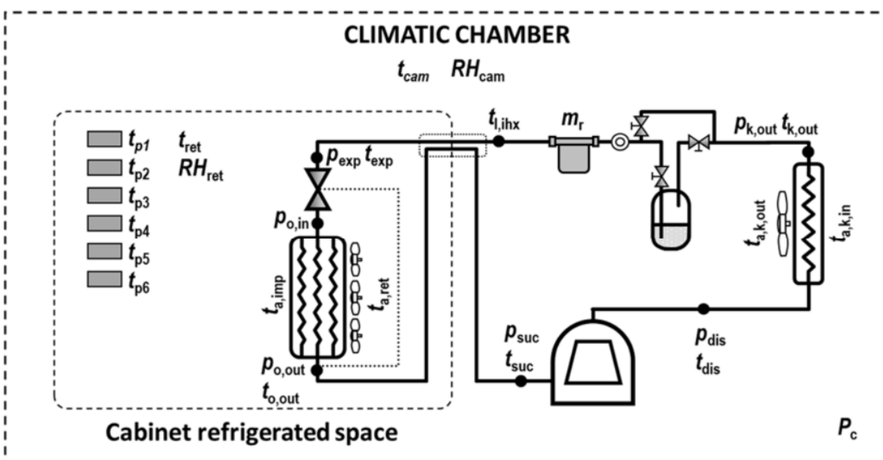

Figure 3.11 – Experimental test bench used in Llopis et al. (2019)

The tests are carried out in the configurations with and without receiver. With this latter configuration, 24 hours tests varying the refrigerant charge with steps of 100g are carried out; the optimal value is obtained in correspondence of the minimum value of the energy consumption. The results of the 24 hours tests are shown in Figure 3.12 for the different refrigerant and charges in the optimization phase.

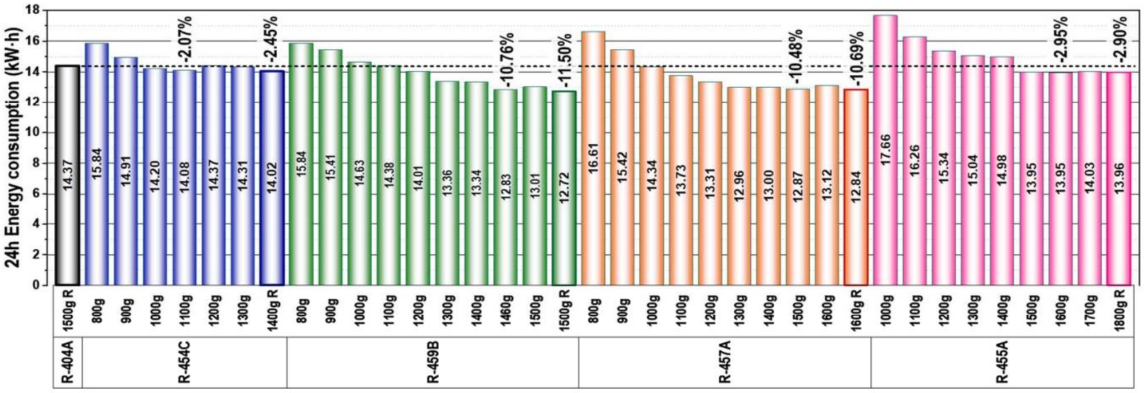

Figure 3.12 – 24h energy consumption of the different tests in charge optimization phase (Llopis et al., 2019)

Finally, in the tests without receiver a 24h energy consumption reduction of 2.07% with R454C, 10.76% with R459B, 10.48% with R457A and 2.95% with R455A have been found than the case with R404A; these values are higher in case of configuration with receiver. With the new refrigerants the optimal charge, in most of configurations, is below the value of R404A resulting in an increase of evaporating temperature and mitigating the negative effect of the high temperature glide.

In small commercial refrigeration appliances, it is possible to easily replace R404A with hydrocarbons, since for these applications 150g (safety limit for flammable refrigerants according to EN378-1:2016 and IEC60335-2-89) of refrigerant are enough to achieve the design cooling capacity. Mastrullo et al. (2014) carried out an experimental activity in a light commercial vertical freezer to replace R404A with propane. The authors tested two configurations: the first with the same components of the standard refrigerator with R404A; instead, the second an optimized one with reduced volume heat exchangers to reduce the refrigerant charge. A reduction of 30% of refrigerant charge is achieved with a 50% reduction in heat exchangers volumes. Then the refrigerant charge and the regenerative capillary tube length are optimized obtaining a 34% reduction of energy consumption than the case of standard system with R404A.

Makhnatch et al. (2017), presented a retrofit of an indirect supermarket refrigeration system from R404A to R449A working in medium temperature conditions with the secondary fluid temperature ranging from -9°C to -4°C. The plant layout is shown in Figure 3.13 where the simplified scheme and the schematic representation of vapor compression system are shown.

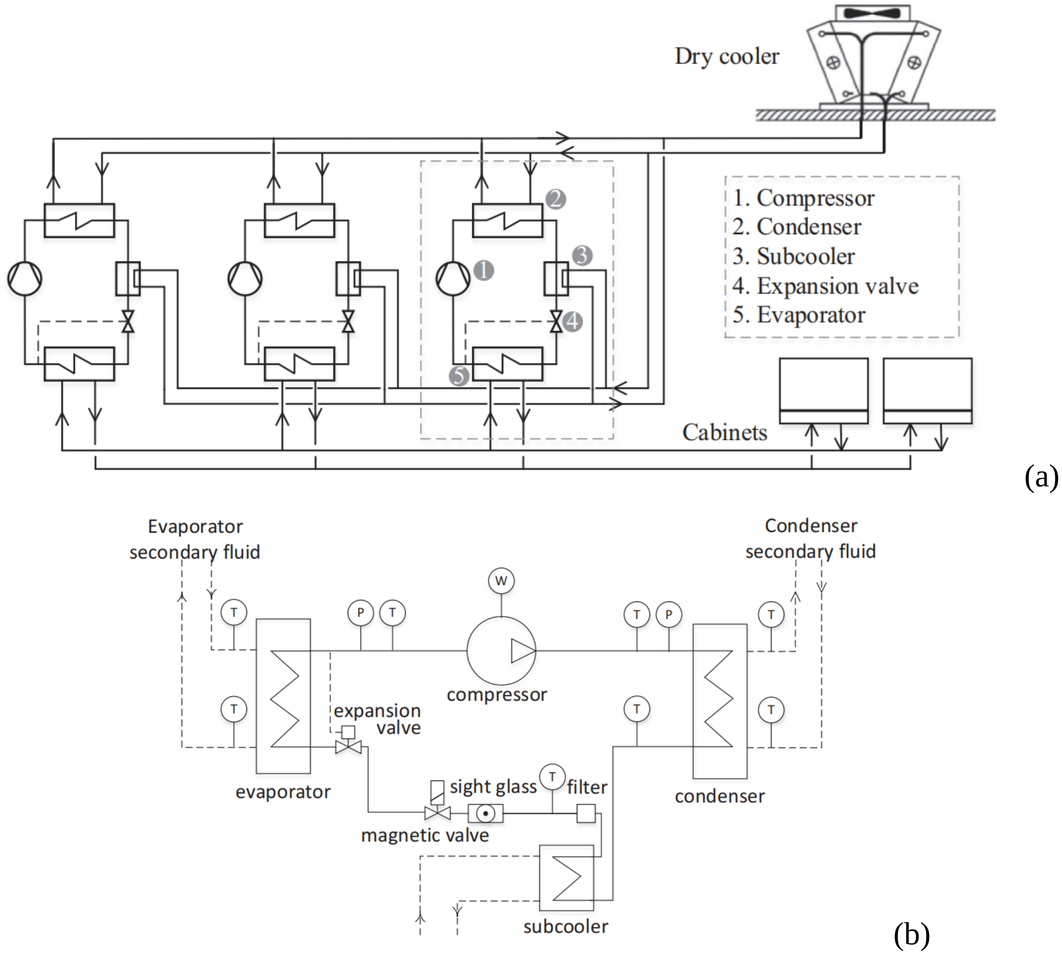

Figure 3.13 – Indirect refrigeration system layout (a) and compression vapour cycle scheme (b) from Makhnatch et al. (2017)

R449A required only a small adjustment of thermostatic expansion valve and a 4% higher refrigerant charge. An increase of compressor discharge temperature of 15K, a 12.8% reduction of cooling capacity but similar COP than R404A (around 3.6% less) was observed with R449A. From a TEWI analysis of the system with both refrigerants, it emerged that the new configuration has a lower environmental impact thanks to lower direct emissions despite similar value of the indirect ones.
In the last part of work of Sethi et al. (2016) a centralized supermarket system located in Miamisburg (Ohio, US) using R404A is analysed. Firstly, field tests are carried out with R404A for four months, then the plant is recharged with R448A. The control logic of the plant is modified to have 6K of temperature difference between refrigerant and air inside the condenser. An energy consumption reduction ranging from 9% to 20% depending on ambient temperature is registered for R448A than the case with R404A. In all the applications 10K – 15K higher discharge compressor temperatures are measured, even if they are below the compressor operational limit.

3.1.3 Environmental impact comparison studies

Environmental impact analyses on small commercial refrigeration appliances are carried out by Llopis et al. (2020) and Cascini et al. (2015). In the first work, the authors used the results presented in Llopis et al. (2017), to carry out an environmental impact analysis using an innovative approach to evaluate TEWI index. The increment of energy consumption due to refrigerant leakages, not considered in the classic TEWI evaluation procedure, is considered. Different scenarios of refrigerant charge reduction and daily energy consumption increase are considered with refrigerant annual leakage ratio (ALR) of 2%, 5% and 10%, as shown in Figure 3.14a. Comparing the new and the classic approaches, emerged that the classic TEWI index is often underestimated. In fact, higher direct and indirect emissions are calculated with the new evaluation approach. Even if the difference in direct emissions ranges from 38.6% to 148.9%, its contribution to the total one is negligible; instead, the difference in the indirect emissions ranges from 4.7% to 19.2% depending on the country due to different value of carbon dioxide emission factors. In Figure 3.14b the TEWI differences between the classic and proposed approach are shown as a function of ALR for each refrigerant and country.
In the second work, instead, the authors evaluated the carbon footprint of two monoblock refrigeration systems for walk-in cold rooms operating at MT and LT refrigeration condition respectively. A life cycle assessment approach is used considering the carbon dioxide emission factor of raw material extraction and transformation phase, refrigerator and refrigerant production phase, commissioning phase, refrigerator operation phase, maintenance and dismissing phases. Three different refrigerants R404A, R410A and R407F are considered, and laboratory tests are performed at MT and LT refrigeration conditions to evaluate the energy consumption of the unit for the evaluation of indirect emissions. There is not a unique configuration having the lowest environmental impact; in fact, this depends by the refrigerant and the operating conditions. For instance, in MT refrigeration conditions (cold room temperature equal to 0°C), R410A is the refrigerant with the lowest environmental impact. Instead, the R407F with a lower leakage ratio value could be the best option in MT whereas it has the lowest environmental impact in LT. The authors found, also, that the indirect emissions cover a range between roughly 70% to 89% of the total one as shown in Figure 3.15, underlining the importance of the improvement of components and plant layout efficiency.

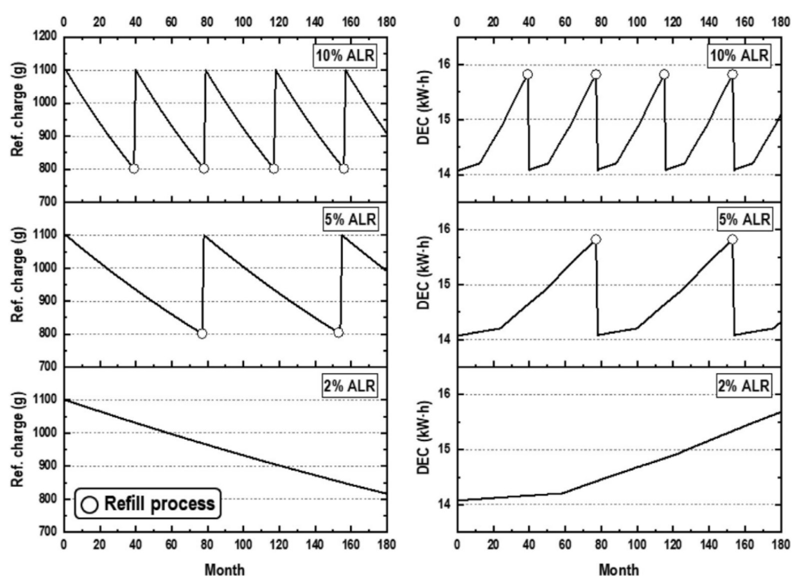

(a)

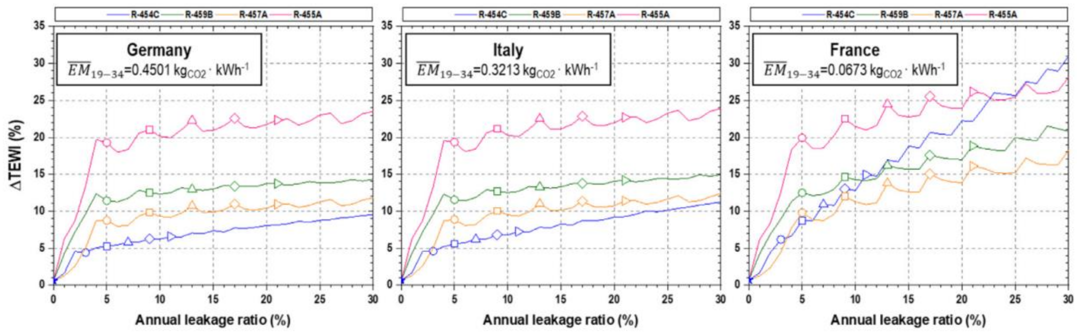

(b)

Figure 3.14 – Refrigerant charge reduction (left) and daily energy consumption increase (right) as a function of time (a), TEWI difference between classic and proposed evaluation approach as a function of ALR for each refrigerant and country (b) (Llopis et al., 2017)

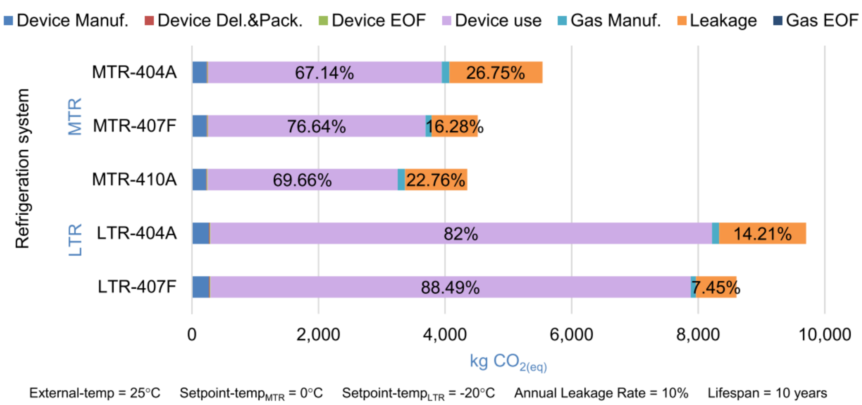

Figure 3.15 – Total emissions of MTR and LTR monoblock system (Cascini et al., 2015)

3.2 Carbon dioxide

3.2.1 Theoretical thermodynamic comparison studies

In the last decades the necessity to reduce the HFC emissions have increased the attention towards the use of carbon dioxide as refrigerant, thanks to its GWP = 1, no flammability and no toxicity (ASHRAE safety class = A1). Due to its thermodynamic peculiarities, such as a lower critical temperature than widely used HFC refrigerants (critical point, T_c = 31°C and p_c = 73 bar), it became widely used in north European countries in “only – CO_2” refrigeration units where it works in subcritical condition for large part of yearly operational time and in transcritical heat pumps for sanitary hot water production.
In transcritical condition the gascooler pressure and temperature are not correlated as in subcritical state; moreover, considering the refrigeration scheme by Liao et al. (1999), shown in Figure 3.16a, an optimal gascooler pressure for a fixed value of outlet gascooler temperature that maximize the COP can be found as shown in Figure 3.16b.

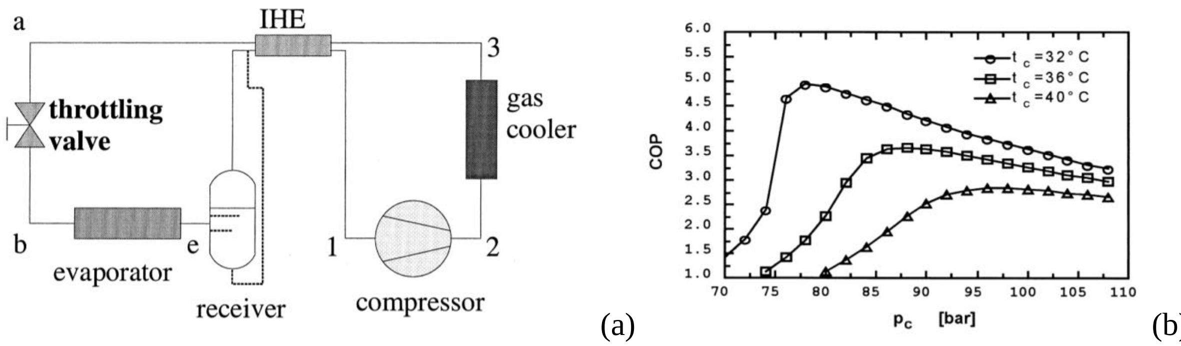

Figure 3.16 – Transcritical carbon dioxide refrigeration diagram with IHE (a) and COP as a function of gascooler pressure for a fixed value of outlet gascooler temperature (b) (Liao et al., 1999)

This means that the gascooler pressure should be regulated to ensure the highest COP according to the trends in Figure 3.16b. In the last part of the work, the authors proposed a correlation to evaluate the optimal gascooler pressure as a function of outlet gascooler and evaporating temperature.
In southern European countries the carbon dioxide uses in “only – CO_2” refrigeration plants is disfavoured since it will operate in transcritical condition for a large part of yearly operational time resulting in worse performances than widely used refrigerants. They are mainly affected by thermodynamic losses during compression and lamination phase, for this reason in these countries it started to be used in LT side of cascade refrigeration systems coupled with HFCs in primary circuit or indirect supermarket refrigeration systems as heat transfer fluid working in subcritical condition. Further improvements in refrigeration plant layout and higher components efficiency are needed to make “only - CO_2” refrigeration systems more competitive from the energetic point of view.
The use of CO_2 in secondary loop indirect refrigeration systems coupled with HFC or HFO fluids brings beneficial effects in terms of environmental impact reduction of supermarket systems as stated by Gullo et al. (2016) that compared different indirect system architectures with direct expansion supermarket refrigeration system (DXS). An energy consumption and environmental impact assessment (TEWI) is carried out considering five scenarios of different cities: Chicago, Albuquerque, Phoenix, Rome and Athens. The couple R134a / CO_2 is used as working fluid in cascade system (CS), R1234ze / CO_2 as working fluids in cascade and indirect systems (COM, CSC, CSC-D, FCSC-D) and R404A in direct expansion system (DXS). In all scenarios, even if a 2% and 5% higher energy consumption than DXS and CS, respectively, is found for the four R1234ze / CO_2 systems, they have the lowest environmental impact as shown by the bar graph in Figure 3.17a and Figure 3.17b, respectively. The differences are mainly due to lower GWP value of R1234ze (GWP = 3) and CO_2 (GWP = 1) than R134a (GWP = 1430) and R404A (GWP = 3922).

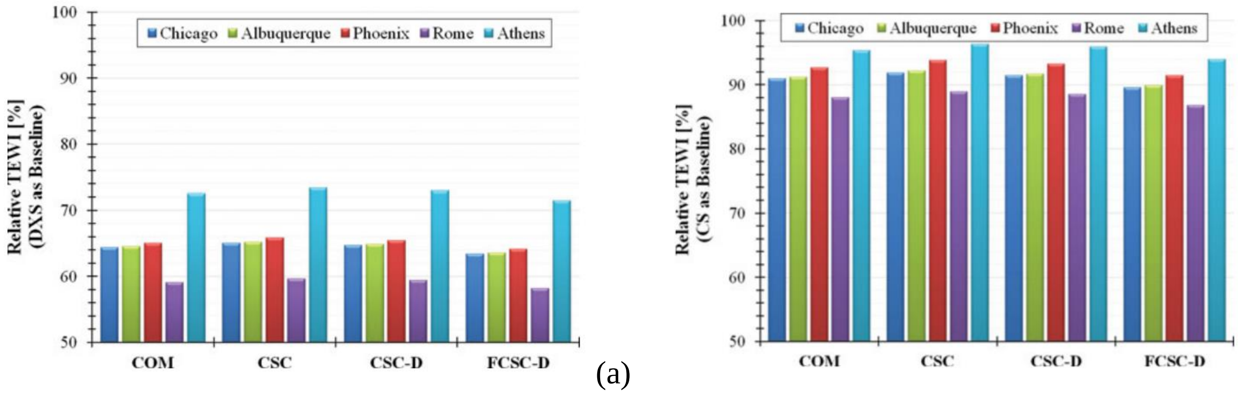

Figure 3.17 – TEWI percentage difference of the four R1234ze/CO_2 systems compared to DXS (a) and CS (b) (Gullo et al., 2016)

A possible solution to overcome the thermodynamic limit of carbon dioxide in transcritical state consists in splitting the lamination and compression phase in two parts using a double stage configuration; Cecchinato et al. (2008) carried out a thermodynamic analysis of different two-stage thermodynamic cycles as shown in Figure 3.18. Some of them are characterized by only split lamination phase, others only split compression phase and others have both transformations split in two parts. Also, the basic cycle (one compression and lamination phase, not shown in Figure 3.18) is analysed.

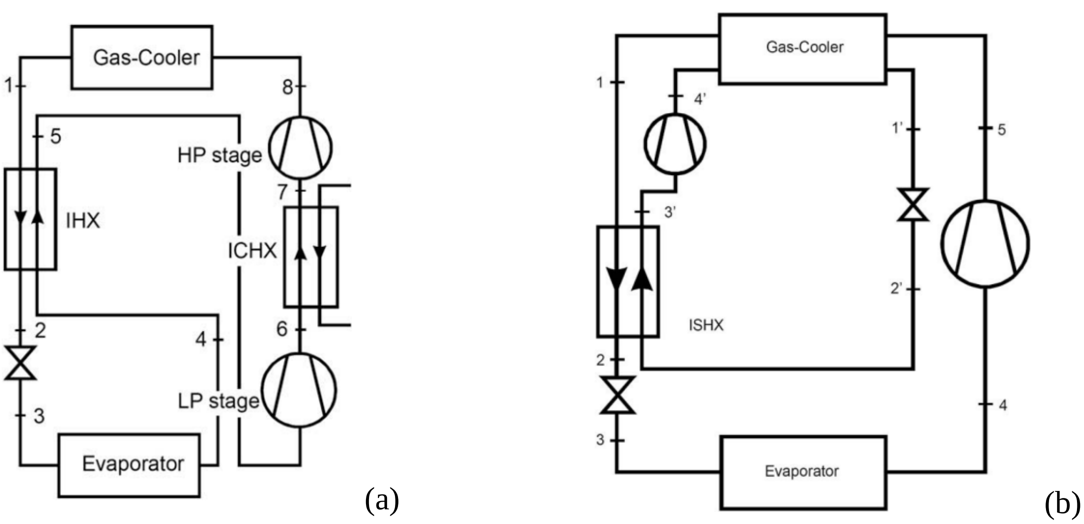

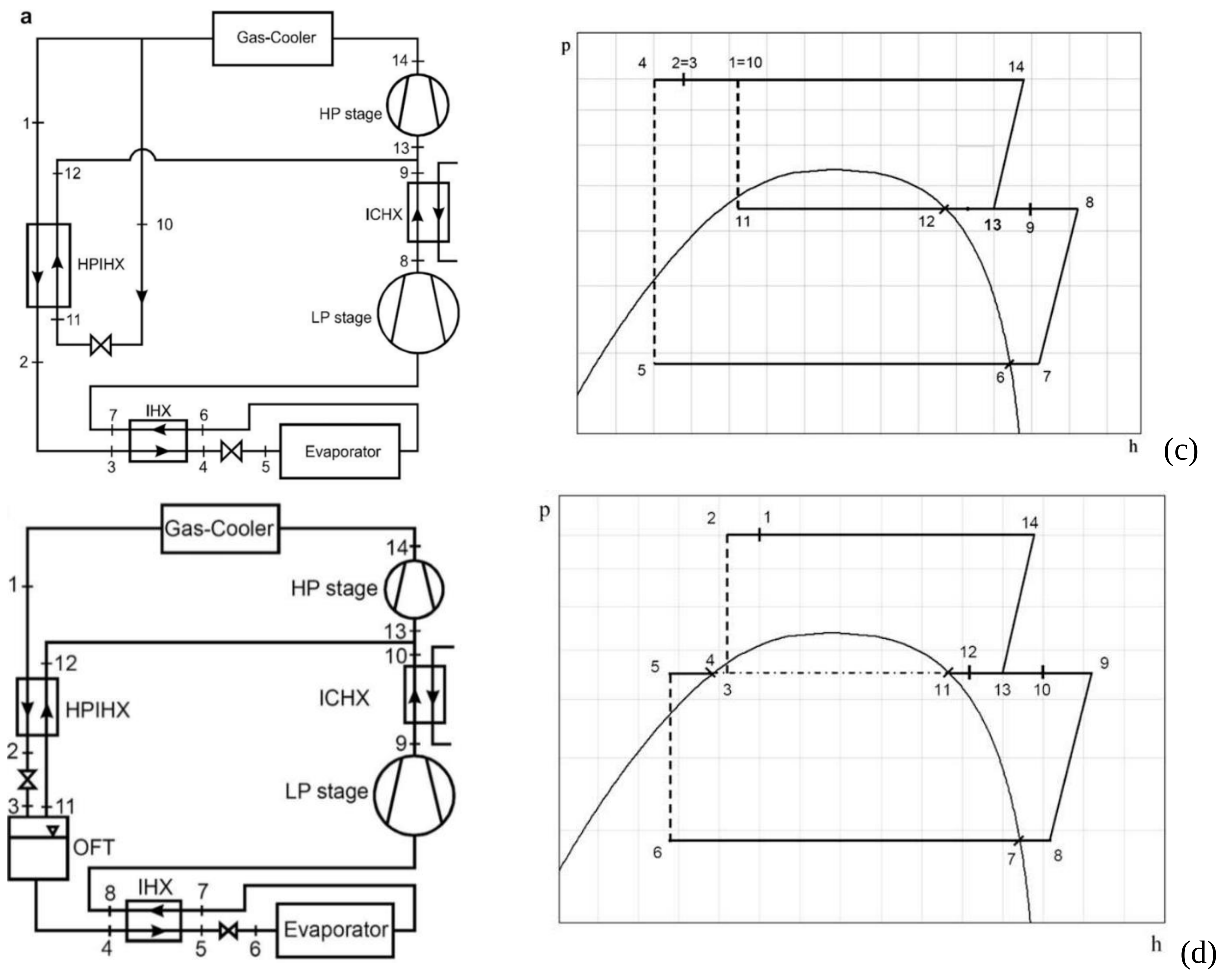

Figure 3.18 – Single-throttling, double-compression cycle (STDC) (a), double-throttling, auxiliary compressor vapour cycle (DTAC) (b), double-throttling, double-compression split cycle (DTDC_SC) and p – h diagram (c), double-throttling, double-compression open flash tank cycle and p – h diagram (DTDC_OFT) (d) (Cecchinato et al., 2008)

Each cycle is optimized in regards of energy consumption by means the calculation of the optimal value of intermediate pressure and in case of split cycle the refrigerant mass flow rate of the auxiliary stream is optimized. Simulations at different evaporating and ambient temperatures are carried out and it was found that the highest energy consumption reduction is achieved with the most complex cycles (DTDC_SC and DTDC_OFT) with an efficiency increase of 70% and 16% in the conditions -30°C / +35°C and +4°C / +30°C respectively (evaporating / ambient temperature). Conversely, the single throttling and double compression cycle showed about 50% efficiency increase. Finally, the authors underlined that the best solution is always a good compromise between installation and running costs. Moreover, technical improvements of components efficiency and reliability should be apported to get more realistic the outcomes of the thermodynamic analysis.

Double compression and / or double throttling “only - CO_2” refrigeration systems are widely studied in the scientific literature by means of energetic and environmental impact analysis and in some works are compared with the HFC based systems. In Gullo et al. (2016), eight configurations are compared among cascade system (R134a / CO_2), conventional and improved booster system, two booster systems with mechanical subcooling and other two with mechanical subcooling and parallel compression. The simulated refrigerant plants are shown in Figure 3.19.

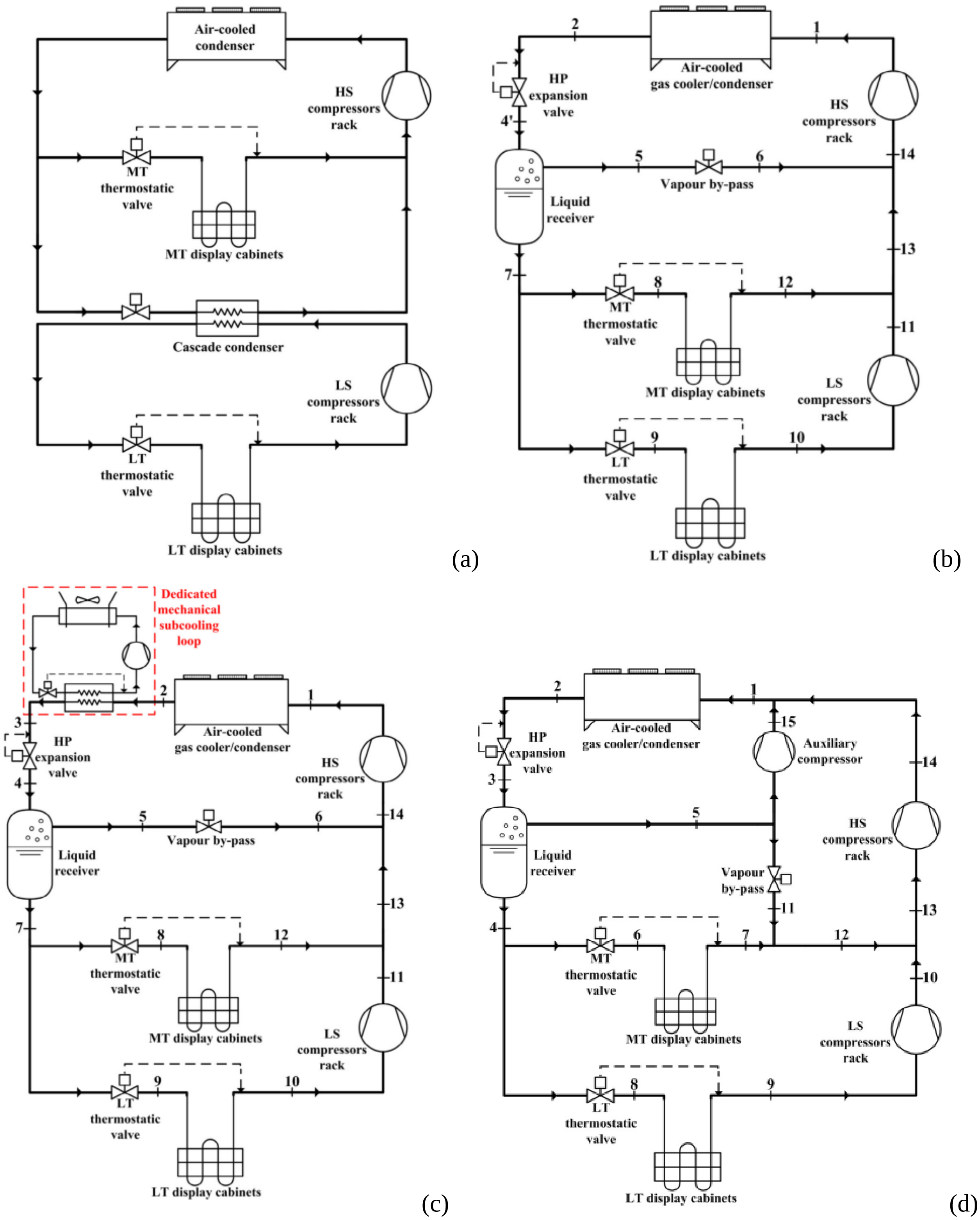

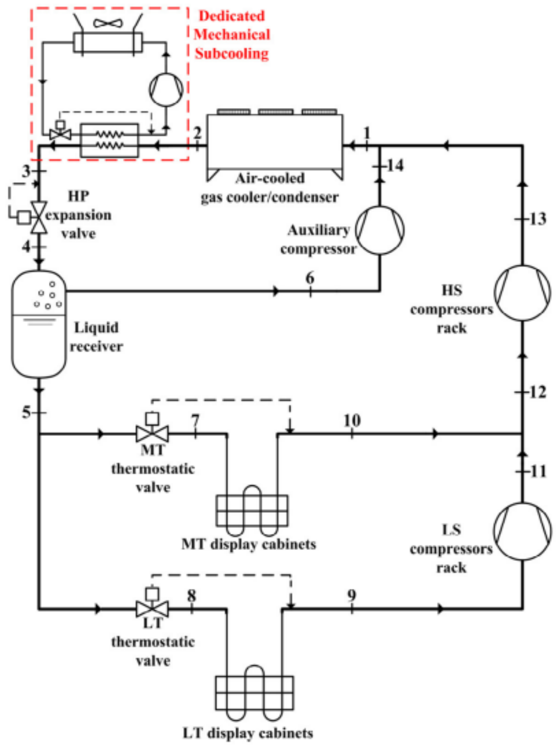

(e)

Figure 3.19 – Cascade system (a), conventional booster system (b), booster system with mechanical subcooling (c), booster system with parallel compression (d), booster system with mechanical subcooling and parallel compression (e) (Gullo et al., 2016)

The cities of Athens and Valencia are considered to carry out the simulations and it was found that the new solutions have similar energy consumption saving than the baseline cascade system (R134a / CO_2) but lower environmental impact up to 9.6%.
Further improvements to the CO_2 basic booster refrigeration plants are implemented such as multi-ejector block at the outlet of gascooler working with vapour and liquid phase. This feature is investigated in the work of Gullo et al. (2017), where an energy consumption analysis among different plants layout is carried out in five different scenarios represented by Oslo, London, Frankfurt, Milan and Athens. Six layouts are considered: R404A DXS, CO_2 conventional booster system, booster system with parallel compression, booster with multi-ejector block, booster with parallel compression and overfed MT evaporators and booster with parallel compression with overfed MT and LT evaporators. The layouts of multi-ejector booster refrigeration systems are shown in Figure 3.20. The use of ejector allows not also the recovery of a part of lost energy during the lamination phase (referring to a basic booster cycle) but also allows to overfeed the evaporators, thus increasing the evaporating temperature with benefit on system performances. This latter has the lowest annual energetic consumption as shown in Figure 3.21. In cold climates the plant with parallel compressor has similar energy consumption than the conventional booster due to less operational time of parallel compressor than in warm climates, thus limiting the advantages of this solution.

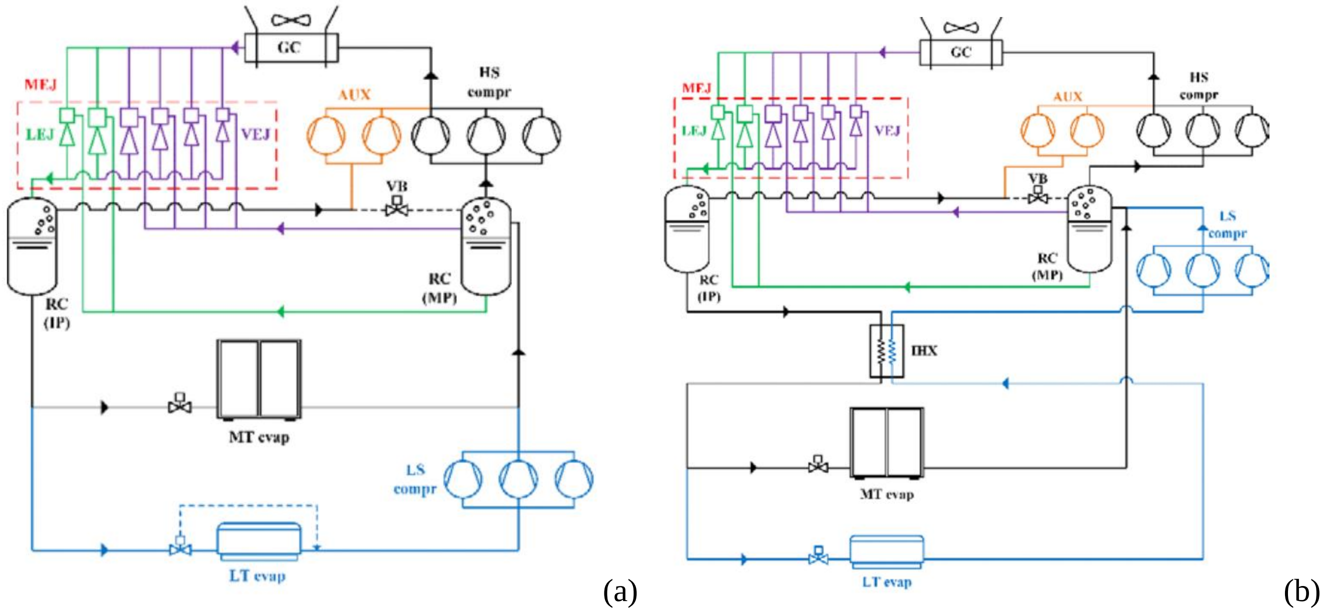

Figure 3.20 – Multi-ejector booster refrigeration system with MT overfed evaporators (a) and MT and LT overfed evaporators (Gullo et al., 2017)

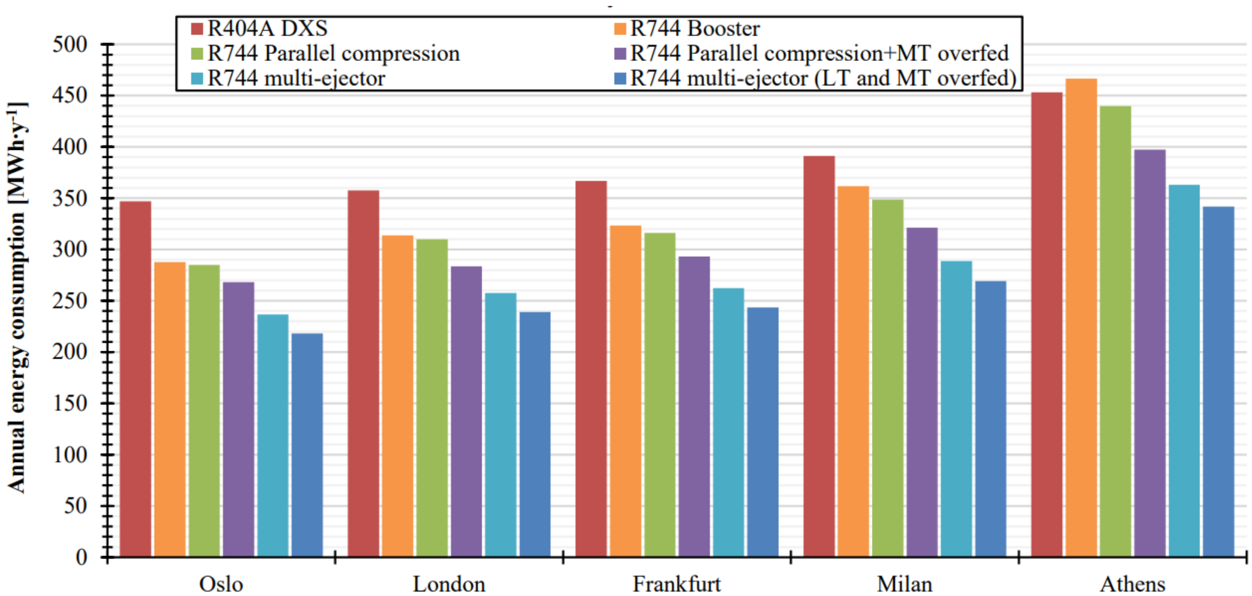

Figure 3.21 – Annual energy consumption of different plant layouts in 5 scenarios (Oslo, London, Frankfurt, Milan and Athens) (Gullo et al., 2017)

In a similar work, Gullo et al. (2016) analysed the energy consumption and the environmental impact of multi-ejector overfeed booster refrigeration systems equipped with energy recovery system for space heating and cooling. Three values of integrated air conditioning load are considered equal to 50%, 100% and 200% of MT refrigeration condition cooling capacity. Different plant layouts are compared considering different locations: Rome, Lisbon, Valencia, Athens and Seville. The performances of the integrated system are compared with the baseline configuration composed by R404A DXS + R410A air conditioning system. Up to 25% reduction of annual energy consumption can be achieved with the integrated system than the baseline. This advantage increases with higher value of AC loads. Different layouts of integrated booster CO_2 system, shown in Figure 3.22, are studied, and compared with other systems by Gullo (2019). The integrated system is capable to meet the requirements of supermarket space heating and cooling, and it is compared with R404A DXS + reverse heat pump (RHP) and R134a / CO_2 cascade system + RHP considered as baseline configurations, R448A cascade system + R1234ze RHP, indirect refrigeration system + R1234ze RHP. The considered booster systems are PC (booster with parallel compressor), PC + LEJ (booster with parallel compressor PC and liquid ejectors LEJ) and PC + MEJ (booster with parallel compressor PC and multi-phase ejectors MEJ liquid + vapour). The assumptions used in the calculations are based on results of field tests reported in the scientific literature. Warm (Barcelona, Lisbon, Athens, Seville, Tunis, Palermo and Tenerife) and hot (Sydney, Guangzhou, Phoenix, Rio de Janeiro, New Delhi, Mombasa) climates are considered in the calculations. The only – CO_2 integrated plants have the lowest annual energy consumption and environmental energy impact (TEWI index) compared to the baseline solutions in warm climates up to 32% and 75.8% respectively, and in hot climates up to 33.3% and 89.5%, respectively.

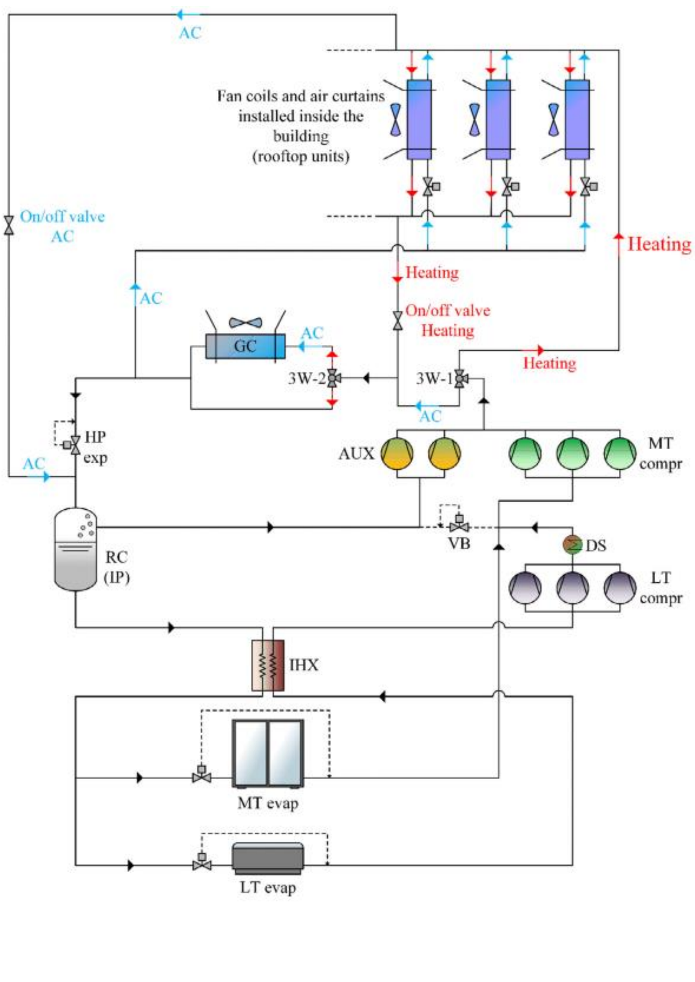

(a)

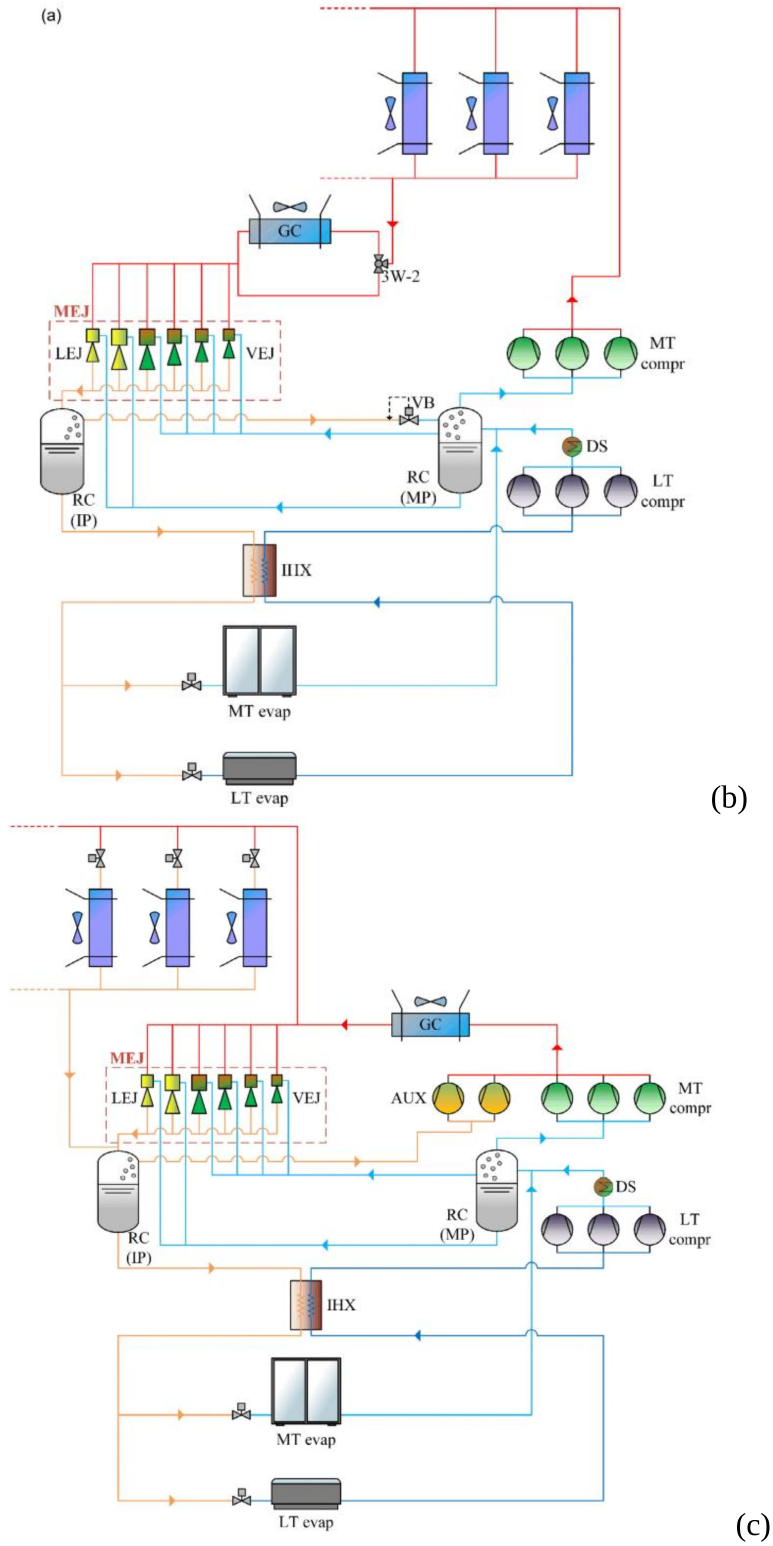

Figure 3.22 – Schematic layout of integrated booster system with IHX (a) and with MEJ (multi-phase ejector) block in space heating mode (b) and space cooling mode (c) from Gullo (2019)

All the improvements to the basic booster CO_2 transcritical system studied separately in scientific literature are fused together in one system in the work of Karampour et al. (2017). Indeed, the authors proposed a simulative study of a "state-of-the-art" CO_2 booster system equipped with flooded evaporators, air conditioning (AC) and heat recovery integration. The proposed system is compared with a R404A direct and indirect system, two cascade systems (ammonia / CO_2 and propane / CO_2) and with CO_2 standard booster system. The "state-of-the-art" system is shown in Figure 3.23 with its thermodynamic diagram.

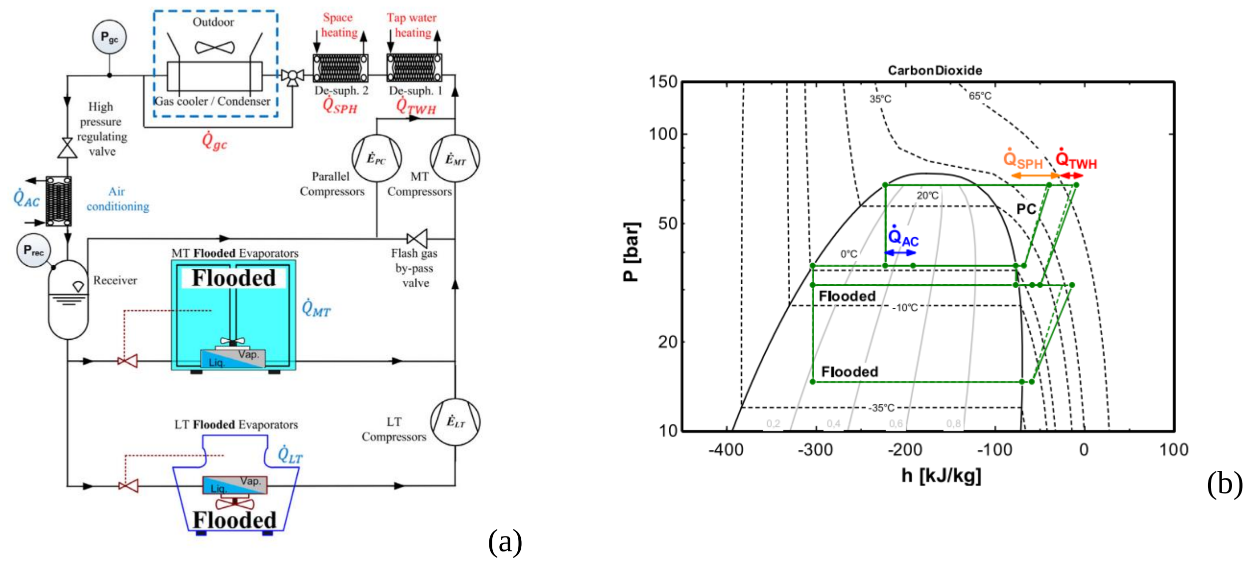

Figure 3.23 – "State-of-the-art" CO_2 booster refrigeration system (a) and thermodynamic p – h diagram (b) (Karampour et al., 2017)

The annual energy consumption and greenhouse gases emissions are evaluated considering the climates of Barcelona and Stockholm with the refrigeration, air conditioning and space heating loads and water supply and return temperature depending on ambient temperature as shown in Figure 3.24a and Figure 3.24b respectively.

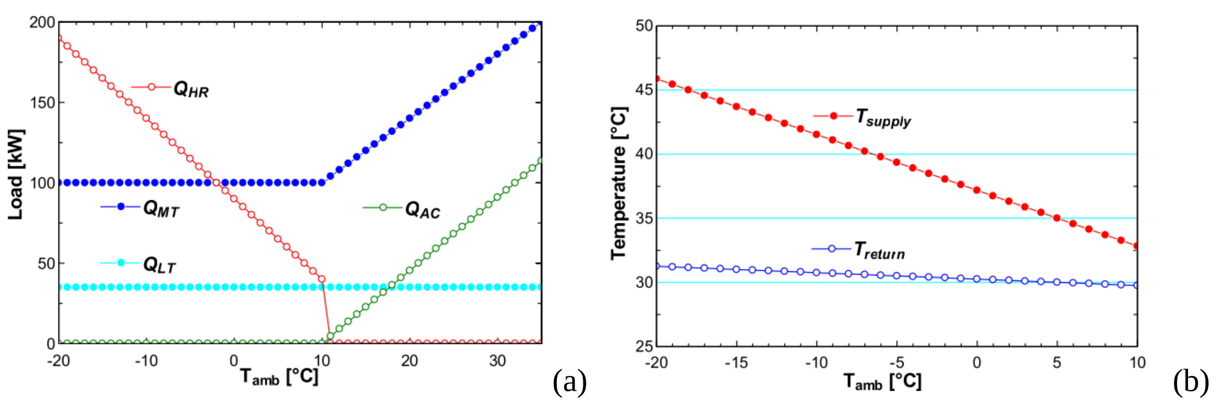

Figure 3.24 – Refrigeration, air conditioning and space heating loads as a function of ambient temperature (a) supply and return water temperature as a function of ambient temperature (b) (Karampour et al., 2017)

The proposed system has less energy consumption and greenhouse gases emissions than the others in Stockholm. In Barcelona, instead, the most efficient and environmentally friendly system is the ammonia / CO_2 cascade one.

Islam et al. (2017) carried out a TEWI assessment of different supermarket refrigeration systems, cascade and direct type with R134a and R507A as refrigerants used in different combination in MT and LT side, and transcritical CO_2 direct expansion system. The system with R134a in MT and LT side and CO_2 transcritical system have the lowest TEWI. Moreover, the authors demonstrated that the TEWI of the transcritical cycle decreases with higher COP values, since the indirect emissions cover a higher percentage of total ones. Furthermore, a refrigerant leakages annual costs evaluation is carried out and they range from 900$ to 1300$.

The energy assessment of supermarket refrigeration systems in China is carried out by Sun et al. (2020), that compared two-stage R134a refrigeration system, transcritical CO_2 booster system and transcritical booster system with parallel compression and subcooler. The climates of the cities Qiqihar, Tianjin, Wuhan, Guangzhou and Guiyang are considered. Annual energy consumption of each plant is compared in all climates, and it is shown in Figure 3.25 together with SEER value.

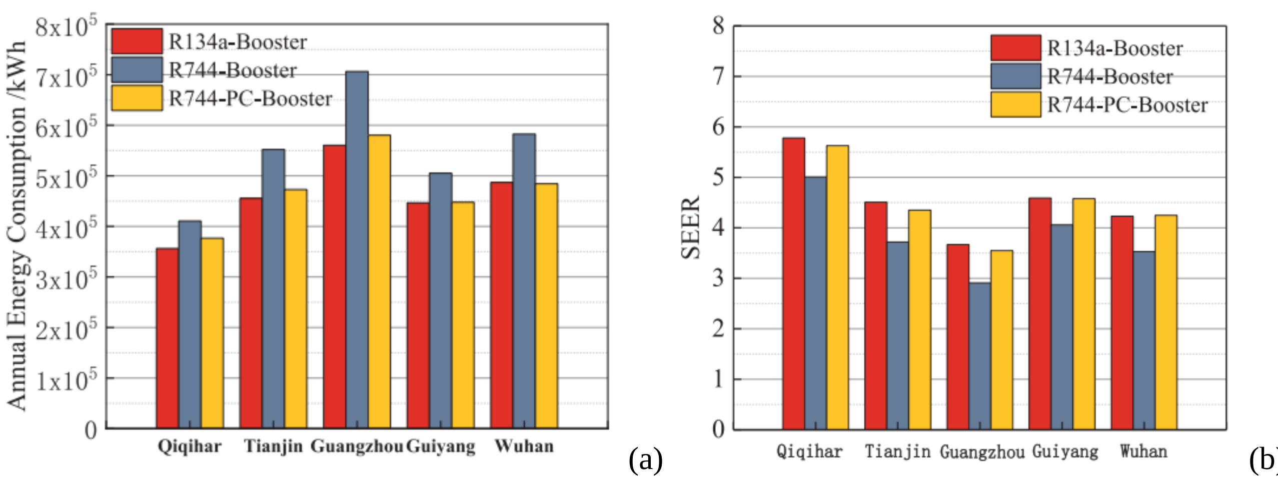

Figure 3.25 – Annual energy consumption (a) and SEER (b) of the analysed systems in different climates (Sun et al., 2020)

From the comparison it was found that the booster system has worse performances than R134a two-stage system especially in hot climates with 39°C ambient temperature. In fact, in this condition the COP of the CO_2 booster plant is half than that of the R134a two-stage. The use of parallel compressor allows to increase COP value of 49% with 39°C ambient temperature, reaching the same COP level than the two-stage plant with a further improvement of SEER that ranges from 11.5 % to 17.8 % (depending on the climate).

3.2.2 Experimental studies

Experimental analyses on CO_2 refrigeration systems by means of field tests of supermarket systems or laboratory tests for smaller appliances are, also, present in scientific literature.
Sawalha et al. (2015) compared the performances of 5 transcritical supermarket refrigeration systems (named from TR1 to TR5) with field test campaigns. All the systems are installed in Sweden and their layout are shown in Figure 3.26. The systems TR4 and TR5 are equipped with flash gas removal, compressor with higher efficiency and works with higher evaporating pressures than TR1 to TR3; moreover, all the systems have heat recovery for space heating. From the measurement 35% to 40% higher total COP is measured for TR4 and TR5 than the TR1 to TR3 systems thanks to the aforementioned features and the fact that they are installed after 2010 than TR1 to TR3 systems (installed in 2007). The contribution of each feature, installed only in TR4 and TR5 systems, on COP increase is evaluated with a software: the flash gas removal contributes for up to 16%, 2K - 3K higher evaporator temperature contributes for up to 14%, the same improvement is achieved also with higher compressor efficiency.

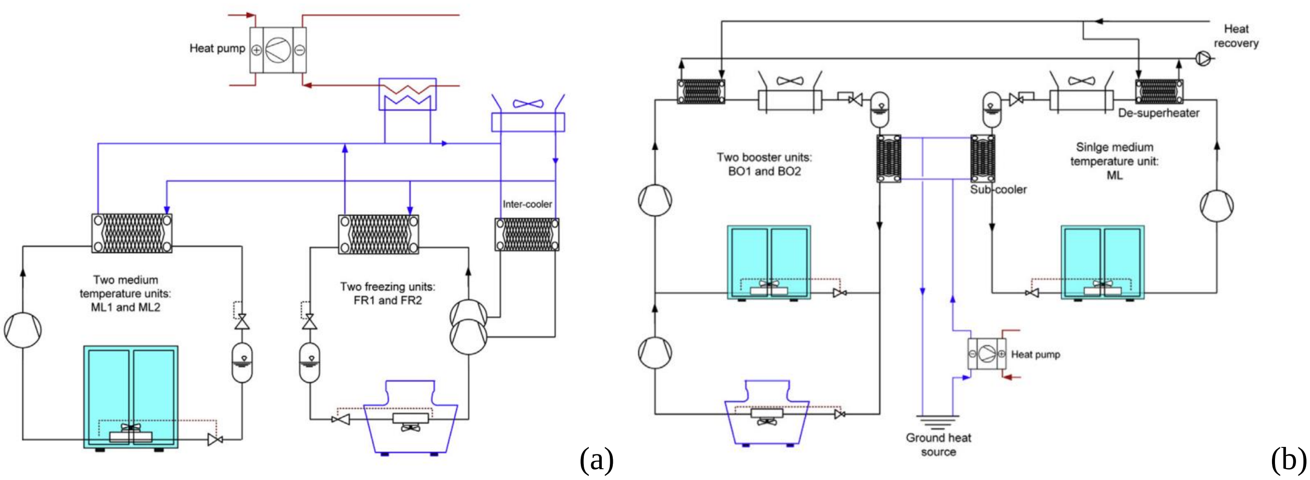

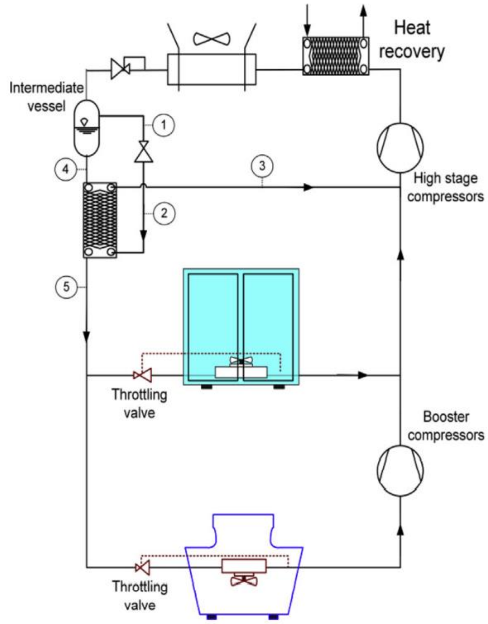

(c)

Figure 3.26 – Schematic layout of TR1 (a), TR2 and TR3 (b), TR4 and TR5 (c) from Sawalha et al. (2015)

The TR1 to TR5 systems are compared to others working with HFC refrigerants in Sawalha et al. (2017); field test measurements of three systems (named RS1, RS2 and RS3) installed in Stockholm are carried out. The layout of the systems is shown in Figure 3.27. The medium temperature side COP (COP_{MT}), low temperature side COP (COP_{LT}) and total COP (COP_{TOT}) are evaluated as in Sawalha et al. (2015). TR4 and TR5 have higher COP_{MT} than the RS systems, conversely, these latter have high COP_{LT}. Nevertheless, TR4 and TR5 COP_{TOT} is higher than the one of HFC systems with lower energy consumption of 20%. The COP_{TOT} values of the modelled systems are shown in Figure 3.28a, as a function of condensing temperature. COP_{MT} and COP_{LT} values of RS and new conception TR systems are instead shown in Figure 3.28b as function of outdoor temperature together with Stockholm bin hours distribution.

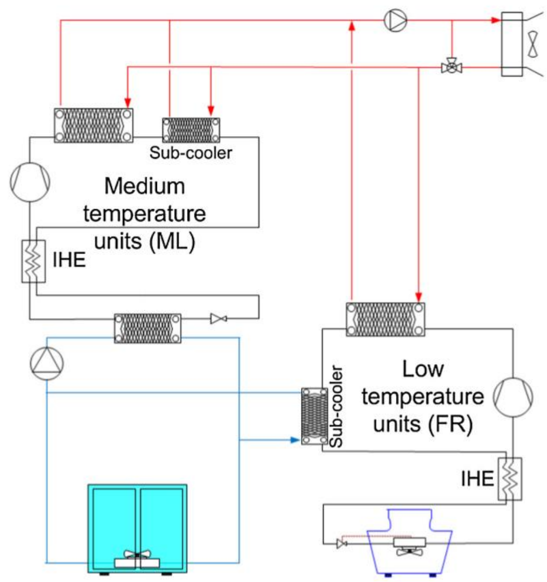

Figure 3.27 – Schematic layout of RS1, RS2 and RS3 systems from Sawalha et al. (2017)

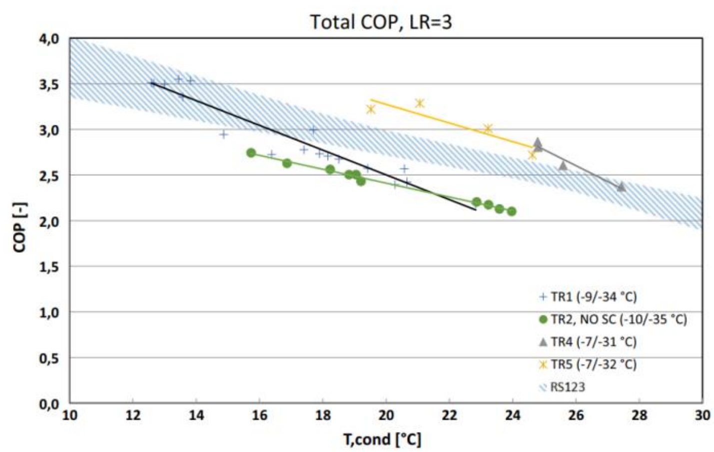

(a)

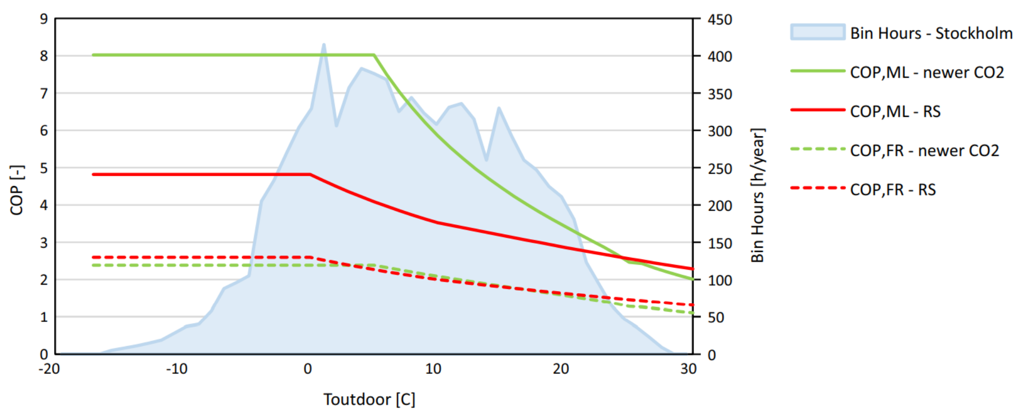

(b)

Figure 3.28 – Total COP of the compared systems as a function of condensing temperature (a), MT and LT COP as a function of outdoor temperature for newer CO_2 systems and HFC systems and Stockholm bin hours distribution (b) (Sawalha et al., 2017)

Tests with small scale experimental facility with CO_2 are also carried out by Cabello et al. (2012), that investigated the optimal position of flash gas injection in a one-stage transcritical refrigeration system whose layout is shown in Figure 3.29.

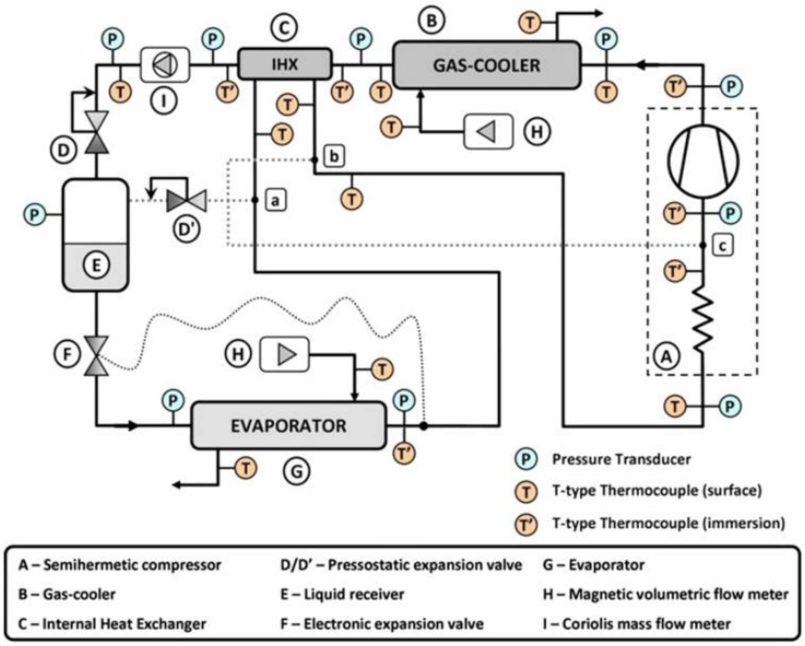

Figure 3.29 – Schematic layout of test facility used in Cabello et al. (2012)

The investigated positions are indicated with a, b and c in Figure 3.29. The advantage of flash gas bypass is to keep lower the receiver pressure thus having low evaporator inlet quality and proper refrigerant distribution avoiding improper operation of thermostatic valve. Up to 9.8% and 7% increase of cooling capacity and COP, respectively, are achieved than the configuration without injection valve. The cooling capacity, COP, compressor discharge temperature and suction superheating with evaporator water/glycol mixture temperature of 5°C and gascooler water inlet temperature of 25°C and 35°C are shown in Figure 3.30, and similar trends are found with water/glycol mixture temperature of 15°C. The effect of vapour injection is also beneficial for the compressor that works with lower discharge temperatures. The advantage of flash gas vapour injection increases at higher gascooler water inlet temperature, meaning that greater efficiency can be achieved in warm and hot climates with a real plant, than the configuration without it.

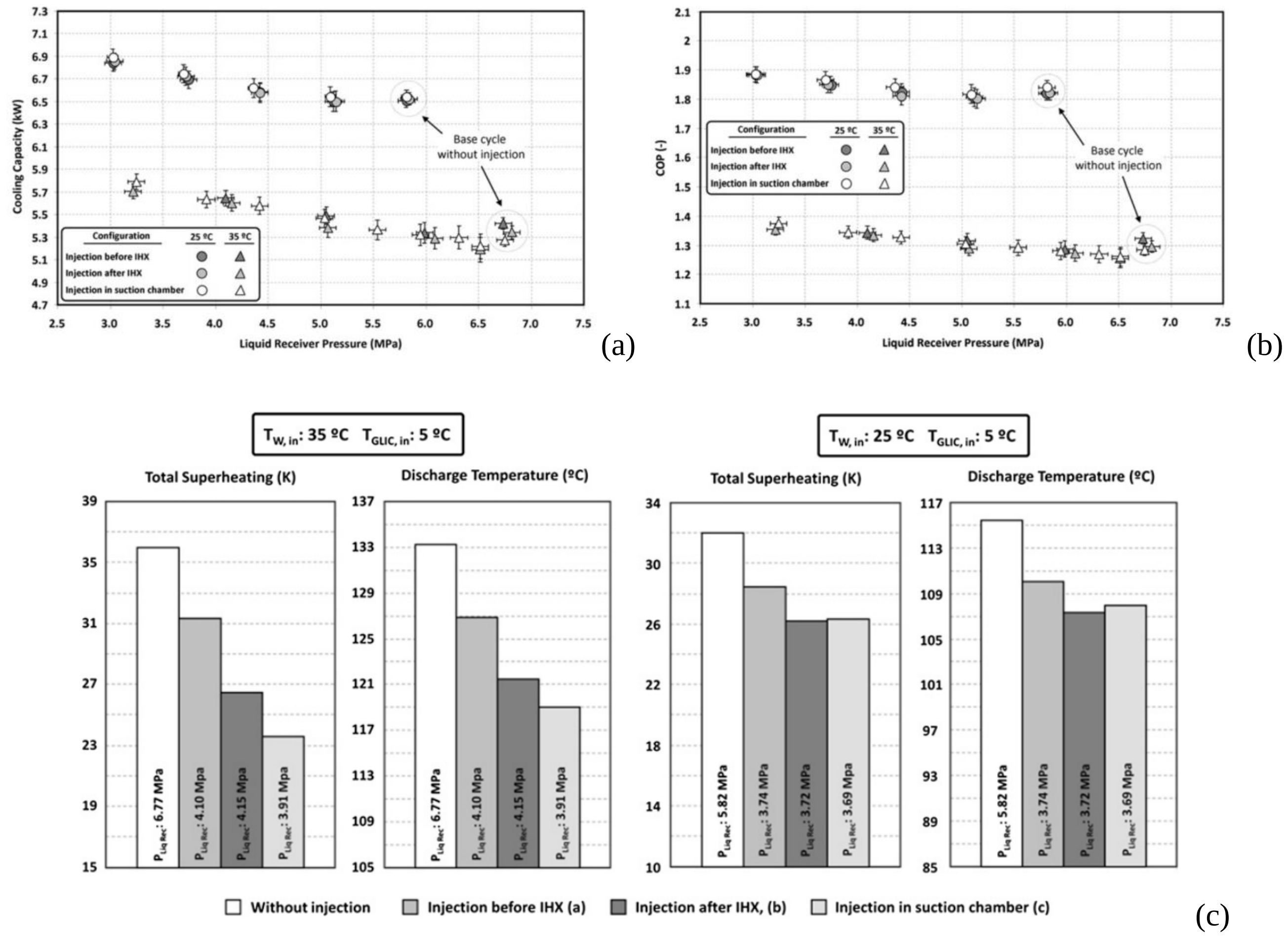

Figure 3.30 – Cooling capacity (a) and COP (b) as a function of liquid receiver pressure, total superheating, and compressor discharge temperature without and with vapour injection (c) (Cabello et al., 2012)

Nebot-Andres et al. (2018), studied the mechanical subcooler (MS) and internal heat exchanger (IHX) effects in a CO_2 direct expansion system connected to a display cabinet as shown in Figure 3.31.
24 hours tests are carried out where power and energy consumption are evaluated. With MS the power consumption of the system is higher from 40% at 17.9°C gascooler water inlet temperature to 20% at 43.6°C due to the extra power consumption of mechanical subcooler compressor as shown in Figure 3.32a. Even if the power consumption of configuration with MS is higher, slight percentage differences are found than the configuration with IHX. They range from 14.5% at gascooler water inlet temperature equal to 17.9°C to a minimum of 1.2% at 32.7°C gascooler water inlet temperature.

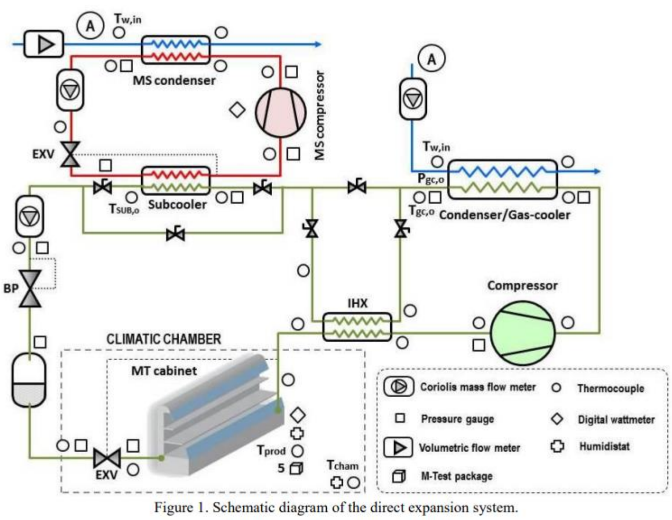

Figure 3.31 – Experimental test facility used in Nebot-Andres et al. (2018)

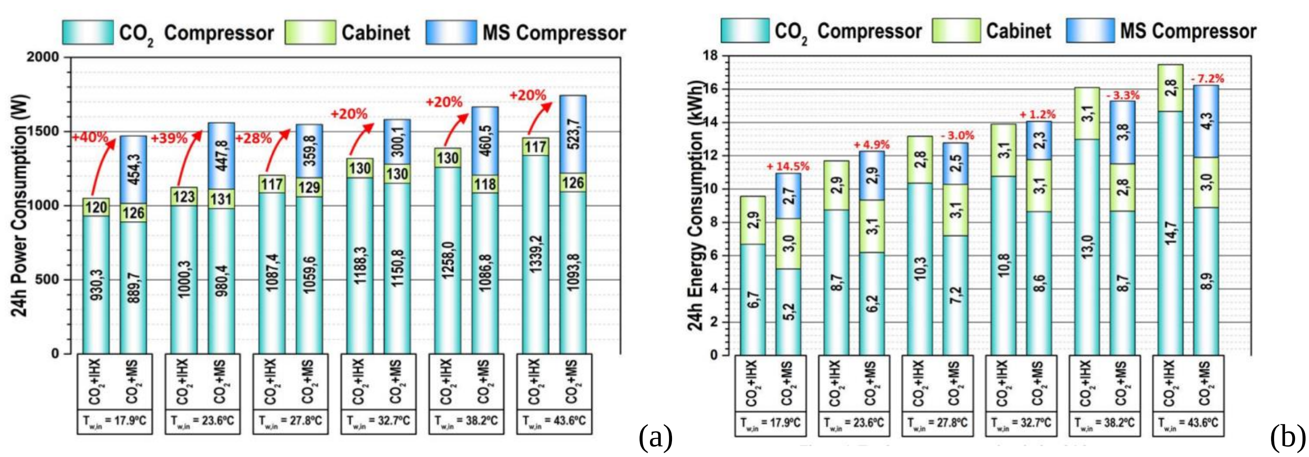

Figure 3.32 – 24h power consumption (a) and 24h energy consumption (b) as a function of gascooler water inlet temperature measured for the configurations with IHX and MS (Nebot-Andres et al., 2018)

Two-stage transcritical CO_2 small scale refrigeration systems are assessed by Catalan-Gil et al. (2020) and Citarella et al. (2020) by means laboratory experimental campaign.

In Catalan-Gil et al. (2020), the effect of a desuperheater placed between LT and MT stage compressors on thermodynamic cycle and performances is assessed. The experimental facility is shown in Figure 3.33, the configuration without (BB = basic booster cycle) and with desuperheater are compared (BB + DSH = basic booster cycle + desuperheater).

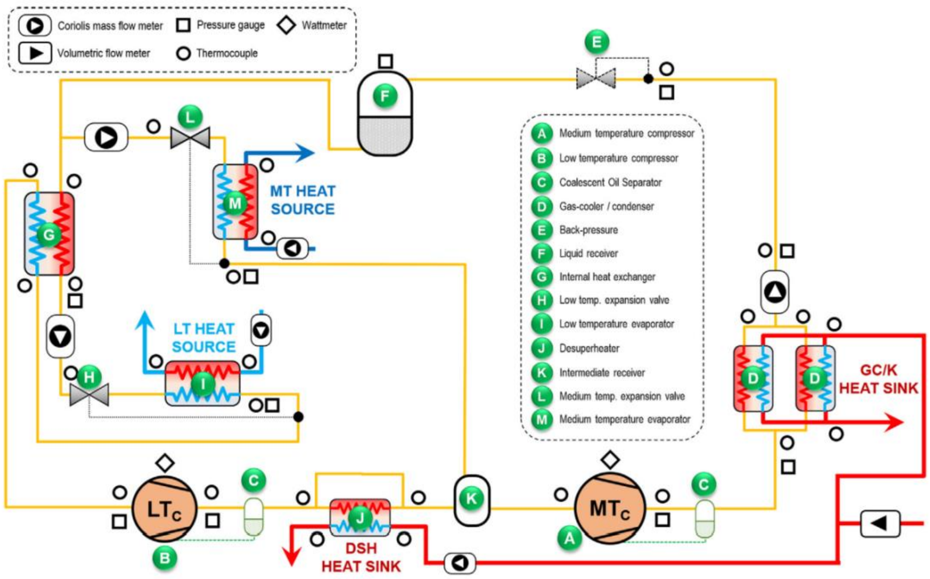

Figure 3.33 – Test facility used in Catalan-Gil et al. (2020)

The use of desuperheater allows the reduction of second stage discharge temperature, a reduction of gascooler pressure and an increase of the receiver inlet vapor quality as shown in Figure 3.34a. Moreover, higher COP up to 7% at 34°C, in Figure 3.34b, thanks to higher compressor global and volumetric efficiency is measured.

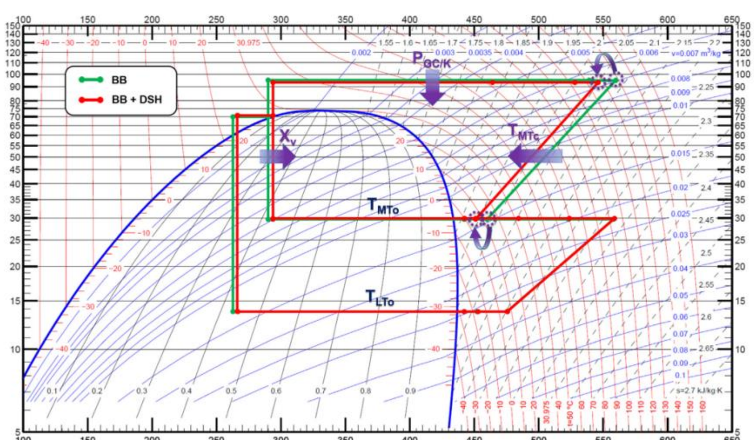

(a)

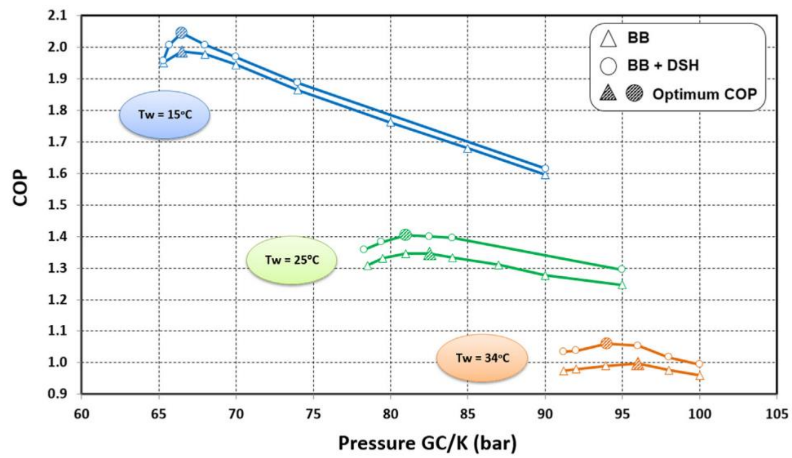

(b)

Figure 3.34 – Thermodynamic cycle with BB and BB + DSH configurations (a) and COP as a function of gascooler pressure in BB and BB + DSH configurations (b) (Catalan-Gil et al., 2020)

Similar conclusions are found in Citarella et al. (2020) regarding the analysis of intercooler effect between the first and second stage of compression with a similar test facility. The influence of intercooler causes an increase of cooling capacity and COP of 10% than the configuration without it. Also, the effect of ambient and evaporating temperatures and flash gas cooling effect as a function of ambient temperature on thermodynamic cycle and performances are analysed.

Thermodynamic cycle analysis and performance assessment is carried out experimentally by Boccardi et al. (2013) in the test facility shown in Figure 3.35, representing a prototype of small-scale commercial refrigerator (such as vending machine or stand-alone vertical freezer) equipped with two hermetic single stage reciprocating compressors, three finned coil heat exchangers (gascooler, evaporator and intercooler) and a double stage expansion system.

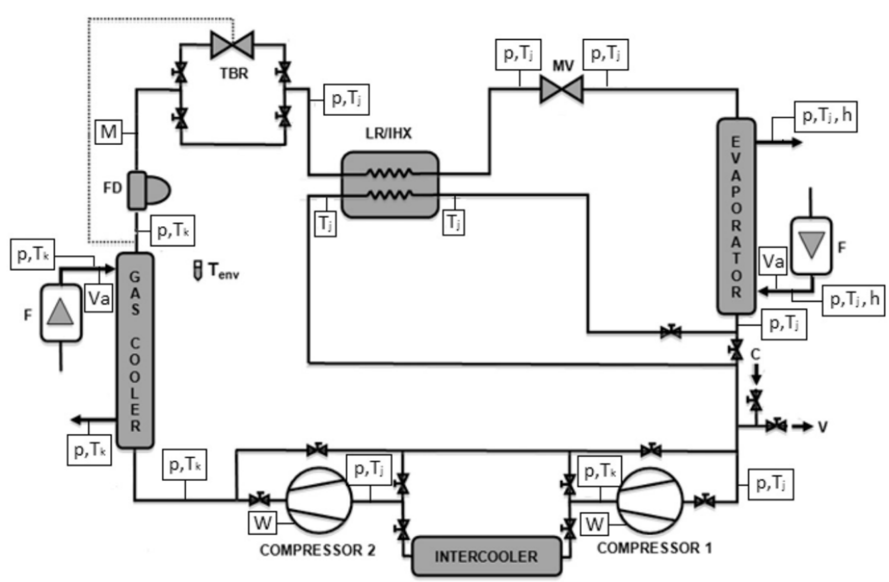

Figure 3.35 – Test facility used in Boccardi et al. (2013)

Tests at different evaporating pressures, gascooler pressures and useful superheating values are carried out, and the effect of these parameters are analysed on the system performance (shown in Figure 3.36a and Figure 3.36b). It is found that the increase of gascooler pressure causes a reduction of cooling capacity by means of reduction of mass flow rate and evaporator latent heat. In addition, the superheat level plays a minor role than the operating pressures on cooling capacity and COP. Finally, the authors analysed the importance of receiver in collecting the excess of refrigerant charge coming from the gascooler by means of tests in overcharge condition. Higher gascooler pressures than the optimal ones at the same ambient temperature conditions are measured as shown in Figure 3.36c, with detrimental effect on the system efficiency.

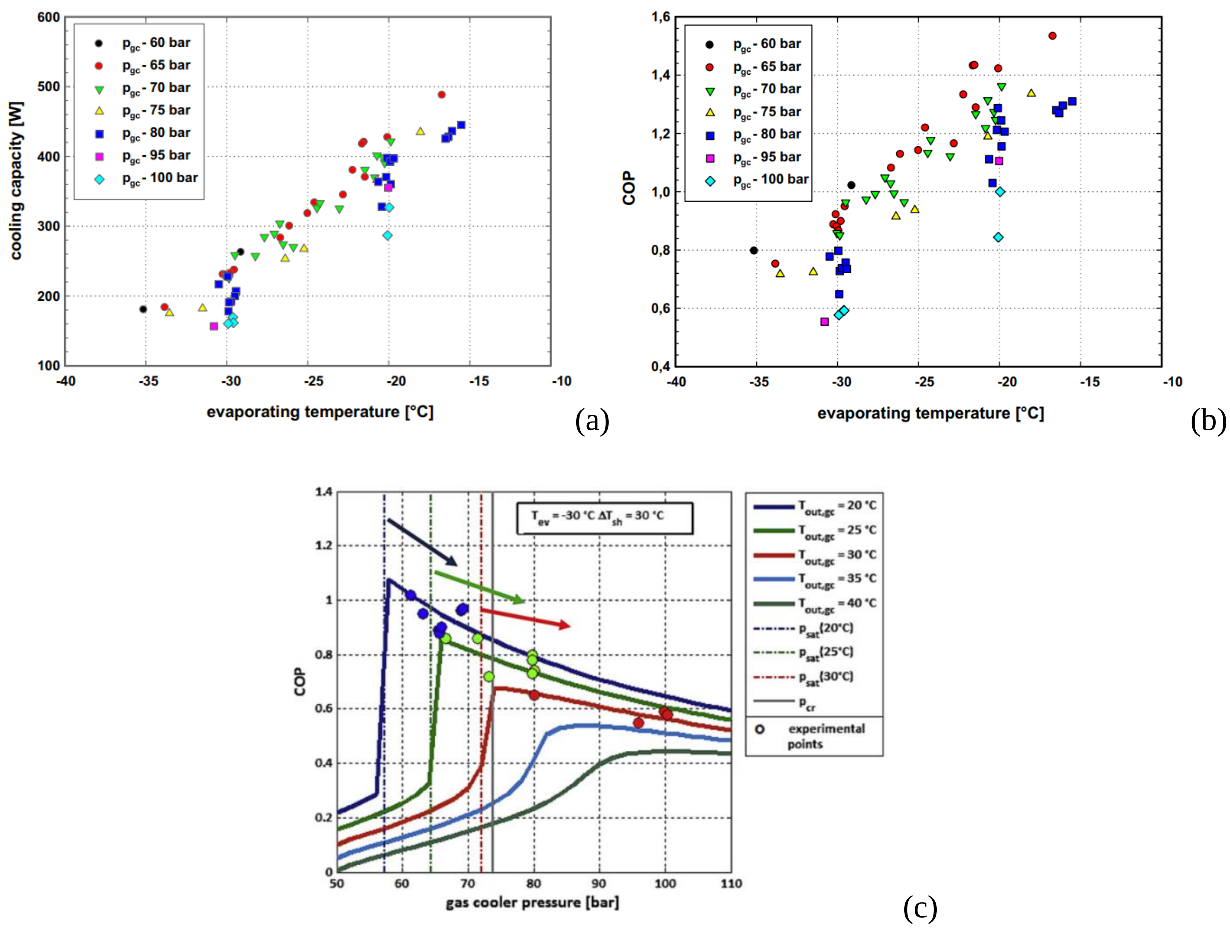

Figure 3.36 – Experimental cooling capacity (a) and COP (b) as a function of evaporating temperature for each value of gascooler pressure, COP as a function of gascooler pressure (line = theorical, dots = experimental points) with dots representing the experimental results in overcharged condition (Boccardi et al., 2013)

Chapter 4 – Low GWP refrigerants in commercial refrigeration

This chapter consists of two studies:

- The first is a multi-criteria (thermo-economic and environmental) computational analysis of R404A mid and long-term replacements in a positive small commercial refrigeration monoblock unit. R404A and four mid and long-term blends R452A, R449A, R454C, R455A and propane are compared in different combinations of temperature difference between air and refrigerant, air temperature variation through heat exchangers, heat exchangers geometries and air flow velocities, obtaining a total amount of 104976 combinations for each refrigerant. Performance (COP), set-up costs, running costs and environmental impact are evaluated for each configuration coping with safety, real dimensions, and technical constraints. The aim of the study is to evaluate which long-term R404A replacement performs better within the conditions explored, as a compromise between COP and set-up costs, running costs and environmental impact.
- The second study is an experimental analysis of a transcritical condensing unit prototype using carbon dioxide as refrigerant, equipped with inverter driven two stage hermetic rolling piston compressor, flash gas removal and intercooler. These solutions are helpful to overcome the thermodynamic peculiarities of carbon dioxide presented in chapter 3, and to reach seasonal performances comparable to those of high-GWP HFC refrigerants. The effect of the ambient temperature, evaporating temperature, intercooler and flash gas removal cooling effect on the thermodynamic cycle and performances are carried out. Finally, the Seasonal Energy Performance Ratio (SEPR) according to EN13215:2016 (CEN, 2016) is evaluated and compared to the value of a condensing unit working with synthetic refrigerant R449A.

4.1 Low-GWP blends and hydrocarbons: thermo-economic and environmental analysis

4.1.1 Working refrigerants thermodynamic analysis

Five HFC / HFO blends R404A, R449A, R452A, R455A, R454C and the hydrocarbon propane (R290) are analysed. The R404A will be used as benchmark refrigerant in results comparison. The main data on refrigerant critical pressure and temperature, composition, GWP and ASHRAE class are listed in Table 4.1.

Table 4.1 – Refrigerants critical point, composition, GWP and Ashrae class

	Critical point		Composition percentage on weight [%]							
Refrigerant	**p [bar]**	**T [°C]**	**R32**	**R125**	**R134a**	**R143a**	**R1234yf**	**R744**	**GWP**	**ASHRAE class**
R404A	37.3	72.0	-	44	4	52		-	3922	A1
R452A	40.7	75.6	11	59	-	-	30	-	2140	A1
R449A	46.6	83.9	24.3	24.7	25.7	-	25.3	-	1397	A1
R455A	48.2	87.5	21.5	-	-	-	-	3	145	A2L
R454C	45.5	88.5	21.5	-	-	-	75.5	-	148	A2L
R290	42.5	96.7	-	-	-	-	-	-	3	A3

The pure fluids R32, R125, R134a, R143a, R1234yf are the most predominant components in the blends. Instead, R455A has also R744 for 3% in weight. The thermodynamic properties of the refrigerants are evaluated using the software Refprop 10.0.

In Figure 4.1, temperature-entropy (T - s) diagram and pressure-enthalpy (p – i) diagram are shown for all substances.

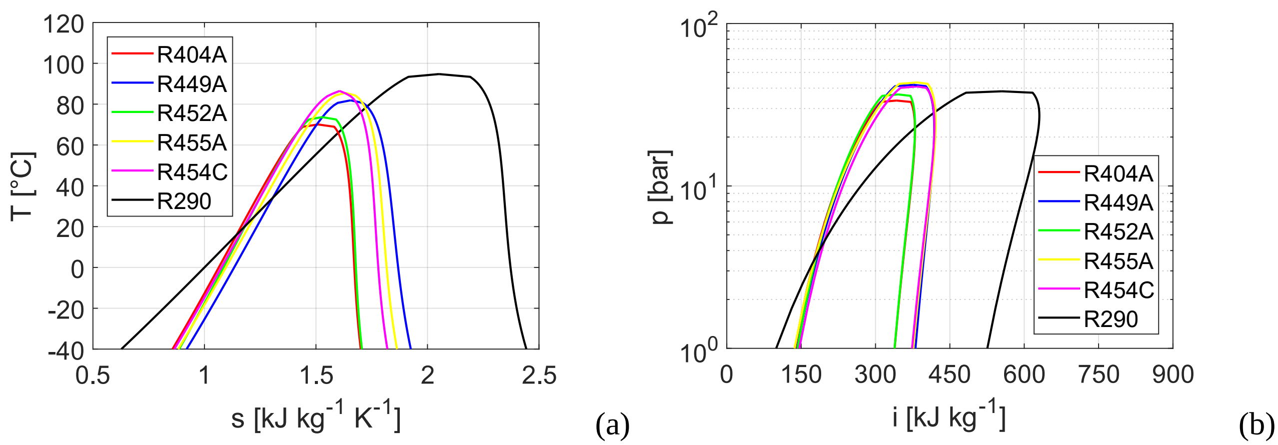

Figure 4.1 – Temperature – entropy (T - s) (a) and pressure – enthalpy (p – i) (b) diagrams of the analysed refrigerants

R404A and R452A have a similar value of critical temperature and saturation curve slopes in T – s and p – i diagrams, the same for the couple R455A and R454C. Propane has the highest value of critical temperature, this means that it will have the highest COP value among the refrigerants due to lower entropic losses related to de-superheating and liquid lamination phase with the hypotheses of same condensing and evaporating temperatures, isentropic compression and heat exchangers with infinite area. The saturated liquid curve in the pressure – enthalpy diagram has the same slope for all mixtures, but they differ in saturated region width. In fact, this latter increases starting from R404A and R452A to the mixtures R449A, R455A and R454C. In black solid lines, propane (R290) has the highest width of the saturated region in both diagrams. The lowest value of refrigerant mass flow rate is expected for propane considering the same cooling capacity, resulting in less pressure drops in heat exchangers than the other

refrigerants. R404A has the lowest value of critical pressure of 37.3 bar, R452A follows with around 40 bar, whereas the group formed by the three blends R454C, R449A and R455A have critical pressure ranging from 45.5 bar to 48.2 bar. Finally, propane is in the middle of the two groups with a value of 42.5 bar.
In Figure 4.2, saturation pressure, volumetric cooling effect and glide are shown as a function of dew point saturation temperature for the analysed refrigerants.

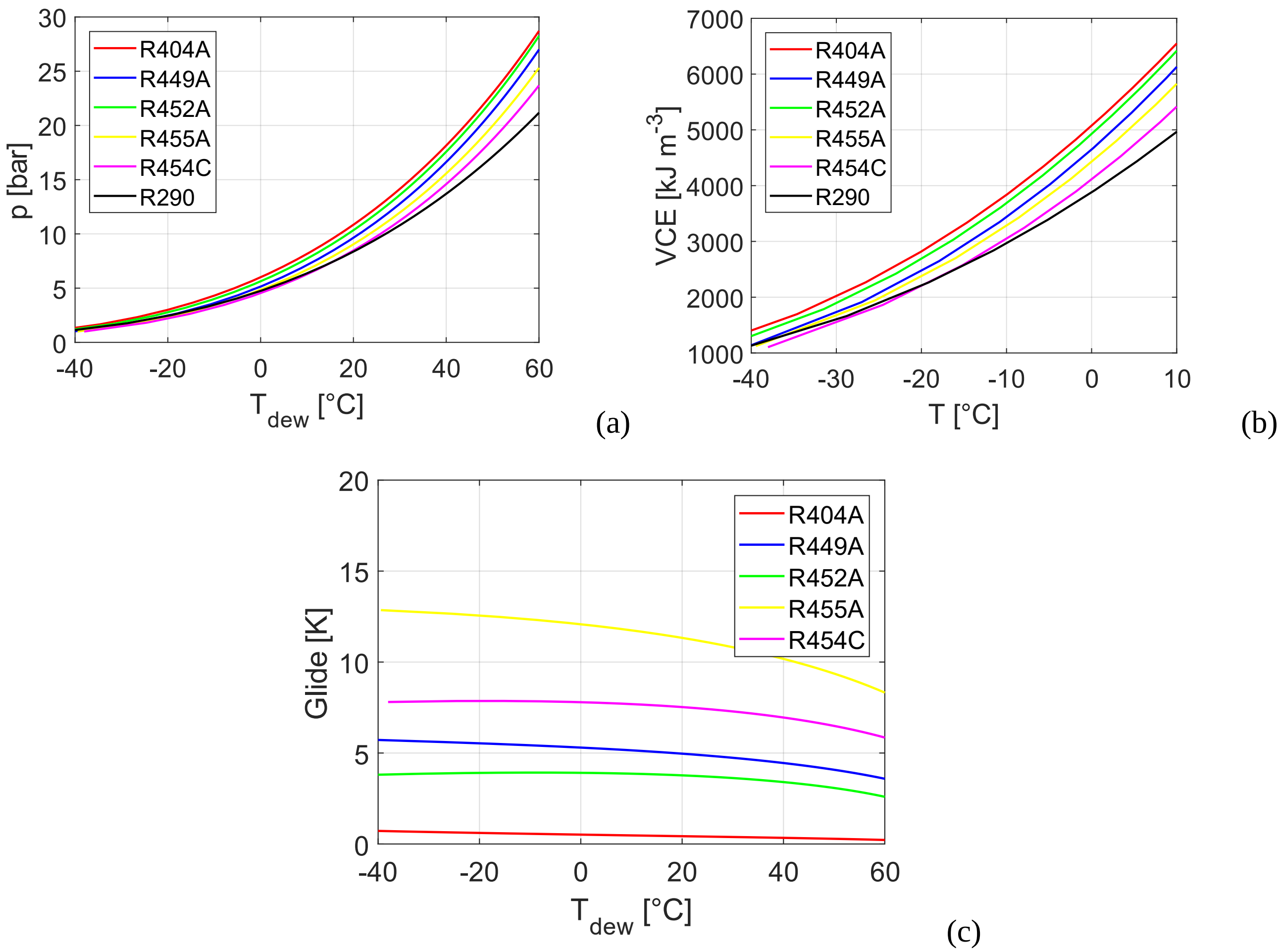

Figure 4.2 – Saturation pressure (a), volumetric cooling effect (b) and glide (c) as a function of dew point saturation temperature for all refrigerants

R404A and R452A have the highest value of saturation pressure, instead, propane has the lowest one as shown in Figure 4.2a. The volumetric cooling effect (*VCE*), depicted in Figure 4.2b, is defined by the following equation:

$$VCE = \rho_{dew} \Delta i_{latent} \qquad \text{Eq. 4.1}$$

Where ρ_{dew} [kg m^{-3}] and Δi_{latent} [kJ kg^{-1}] are the dew point density and the latent heat at the same pressure. *VCE* has influence on the compressor displacement and the suction pipe diameter. Propane has the lowest value of the volumetric cooling effect due to the lowest value of vapour density whose effect is higher than the latent heat one. Going through R454C, R455A, R449A, R452A and R404A the volumetric cooling effect increases with benefit in smaller compressor displacement and suction pipe size.

The glide is the temperature difference between dew and bubble saturation points at the same pressure and it is shown in Figure 4.2c. R455A has the highest value of glide ranging from 13 K at -40°C to 8 K at +60°C. Conversely, R404A has negligible glide in the entire temperature range. In the middle, there are R454C which glide is 7.8 K at -40°C and ranges of 1.8 K until +60°C. The R449A glide ranges from 5.8 K to 3.6 K and for R452A it ranges from 4 K to 2.6 K. The glide can affect the size of the heat exchanger. In fact, considering the same transferred heat rate between air and refrigerant, a value of glide such that air and refrigerant have parallel trends in the condensing or evaporating region leads to a lower mean logarithmic temperature difference, resulting in a higher overall heat transfer coefficient that can be reached increasing the heat transfer surface areas if the refrigerant and air mass flow rates are the same.

4.1.2 Refrigeration unit model and thermodynamic cycle sub-model

The unit considered in the evaluation is a one-stage monoblock unit for walk-in cold rooms, with the main piping layout shown in Figure 4.3a.

The thermodynamic cycles on the temperature – entropy diagram for all investigated refrigerants are shown in Figure 4.4.

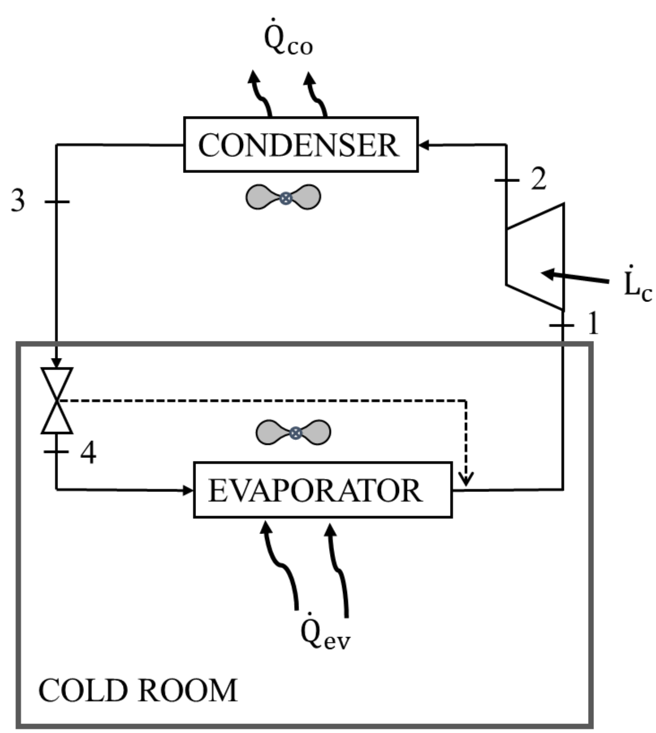

Figure 4.3 – Piping layout scheme of the analysed unit

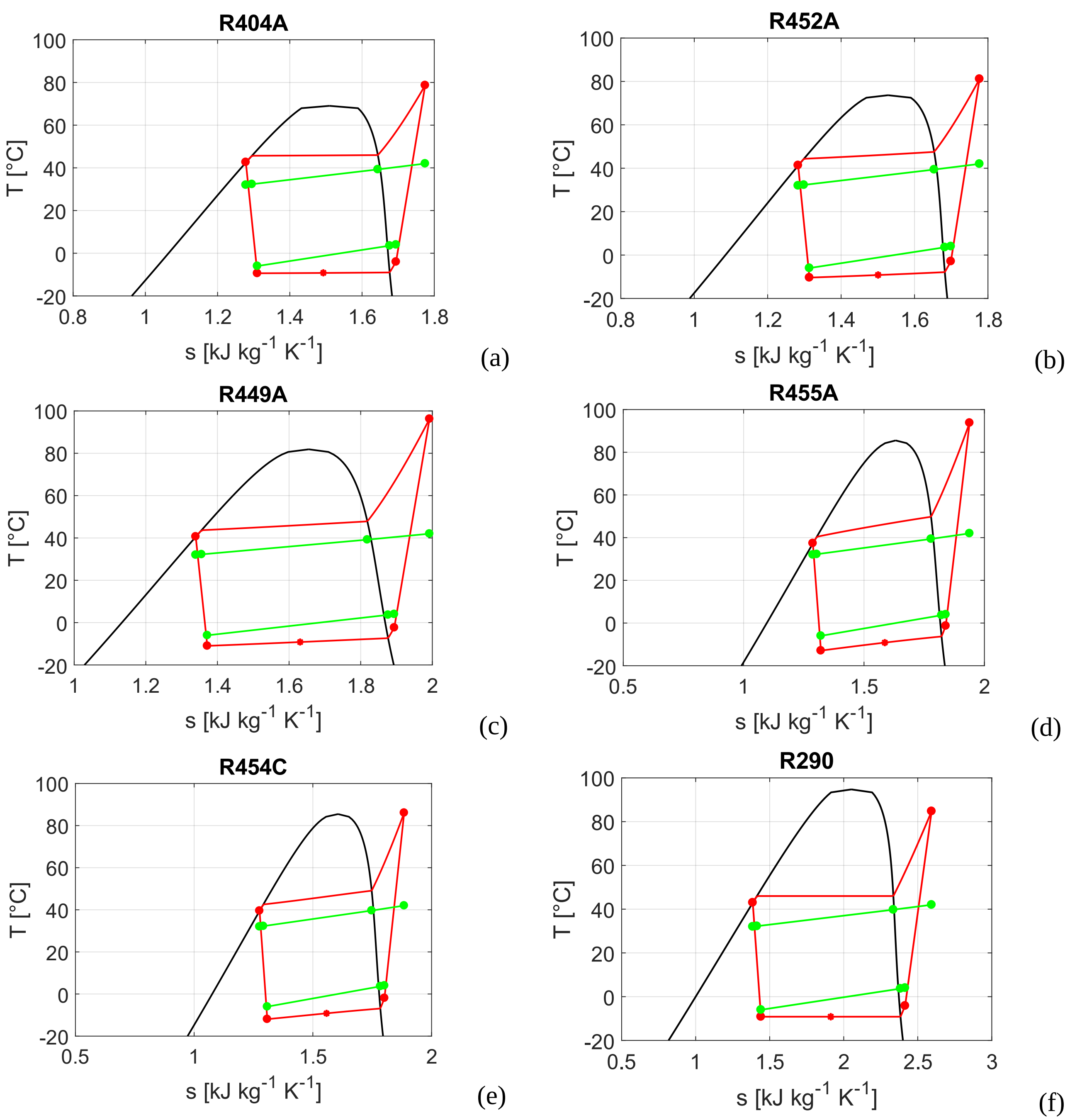

Figure 4.4 – Thermodynamic cycle on temperature – entropy diagram of analysed unit for R404A (a), R452A (b), R449A (c), R455A (d), R454C (e) e R290 (f) in the following conditions: T_{amb} = 32 °C, T_{cr} = +4 °C, $\Delta T_{co,mid}$ = 10 K, $\Delta T_{ev,mid}$ = 8 K, $\Delta T_{air,co} = \Delta T_{air,ev}$ = 10 K

The refrigerator is equipped with a hermetic reciprocating compressor, two fin and coils heat exchangers where the refrigerant transfers heat with air in forced convection, and a thermostatic expansion valve. To design the heat exchangers and the compressor, the thermodynamic cycle is evaluated using an iterative procedure. The main inlet parameters of the algorithm are: ambient temperature T_{amb} (air condenser inlet), cold room temperature T_{cr} (air evaporator inlet), outlet condenser subcooling value (ΔT_{sc}), outlet evaporator superheating value ($\Delta T_{sh,out,ev}$), air temperature variation through condenser and evaporator ($\Delta T_{air,co}$ and $\Delta T_{air,ev}$), refrigerant-air temperature difference measured at vapour mid-point at condenser and evaporator ($\Delta T_{co,mid}$ and $\Delta T_{ev,mid}$) and air velocity across both heat exchanger w_{co} and w_{ev}. After inputting the parameters, the pressures, and the temperatures in points 1, 2, 3 and 4 of Figure 4.3, are evaluated with the following procedure:

1) Assume a guess value of evaporating and condensing pressure p_{ev} and p_{co}

2) Calculate inlet compressor temperature T_1 as:

$$T_1 = T_{dew}(p_{ev}) + \Delta T_{sh} \qquad \text{Eq. 4.2}$$

where $T_{dew}(p_{ev})$ is the dew-point saturation temperature at evaporating pressure.

3) Evaluate the compressor outlet enthalpy i_2 as:

$$i_2 = i_1 + \left(\frac{i_{2,is} - i_1}{\eta_{is}}\right) \qquad \text{Eq. 4.3}$$

where i_1 and $i_{2,is}$ are, respectively, the enthalpy values at compressor inlet and isentropic compressor outlet and η_{is} is the isentropic compressor efficiency whose evaluation and validation procedure will be shown in next section.

4) Calculate air temperatures $T^*_{air,1}$ and $T^*_{air,2}$ corresponding to refrigerant bubble and dew point respectively, as defined in Figure 4.5 by means Eq. 4.4 and Eq. 4.5.

The refrigerant temperature profile is in blue with the indication of all points from condenser inlet with subscript "2", the dew and bubble points and the outlet section defined with subscript "3". The air temperature is indicated with red arrows in the opposite directions thanks to the hypothesis of counter flows. $T_{air,out,co}$ is the air temperature at the outlet section of heat exchanger. $\dot{Q}_{des}$, $\dot{Q}_{cond}$ and $\dot{Q}_{sc}$ are the heat transferred in de-superheating, condensing and subcooling sections, instead, $\dot{Q}_{co}$ [W] is the total heat transferred in the condenser.

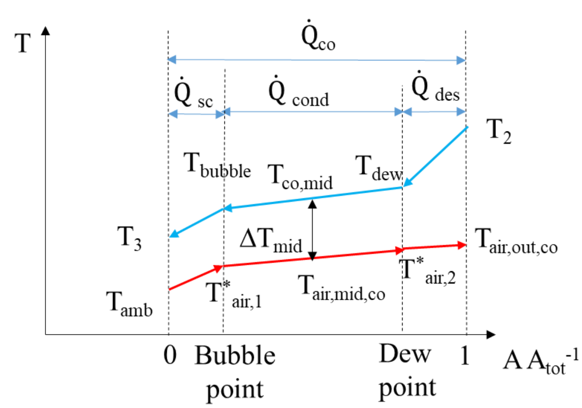

Figure 4.5 – Schematic representation of refrigerant and air temperature profiles as a function of dimensionless condenser area

The following equations are used to evaluate $T^{*}_{air,1}$ and $T^{*}_{air,2}$, namely the air temperature differences proportional to the refrigerant enthalpy (i) variation:

$$\frac{T^{*}_{air,1}-T_{amb}}{T_{air,out,co}-T_{amb}} = \frac{i_{co,bubble}-i_3}{i_2-i_3} \qquad \text{Eq. 4.4}$$

$$\frac{T_{air,out,co}-T^{*}_{air,2}}{T_{air,out,co}-T_{amb}} = \frac{i_2-i_{co,dew}}{i_2-i_3} \qquad \text{Eq. 4.5}$$

5) Calculate $T_{co,mid}$ and the new value of condenser pressure p'_{co} with the following equations:

$$\frac{T^{*}_{air,1}+T^{*}_{air,2}}{2} \qquad \text{Eq. 4.6}$$

$$T_{co,mid} = +\Delta T_{co,mid} \qquad \text{Eq. 4.7}$$

$$p'_{co} = p_{sat}(T_{co,mid}\,, x = 0.5) \qquad \text{Eq. 4.8}$$

In Eq. 4.6, $T_{air,mid,co}$ is defined in Figure 4.5.

6) Repeat the steps 1 to 5 until the relative difference between p_{co} and p'_{co} is below a fixed threshold ε as in the following equation:

$$\left|\frac{p'_{co}-p_{co}}{p_{co}}\right| < \varepsilon \qquad \text{Eq. 4.9}$$

7) Calculate the refrigerant evaporator inlet quality x_4 as follows:

$$i_4 = i_3 = f(p_{co}, T_3) \qquad \text{Eq. 4.10}$$

$$x_4 = f(p_{ev}, i_4) \qquad \text{Eq. 4.11}$$

8) Calculate the mid-point quality at evaporating pressure with the following equation:

$$x_{ev,mid} = \frac{x_4+1}{2} \qquad \text{Eq. 4.12}$$

9) Evaluate the air temperature $T^{*}_{air,ev}$ corresponding to refrigerant dew point as shown in Figure 4.6 using Eq. 4.13.

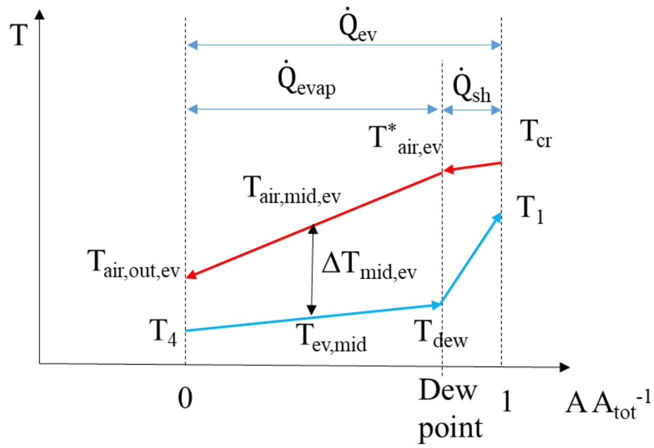

Figure 4.6 - Schematic representation of refrigerant and air temperature profiles as a function of dimensionless evaporator area

Similarly, to the definition given for Figure 4.5 $\dot{Q}_{evap}$ and $\dot{Q}_{sh}$ are the heat transferred in evaporating and superheating sections, whereas their sum is $\dot{Q}_{ev}$.

$$\frac{T^*_{air,ev}-T_{air,out,ev}}{T_{cr}-T_{air,out,ev}} = \frac{i_{dew,ev}-i_4}{i_1-i_4} \qquad \text{Eq. 4.13}$$

10) Evaluate the refrigerant mid-point temperature $T_{ev,mid}$ and evaporator pressure p'_{ev} as:

$$T_{air,mid,ev} = \frac{T_{air,out,ev}+T^*_{air,ev}}{2} \qquad \text{Eq. 4.14}$$

$$T_{ev,mid} = T_{air,mid,ev} - \Delta T_{mid,ev} \qquad \text{Eq. 4.15}$$

$$p'_{ev} = p_{sat}(T_{ev,mid},\ x_{ev,mid}) \qquad \text{Eq. 4.16}$$

In Eq. 4.15 $T_{air,mid,ev}$ is the air temperature corresponding to mid-point condition as shown in Figure 4.6.

11) Repeat the steps 1 to 10 until the relative difference between p_{ev} and p'_{ev} is below a fixed threshold ε as in the following equation:

$$\left|\frac{p'_{ev}-p_{ev}}{p_{ev}}\right| < \varepsilon \qquad \text{Eq. 4.16}$$

After the evaluation of the thermodynamic cycle, refrigerant mass flow rate ($\dot{m}_{ref}$), the design heat exchangers rate ($\dot{Q}$) and compressor displacement (CC) can be evaluated as follows:

$$\dot{m}_{ref} = \frac{\dot{Q}_{ev}}{i_1-i_4} \qquad \text{Eq. 4.17}$$

$$\dot{Q} = \dot{m}_{ref}\Delta i \qquad \text{Eq. 4.18}$$

$$CC = \frac{\dot{m}_{ref}}{\rho_1 n\, \eta_v} \quad \text{Eq. 4.19}$$

The air mass and volumetric flow rates at condenser and evaporator are evaluated with the following equations:

$$\dot{m}_{air,ev} = \frac{\dot{Q}_{ev}}{\bar{c}_{p,air,ev} \Delta T_{air,ev}} \quad \text{Eq. 4.20}$$

$$\dot{V}_{air,ev} = \frac{\dot{m}_{air,ev}}{\rho_{air,ev}} \quad \text{Eq. 4.21}$$

$$\dot{m}_{air,co} = \frac{\dot{Q}_{co}}{\bar{c}_{p,air,co} \Delta T_{air,co}} \quad \text{Eq. 4.22}$$

$$\dot{V}_{air,co} = \frac{\dot{m}_{air,co}}{\rho_{air,co}} \quad \text{Eq. 4.23}$$

4.1.3 Compressor sub-model

The compressor isentropic and volumetric efficiencies as a function of pressure ratio are evaluated after a fitting process of the best-in-class hermetic reciprocating compressor. Four compressor manufacturers catalogue data are analysed for blends and propane and the best-in-class in terms of isentropic efficiency is used in the model. Since the compressor of the same manufacturer has similar effect with different blends, they are unified in one class named "HFC / HFO". In Figure 4.7, isentropic and volumetric efficiencies are shown as a function of the pressure ratio $\beta = p_{co}\, p_{ev}^{-1}$. The scatters represent the real values from the catalogue for different manufacturers, whereas the dotted and dash-dotted lines are the fitted functions used in the calculations for HFC / HFO blends and propane, respectively.

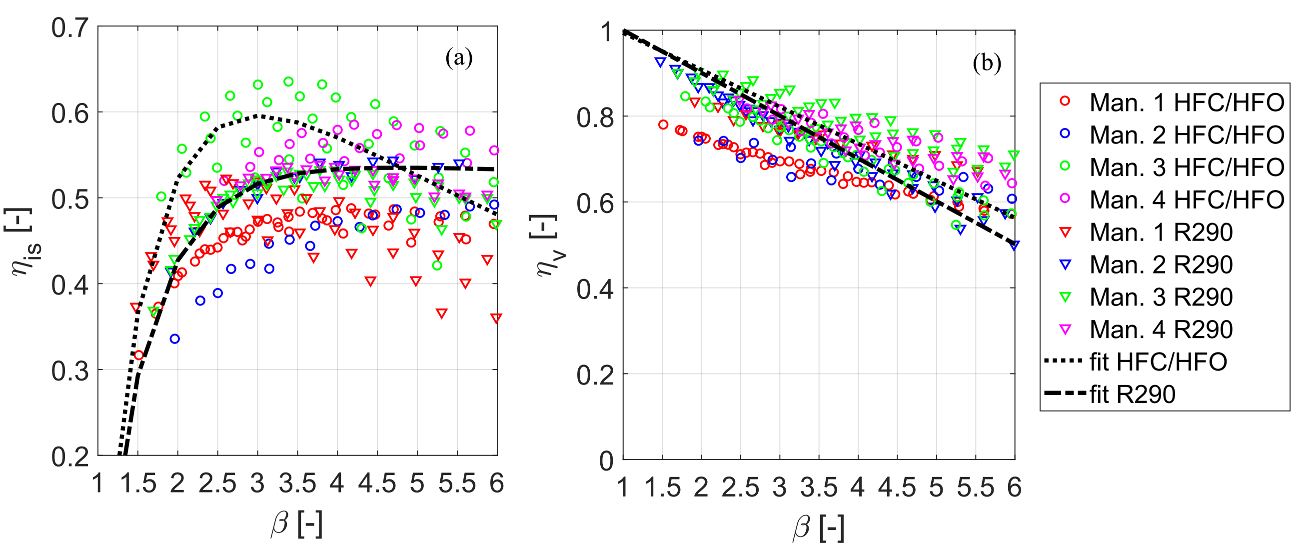

Figure 4.7 – Isentropic and volumetric efficiencies as a function of pressure ratio. Scatter = real compressor data, dashed lines = best-in-class fittings

From the analysis of the catalogue data, the compressors of manufacturers 2 and 3 have been chosen as the best-in-class for HFC / HFO blends and propane, respectively. From Figure 4.7a, the highest value of the compressor isentropic efficiency for HFC / HFO is 0.6, higher than the propane one. This difference will be reduced soon, thanks to propane technology improvement.
The compressor model has been validated with the experimental data of same application using R407H as refrigerant. The experimental points used in the validation are listed in Table 4.2.

Table 4.2 – Experimental data used for compressor model validation

#	T_{co} [°C]	T_{ev} [°C]	$\dot{Q}_{ev}$ [W]	$\dot{L}_{cp}$ [W]	$\Delta T_{sh,out,\ ev}$ [°C]	$\Delta T_{sh,in,cp}$ [°C]	ΔT_{sc} [°C]
1	44.1	-11.4	1663.1	1551.0	11.6	15.1	2.3
2	45.7	-9.3	2072.1	1620.6	7.8	11.2	2.7
3	47.0	-7.2	2270.5	1745.4	0.7	5.7	3.0
4	42.3	-15.3	1164.2	1387.9	16.9	22.0	2.0
5	43.8	-12.3	1426.6	1493.5	12.9	18.7	2.2
6	46.0	-10.1	1571.2	1602.8	10.9	16.3	2.6
7	47.5	-7.8	2022.8	1713.1	2.8	8.5	2.9
8	44.1	-13.5	1460.4	1451.8	14.7	21.6	2.9
9	46.4	-10.1	1968.7	1628.5	11.2	16.4	3.4
10	48.3	-7.8	2269.0	1736.0	4.8	11.3	3.8
11	49.3	-7.1	2417.0	1802.0	2.3	9.3	3.9

Tests 4, 7 and 9 have been used to calibrate isentropic efficiency, instead, all tests have been used to calibrate volumetric efficiency. After the calibration, the model has been validated comparing the experimental value of cooling capacity $\dot{Q}_{ev}$ and the power consumption $\dot{L}_{cp}$ with the ones evaluated in the model with Eq. 4.18 and Eq. 4.25, respectively:

$$\dot{m}_{ref} = \rho_1 \cdot CC \cdot n \cdot \eta_v \qquad \text{Eq. 4.24}$$

$$\dot{L}_{cp} = \frac{\dot{m}_{ref}(i_{2,is} - i_1)}{\eta_{is}} \qquad \text{Eq. 4.25}$$

The results of validation are shown in Figure 4.8, where experimental and model evaluated values of cooling capacity and power consumption are shown on vertical and horizontal axes, respectively.

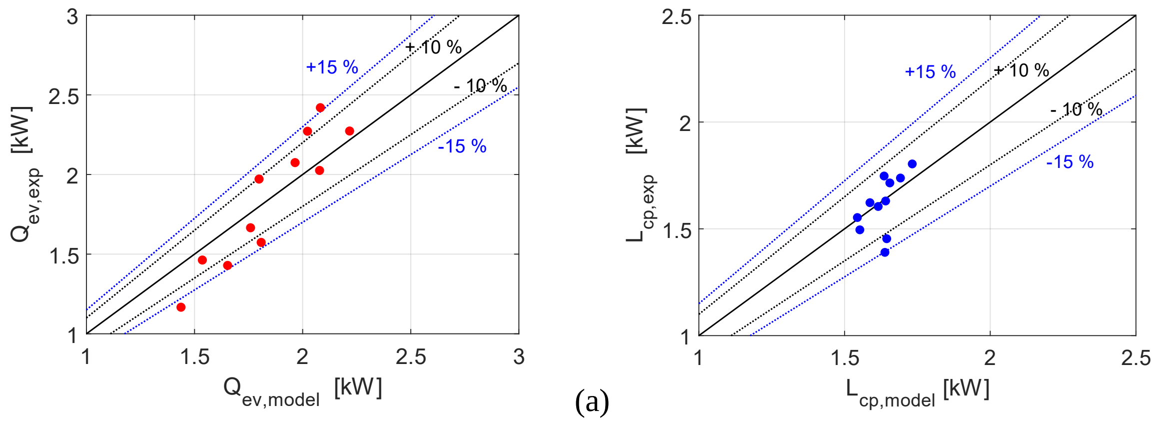

(a) (b)

Figure 4.8 – Compressor model validation results, cooling capacity (a) and power consumption (b) comparison between experimental and evaluated values

The evaluated cooling capacity values are within ±15% (blue dotted lines) error band than the measured ones, except one point. Instead, the evaluated power consumption is within ±10% (black dotted lines) than the measured one, only two are within ±15% error band.

4.1.4 Heat exchanger sub-model

The finned and coil heat exchangers used as condenser and evaporator, have louvered fins and tubes arranged as in-line configuration. The refrigerant flows inside the tubes, and the air passes through the fins, forming a cross-counter flow pattern. Aluminium and copper are the materials used for fins and tubes respectively (k_{cu}=390 W $m^{-1}K^{-1}$ and k_{al}=230 W m^{-1} K^{-1}). A schematization of heat exchanger with the definition of the elementary geometry (black dotted lines) and the discretization scheme (red dotted line) with the flows pattern used in the model are shown in Figure 4.9a and Figure 4.9b, respectively.

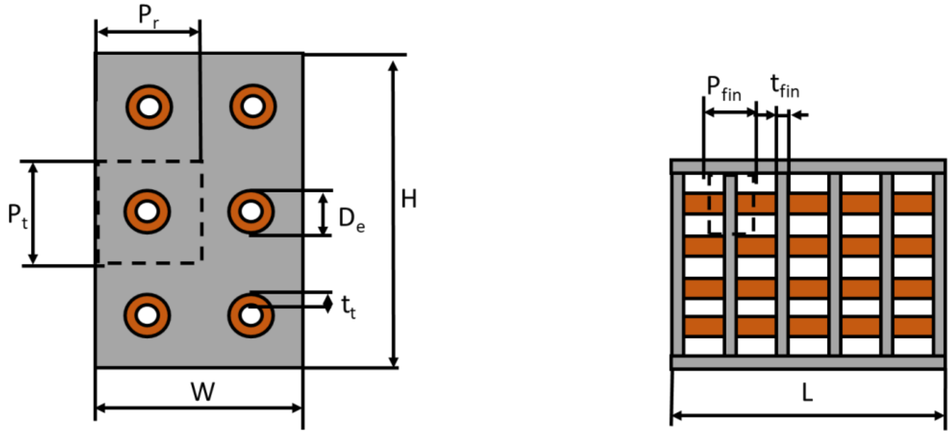

(a)

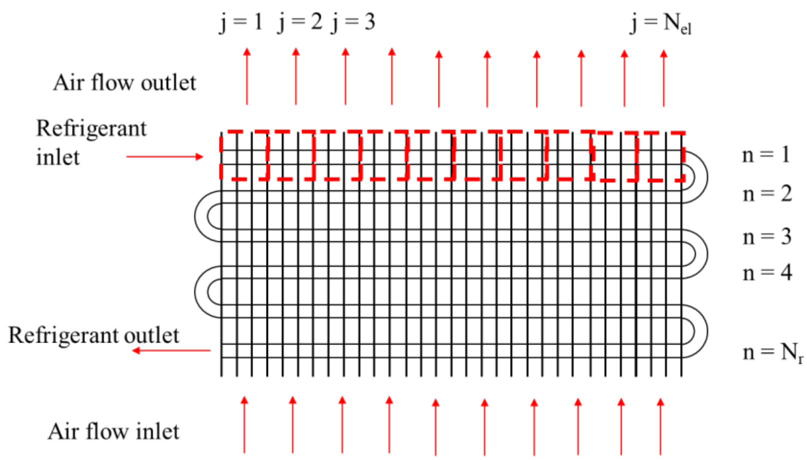

(b)

Figure 4.9 – Heat exchanger geometrical features and dimension (a), flows patterns and discretization scheme (b) for one refrigerant circuit

The inputs to define the geometry of heat exchanger are tube internal diameter (D_{in}), tube thickness (t_t), tube pitch (P_t), fin pitch (P_{fin}) and fin thickness (t_{fin}). The overall dimensions H, L and W, as depicted in Figure 4.9, are evaluated with the following equations:

$$H = \sqrt{\frac{P_t * A_{free-flow}}{(P_t - D_e) * N_{fan}}} \qquad \text{Eq. 4.26}$$

$$L = N_{fan} \, H \qquad \text{Eq. 4.27}$$

$$W = N_r \, P_r \qquad \text{Eq. 4.28}$$

In Eq. 4.26, $A_{free\text{-}flow}$ [m^2] is the air free flow cross sectional area of the heat exchanger and is evaluated with the following equation:

$$A_{free-flow} = \frac{\dot{V}_{air}}{w} \qquad \text{Eq. 4.29}$$

$\dot{V}_{air}$ [m^3 s^{-1}] and w [m s^{-1}] are volumetric air flow rate and air velocity, respectively. N_{fan} is the number of fans moving the air. Its value is fixed as 2 for condenser and evaporator meaning that the length of the evaporator is twice the height according to Eq. 4.27. N_r is the total number of heat exchanger rows, and represents the outcome of the design procedure and therefore of the whole model. N_{el}, shown in Figure 4.9b, is the total number of elements in each row where the mass and heat balances and heat transfer equations are applied to evaluate the surface.

Once the frontal area $L \times H$ has been evaluated, the number of tubes for each row ($N_{t,r}$) and the number of the fins (N_{fin}) can be evaluated as follows:

$$N_{t,r} = \frac{H}{P_t} \qquad \text{Eq. 4.30}$$

$$N_{fin} = \frac{L}{P_{fin}} \qquad \text{Eq. 4.31}$$

$$dA_e = N_{el}^{-1}\left[(\pi D_e L) + 2\,\eta_{fin} N_{fin}\left(P_t P_r - \pi\frac{D_e^2}{4}\right)\right] \qquad \text{Eq. 4.32}$$

$$dA_{in} = N_{el}^{-1}\pi\frac{(D_e - 2t_t)^2}{4}L \qquad \text{Eq. 4.33}$$

In the Eq. 4.32, η_{fin} is the fin efficiency evaluated with the model of Wang et al. (1999).
The refrigerant flow is divided into several circuits (N_{circ}) working in parallel. The temperature profiles are evaluated with the model referring for one circuit, with the assumption that the total air and refrigerant mass flow rates are equally distributed in all circuits. In the algorithm, the combinations of the number of circuits are equal to the divisors of the number of tubes in each row (e.g. if $N_{t,r} = 6$ the circuits can be 1, 2, 3 and 6 with four possible combinations in total).
To evaluate the total heat exchanger surface and its dimensions, mass and energy balances and heat transfer equations are applied in each section (identified by red dotted line in Figure 4.9b) to calculate enthalpy and temperature of air and refrigerant:

$$\dot{Q} = UA\,\Delta T = \frac{\Delta T}{dR} \qquad \text{Eq. 4.34}$$

The overall heat transfer coefficient UA [W K^{-1}] is evaluated by means the calculation of the thermal resistances:

$$dR = dR_{air} + dR_t + dR_{ref} \qquad \text{Eq. 4.35}$$

In the model, the thermal conductive resistance of the tubes has been neglected and only convective resistance at refrigerant (dR_{ref}) and air (dR_{air}) sides are evaluated as follows:

$$dR_{air} = \frac{1}{h_{air}\,dA_e} \qquad \text{Eq. 4.36}$$

$$dR_{ref} = \frac{1}{h_{ref}\,dA_{in}} \qquad \text{Eq. 4.37}$$

The convective air heat transfer coefficient is evaluated with the model of Wang et al. (1999) that considers the dew formation of the piping (Wang et al., 2000). Refrigerant convective heat transfer coefficient h_{ref}, instead, is evaluated with Dittus and Boelter correlation (Dittus and Boelter, 1930) in single phase state in de-superheating, subcooling and superheating sections; conversely, in two-phase state, particular correlations for zeotropic mixtures are used in condensation and evaporation phase Deng et al. (2019), Mastrullo et al. (2019) and Mauro et al. (2020). Pressure drops at air side are evaluated using the model of Wang et al. (1999). Instead, refrigerant side pressure drops are evaluated with Muller-Steinhagen and Heck correlation in two-phase flow condition (Muller-Steinhagen and Heck, 1986) and Blasius correlation in single phase condition (Blasius, 1913).
The iterative calculation starts at the first row (n = 1 in Figure 4.9b) and the model adds another row n = n + 1 if the total evaluated heat rate is below its design value. This latter can be expressed with the

following equation considering a number of elements for each row N_{el} and the total number of the rows N_r.

$$\dot{Q} = N_{circ} \sum_{j=1}^{N_{el}} \sum_{n=1}^{N_r} \dot{Q}_{n,j} \qquad \text{Eq. 4.38}$$

$\dot{Q}_{n,j}$ is the transferred heat rate in each elementary section, when it is equal to its design value the algorithm stops the calculation without adding further rows. Subsequently, it is possible evaluate the total heat exchanger internal and external surface area A_{in} and A_e:

$$A_e = N_r \left[\left(N_{t,r} \pi D_e \, L \; - N_{fin} \pi D_e t_{fin} \right) + 2 N_{fin} \left(HP_r - N_{t,r} \frac{\pi D_e^2}{4} \right) \right] \qquad \text{Eq. 4.39}$$

$$A_{in} = N_r \, N_{t,r} \, \pi \, (D_e - 2t_t) \, L \qquad \text{Eq. 4.40}$$

To calculate the costs of the heat exchanger, tubes and fins weight are evaluated with the following procedure:

$$m_t = N_r \, N_{t,r} \, \rho_{cu} \, \pi \, t_t \, (D_e - t_t) \, L \qquad \text{Eq. 4.41}$$

$$m_{fin} = N_{fin} \, \rho_{al} \, t_{fin} \left[HW - \left(N_r N_{t,r} \pi \frac{D_e^2}{4} \right) \right] \qquad \text{Eq. 4.42}$$

The copper (ρ_{cu}) and alluminium (ρ_{al}) densities are equal to 8960 and 2700 kg m^{-3}.
Similarly, to the compressor, the heat exchanger model is validated considering the case of condenser and evaporator using experimental data collected on a refrigerator working with R407H. The thermodynamic and geometric data used in the validation of condenser and evaporator are listed in Table 4.3 and Table 4.4, respectively.

Table 4.3 – Experimental thermodynamic and geometric data used for condenser validation

#	T_{amb} [°C]	p_{co} [bar]	Q_{co} [W]	$T_{ref,in,cond}$ [°C]	$T_{air,out,co}$ [°C]	ΔT_{air} [°C]	$\dot{V}_{air}$ [m^3 s^{-1}]	w_{air} [m s^{-1}]	$\dot{m}_{ref}$ [g s^{-1}]
1	29.8	17.7	2278.5	98.2	40.4	10.6	0.19	1.37	9.18
2	29.7	18.45	2793.5	96	41.2	11.5	0.21	1.55	11.51
3	30	19.09	3093.9	93.7	41.8	11.8	0.23	1.67	13.03
4	29.9	16.93	1554.5	95.3	39	9.2	0.15	1.08	6.26
5	30.4	17.57	1911.1	94.1	39.8	9.4	0.18	1.29	7.83
6	30.8	18.62	2107.3	94	41.5	10.7	0.17	1.26	8.8
7	30.3	19.3	2715.6	86.7	41.9	11.6	0.2	1.49	11.9
8	30.1	16.7	1206.4	105.3	35.2	5.1	0.21	1.52	4.62
9	29.8	17.7	2035.2	100	38.5	8.7	0.2	1.49	8.1
10	29.7	18.8	2678.9	99.2	39.7	10	0.23	1.7	10.9
11	29.9	19.7	3149.6	96.8	40.9	11	0.25	1.83	13.17
12	30.1	20.2	3383.4	96	41.7	11.6	0.25	1.87	14.33
13	29.9	17.61	2082.5	104.1	37.5	7.6	0.24	1.74	8.15

Available geometrical features

D_e [mm]	t_{tube} [mm]	t_{fin} [mm]	P_{fin} [mm]	P_t [mm]	P_r [mm]	N_{circ} [-]	$N_{t,r}$ [-]	N_r [-]	H [mm]	L [mm]
7.0	0.3	0.1	2.5	25	12.7	4	16	5	400	470

Table 4.4 – Experimental thermodynamic and geometric data used for evaporator validation

#	T_{cr} [°C]	p_{co} [bar]	p_{ev} [bar]	Q_{ev} [W]	ΔT_{sc} [°C]	ΔT_{sh} [°C]	$T_{air,out}$ [°C]	ΔT_{air} [°C]	$\dot{V}_{air}$ [m^3 s^{-1}]	w_{air} [m s^{-1}]	$\dot{m}_{ref}$ [g s^{-1}]
1	-1.4	16.8	2.7	2100	2	12.3	-6.7	5.3	0.33	3.54	11.9
2	-3.5	17.5	3	2310	2.2	7.1	-8.6	5.1	0.32	3.54	13.5
3	-1.1	18.4	3.29	2310	2.6	7.2	-6.6	5.5	0.33	3.54	13.6
4	-2.1	19	3.41	2520	2.9	0.5	-8.1	6	0.33	3.54	15.6
5	-2.1	17.8	2.87	2730	3.1	9.2	-8.8	6.7	0.33	3.54	15.8

Available geometrical features

D_e [mm]	t_{tube} [mm]	t_{fin} [mm]	P_{fin} [mm]	P_t [mm]	P_r [mm]	N_{circ} [-]	$N_{t,r}$ [-]	N_r [-]	H [mm]	L [mm]
10	0.5	0.1	5	25	25	5	14	6	350	440

The results of validation process, in terms of dimensionless area referring to the real heat exchanger one calculated in each test, are shown in Figure 4.10a and Figure 4.10b, for condenser and evaporator, respectively.

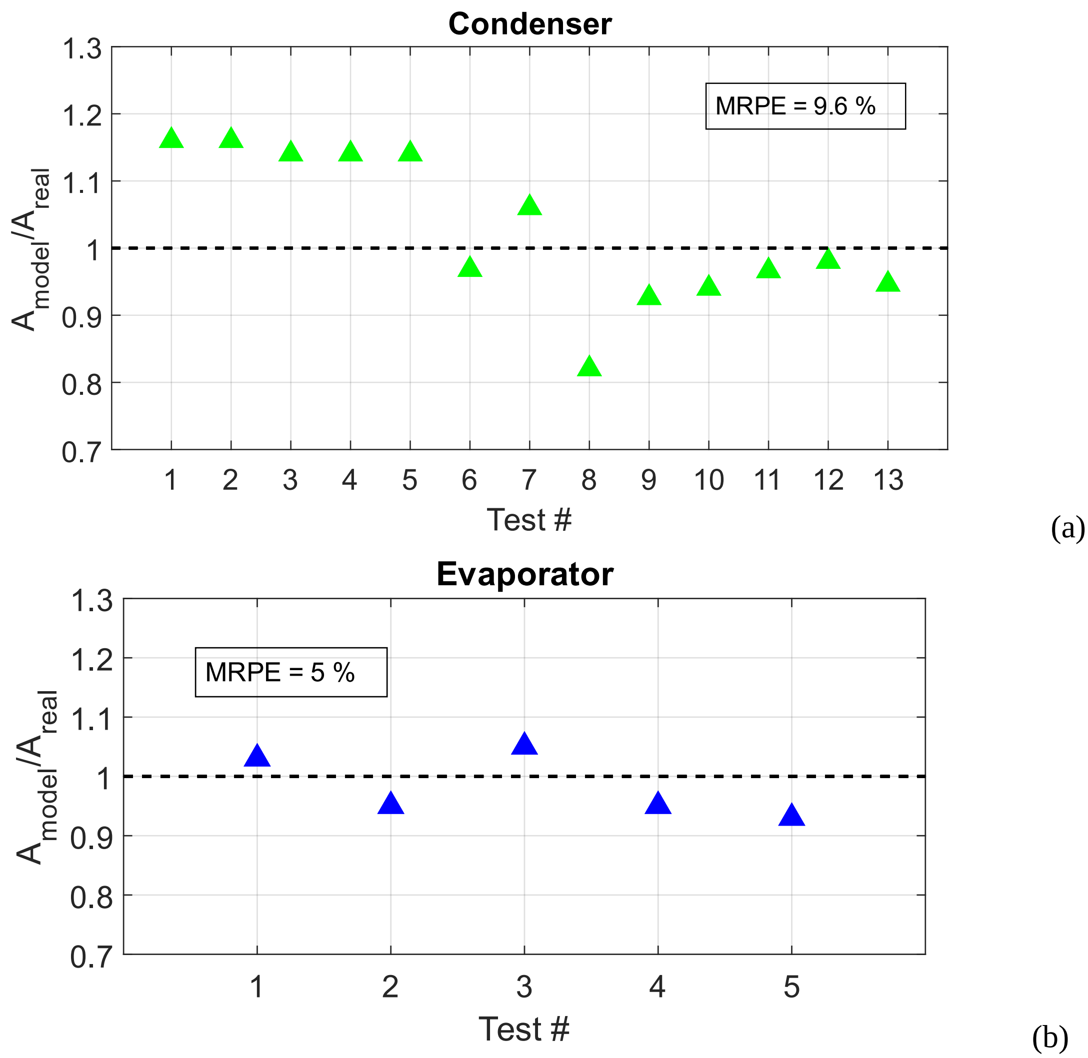

Figure 4.10 – Validation results for condenser (a) and evaporator (b) for each test

The evaluated condenser heat exchanger surface is within ± 20% error band than the real one with a MRPE = 9.6% (mean relative predicted error); the calculated evaporator surface is within the error band of ± 5% than the real one with a MRPE = 5%.

4.1.5 Coefficient of performance calculation

The performance of the modelled refrigerator is indicated by means of COP value that takes in consideration also the ancillaries:

$$COP = \frac{\dot{Q}_{ev}}{\dot{L}_c + \dot{L}_{fan,co} + \dot{L}_{fan,ev}} \qquad \text{Eq. 4.43}$$

$\dot{L}_c$, $\dot{L}_{fan,co}$ and $\dot{L}_{fan,ev}$ are respectively, compressor, condenser fan and evaporator fan power consumption. The fans power consumption are calculated with volumetric air flow rate, the air side pressure drops across the heat exchangers and the fan efficiency set equal to 0.65, in line with the limit imposed by European Regulations and in line as possible value for low-budget devices. To estimate the annual energy consumption, an on / off operation is considered, for this reason *COP* value is corrected to consider the effect of cyclic operation, obtaining a COP_{CR} value:

$$COP_{CR} = COP\ [1 - 0.25\ (1 - CR)] \qquad \text{Eq. 4.44}$$

The CR parameter is the capacity ratio between the cooling demand and the cooling capacity of the unit, fixed to 0.6, since it is a typical value for on / off appliances in commercial refrigeration sector.

4.1.6 Refrigerant charge evaluation

The refrigerant charge (m_{ref}) inside the refrigerator is evaluated as the sum of the refrigerant inside the condenser, evaporator and the liquid line, the contribution of discharge and suction lines are neglected.

$$m_{ref} = m_{co} + m_{ev} + m_{liq} \qquad \text{Eq. 4.45}$$

The refrigerant charge inside the heat exchangers (m_{hx}, for both condenser or evaporator) is calculated as the sum of contributions of the charge in one (m_{1p}) and two-phase (m_{2p}) sections.

$$m_{hx} = m_{1p} + m_{2p} \qquad \text{Eq. 4.46}$$

In one-phase sections, the mass of the refrigerant is evaluated as follow:

$$m_{1p} = \rho\ V \qquad \text{Eq. 4.47}$$

Where ρ and V are, respectively, the refrigerant density (vapour or liquid) and the volume occupied by the refrigerant. The refrigerant inside the liquid line, m_{liq}, is evaluated with Eq. 4.47. In two-phase sections, the refrigerant charge is evaluated with the following equation:

$$m_{2p} = \int [\rho_{dew}\, \alpha + \rho_{bubble}(1 - \alpha)]\ dV_{in} \qquad \text{Eq. 4.48}$$

In Eq. 4.48, ρ_{dew} and ρ_{bubble} are the densities at dew and bubble point, respectively; α is the void fraction value, calculated according to Rouhani-Axelsson model (Rouhani et Axelsson, 1970).

4.1.7 Economic and environmental impact equations

The economic analysis is carried out by means the evaluation of investment cost ($C_{set\text{-}up}$) and the running costs (C_{run}).
The investment cost is defined as the sum of compressor, heat exchangers, refrigerant charge, ancillaries, metal cover and manufacturing costs:

$$C_{set-up} = C_{cp} + C_{co} + C_{ev} + C_{ref} + C_{anc} + C_{met} + C_{man} \qquad \text{Eq. 4.49}$$

The compressor cost C_{cp} is evaluated using a cost function that depends on the compressor displacement value. This latter is obtained by fitting the costs of hermetic reciprocating compressors imposed by manufactures and distribution channels. The equation to evaluate compressor cost has the following expression:

$$C_{cp} = f_{R290,cp}[(a_{cp}CC + b_{cp}) - (c_{cp}\exp(-d_{cp}CC))] \qquad \text{Eq. 4.50}$$

a_{cp}, b_{cp}, c_{cp} and d_{cp} are the coefficients evaluated with the fitting operation; $f_{R290,\ cp}$ (equal to 1.1 for propane and 1 otherwise) is the correction factor to consider the extra costs of compressor with propane (that requires sparkless motors or ATEX certification).

Heat exchangers costs (C_{co} and C_{ev}) are evaluated using the weight of tubes and fins multiplied for the specific material cost per unit of weight as follows:

$$C_{co} = C_{cu}m_{t,co} + C_{al}m_{fin,co} \qquad \text{Eq. 4.51}$$

$$C_{ev} = C_{cu}m_{t,ev} + C_{al}m_{fin,ev} \qquad \text{Eq. 4.52}$$

C_{cu} and C_{al} are the specific material costs per unit of weight [€ kg^{-1}] for copper and aluminium, respectively. The refrigerant cost, C_{ref} is evaluated by multiplying the refrigerant specific cost per unit of weight ($C_{u,ref}$) [€ kg^{-1}] with the total refrigerant charge inside the refrigerator m_{ref}.

$$C_{ref} = C_{u,ref}m_{ref} \qquad \text{Eq. 4.53}$$

The cost of ancillaries C_{anc} comprises the cost of solenoid valve ($C_{solenoid}$) to operate hot gas bypass defrost cycle and heat exchanger fans ($C_{co,fan}$ and $C_{ev,fan}$).

$$C_{anc} = f_{R290,anc}(C_{co,fan} + C_{ev,fan} + C_{solenoid}) \qquad \text{Eq. 4.54}$$

$f_{R290,anc}$ is the correction factor similar to what described for compressor, it is equal to 2 for propane otherwise it is 1.

The material used for refrigerator cover and frame is galvanized steel, the cost of the cover is evaluated as a function of its weight as follows:

$$C_{met} = C_{steel}\rho_{steel}V_{cover} \qquad \text{Eq. 4.55}$$

C_{steel}, ρ_{steel} and V_{cover} are the specific galvanized steel cost per unit of weight [€ kg^{-1}], steel density (equal to 7850 kg m^{-3}) and cover volume [m^3]. This latter is evaluated after the definition of cover shape: in the exterior side of the unit (referring to the cold room), the compressor, the condenser, the thermostatic valve, control box and pipelines are enclosed by four panels thick 1 mm, the top and bottom side are supposed to be perforated to allow air flow circulation, so they are not included in calculation. Instead, on the cold room side (interior side), the evaporator and its fan are enclosed by four panels of the same material and thick as exterior side. The exterior and interior sides are connected mechanically by means of C-shaped spar. In Figure 4.11, a schematization of the cover and connection structure with dimension symbols is shown.

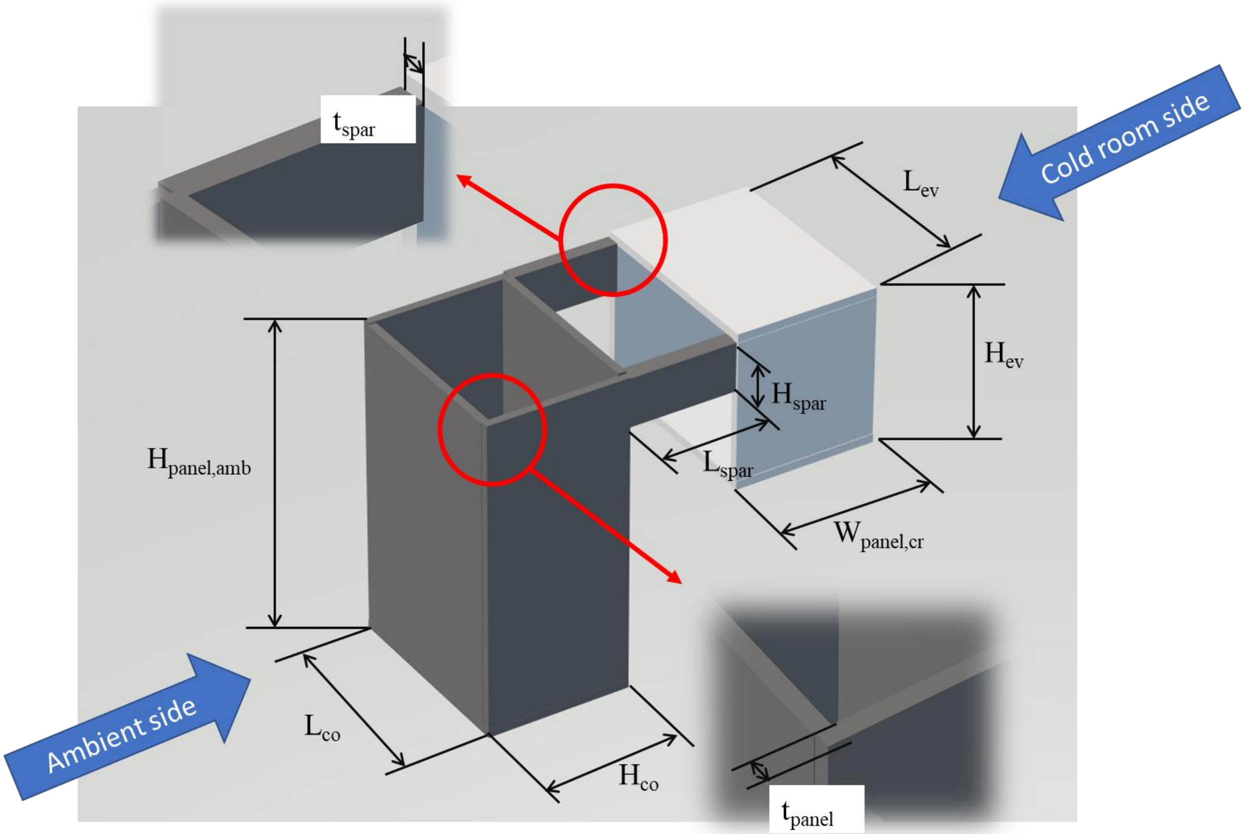

Figure 4.11 – Cover schematization and dimension symbol legend

Finally, the cover volume is evaluated with the following equation:

$$V_{cover} = 2[t_{panel}(L_{co}H_{panel,amb} + H_{co}H_{panel,amb} + H_{ev}W_{panel,cr} + L_{ev}W_{panel,cr}) + t_{spar}(L_{spar}H_{spar})] \quad \text{Eq. 4.56}$$

The meaning of the symbols is clarified in Figure 4.11. L_{spar} include the cold room wall thickness and free space to allow evaporator air-flow circulation, it is kept equal to 0.2 mm. $H_{panel,amb}$ equal to 1.4 times the condenser length L_{co}.

The last element of Eq. 4.49 is C_{man}, that is the manufacturing cost equal to 40 € for each refrigerant circuit.

The running (operational) cost, C_{run} during the entire lifetime of the refrigerator is evaluated with the following equation:

$$C_{run} = C_{u,en} \frac{\dot{Q}_{ev}}{COP_{CR}} \; yy_{run} \, hh_{run} \quad \text{Eq. 4.57}$$

Where $C_{u,en}$ is the specific cost of the energy [€ kWh], $\dot{Q}_{ev}$ and COP_{CR} are cooling capacity and corrected *COP* according to Eq. 4.44, yy_{run} and hh_{run} are respectively the lifetime and the annual operation hours of the refrigerator.
The total costs C_{tot} for the customer is the sum of set-up costs charged of 40% to include local taxes and manufacturer management costs and the running costs C_{run}.

$$C_{tot} = 1.4\, C_{set-up} + C_{run} \qquad \text{Eq. 4.58}$$

The environmental impact is evaluated with TEWI index (Total Equivalent Warming Impact), as defined in EN378-1:2016 (CEN, 2016). The emissions related to manufacturing process, commissioning, and disposal (related to the dismissing of components and materials) operations are not included in the calculation.

$$TEWI = m_{ref}\, GWP\, [(\, ALR\;\; yy_{run}\,) + EOL] + \frac{\dot{Q}_{ev}}{COP_{CR}}\, yy_{run} hh_{run}\, EF \qquad \text{Eq. 4.59}$$

Where GWP is the global warming potential index of the refrigerant, *ALR* is the annual leakage ratio defined as the percentage of total refrigerant mass, *EOL* is the end-of-life refrigerant emission during disposal operation defined as percentage of total refrigerant charge and *EF* is the carbon dioxide emission factor related to the electric energy production.

4.1.8 Calculation procedure

All the sub-models and the equations used to evaluate the costs and the environmental impact are implemented in MATLAB environment. The flow chart of the algorithm is shown in Figure 4.12. The configurations violating the constraints of maximum compressor discharge temperature, maximum heat exchanger length, maximum refrigerant and air side pressure drops, and maximum refrigerant charge are discarded and not included in the analysis.

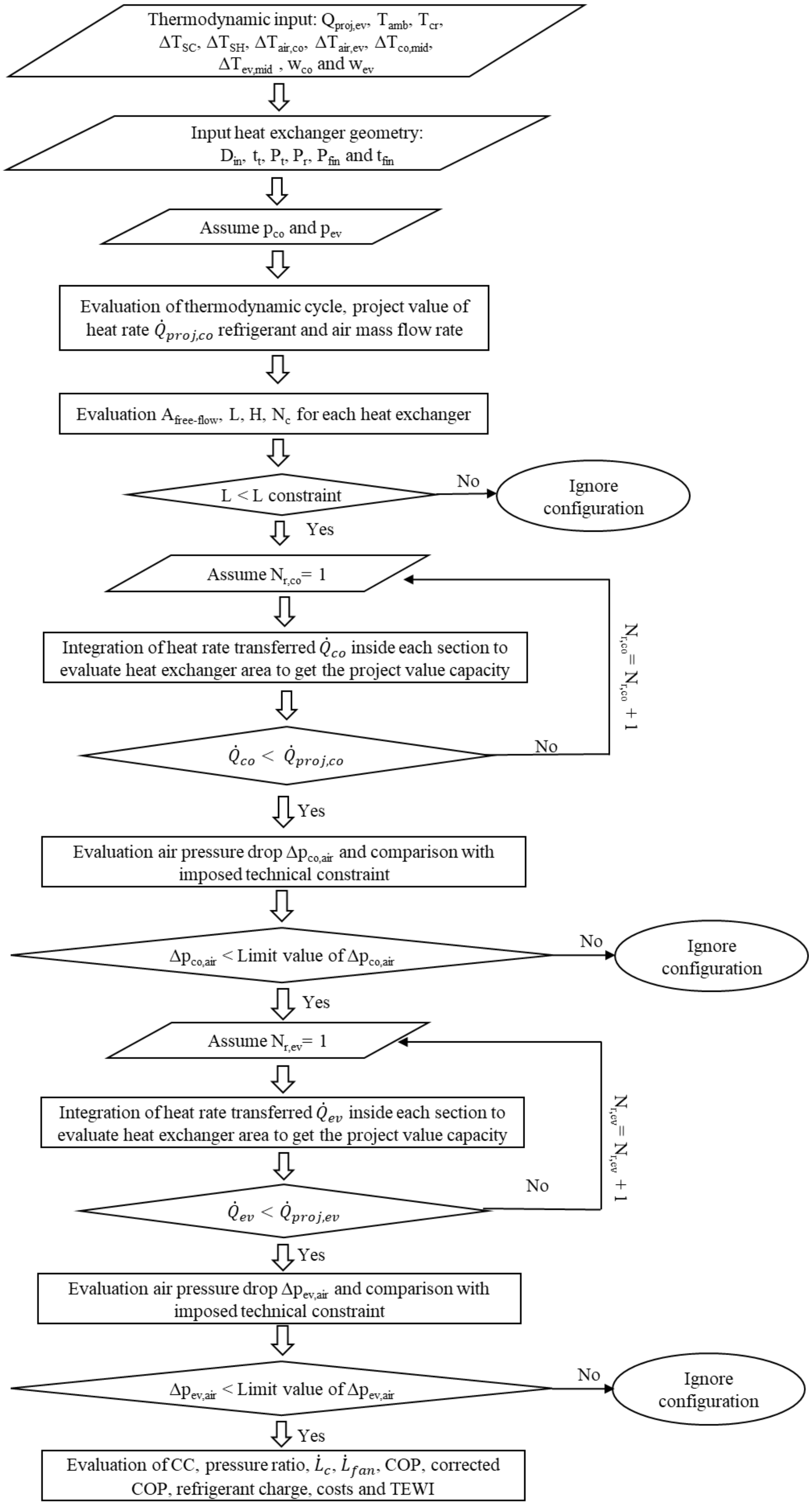

Figure 4.12 – Algorithm flow chart

4.1.9 Input values and assumption of the analysis

The values and ranges of main input parameter relating thermodynamic cycle, heat exchangers geometry and constraints are listed in Table 4.5.

Table 4.5 – Values of thermodynamic boundary conditions data and their ranges used in the algorithm

Parameter	Value / ranges
Fixed parameters	
$\dot{Q}_{ev}$	2.5 [kW]
T_{amb}	32 [°C]
T_{cr}	4 [°C]
ΔT_{sc}	3 [°C]
ΔT_{sh}	5 [°C]
Liquid line	0.1 [m]
Length of line between thermostatic valve and evaporator distributor L_{2p}	$1.83 \times W_{ev}$ [m]
η_{is}	Fitting best-in-class compressor efficiency
η_{v}	Fitting best-in-class compressor efficiency
η_{fan}	0.65
N_{fan}	2
n	50 [rev s^{-1}]
ε	0.05
Variable parameters	
$\Delta T_{air,co}$	[5; 7; 9] [°C]
$\Delta T_{air,ev}$	[5; 7; 9] [°C]
$\Delta T_{co,mid}$	[6; 8; 10] [°C]
$\Delta T_{ev,mid}$	[4; 6; 8] [°C]
w_{co}	[1; 2; 3; 4] [m s^{-1}]
w_{ev}	[1; 2; 3; 4] [m s^{-1}]
Maximum values of the constrained parameters	
Compressor outlet temperature	110 [°C]
Heat exchanger length L	1 [m]
Air side pressure drop	100 [Pa]
Refrigerant side pressure drops in terms of temperature glide	2 [K]
Refrigerant charge in each refrigerant circuit (one condenser + one compressor + one thermostatic valve + one evaporator)	8.93 kg (A1 ASHRAE class refrigerant); 2.54 kg (A2L ASHRAE class refrigerant); 0.15 kg (A3 ASHRAE class refrigerant)

In the calculations two kind of configurations with one and two refrigerant circuits (each of them composed by one compressor, one condenser, one evaporator and one thermostatic expansion valve and of cooling capacity half than the total) are considered with propane, since poor number of configurations compliant to the refrigerant charge limit imposed by EN378-1:2016 (CEN, 2016) are found. However, the two refrigerant circuit arrangement is common in the marketplace.

During the simulation the effect of frost accumulation related to air humidity (due to food transpiration or door openings) is neglected. This aspect requires a transient simulation which results depend by the initial condition of each configuration, not available due to high number of simulated combinations. For this reason, the fair comparison is carried out in the condition of no-frost formation. Nevertheless, the combination of evaporator geometries is compatible to the implementation of hot gas bypass defrost system. Compressor manufacturers recommend to not overcome a refrigerant outlet temperature value of 110°C, especially with low-GWP blends, since high temperature values cause thermal stresses in compressor crank mechanism with reduction of oil viscosity, with detrimental effect on lubricating performances and seizures risks. Air and refrigerant pressure drop value limits are imposed to avoid high fans power consumption and to limit the pressure ratio allowing the compressor operation with lower value of power consumption.

Refrigerant charge limits in one refrigeration circuit (comprising one compressor, one condenser, one thermostatic valve and one evaporator) are imposed by EN378-1:2016 (CEN, 2016) depending by refrigerant ASHRAE safety class, room volume, class and access category of the refrigerator installation place. In this case, the installation above the ground, a site of access category *a* (defined as general access) and class I location (defined as *"Mechanical equipment located in the occupied space"*) and a cold room volume of 25 m^3 is considered.

Considering the combinations of $\Delta T_{air,co}$, $\Delta T_{air,ev}$, $\Delta T_{co,mid}$, $\Delta T_{ev,mid}$, a total of 81 thermodynamic cycles are evaluated.

In Table 4.6, heat exchanger geometrical data are listed with the ranges for variable parameters.

Table 4.6 – Heat exchanger geometry parameter values and ranges

Parameter	**Value / ranges**
Fixed parameters	
P_t	$3 \times D_{ex}$
P_r	$3 \times D_{ex}$
t_t	0.5 [mm]
Variable parameters	
$D_{co,e}$	[5; 7; 9] [mm]
$D_{ev,e}$	[6; 8.2; 10] [mm]
$P_{fin,co}$	[3; 4; 5] [mm]
$P_{fin,ev}$	[4; 5; 6] [mm]

The total achievable combinations for each heat exchanger are 36. Putting together the total combinations of thermodynamic cycle, condenser and evaporator geometries, a total of 104976 combinations are simulated for each refrigerant.

The data of economic and environmental analysis are listed in Table 4.7, comprising the coefficient of the fitted cost functions for compressor. Refrigerant and raw material costs are the prices applied by manufacturers and distributors. The energy costs are referred to a non-household consumer according to Eurostat (Eurostat, 2021). The emission factors are taken consulting document of European Environmental Agency available online (EEA, 2012). The data about total lifetime (yy_{run}), end of life refrigerant emissions (EOL) and annual leakage rate (ALR) are obtained from the work of Troch et al. (2016) considering stand-alone commercial refrigeration appliances.

Table 4.7 – Economic and environmental data used in the calculation

Economic parameters	
Parameter	**Value**
a_{cp}	1.133 [€ m^{-3}]
b_{cp}	220.6 [€]
c_{cp}	225.2 [€]
d_{cp}	0.05974 [$€^{-1}$]
$C_{co,fan}+C_{ev,fan}+C_{solenoid}$	68 [€]
C_{cu}	8 [€ kg^{-1}]
C_{al}	2 [€ kg^{-1}]
C_{steel}	1.7 [€ kg^{-1}]
C_{R404A}	34.1 [€ kg^{-1}]
C_{R452A}	43.2 [€ kg^{-1}]
C_{R449A}	31.8 [€ kg^{-1}]
C_{R455A}	48 [€ kg^{-1}]
C_{R454C}	37.3 [€ kg^{-1}]
C_{R290}	36.9 [€ kg^{-1}]
$f_{R290,\ cp}$	1 (HFC/HFO blends); 1.1 (R290)
$f_{R290,\ anc}$	1 (HFC/HFO blends); 2 (R290)
hh_{run}	5256 [h]
yy_{run}	15 [years]
$C_{u.en}$	0.15 [€ kWh^{-1}] (Italy) (Eurostat, 2021)
	0.18 [€ kWh^{-1}] (Germany) (Eurostat, 2021)
	0.095 [€ kWh^{-1}] (France) (Eurostat, 2021)
Environmental parameters	
EF	0.405 [$kgCO_2eq$ kWh^{-1}] (Italy) (EEA, 2012)
	0.503 [$kgCO_2eq$ kWh^{-1}] (Germany) (EEA, 2012)
	0.092 [$kgCO_2eq$ kWh^{-1}] (France) (EEA, 2012)
EOL	Troch et al. (2016)
ALR	Troch et al. (2016)

4.1.10 Results for the manufacturer point of view: COP and set-up costs analysis

Before proceeding with the analysis of the results, the total evaluated combinations are reduced by applying the technical, safety and real dimension constraints as described before. In Figure 4.13, all configurations in blue and the configuration used in the analysis, in red, are shown for each constraint as a function of COP with R455A. Refrigerant charge constraint is the most restrictive, in fact the highest density of blue dots are above the imposed threshold than in other thresholds. The same conclusion can be extended also to other refrigerants, especially for propane where the refrigerant charge values in all configurations is depicted as function of COP in Figure 4.14 for single and double configuration respectively. The number of total configurations within the constraints and its percentage differences with the total combinations are listed in Table 4.8, for each refrigerant.

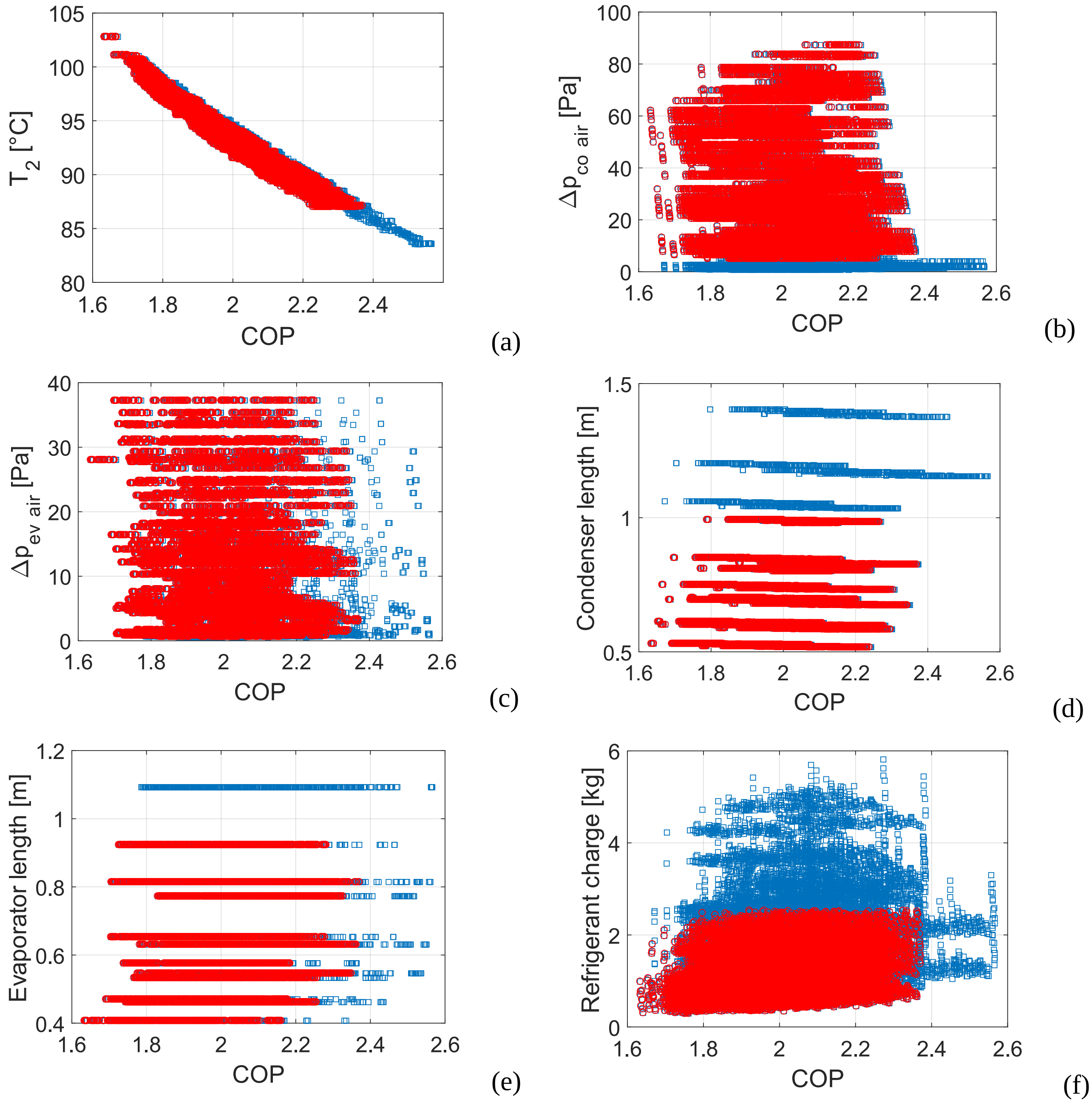

Figure 4.13 – Compressor discharge temperature (a), air pressure drops at condenser (b) and evaporator (c), condenser length (d), evaporator length (e) and refrigerant charge (f) as a function of COP for all evaluated configurations (blue dots) and analysed configuration (red dots) after constraints application for R455A

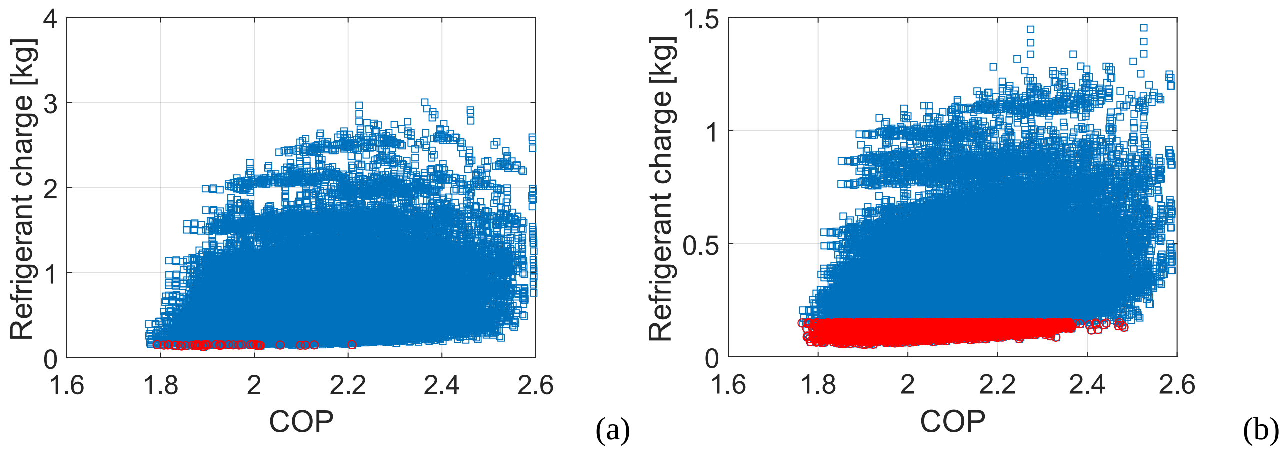

Figure 4.14 – Refrigerant charge as a function of COP for all evaluated configurations (blue dots) and analysed ones (red dots) for propane single circuit arrangement (a) and propane double circuit arrangement (b)

Table 4.8 – Total combinations, number of combinations within constraints and percentage difference on the total for each refrigerant

Refrigerant	Total combinations	Combinations within constraints	Percentage of analysed combinations within constraints on the total
R404A	104976	42331	40%
R452A		45861	44%
R449A		46089	44%
R455A		27211	26%
R454C		41138	39%
R290		43	0.04%
R290 2 circuit		8080	8%

The solutions not excluded by constraints applications, are firstly analysed by considering the combination of *COP* and dimensionless set-up costs $C_{set\text{-}up}\,C_{set\text{-}up,\,min}^{-1}$ (referred to the minimum value found among the configurations) for each refrigerant. This represents the manufacturer point of view that wants to minimize the set-up costs but ensuring the best performances compared to the market. In this analysis the configurations are divided based on the possible combinations of refrigerants in mid-point condition and air temperature difference inside the condenser $\Delta T_{co,mid}$ and the evaporator $\Delta T_{ev,mid}$, since they are the first parameter to be fixed affecting the thermodynamic cycle and the heat exchanger size. Considering R404A as reference fluid for this application, in Figure 4.15 the dimensionless costs are expressed as a function of COP value for each couple of heat exchanger refrigerant-air temperature difference.

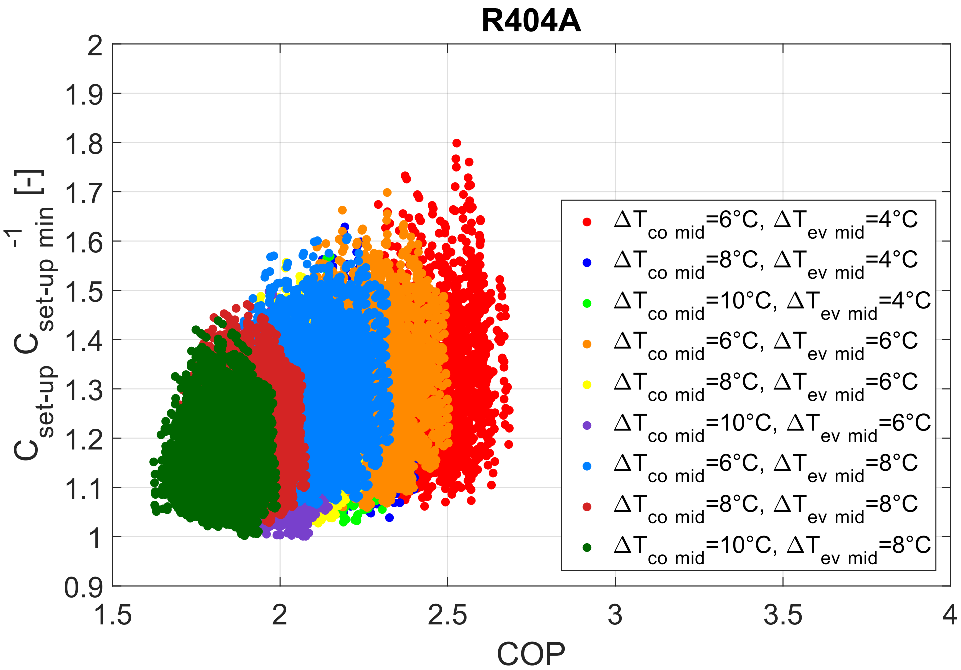

Figure 4.15 – COP and dimensionless set-up costs ($C_{set\text{-}up}\, C_{set\text{-}up,\, min}^{-1}$) for different couples of refrigerant-air temperature difference inside the heat exchanger $\Delta T_{co,mid}$ and $\Delta T_{ev,mid}$ for R404A

The configurations forming the red cloud have the highest COP value, in fact they are characterized by the lowest simulated temperature differences between refrigerant and air. At the same time, they have the highest set-up costs due to highest size of heat exchangers among all the analysed configurations, in fact the red dots are concentrated on the upper right side of the diagram. Conversely, the configurations having the highest value of mid-point refrigerant-air temperature differences are the ones forming the dark green cloud located on the bottom left side of the diagram. A Pareto front can be identified for each cloud of dots, as depicted in Figure 4.16.

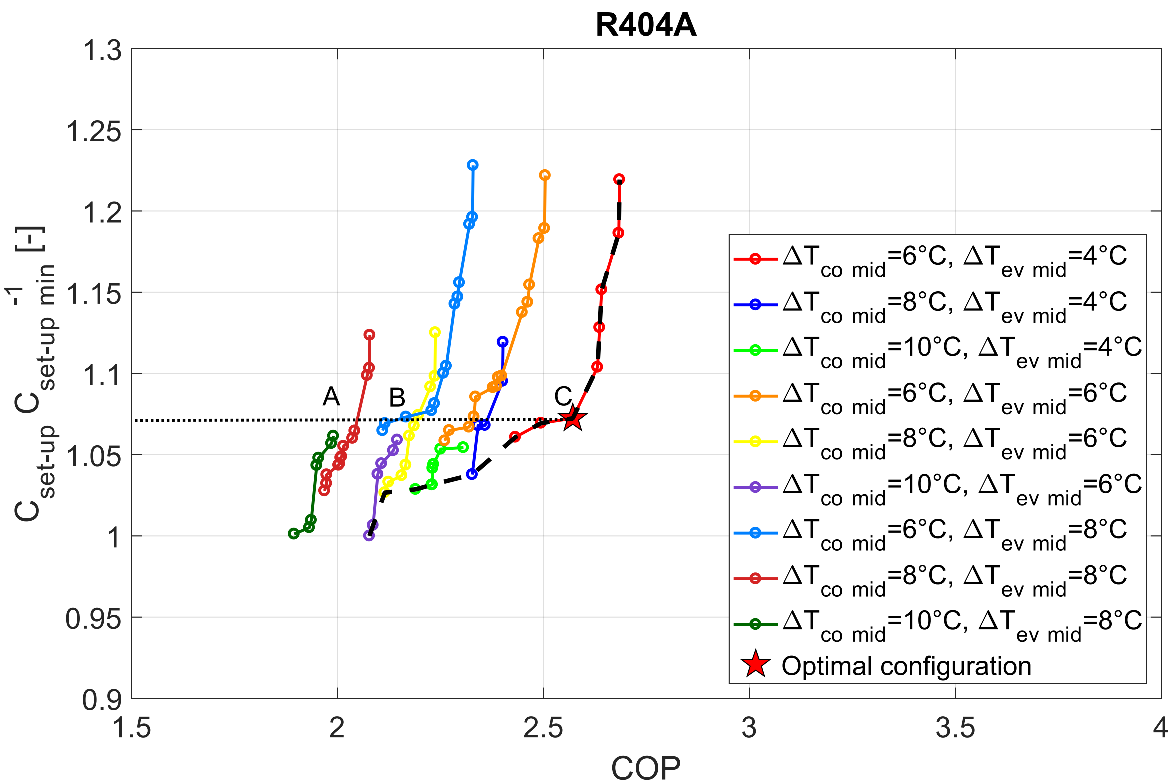

Figure 4.16 – Pareto front for each cloud of configurations as defined in Figure 4.15 for R404A in dimensionless set-up costs ($C_{set\text{-}up}\,C_{set\text{-}up,\,min}^{-1}$) – COP diagram

The black dotted horizontal line in Figure 4.16 represents a possible ensemble of design combinations that the manufacturer can choose with the same investment. The line intercept three Pareto fronts in A, B and C points. The A configuration has the lowest value of COP ($\Delta T_{co,mid}$ = 8°C and $\Delta T_{ev,mid}$ = 8°C), but with a reduction of 25% of temperature difference in the condenser a 6% COP increase can be achieved from 2.04 to 2.17. Finally, by halving the evaporator temperature difference a further COP increase of 18.4% can be reached. This means that with the same expense it is possible to design and manufacture a refrigerator with the highest value of COP by carefully designing the thermodynamic cycle and the heat exchangers. All the Pareto fronts with the highest COP values can be combined in a unique one defined "total Pareto front", depicted with the black dotted line in Figure 4.16, where there are the best achievable configurations with R404A. Among them, the optimal configuration, depicted with the red star in Figure 4.16, can be identified using the utopia point criterion.

The same analysis is carried out for all refrigerants, whose "total Pareto fronts" are identified and depicted together in Figure 4.17 with different colours.

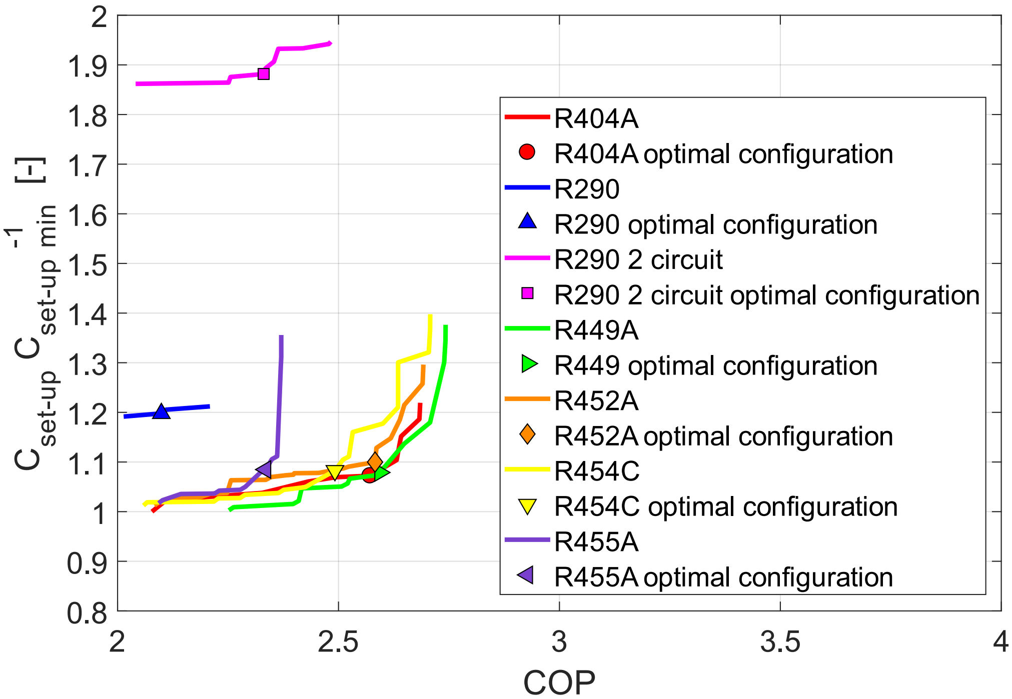

Figure 4.17 – Total Pareto fronts for all refrigerants and optimal configurations (dots) on dimensionless set-up costs ($C_{set-up}\,C_{set-up,\ min}^{-1}$) – COP diagram

Similar dimensionless set-up costs are found with the blends ranging from 1 to 1.4, with slight differences in COP, except for R455A whose Pareto front slope increases around a COP value of 2.28. R449A is the refrigerant with the lowest set-up costs, for a fixed value of COP than the others, and it is already used as R404A drop-in replacement together with R452A. In the optimum point, the COP values of R404A, R449A and R452A are similar with differences within 1%. The set-up cost of R404A is 1% and 3% lower than the R449A and R452A ones, respectively. Among blends having GWP lower than 150, R454C has the highest COP, but it is 3% and 4% lower than the ones of R404A and R449A, respectively. Due to the lack of feasible configurations with $\Delta T_{co,mid}$ = 6°C, COP 10% lower than the one of R404A is found for R455A. Finally, propane with single and double circuit arrangements are shown, the width of the Pareto front for single circuit is lower than the case of double arrangement. This is due to the 150g charge limit for this application as shown in Figure 4.14. By considering the propane double circuit configuration arrangement, the COP value in the optimum point is 9.3% less than R404A. The highest set-up costs with propane in both configurations are found among the analysed refrigerants. This is due to the higher components' costs and in case of double circuit arrangement the manufacturing costs are twice. The different rate of compressor technology development for propane is the main cause of 10% efficiency difference disfavouring the performances (COP) of this refrigerant compared to the blends. The dimensionless set-up costs and COP values of each refrigerant are listed in Table 4.9, for the minimum, maximum and optimal COP point of Pareto front.
From the obtained results, R454C can represent a good long-term solution of R404 for this particular application.

Table 4.9 – Summary of minimum, optimal and maximum COP points belonging to total Pareto front for each refrigerant, with dimensionless set-up costs referring to the minimum value among all considered configuration

	Minimum COP point		**Optimal configuration**		**Maximum COP point**	
Refrigerant	**COP**	**$C_{set\text{-}up}\,C_{set\text{-}up\,min}^{-1}$ [€]**	**COP**	**$C_{set\text{-}up}\,C_{set\text{-}up\,min}^{-1}$ [€]**	**COP**	**$C_{set\text{-}up}\,C_{set\text{-}up\,min}^{-1}$ [€]**
R404A	2.08	1.00	2.57	1.07	2.68	1.22
R290	2.01	1.19	2.10	1.20	2.21	1.21
R290 2 circuit	2.04	1.86	2.33	1.88	2.48	1.95
R452A	2.08	1.01	2.58	1.10	2.69	1.30
R449A	2.25	1.00	2.59	1.08	2.74	1.38
R455A	2.09	1.02	2.33	1.08	2.37	1.36
R454C	2.06	1.01	2.49	1.08	2.71	1.40

4.1.11 Results for the customer point of view: environmental impact evaluation (TEWI) and total costs

The customers buying a new refrigerator want to minimize, at the same time, the total costs and the environmental impact. In this paragraph, the customer point of view is presented by presenting the total costs and TEWI index of the solutions belonging to Pareto front for each refrigerant. Three different countries scenario are considered: France, Italy and Germany that are representative of three European countries with different values of specific energy costs and carbon dioxide emission factors, listed in Table 4.7. France and Germany are the European representative of respectively the lowest and highest value of the specific energy cost and carbon dioxide emission factor. Italy, instead, stands for average values of the two parameters. Instead, the ambient temperature of 32°C and cold room temperature of +4°C are considered for the annual energy consumption evaluation in all countries. In Figure 4.18, the total costs and TEWI values are reported for the configuration belonging to set-up costs – COP Pareto front.

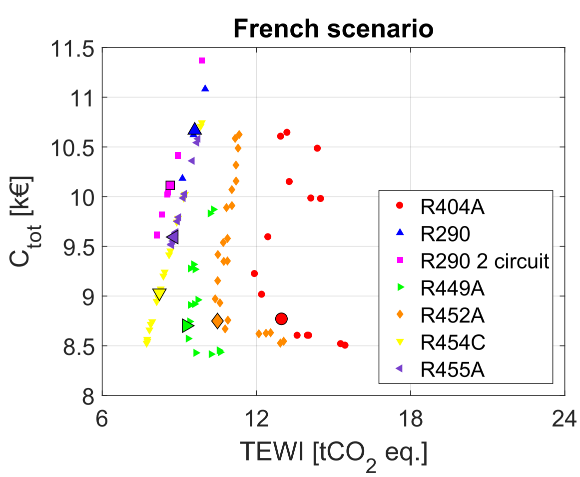

(a)

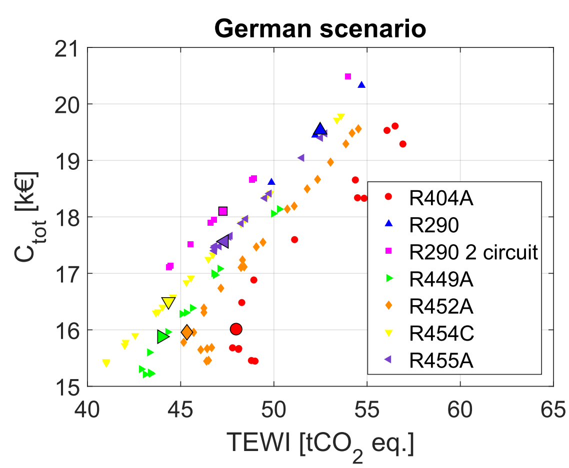

(b)

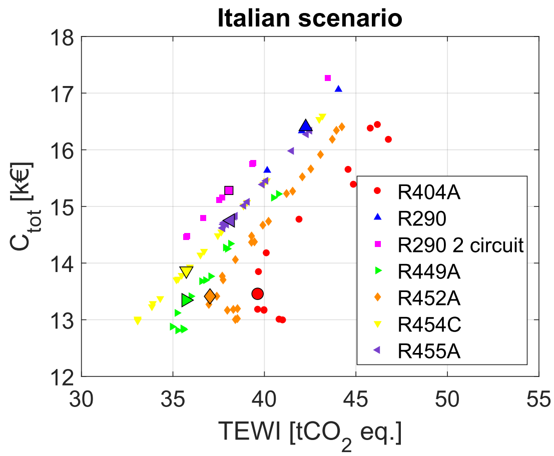

(c)

Figure 4.18 – Total costs and TEWI index of the configurations belonging to Pareto front for each refrigerant in France (a), Italy and Germany (c). The biggest dots represent the optimal configuration in terms of set-up costs – COP

From Figure 4.18a, refrigerants with GWP lower than 150 in France have lower TEWI than the others due to the higher contribution of direct emissions. Conversely, in Italy and in Germany the indirect emission covers higher percentage weight on the total ones, due to higher values of carbon dioxide emission factor (0.405 and 0.503 $kgCO_2eq\ kWh^{-1}$) than France (0.095 $kgCO_2eq\ kWh^{-1}$). As the emission factor increases, the trend of the scatters becomes more linear in Figure 4.18.
Due to its highest GWP value, the trend of TEWI for R404A follows the one of refrigerant charge distribution with a minimum value; in fact, refrigerant charge is lower for configurations characterized by lower COP (high TEWI) due to smaller heat exchanger volumes than the ones with higher COP (smaller TEWI). The shape of TEWI for R404A is less marked with R452A and R449A due to lower GWP. Finally, the indirect emissions are predominant for R454C and propane with the disposition of the optimal configuration dots in Figure 4.18, reflecting the one in set-up cost – COP diagram.
The bigger dots represent the optimal configuration identified in set-up costs – COP diagram for each refrigerant have not the lowest environmental impact, since it depends by refrigerant and country. The lowest value of TEWI is found in correspondence of the optimal configuration for R404A and R452A in Italy and Germany. Instead, for R449A, the minimum TEWI value is only 2% less than the one evaluated in the optimal configuration in Italy and Germany. For R454C, the TEWI value in the optimal configuration is 6%, 8% and 7% higher than the minimum one in France, Germany and Italy, respectively. These differences are lower for propane and R455A with values of 5% and 1%, respectively. Maximum 10% differences in TEWI and total costs are found comparing the configuration with lowest environmental impact with the optimal one in set-up costs – COP diagram; for this reason, the customer can choose, at the same time, the solution representing the best compromise between set-up costs – COP and total costs – TEWI, and in some scenarios the solution with the lowest environmental impact. The R454C has the lowest environmental impact in France with a TEWI of 7.73 tCO_2eq, 35% less than R404A. In Italy, TEWI value with R454C is the same of R449A equal to 35.7 tCO_2eq. Despite the similar COP value than the other refrigerants, R404A has the highest environmental impact in all scenarios. The other low-GWP refrigerants have total costs 20% higher than their lowest value in all countries.

Total costs and TEWI evaluated for the optimal configurations are listed in Table 4.10 for all the investigated scenarios, sorted in ascending COP values.

Table 4.10 – TEWI and total cost values for all optimal solutions belonging to Pareto front for all the refrigerants analysed, in Italy, Germany and France

		Italy		Germany		France	
Refrigerant	**COP**	**TEWI [tCO_2 eq.]**	**C_{tot} [k€]**	**TEWI [tCO_2 eq.]**	**C_{tot} [k€]**	**TEWI [tCO_2 eq.]**	**C_{tot} [k€]**
R290	2.10	42.5	16.4	52.5	19.5	9.6	10.7
R290 2 circuit	2.33	38.1	15.3	47.3	18.1	8.6	10.1
R455A	2.33	38.2	14.8	47.3	17.6	8.8	9.6
R454C	2.49	35.7	13.9	44.4	16.5	8.2	9.0
R404A	2.57	39.7	13.5	48.0	16.0	13.0	8.8
R452A	2.58	37.0	13.4	45.3	16.0	10.5	8.7
R449A	2.59	35.7	13.4	44.0	15.9	9.3	8.7

4.2 Carbon dioxide: experimental analysis of a small cooling capacity condensing unit prototype

4.2.1 Test facility and experimental apparatus

The tested prototype is a condensing unit installed in a calorimetric chamber, depicted in Figure 4.19, composed by insulated panels (walls and ceiling) of 7 cm of thickness and a plant to control the environmental temperature. The condensing unit is connected to an evaporator (not under evaluation) placed inside a calibrated box. The dimensions of the calorimetric chamber and calibrated box are indicated in Table 4.11.
The conditioning plant is composed by two direct expansion evaporators connected to a remote compressor rack, in Figure 4.19b, and electrical heaters placed inside them, controlled with PID to maintain the target temperature inside the chamber. The air circulation is ensured by variable speed evaporator fans.

(a) (b)

Figure 4.19 – Calorimetric chamber (a) and external compressor rack (b)

Table 4.11 – Calorimetric chamber and calibrated box dimensions

Calorimetric chamber			
	Length	**Width**	**Height**
	[mm]	*[mm]*	*[mm]*
External	7794	6014	3207
Internal	7780	6000	3200
Calibrated box			
	Length	**Width**	**Height**
	[mm]	*[mm]*	*[mm]*
External	4000	3200	2600
Internal	3800	3000	2200

In Figure 4.20, piping scheme together with instrument layout is shown; the compressor of the condensing unit is a hermetic, inverter driven (INV in Figure 4.20, the following abbreviations are referred to the same figure), two stage rolling type, two fin and tube heat exchangers as gascooler (GC) and intercooler (IC), a receiver (REC), high pressure valve (HPV), flash gas valve (FGV) and fixed velocity gascooler fans. The main features of the prototype are listed in Table 4.12; the compressor speed ranges from 30 rps to 60 rps. As shown by the blue arrow in Figure 4.20, the air passes through gascooler firstly and then the intercooler forming a cross-counter flow path with the refrigerant. The ball valves (BV) A, B and C are used to exclude intercooler: when it is bypassed BV_C is opened and BV_A and BV_B are both closed. Otherwise, the opposite combination is implemented. FGV is an electronic stepper motor back pressure valve that regulates the receiver pressure on its set point value. HPV is an electronic stepper motor back pressure valve that regulates the gascooler pressure depending on refrigerant outlet temperature T_7 in transcritical operation condition based on the algorithm proposed by Zhao et al. (2000). When the prototype operates in subcritical condition, the valve regulates its opening to maintain the set value of subcooling at the outlet of the gascooler. When the pressure is above 100 bar the valve stays fully opened for safety.
In all tests, the FGV valve is forced to be fully opened in order to reach a value of intermediate pressure close the optimal value depending on the volumetric ratio of both stages. This allows to reach the largest cooling capacity for fixed boundary conditions at gascooler and evaporator. The lines and receiver are insulated, except for the connection lines between compressor, intercooler and gascooler.
In Figure 4.20, EEV is the electronic expansion valve that regulate the superheat at the evaporator (EV) outlet. A variable capacity heater (H) is placed inside the calibrated box to balance the cooling capacity of the unit by means its thermal power Q_h.

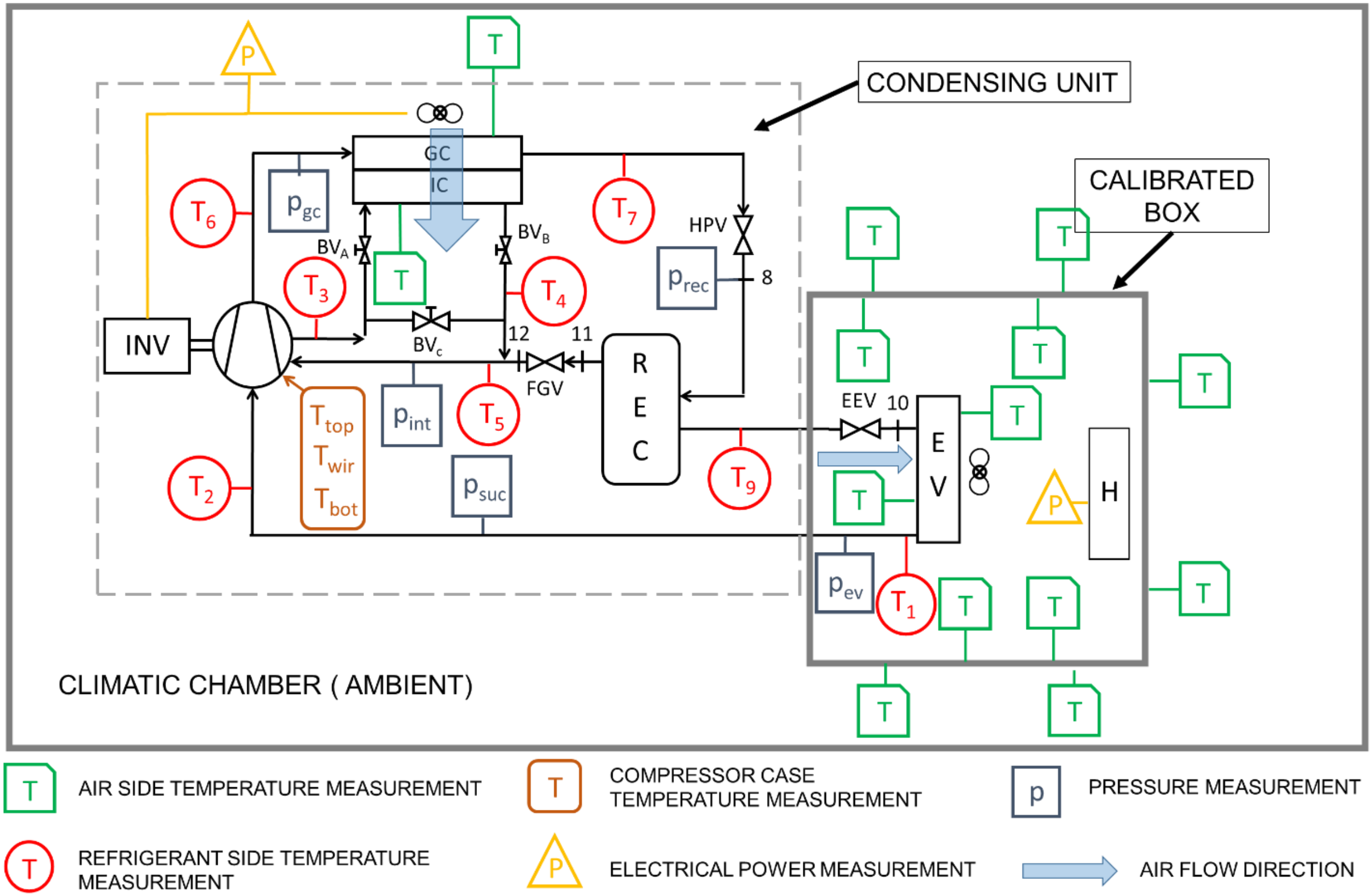

Figure 4.20 – Piping scheme and instrument layout on the prototype

Table 4.12 – Main features of the condensing unit

	GASCOOLER	**INTERCOOLER**
Inside tube diameter [mm]	5	5
Number of tubes	68	68
Number of rows	3	1
Longitudinal tube spacing [mm]	17	17
Transverse tube spacing [mm]	20	20
Fin spacing [mm]	2.1	2.1
Tube material	Copper, smooth	Copper, smooth
Fin material	Aluminium	Aluminium
COMPRESSOR		
Type	Hermetic, two stage rolling piston	
Displacement ratio (First stage/ second stage)	1.42	
Rotation speed range [rps]	30 - 60	
GASCOOLER AND INTERCOOLER FAN		
Number	2	
Rotational speed [rpm]	870	
Fan diameter [mm]	450	
Volumetric-flow rate [$m^3\,h^{-1}$]	2385	
HPV valve regulation		
Condition	**Regulation type**	**Parameter value / Equation**
Subcritical	PI control that follows set outlet gascooler subcooling	3 K
Transcritical	PI control to mantain p_{gc} depending on T_7 in order to guarantee the best COP	Zhao equation up to 100 bar where the valve is fully open for safety (Zhao et al, 2000)

4.2.2 Instrument and measurement uncertainties

Refrigerant side temperature is measured with T-type thermocouples that are fixed to the copper pipe by means of adhesive tape and insulated with flexible material. The measurement points are indicated with red circles in Figure 4.20. Air side temperature is measured, also, with T-type thermocouples placed according to the green boxes in Figure 4.20; the thermocouples measuring temperature at gascooler inlet and outlet sides are installed at 30 mm of distance from the heat exchanger surface. Six thermocouples are located on the external and four on internal cold room surface, at 10 mm of distance from the actual surface, in order to measure ambient T_{amb} and calibrated box temperatures T_c. To check if the compressor case temperature is within the operation range, three temperature measurement are carried out on the top (T_{top}), middle and bottom (T_{bot}) by means T-type thermocouples. The middle point is representative of compressor motor winding (T_{win}). Pressure transducers with 0 – 10 V output signal are used to measure refrigerant circuit pressure; they are mounted according to the blue boxes as shown in Figure 4.20. Power meters are used to measure the condensing unit ($\dot{L}_{el}$) and heater power consumption. In Table 4.13, the measurement instrumentation is listed with the direct uncertainties.

Table 4.13 - Measurement instrument and uncertainties

Direct measurement	**Instrument**	**Calibration range**	**Uncertainty**
Temperature (air, refrigerant and compressor case)	T-type thermocouple	-30°C - +90°C	± 1.5 K
Gascooler pressure p_{gc}	Pressure transducer	0 – 250 bar	± 0.5 bar
Intermediate pressure p_{int}	Pressure transducer	0 – 250 bar	± 0.5 bar
Receiver pressure p_{rec}	Pressure transducer	0 – 250 bar	± 0.5 bar
Evaporating pressure p_{ev}	Pressure transducer	0 – 50 bar	± 0.1 bar
Suction pressure p_{suc}	Pressure transducer	0 – 50 bar	± 0.1 bar
Unit power consumption	Powermeter	0 - 975V (voltage) 0 - 29A (current)	± 0.0013 % of reading
Heater power consumption	Powermetere	0 - 20kW	±0.5 % of reading

4.2.3 *Test method*

The calorimeter method B is used to carry out the tests as in Tammaro et al. (2018) and according to EN13771-2:2017 (CEN, 2017). The trends of ambient temperature (T_{amb}), calibrated box temperature (T_c) and evaporating temperature (T_{ev}) as a function of time with the test phases definitions are shown in Figure 4.21.

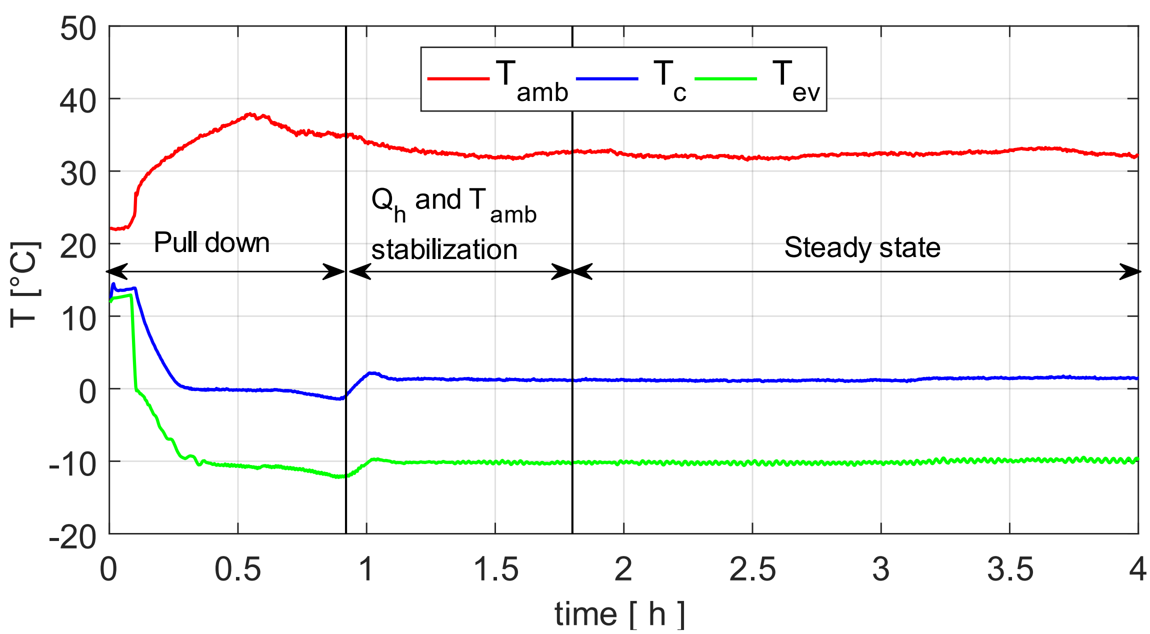

Figure 4.21 – Ambient temperature (T_{amb}), calibrated box temperature (T_c) and evaporating temperature (T_{ev}) as a function of time with test phase definition

The test procedure is composed by three phases:

1) Pull - down
2) $\dot{Q}_h$ and T_{amb} stabilization
3) Steady state

In pull down phase, the calorimetric chamber and the unit are turned on to increase the temperature up to the target test conditions in terms of ambient and to reach evaporating temperature lower than the target value, respectively. It is worth noting that, according to EN13771-2:2017 and EN13215:2016, the parameter to be controlled at evaporator side is the refrigerant pressure and not the air temperature. In phase 2 called "$\dot{Q}_h$ and T_{amb} stabilization" the calorimetric chamber PID starts to modulate to stabilize the ambient temperature. In the meantime, the heater inside the calibrated box is turned on and the power is variated to reach the target value of evaporating temperature. The last phase is the steady state, where the unit operate at target value of T_{amb} and T_{ev}; the calibrated box temperature T_c is a consequence of evaporator size matched with the cooling capacity of the unit. The maximum fluctuations allowed in steady state conditions are ± 1°C and ± 0.5°C for ambient and cold room temperature, while the power of the heaters varies within ± 1%. The length of steady state phase is at least 30 minutes.

4.2.4 Data reduction

The mean value of all measurement in steady state phase is evaluated for each test. The cooling capacity of the unit ($\dot{Q}_{ev}$) [W] is evaluated as the sum of the heat supplied with the heaters ($\dot{Q}_h$) and the thermal leakages between the ambient side at T_{amb} and calibrated box interior side at T_c as follows:

$$\dot{Q}_{ev} = \dot{Q}_h + UA\,(T_{amb} - T_c) \qquad \text{Eq. 4.60}$$

Where UA [W K^{-1}] is the heat leakage factor of the box, calibrated according to EN13771-2:2017 (CEN, 2017) before the test campaign.

The coefficient of performance *COP* is evaluated according to the following equation:

$$COP = \dot{Q}_{ev}\dot{L}_{el}^{-1} \qquad \text{Eq. 4.61}$$

The indirect measurement uncertainties are calculated as specified in the work of Moffat (1988). They are listed in Table 4.14.

Table 4.14 – Indirect measurement uncertainties

Parameter	Unit	Uncertainty
$\dot{Q}_{ev}$	W	± 1.13%
COP	[-]	± 1.1%

The thermodynamic properties of the refrigerant are calculated by means the software Refprop (Lemmon et al., 2013) combining the measured pressures and temperature in each point of the refrigeration plant.

The standard EN13215:2016 (CEN, 2016), illustrates the procedure to evaluate the SEPR (Seasonal Energy Performance Ratio) fundamental to decide if the unit is compliant to the Ecodesign Directive (European Parliament, 2015) and to join the European market. Tests according points A, B, C and D as defined in the standard are carried out and the measured $\dot{Q}_{ev}$ and *COP* are corrected considering 10 K of superheat at condensing unit inlet (point 1 in Figure 4.20). The corrected values of cooling capacity $Q_{ev,cor}$ and COP_{cor} are evaluated with the following equations:

$$\dot{Q}_{ev,cor} = \dot{Q}_{ev}\, \rho_{1,cor}\, \left(i_{1,cor} - i_9\right)[\rho_1(i_1 - i_9)]^{-1} \quad \text{Eq. 4.62}$$

$$COP_{cor} = \dot{Q}_{ev,cor}\, \dot{L}_{el}^{-1} \quad \text{Eq. 4.63}$$

After the SEPR is evaluated according to EN13215:2016 (CEN, 2016) by means Eq. 4.64 as weighed average of corrected COP values on hours of operation at a specified ambient temperature:

$$SEPR = \sum_{j=1}^{58}\left(\dot{Q}_{dm,MT\ j} d_j\right)\left\{\sum_{j=1}^{58}\left[\dot{Q}_{dm,MT\ j} d_j \left(COP_{cor,SEPR,j}\right)^{-1}\right]\right\}^{-1} \quad \text{Eq. 4.64}$$

$\dot{Q}_{dm,MT}$ is the cooling demand [W], the symbol d_j is the duration in hours of each binned ambient temperature j. $COP_{cor,SEPR,j}$ is the corrected *COP* evaluated for each value of temperature bin. The number of bins is 58 according to climate defined in the standard.

4.2.5 Test conditions

The tests and their corresponding parameters such as ambient temperature, evaporating temperature, compressor speed values and intercooler use are listed in Table 4.15. The tests are compared together in order to discuss the effect of ambient and evaporating temperatures, intercooler usage, flash gas removal cooling influence on thermodynamic cycle and to evaluate the SEPR to be compared with the one of similar unit using R449A as refrigerant.

Table 4.15 – Test list

Test number	***T_{amb}***	***T_{ev}***	***n***	***IC***
#	*[°C]*	*[°C]*	*[rps]*	
1	43	-10	60	On
2	32	-10	60	On
3	25	-10	60	On
4	15	-10	60	On
5	5	-10	60	On
6	43	-20	60	On
7	32	-20	60	On
8	25	-20	60	On
9	15	-20	60	On
10	5	-20	60	On
11	25	-10	51	On
12	25	-10	51	Off
13	15	-10	44	On
14	5	-10	36	On

4.2.6 Thermodynamic cycle description

The thermodynamic cycle of the prototype is shown in Figure 4.22 on pressure – enthalpy diagram with the numbers referred to Figure 4.20. In point 1, the refrigerant from the evaporator outlet at pressure p_{ev} enters in the first stage of compressor at suction pressure p_{suc} (point 2) lower than the previous one due to the pressure drops along the connection line. The refrigerant is compressed up to intermediate pressure value (p_{int}) in point 3, after that it goes in the intercooler where it is cooled down up to T_4. Then it mixes with the saturated vapour coming from the FGV (point 11), in the thermodynamic point 5 where it is sucked from the compressor second stage. After the compression in point 6, the refrigerant goes to the gascooler to be cooled up to T_7. After the HPV valve, the liquid and vapour phases with the quality x_8 are separated inside the receiver at pressure p_{rec} in points 9 and 11, respectively. From point 9, the refrigerant in liquid state goes into the evaporator (point 10) through EEV. In all tests, the pressure difference between intermediate pressure (p_{int}) and receiver pressure (p_{rec}) is less than 4 bar.

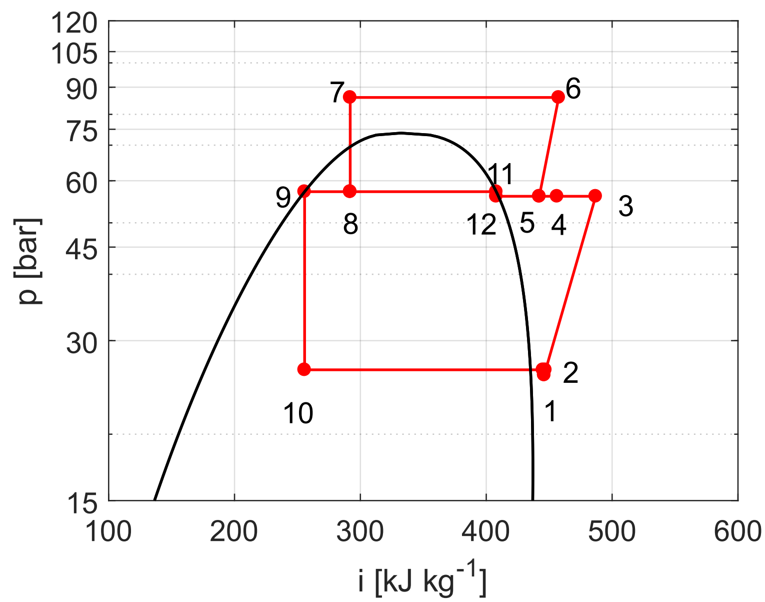

Figure 4.22 – Thermodynamic cycle on pressure – enthalpy diagram

4.2.7 Evaporating temperature effect analysis

To analyse the effect of the evaporating temperature, tests #3 and #8 are considered, their thermodynamic cycles are shown in Figure 4.23 with red and blue lines respectively. In test #8, with T_{ev} = -20°C compressor discharge temperatures T_3 and T_6 are higher than the ones in test #3 due to lower isentropic efficiency and suction density than the case with T_{ev} = -10°C. In test #8, a lower cooling capacity is measured since this is affected by the lower values of mass-flow rate and suction density. Also, the *COP* is lower in test #8 than in test #3.

The effect of evaporating temperature increases with ambient temperature. In fact, Q_{ev} and *COP* decrease, respectively, of 30% and 28% from -10°C to -20°C evaporating temperature at 5°C ambient temperature; instead, the decrements are about 54% and 53%, respectively with 43°C ambient temperature.

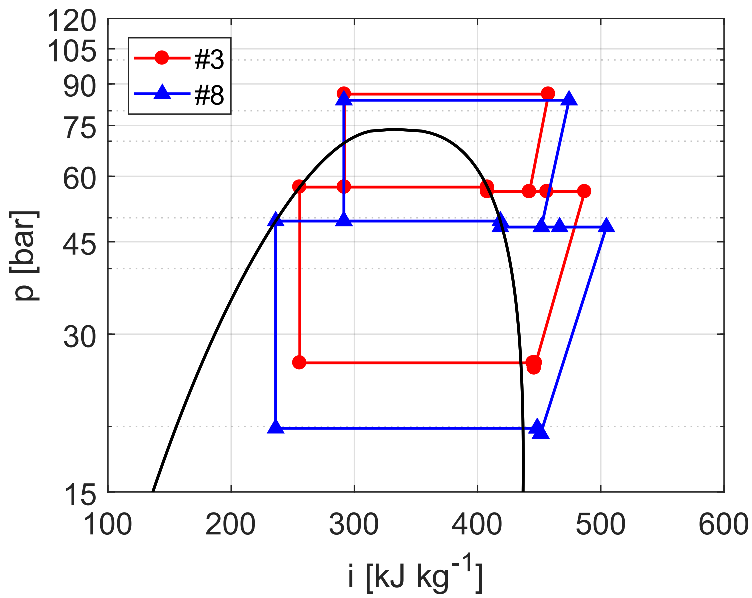

Figure 4.23 – Thermodynamic cycle on pressure - enthalpy diagram of tests #3 and #8 with T_{ev} = -10°C and T_{ev} = -20°C, respectively, T_{amb} = 25°C, intercooler on and maximum compressor speed

4.2.8 Ambient temperature effect analysis

Tests #1 to #10 are considered to analyse the effect of the ambient temperature variation on thermodynamic cycle, five tests are carried out at T_{ev} = -10°C the others are at T_{ev} = -20°C with ambient temperatures ranging from 5°C to 43°C. In all tests the intercooler is active, and the compressor speed is the maximum. In Figure 4.24a and Figure 4.24b the thermodynamic cycles of the considered tests are shown at, respectively, -10°C and -20°C evaporating temperature.

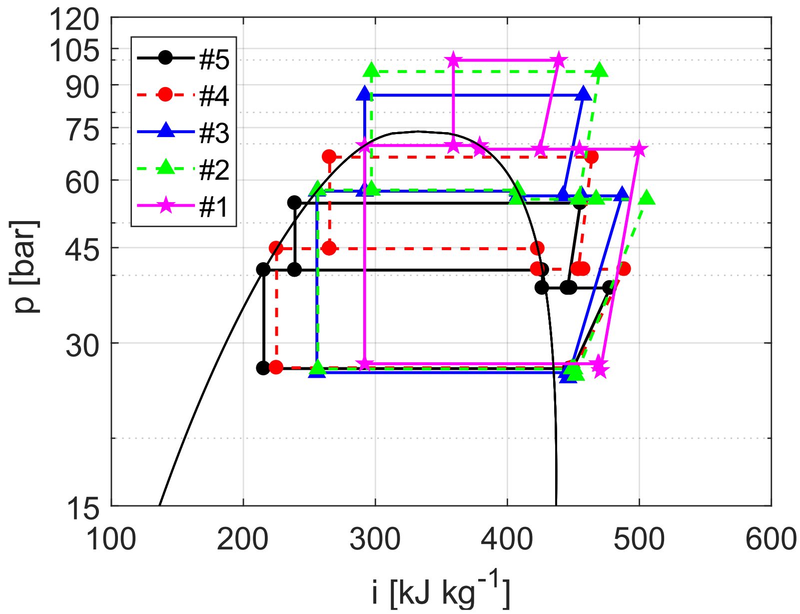

(a)

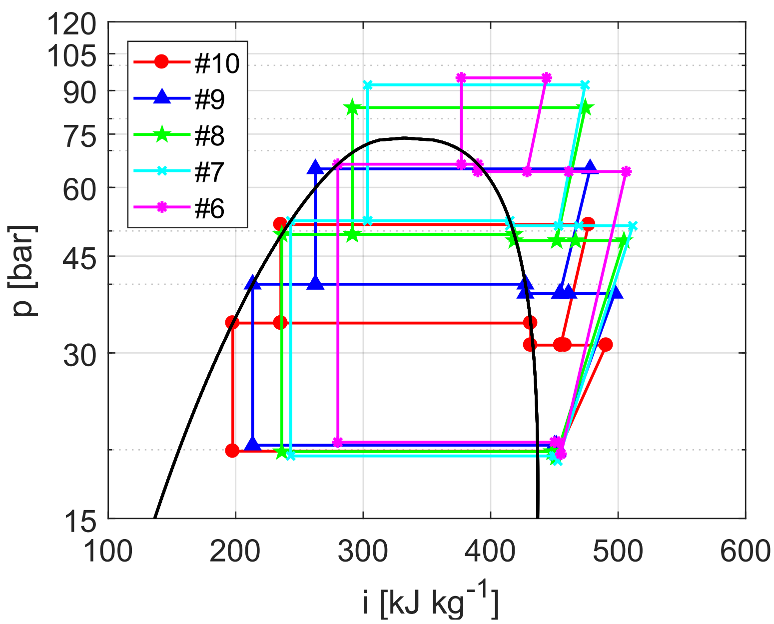

(b)

Figure 4.24 – Thermodynamic cycle on pressure - enthalpy diagram of tests #1 to #5 with T_{ev} = -10°C (a) and tests #6 to #10 with T_{ev} = -20°C (b) varying ambient temperature from 5°C to 43°C, with intercooler active and maximum compressor speed

In both evaporating temperatures conditions, for ambient temperatures below 15°C the prototype works in subcritical conditions. Instead, when the ambient temperature is equal or greater than 25°C, the thermodynamic cycle is transcritical. The transition from subcritical to transcritical thermodynamic cycle is due to CO_2 critical temperature and pressure of 31°C and 73.77 bar, respectively. In transcritical operating conditions the temperature difference refrigerant and air T_7-T_{amb} is roughly 3 K, instead, in subcritical condition it is about 10 K due to different control logic of the HPV valve as described in section 4.2.1. First and second discharge temperatures increase with ambient temperature, due to the increase of pressure ratio with a reduction of compressor isentropic efficiency, at both evaporating temperatures values. The increase of pressure ratio as a function of ambient temperature in first and second compressor stages is shown in Figure 4.25.

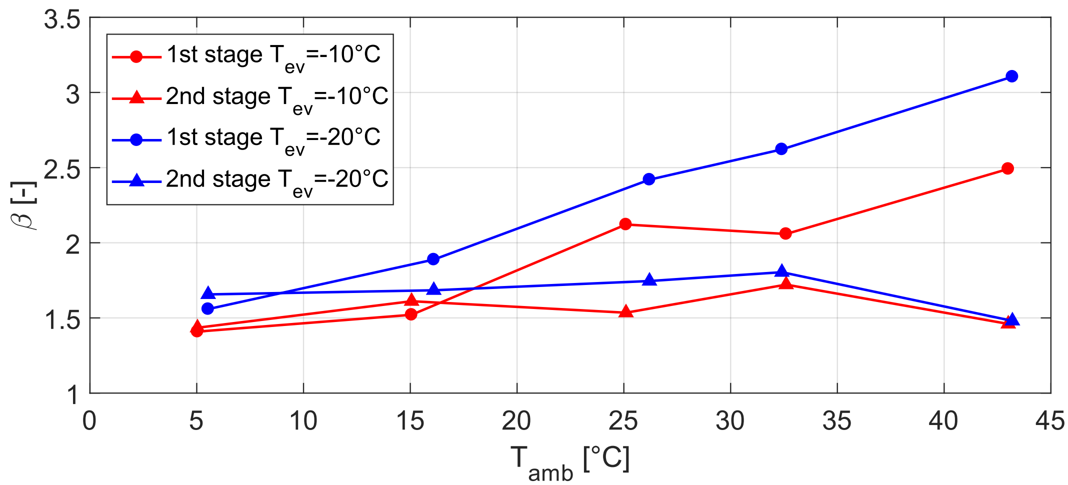

Figure 4.25 – First and second compressor stages pressure ratio as a function of ambient temperature for tests #1 to #10

From Figure 4.25, the second stage discharge pressure ratio at T_{amb} = 43°C is lower than the value at T_{amb} = 32°C, this is because the HPV valve stays fully opened since the gascooler pressure is close to safety value of 100 bar, with the increase of receiver pressure. Consequently, the second stage discharge temperature T_6 increases up to 32°C ambient temperature and decreases after that point.

In all tests, p_{rec} increases with ambient temperature with the increase of receiver and evaporator inlet quality; the first effect results in a reduction of liquid fraction on the total mass flow rate that goes to the evaporator. The second effect, instead, brings to a reduction of the latent heat that can be transferred between the refrigerant and the air. These two effects combined with the reduction of mass flow rate inside the first compressor stage cause a reduction of both cooling capacity and *COP*. In Figure 4.26, the trends of dimensionless cooling capacity and *COP* as a function of ambient temperature are shown, referred to the maximum value of each variable measured at 5°C ambient temperature.

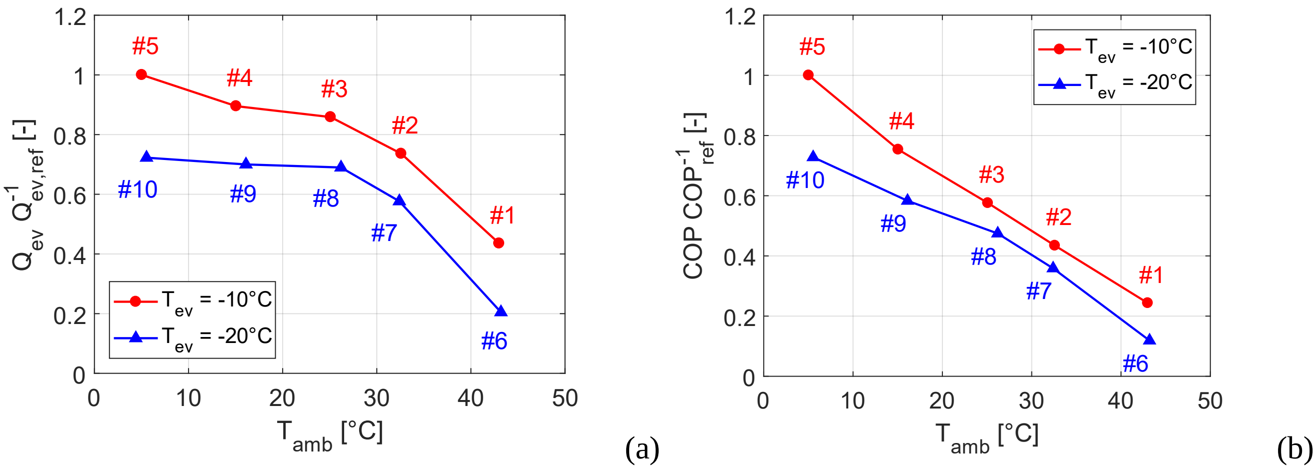

Figure 4.26 – Dimensionless cooling capacity (a) and dimensionless COP (b) as a function of ambient temperature measured in tests #1 to #10. Subscript "ref" indicate the reference highest value of each variable measured in test #5

In Figure 4.26a a decrease of 58% of cooling capacity is found from reference value in test #5, to test #1 and 71% from test #10 to #6. The trends of cooling capacity in Figure 4.26a, can be divided in two regions, the first with flat trend from test #5 to #3 and from #10 to #8 with ambient temperature values below 25°C, where the unit operates in subcritical conditions. In the second region with ambient temperatures above 25°C where the unit works in transcritical condition, the cooling capacity drops sharply. The flatter slope of subcritical region could be caused by reduction of receiver inlet quality (from 30% in test #8 to 16% in test #10) with the increase of liquid fraction that goes into the evaporator. This variation is mitigated by lower mass flow rate increase from ambient temperature value of 25°C to 5°C. The sharp reduction of cooling capacity in the transcritical region is caused by the sudden increase of receiver inlet quality from 32°C to 43°C ambient temperature with the reduction of liquid fraction accompanied by total mass flow rate reduction due to the decrease of volumetric efficiency.
Dimensionless COP shows linear trend with ambient temperature, in Figure 4.26b due to the decrease of cooling capacity and the increase of total power consumption. COP decreases of 24% from test #5 to test #1 at T_{ev} = -10°C, instead, 84% difference is found in test #6 compared to the reference value of test #5.

4.2.9 Intercooler effect analysis

To analyse the effect of the intercooler operation on the thermodynamic cycle and performances, tests #11 (intercooler active) and #12 (intercooler disabled) are considered. They are carried out at T_{amb} = 25°C, T_{ev} = -10°C, compressor speed = 51 rps. The intercooler is excluded by means of the application of ball valves A, B and C (BV) opening combination as described in section 4.2.1, following a procedure that minimizes the refrigerant charge in the intercooler volume in order to always have configurations at similar refrigerant charge. In Figure 4.27, the thermodynamic cycles on pressure – enthalpy diagram of tests #11 and #12 are shown.

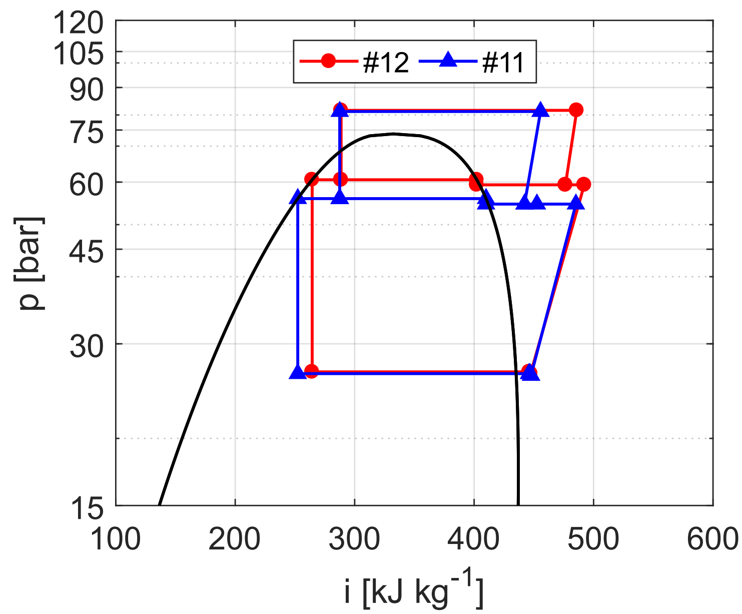

Figure 4.27 – Thermodynamic cycle on pressure – enthalpy diagram of tests #11 (intercooler active) and #12 (intercooler disabled) with T_{amb} = 25°C, T_{ev} = -10°C, compressor speed = 51 rps

Without intercooler compressor first stage (T_3) and second stage (T_6) discharge temperatures are higher than the case with intercooler. The higher value of T_3 without intercooler is mainly due to the higher first stage pressure ratio. Instead, the higher value of T_6, in test #12 is due to lower suction density (point 5 according to Figure 4.22) and higher suction superheat at p_{int}. In test #11, receiver and intermediate pressures are lower since T_5 is lower than in test #12 thanks to intercooler effect, causing the increase of suction density ρ_5 with the same pressure. Subsequently, the system working point changes with a decrease of pressures at receiver and first stage discharge. The intercooler operation has influence on compressor operating temperatures, in fact they are higher without intercooler. The evaporator inlet quality in test #11 is lower than in test #12, and this is mainly due to a lower receiver pressure, with higher latent heat that can be transferred in the evaporator. The combination of this effect together with the higher refrigerant mass flow rate in test #11 results in a 10% increase in cooling capacity and *COP*.

4.2.10 Flash gas removal cooling effect analysis

Test #1 to #5 at -10°C and tests #6 to #10 at -20°C evaporating temperature, are considered to analyse the cooling effect of vapour injected by flash gas valve that is fixed in fully opened position. To better show the cooling effect, in Figure 4.28 are reported the temperature T_4 (outlet intercooler), T_5 (second stage compressor suction), saturation temperature at intermediate pressure $T_{sat}(p_{int})$ on the left axis and the inlet receiver quality x_8 on the right axis as function of ambient temperature.

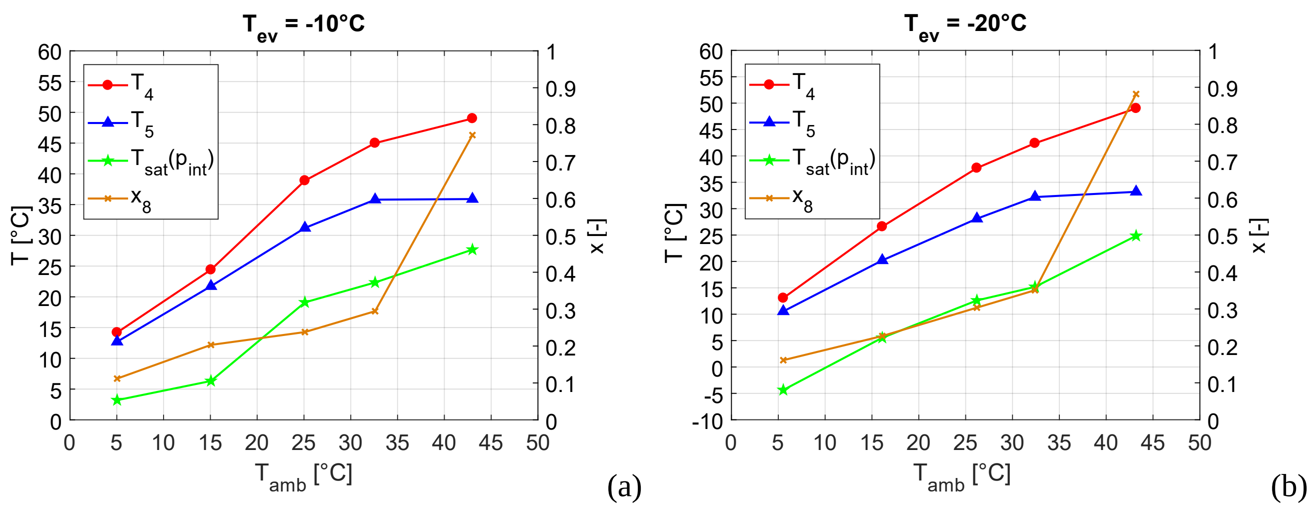

Figure 4.28 – Outlet intercooler temperature T_4, compressor second stage suction temperature T_5, saturation temperature at intermediate pressure $T_{sat}(p_{int})$ and receiver inlet quality (x_8) as a function of ambient temperature for tests #1 to #5 (a) and #6 to #10 (b)

The temperature T_5 is the result of mixing process between the mass flow rate coming from the intercooler at T_4 and the one coming from receiver at $T_{sat}(p_{int})$

As the ambient temperature increases the flash gas removal cooling effect is higher, and this is proved by the trend of temperature T_5 even closer to $T_{sat}(p_{int})$ curve as the ambient temperature increases. The increase of flash gas removal cooling effect is due to the increase of receiver inlet quality x_8, leading to higher vapour mass flow rate on the total one.

The increase of mass flow rate of the injected vapour together with the reduction of the total mass flow rate with the ambient temperature, leads to the highest reduction of cooling capacity in transcritical state, around 40% and 65%, at T_{ev} = -10°C and -20°C respectively from 32°C to 43°C ambient temperature.

4.2.11 SEPR calculation

To evaluate the SEPR, tests #2, #12, #13 and #14 are carried out with the boundary conditions of points A, B, C and D according to EN13215:2016 (CEN, 2016). Then the SEPR is evaluated following the procedure described in the same standard and in paragraph 4.2.4. and it is found that it is 33% higher than the threshold value imposed by 2015/1095 EU Regulation (European Commission, 2015). Moreover, the SEPR value of the prototype is compared to the one of another condensing unit, manufactured by Zanotti, using R449A (GWP = 1397) (unit 2) as refrigerant. This latter is equipped with single stage fixed speed semi-hermetic reciprocating compressor that is the most common architecture in commercial condensing unit market. The keynote differences between the two units are listed in Table 4.16.

For unit 1, the SEPR is 2% higher than that of unit 2, meaning that the CO_2 unit has higher efficiency of R449A unit but with a more complex architecture to overcome its thermodynamic limits. This means that higher costs are expected with CO_2, but the plant will have more longevity since the R449A will be gradually phased-out in favour of very low-GWP blends and natural refrigerants.

Table 4.16 – Keynote features of units considered in the SEPR comparison

	Unit 1	**Unit 2**
Refrigerant	CO_2	R449A
Compressor type	Hermetic rolling piston double stage	Semi-hermetic reciprocating single stage
Capacity control	Stepless (with inverter)	Fixed (no inverter)
Intercooler	Yes	No

Chapter 5 – State of the art on frosting phenomena and defrost control logic optimization

In this chapter, a review of works relating on frost deposition and growth on cold surfaces and defrost control logic optimization is presented. Firstly, basic experimental and simulated works on frost growth on flat surfaces with recognition of shape and evaluation of thickness, density and thermal conductivity are presented with comparison of different models and correlations to predict them as a function of air temperature, specific humidity and cold plate temperature. Subsequently, analyses of frost characteristics and performances variation applied to fin and coil and microchannel heat exchangers, heat pumps and refrigerator evaporators are mentioned. In the last part of the chapter, works on defrost control logic optimization and innovative frost detection techniques are mentioned. Experimental and theoretical approaches are used in the reviewed works.

5.1 Frost formation on plate surface: appearance, thickness and thermal conductivity

The frost formation occurs when the air is in contact with a cold surface with a temperature below the water triple point. Several authors and research groups studied the frost formation and thermophysical characteristics with experimental and theoretical approaches.

The first works are dated 60s and 70s: Hayashi et al. (1977) carried out an experimental activity with photographical observation of frost growth on a cold stainless-steel plate invested by a controlled air flow rate using the experimental setup shown in Figure 5.1.

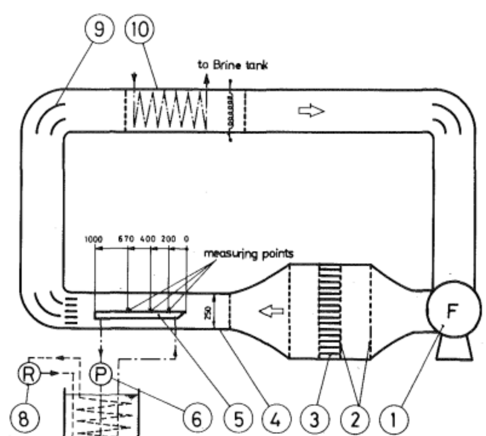

Fig. 1. **Experimental setup: 1 blower 2 screen 3 honeycomb 4 test section 5 test plate 6 pump 7 brine tank 8 refrigerator 9 regulating fin 10 temperature-humidity controlling section**

Figure 5.1 – Experimental test setup for frost growth observation (Hayashi et al., 1977)

Three phases of frost formation have been identified named respectively, "crystal growth period", "frost layer growth period" and "frost layer full growth period"; these phases are represented also in Figure 5.2 where a photographic observation is reported. In the first phase, the nucleus of frost begins to form, building thin layer of ice that will grow in perpendicular direction to the cold surface. In the second phase, the branched structures continue to growth interacting one to each other with an increase of frost density and the diffusion of water vapour inside the bottom layers. The interface of the frost appears to be flat. As the frost thickness increases, the thermal resistance increase, in fact in the third phase the frost thickness does not vary so much especially when the surface temperature is around 0°C. At this moment, the frost on the surface melts going on the bottom layers where it freezes with an increase of density and decrease of thermal resistance. This process continues cyclically until the establishment of a thermodynamic equilibrium is reached.

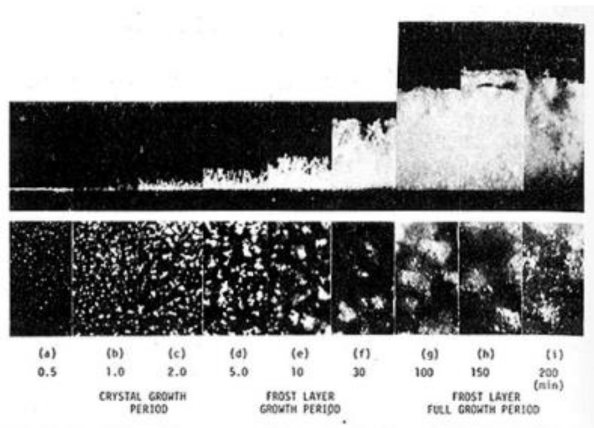

Figure 5.2 – Photographic observation of frost growth with the identified phases (Hayashi et al., 1977)

The shape of frost crystals can be classified in a map in function of specific humidity difference between air and cold surface (named: supersaturated degree of water $\Delta\omega$ [$kg_w\ kg_a^{-1}$] or [$g_w\ kg_a^{-1}$]) and cold surface temperature T_S [°C]; Hayashi et al. (1977) and Wu et al. (2007) built experimentally this kind of maps shown respectively in Figure 5.3a and 5.3b.

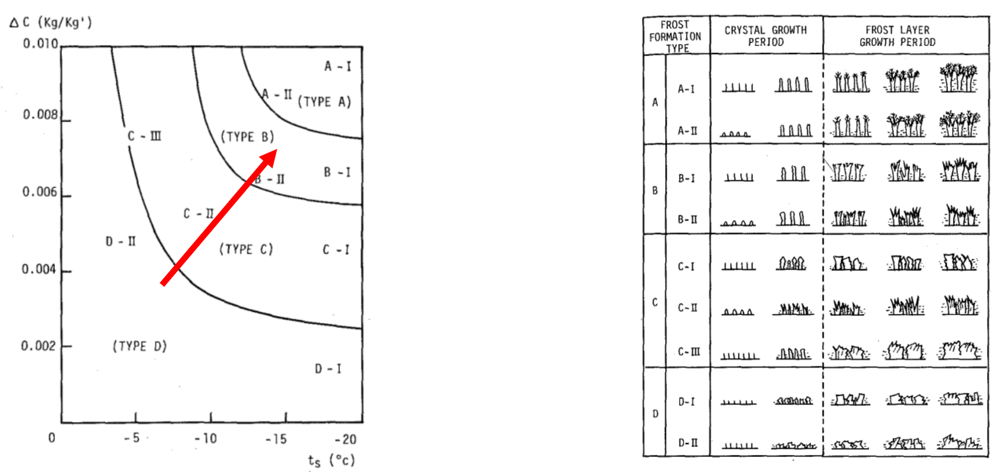

(a)

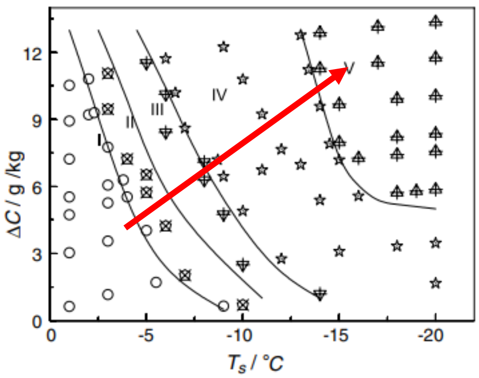

Legend I = super-cooled water droplets; II: irregular crystals; III: flake crystals; IV needle; V feather crystals

(b)

Figure 5.3 – Frost crystal shape map as a function of specific humidity difference between air and cold surface (expressed in [kg kg'$^{-1}$] or [g_w kg_a^{-1}] indicated as ΔC in figure and $\Delta\omega$ in the text)and surface temperature T_S [°C] from Hayashi et al. (1977) (a) and Wu et al. (2007) (b)

Wu et al. (2007) used the same approach of Hayashi et al. (1977), but in this case with a map referring only to the initial formation stage. Similar results have been found in both works; in Figure 5.3 in correspondence of high values of T_S and low values of $\Delta\omega$, numerous small droplets forms on the cold surface (super-cooled droplets). Following the red arrow direction, the shape of crystals changes to super-cooled droplets, irregular crystal, needle and pole crystals and feather crystal. This means that the shape of crystal is strictly correlated with the value of surface temperature T_S, air temperature and its specific humidity. The effect of these parameters on shape and density are also studied by Sahin (2006) and Leoni et al. (2017); in this latter work, the frost thermal conductivity has been studied. In Leoni et al. (2017), a summary of principal observation on the effect of air temperature (T_{air}), relative humidity (RH), air velocity (v_{air}), and cold plate top temperature ($T_{CP,top}$) on frost thickness (δ_f) and the thermal conductivity (λ_f) is provided and it is reported in Figure 5.4.

Studied parameter	Influencing parameter	Parameters kept constant
	T_{air} ↗	RH, v_{air}, $T_{CP,top}$
	T_{air} ↘	ω, v_{air}, $T_{CP,top}$
δ_f ↗	$T_{CP,top}$ ↘	RH, v_{air}, T_{air}
	v_{air} ↘	RH, $T_{CP,top}$, T_{air}
	RH ↗	v_{air}, $T_{CP,top}$, T_{air}
	T_{air} ↗	RH, v_{air}, $T_{CP,top}$
λ_f ↗	v_{air} [a]	RH, $T_{CP,top}$, T_{air}
	$T_{CP,top}$ ↘	RH, v_{air}, T_{air}
	RH ↘	v_{air}, $T_{CP,top}$, T_{air}

[a] Low velocities tend to increase λ_f during the first minutes. Then no more effect of the velocity on λ_f.

Figure 5.4 – Summary of influencing parameters on frost thickness and thermal conductivity from Leoni et al. (2017)

The same conclusions about the influence on frost thickness have been found by Sahin (2006); in general, higher cold surface temperatures leads lower thickness of frost, due to its different shape (needle for lower temperatures and irregular or supercooled water droplets for higher temperatures) as shown in Figure 5.5, resulting in a lower thermal conductivity.

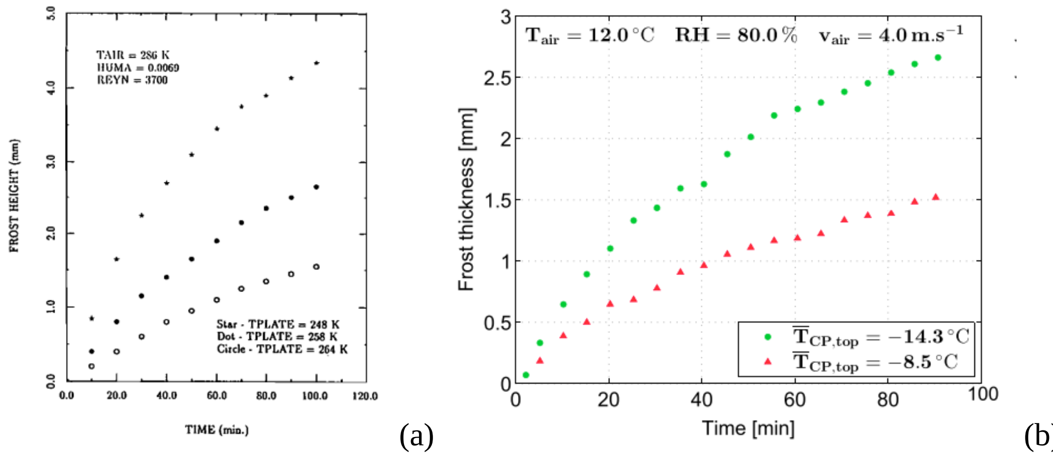

Figure 5.5 – Frost thickness as a function of time for different cold surface temperatures from Sahin (2006) (a) and Leoni et al. (2017) (b)

Higher value of air temperature with the same specific humidity (ω) leads to lower thickness due to melting phenomenon that occurs on frost surface with the same specific humidity, as shown in Figure 5.6.

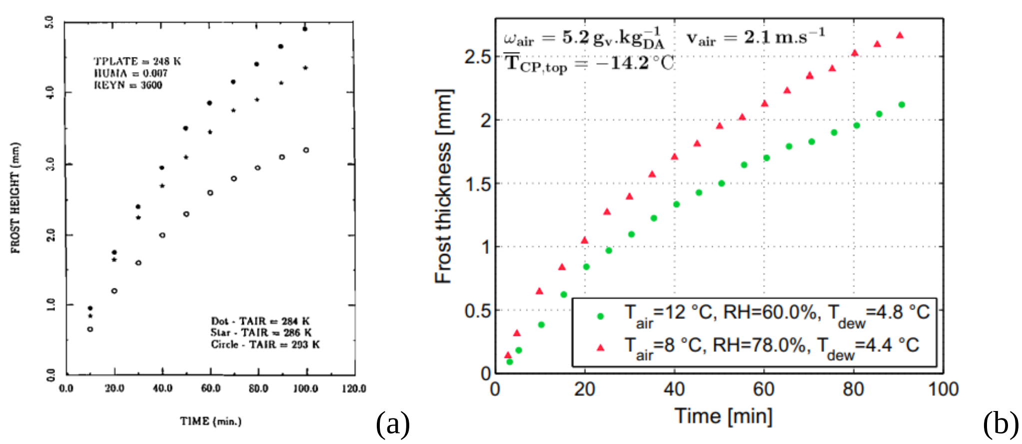

Figure 5.6 – Frost thickness as a function of time for different values air temperatures from Sahin (2006) (a) and Leoni et al. (2017) (b)

In Leoni et al. (2017), the thermal conductivity of thinner frost is lower than the other in the first time, but it increases due to the melting of frost surface with densification in the bottom layers as shown in Figure 5.7.

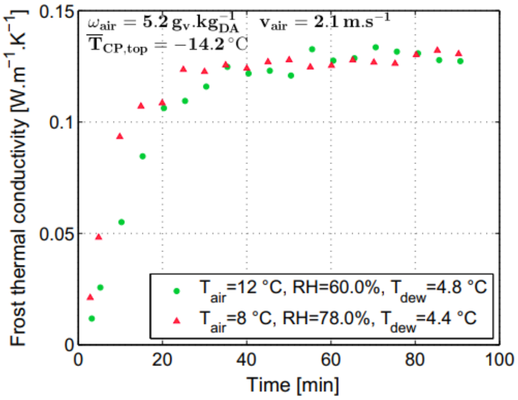

Figure 5.7 – Frost thermal conductivity as a function of time for different air temperatures (Leoni et al., 2017)

Higher is the specific humidity and thicker is the frost layer due to higher pushing force that causes the frost formation and grows up as represented in Figure 5.8.

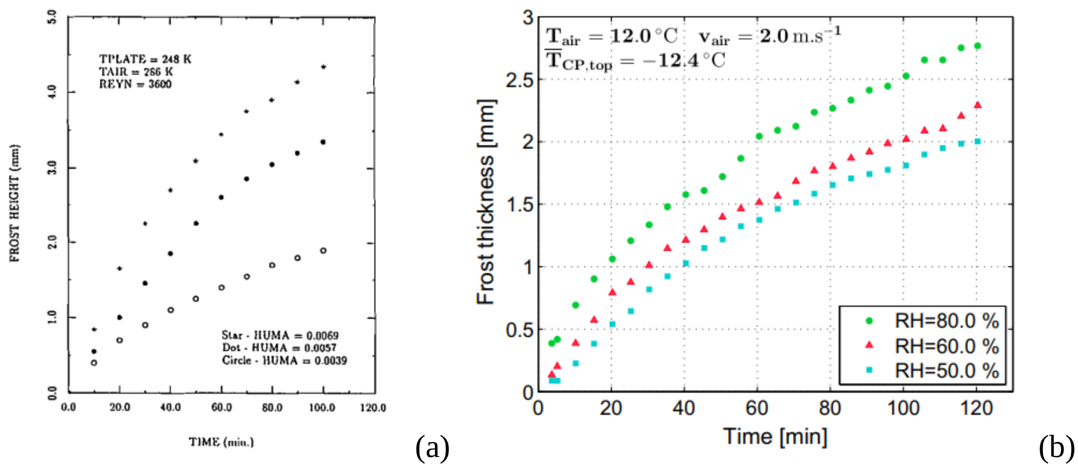

Figure 5.8 – Frost thickness as a function of time for different values of specific (a) and relative humidity values from Sahin (2006) and Leoni et al. (2017)

The thermal conductivity is analysed by Leoni et al. (2017) and shown in Figure 5.9 where it is higher with lower frost thickness due to higher density.
Both works stated that the effect of air flow velocity on frost thickness is negligible, as shown in Figure 5.10.

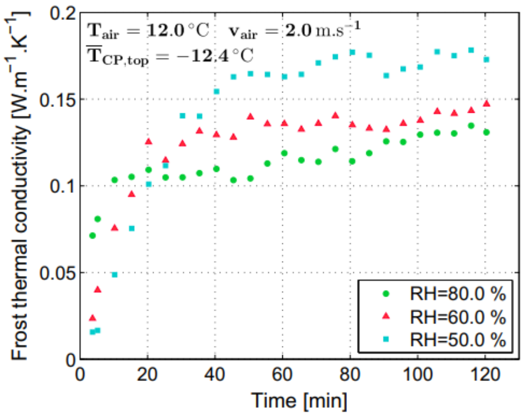

Figure 5.9 – Frost thermal conductivity as a function of time for different values of relative humidity from Leoni et al. (2017)

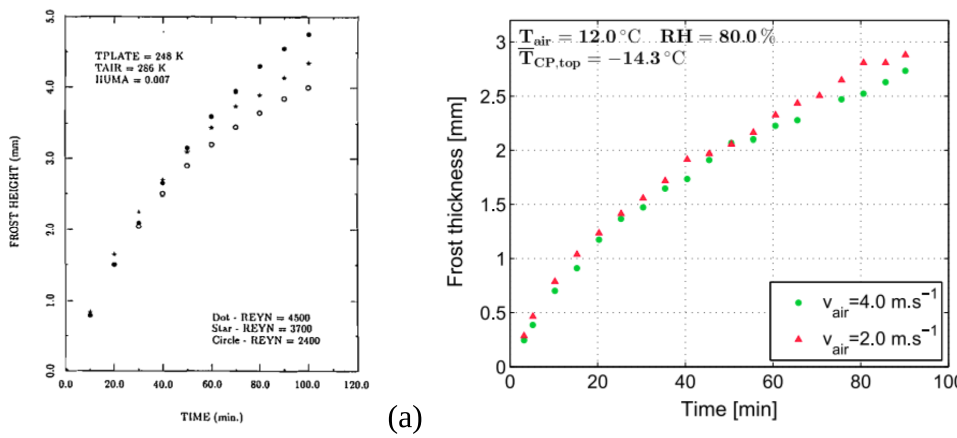

Figure 5.10 – Frost thickness as a function of time for different Reynolds number (a) and airflow velocity (b) from Sahin (2006) (a) and Leoni et al. (2017) (b)

In Leoni et al. (2017) a comparison between experimental points and predictive model of frost growth and thermal properties has been carried out; the main outcomes are that good agreement has been found regarding frost thickness and conductivity but less with frost density predictive models. Other comparison between experimental points from the literature and predictive models has been carried out in the review of Leoni et al. (2016), where 382 and 149 data points have been compared, respectively, with frost thickness and density prediction models.

An improved one-dimensional prediction model of frost density, thickness and thermal conductivity is proposed by Li et al. (2021). The authors modified the crystal shape map of Wu et al. (2007) substituting the excess of ambient vapour with a dimensionless parameter that depends by water triple point temperature and dew point saturation temperature. This improves the crystal shape recognition using linear correlations in the model. This latter can predict the frost thickness and thermal conductivity with the same prediction ability of Na and Webb correlation (Na and Webb, 2004), instead it has 5% better prediction performances than the latter in terms of frost density evaluation.

5.2 Frost formation on evaporator surface for refrigeration and heat pump units and its impact on performances

In this paragraph the works are grouped basing on the application, in the first part, studies that rely on frost formation and the effects on fin and coils and microchannel heat exchangers are presented; subsequently, in the second part, experimental and numerical works analysing the effects frost formation on heat pumps and refrigerator evaporators are reported. In the reviewed works the effect of heat exchanger geometry and operating parameters of air temperature, relative humidity, air velocity and heat exchanger temperature on frost growth, its characteristic (shape, thermal conductivity and density) and the effect on performances are studied with experimental and modelling approaches. Da Silva et al. (2010) studied experimentally the frost accumulation on four different fin and tube evaporator coils geometries in a closed loop test section where coil and air temperatures, specific humidity and volumetric air flow rate are controlled. Inside the tubes water glycol mixtures flowed. The tested boundary conditions covered the operating conditions of MBP (medium back pressure) light commercial refrigeration applications. The effect on accumulated mass frost, cooling capacity and air side pressure drop of different parameters such as: supercooling degree (which depends on air temperature and humidity and coil temperature), fin density (geometry of the evaporator) and the volumetric air flow rate is studied. The results are shown in Figure 5.11 where mass frost (a), cooling capacity (b), overall heat transfer (c) and air pressure drop (d) are plotted as a function of time for different fin densities.

The authors found that frost formation is faster with higher degrees of supercooling, since it is the driving force of the phenomenon. This causes faster mass frost accumulation, drop of the cooling capacity and overall heat transfer, and the increase of the air side pressure drop. The frost on evaporator surface acts as a thermal resistance to forced convection and in the same time it causes the reduction of air flow free passage. The reduction of air flow rate plays higher role than the thermal resistance to the jeopardization of the overall heat transfer coefficient. More denser are the fins and faster is the occlusion process of the frost on evaporator surface. The authors analysed also the effect of fans and geometric difference between louvered and wavy fins; higher volumetric flow rate imposed by the fans and louvered fins are characterized by faster formation of frost.

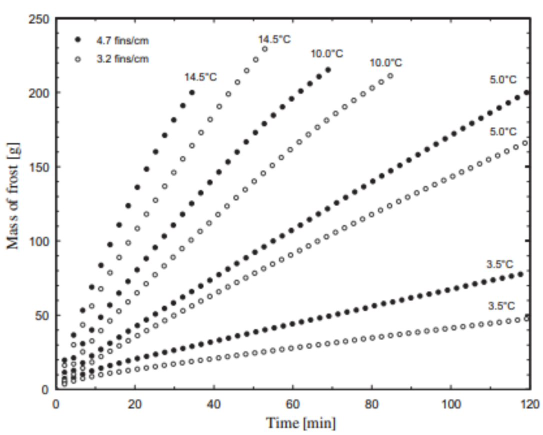

(a)

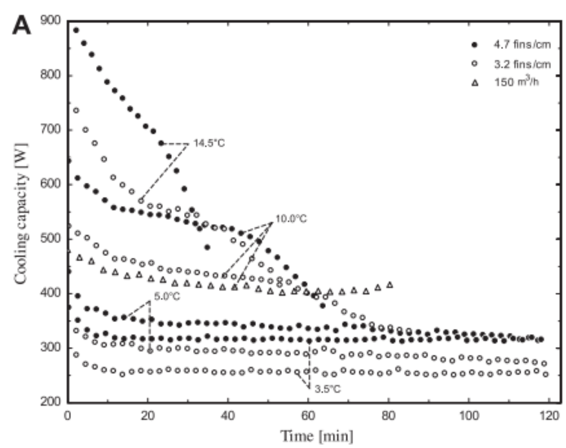

(b)

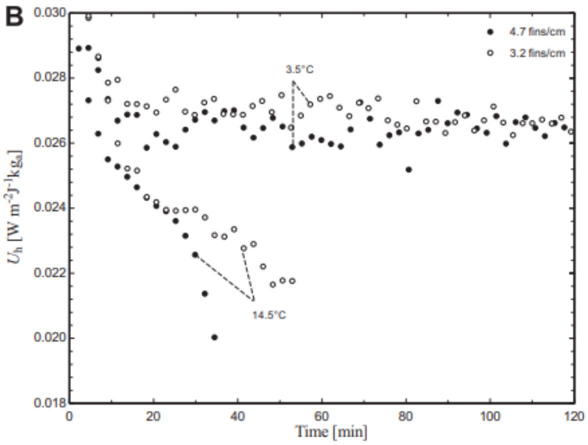

(c)

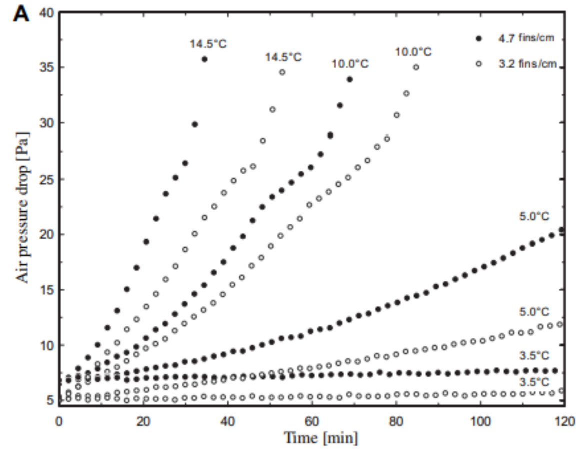

(d)

Figure 5.11 – Collected mass of frost (a), cooling capacity (b), overall heat transfer (c) and air pressure drop (d) as a function of time for different fin densities and supercooling degrees (Da Silva et al. 2010)

The same approach is used in Da Silva (2012), that carried out tests with visual inspection of frost formation on evaporator surface and developed a model that predicts the amount of frost mass, the frost thickness, the air flow rate reduction and the cooling capacity. The visual inspection of fins before and after the frosting process is shown in Figure 5.12a with frost morphology in Figure 5.12b.
The comparison between the model and the experimental results are presented in Figure 5.13.

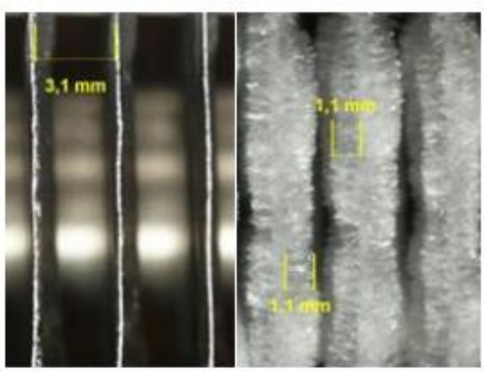

(a)

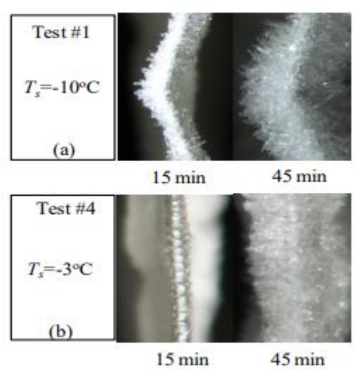

(b)

Figure 5.12 – Fins visual inspection before and after the frosting process (a) and frost morphology with different surface temperature (b) from Da Silva (2012)

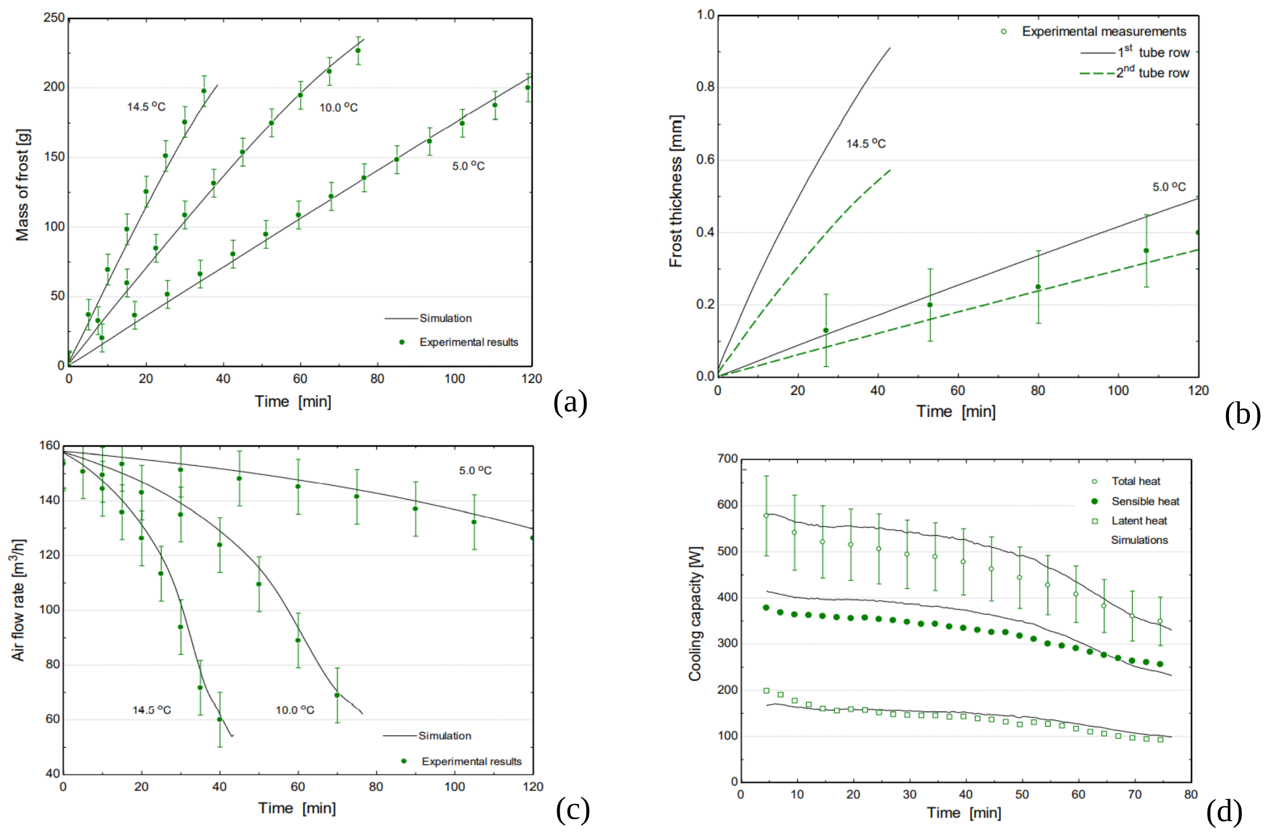

Figure 5.13 – Comparison between measured and evaluated mass of frost (a), frost thickness (b), air flow rate (c) and cooling capacity (d) from Da Silva (2012)

The authors obtained a good agreement between experimental points and simulations under different boundary conditions. Higher supercooling degrees leads faster frost accumulation and grow up with higher thickness; moreover, from the simulation the thickness of the frost decreases from the first to the second tube row due to lower value of air specific humidity difference that leads to slower frost growing. Another numerical model of frost deposition is proposed by Seker et al. (2004) and validated with experimental data from literature obtaining good agreement.

As regards micro-channel evaporators, Moallem et al. (2013) carried out an experimental campaign on 7 different micro-channel geometry samples. The effect of surface temperature, geometry, air humidity and velocity are analysed. A visual inspection is carried out during the experiments to compare the frost distribution to the different geometries, and an example is shown in Figure 5.14.

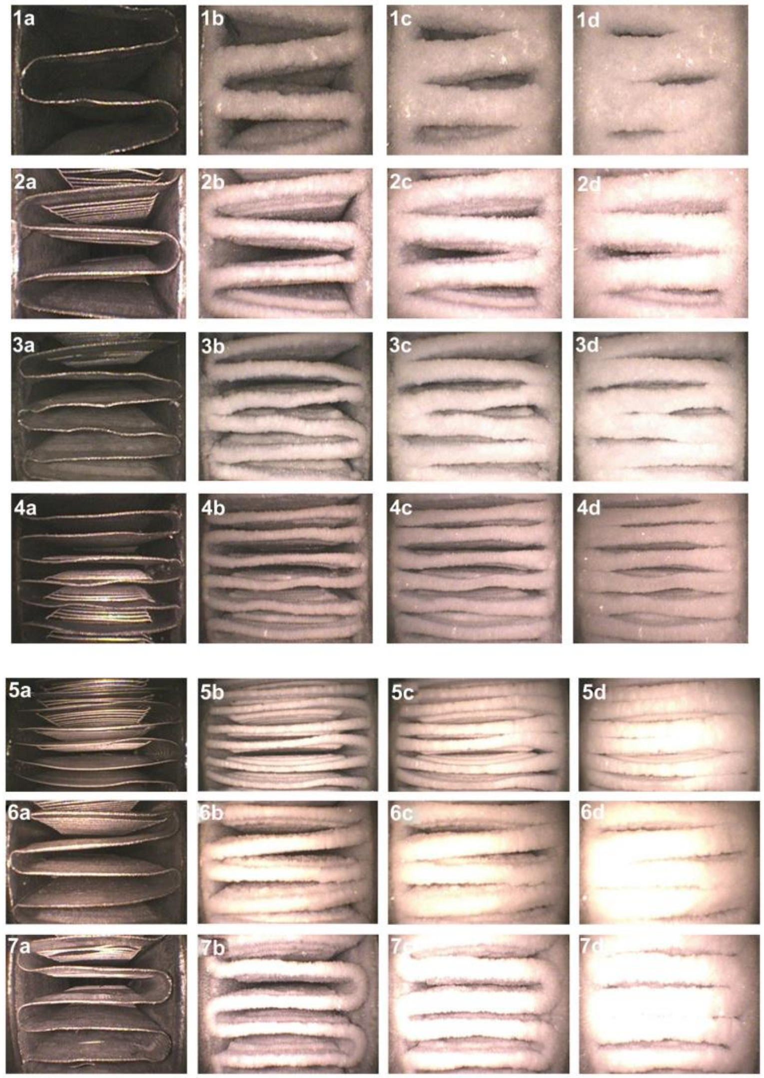

Figure 5.14 – Visual inspection of frost formation and grow up on surface for different fin geometries (Moallem et al., 2013)

The influence of environmental parameters (surface temperature, air temperature and humidity) on cooling capacity reduction and pressure drop increase are in agreement with what shown in the previous works regarding the study of fin and coils evaporators. The authors also analysed the influence of fin density, width and depth on frosting time and capacity: some results are shown in Figure 5.15.

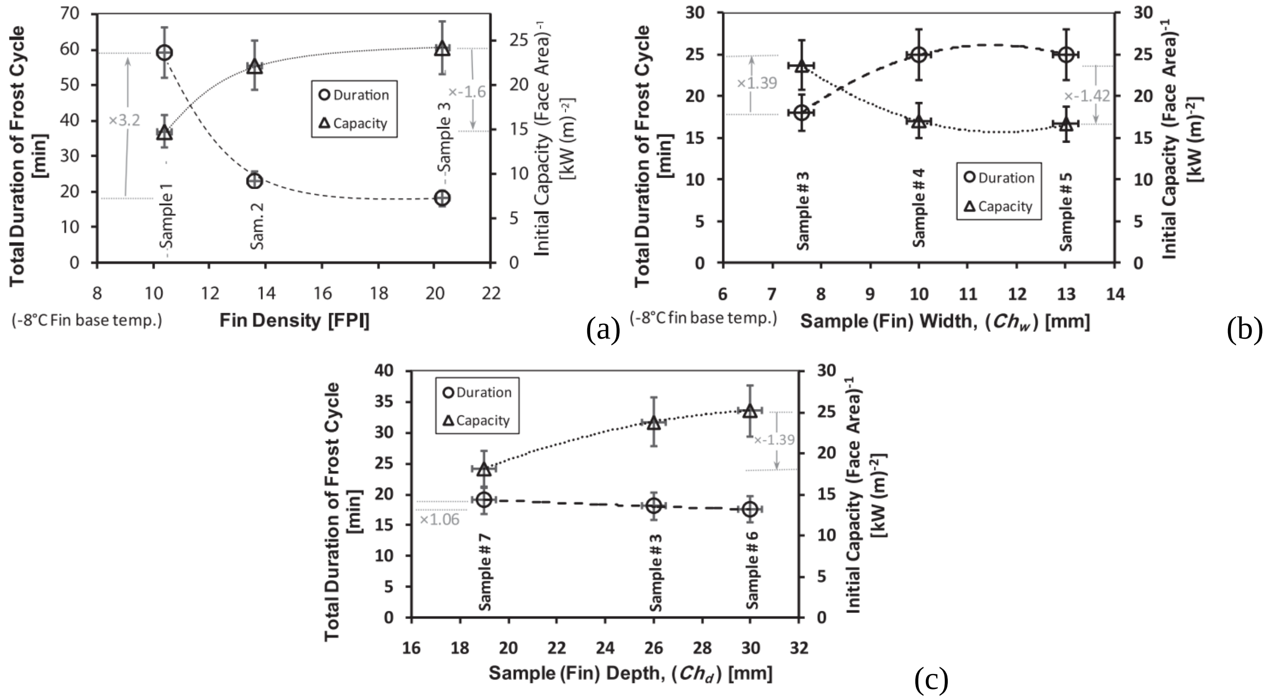

Figure 5.15 – Effect of fin density , width and depth on Total Duration of Frost Cycle and Initial Capacity (Moallem et al., 2013)

The increase of fin density leads to a decrease of the duration of frost cycle and an increase of initial capacity (value of capacity at the beginning of test without frost) up to 40%; instead, the increase of width (tube spacing) causes an increase of duration of frosting time of 60% and a reduction of around 58% in initial capacity. Finally, the fin depth has less influence on frost formation time but leads an increase of 41% in initial capacity.

Studies about the impact of cycling operation of frosting and defrosting on performances of heat exchangers have been carried out by Xu et al. (2012) and Xia et al. (2005). In the first work, two different microchannel heat exchangers have been studied experimentally: one with horizontal tube and the other with vertical ones. Tests at different air temperatures and humidity, refrigerant temperature and air flow rate with frosting and defrosting cycles have been performed. Visual frost observation has been carried out during the tests for both heat exchanger samples as shown in Figure 5.16.

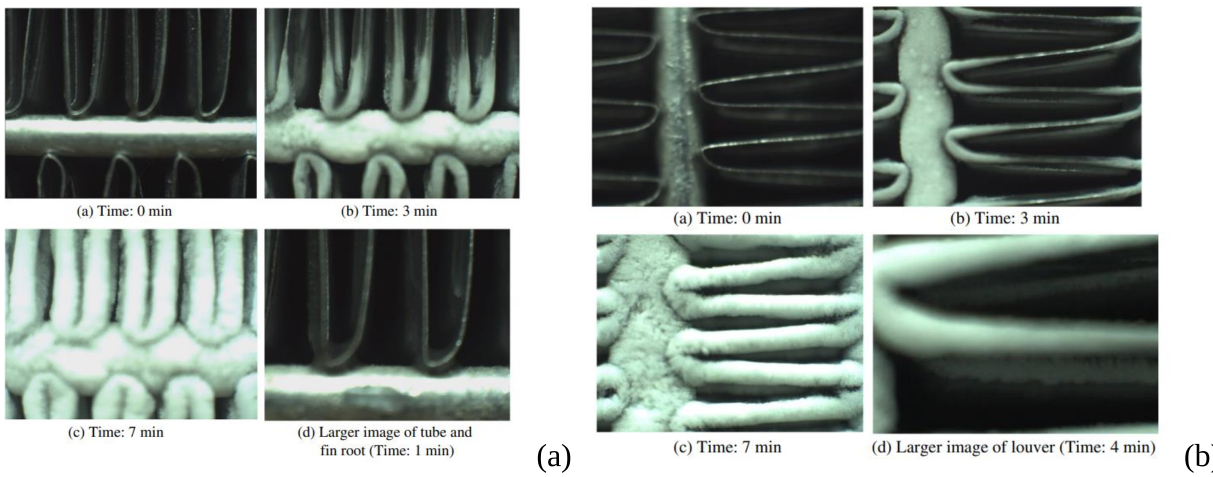

Figure 5.16 – Visual frost inspection on horizontal tube sample (a) and on vertical tube sample (b) (Xu et al., 2012)

It was found that after each defrost cycle the horizontal tube sample has higher water retention than the vertical one, with 800 g of water collected after 4 operating cycles. The water retention affects the frosting time, pressure drop and the capacity of the following cycles: in fact, after three operating cycles the pressure drops increased three times more than the beginning of the first cycle and the capacity decreased by 27% in the horizontal tube sample. Conversely, in the vertical tube sample, similar degradation rate has been observed for pressure drops and capacity since no water retention has been observed. Some results are shown in Figure 5.17.

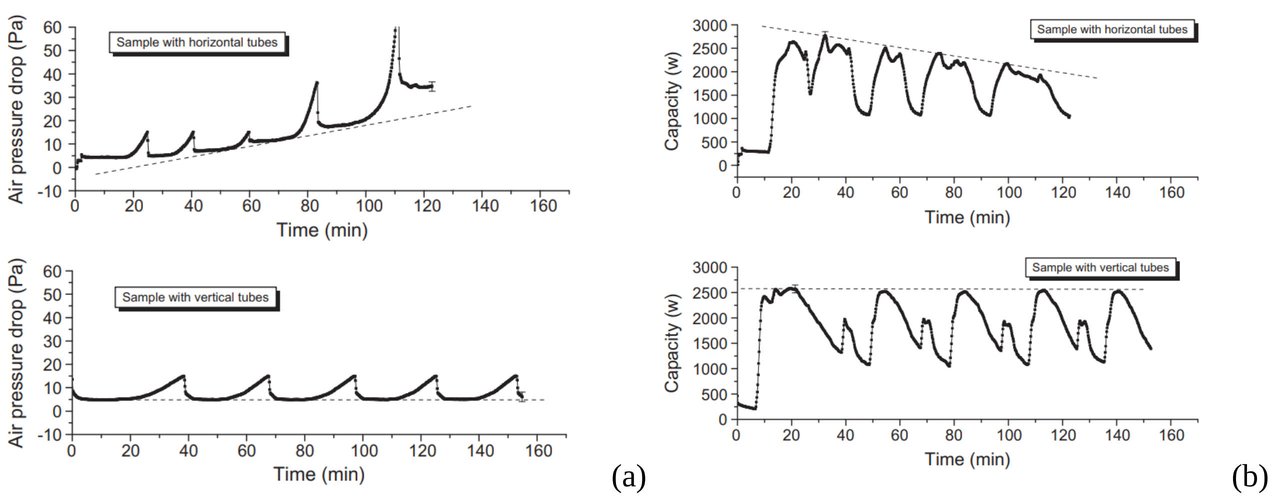

Figure 5.17 – Air pressure drop (a) and capacity (b) as a function of time for horizontal and vertical tube sample (Xu et al., 2012)

In Xia et al. (2005), four different geometries of microchannel heat exchangers with horizontal tubes have been analysed on frosting operation. Two of them are analysed with cyclical operation (frosting, defrosting, and re-frosting) obtaining similar results of previous work with the less shallow specimen more sensible to pressure drop increase and overall heat transfer decrease in the different cycles.

Nevertheless, the authors declared that in order to evaluate the impact of geometry on cyclic frost formation, more data points with higher geometry combinations were required.
The effect of frost formation and growth on performances of heat pump system has been studied with experimental and modelling approach by Guo et al. (2008). The authors carried out tests with different values of relative humidity and temperature at outdoor heat exchanger side as shown in Figure 5.18, where the experimental facility is represented.

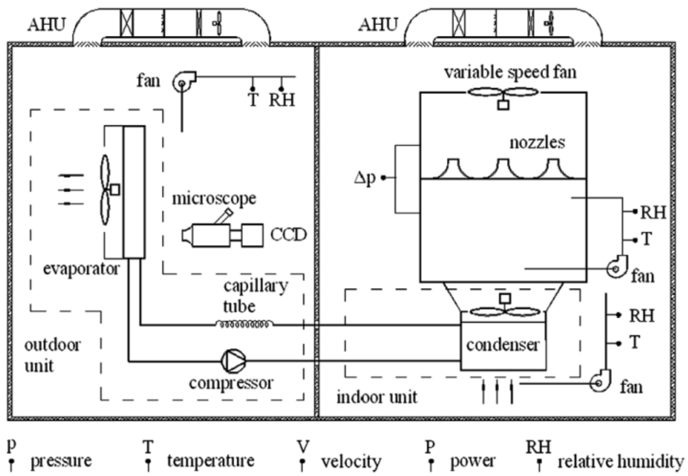

Figure 5.18 – Experimental test facility used in Guo et al. (2008)

They associated the trends of pressures, heating capacity and COP to frost formation stage. From Figure 5.19a, in the first 15 minutes of test the COP and heating capacity increases from their initial value due to water droplets deposition and solidification on fins surface that increase the roughness of evaporator surface and the convective heat transfer coefficient. In the second phase, the frost grows towards its radius rather than its length and the heating capacity and COP are almost constant. Then, the frost grows in length reducing the evaporator air flow with a reduction of operating pressures (see Figure 5.19b), COP and heating capacity. The final frost structure appears cylindrical with branches that are in contact one to each other.

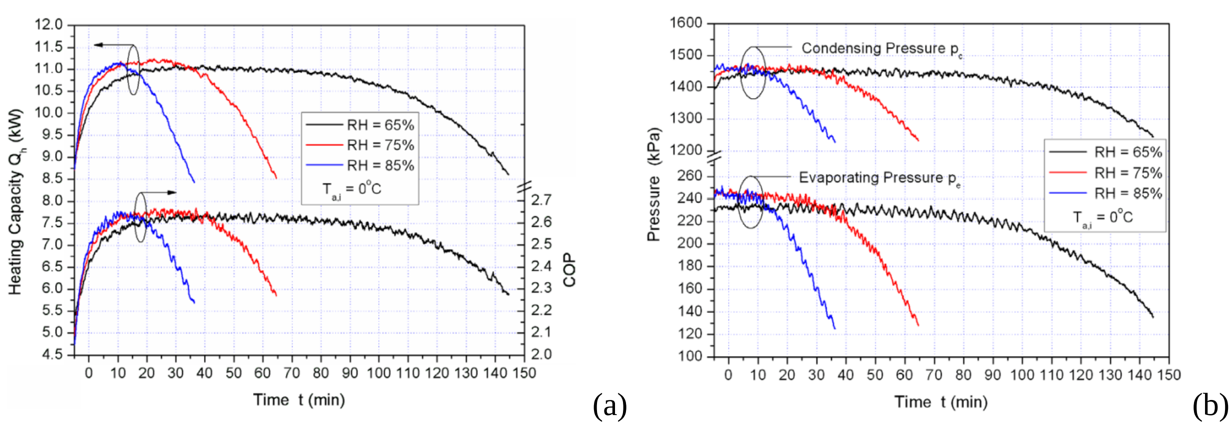

Figure 5.19 – Heating capacity and COP (a) and operating pressures (b) as a function of time for different relative humidity values (Guo et al., 2008)

In the last part of the work, the experimental data are compared to the results of a dynamic model (Chen et Guo 2005 and Guo et al. 2006), with a 25% of difference in frost thickness prediction; instead, 8% of agreement is found in performances prediction, except for the last part of the test where the experimental ones fall faster than the simulated one. The differences in the last part is due to the fact that the model doesn't consider the real frost disposition and morphology on the evaporator surface.

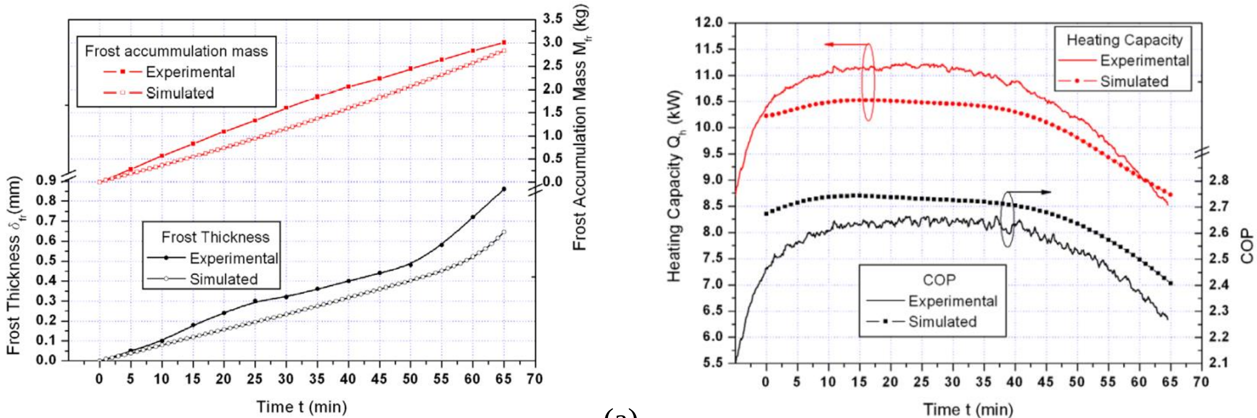

(a) (b)

Figure 5.20 – Comparison between experimental and simulated results of frost mass and thickness (a), heating capacity and COP (b) as a function of time (Guo et al., 2008)

Getu et Bansal (2006) carried out an experimental and modelling analysis "in-situ" focused on the performances of supermarket display cabinets (through-frozen-food TFF and glass-door-frozen-food GFF, in Figure 5.21), to develop a useful design tool for engineers involved in this issue.

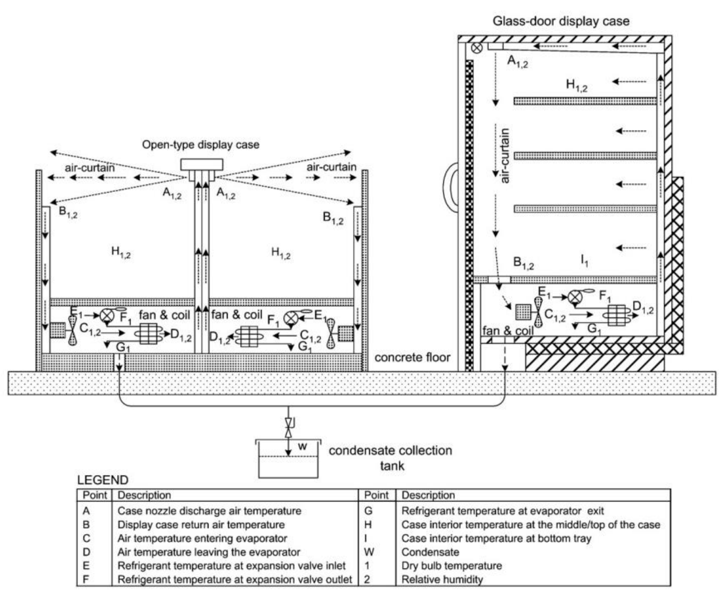

Figure 5.21 – TFF (left) and GFF (right) application analysed by Getu et Bansal (2006)

Measurements of store relative humidity and temperature, display cabinet temperatures, pressures and refrigerant mass flow rate have been carried out. These data have been used to validate a model of frost properties (mass and thickness) and cabinet performances basing on store ambiental condition. Some results of the model are shown in Figure 5.22, where the measured and predicted frost mass and thickness are compared.

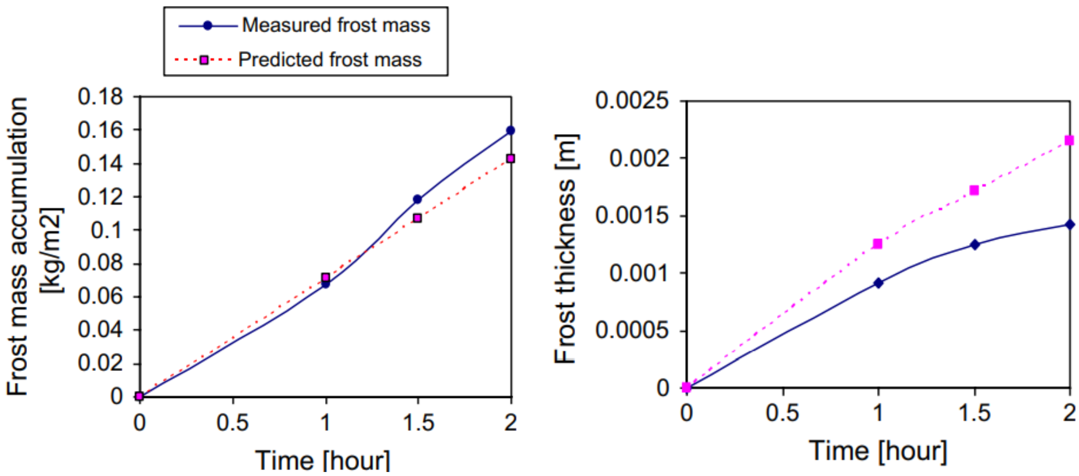

Figure 5.22 – Comparison between experimental and measured frost mass and thickness (Getu et Bansal, 2006)

The authors found that the frost thickness and thermal resistance is lower in the case of GFF than in TFF due to less influence of the first to the moisture of the store as depicted in Figure 5.23, where the absolute humidity, pressure drops, frost thickness and thermal resistance are plotted as a function of time.

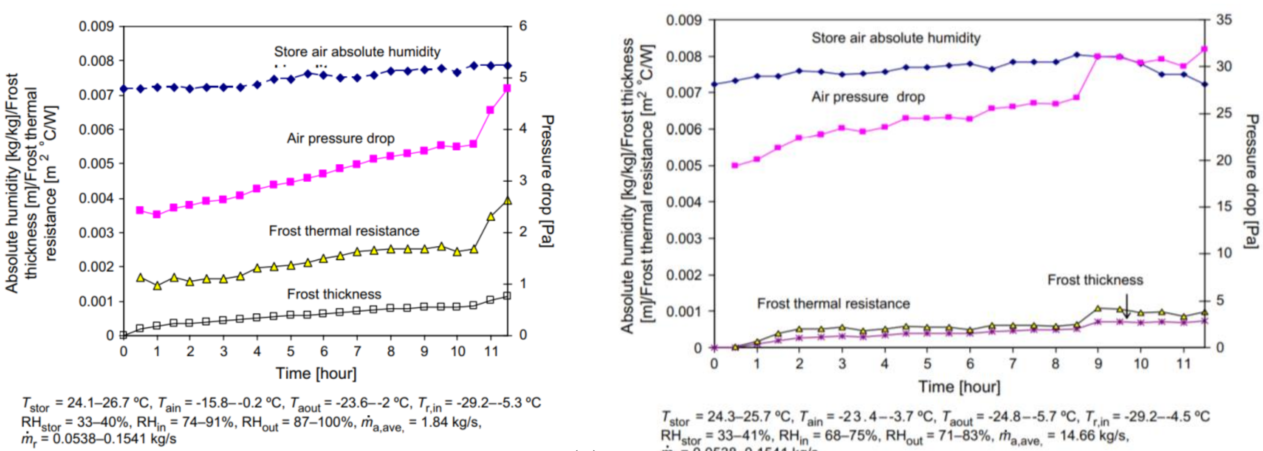

(a) (b)

Figure 5.23 – Store air absolute humidity, air pressure drop, frost thermal resistance and thickness as a function of time for TFF (a) and GFF (b) (Getu and Bansal, 2006)

Similar appliances have been studied experimentally by Datta et al. (1998) with an experimental campaign. The experiments have been carried out with different ambient tempeatures and relative humidity. They observed that the relative humidity at ambient temperature of 22°C have less influence on product temperature as shown in Figure 5.24.

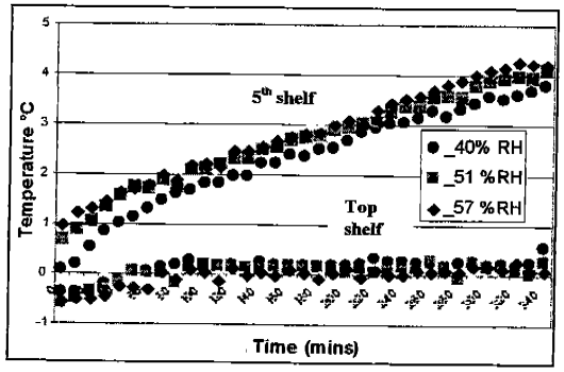

Figure 5.24 – Product temperature as a function of time for different relative humidity values (Datta et al., 1998)

The amount of frost is influenced mainly by the relative humidity and temperature inside the store than the refrigerant inlet evaporator temperature as shown in Figure 5.25 where the frost mass has been reported for different relative humidity values (a), ambient air temperature (b) and refrigerant inlet evaporator temperatures (c).

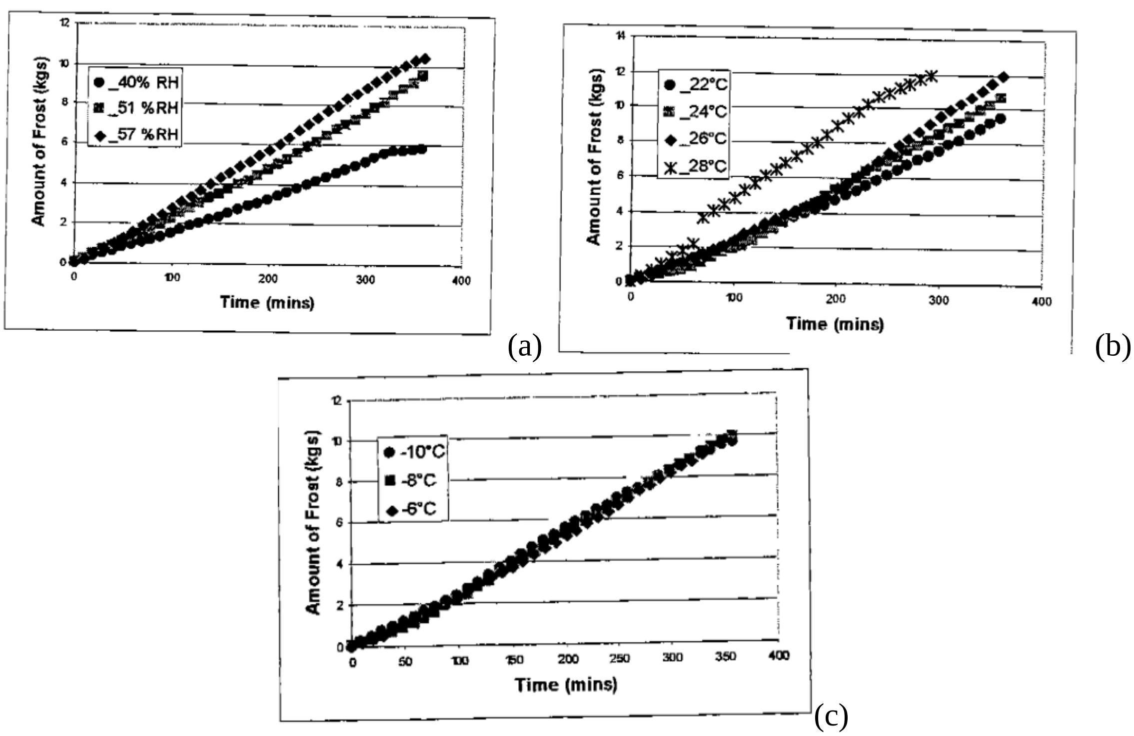

Figure 5.25 – Amount of frost for different relative humidity (a), ambient temperature (b) and refrigerant inlet temperature (c) as a function of time (Datta et al., 1998)

Mastrullo et al. (2014) developed a quasi-steady model of energy consumption considering the effect of door openings, frost formation, air leakages and defrost applied on vertical freezer. The effect of air temperature and humidity, frequency of door openings and defrosting have been analysed. Mass and energy balances have been carried out in control volume of frost and evaporator metal, refrigerated space, and containing walls of the refrigerator. The frost growth model of Hermes et al. (2009), has been used. The model has been validated with data collected with an experimental campaign in a climatic chamber and others from scientific literature as depicted in Figure 5.26 showing good agreement.

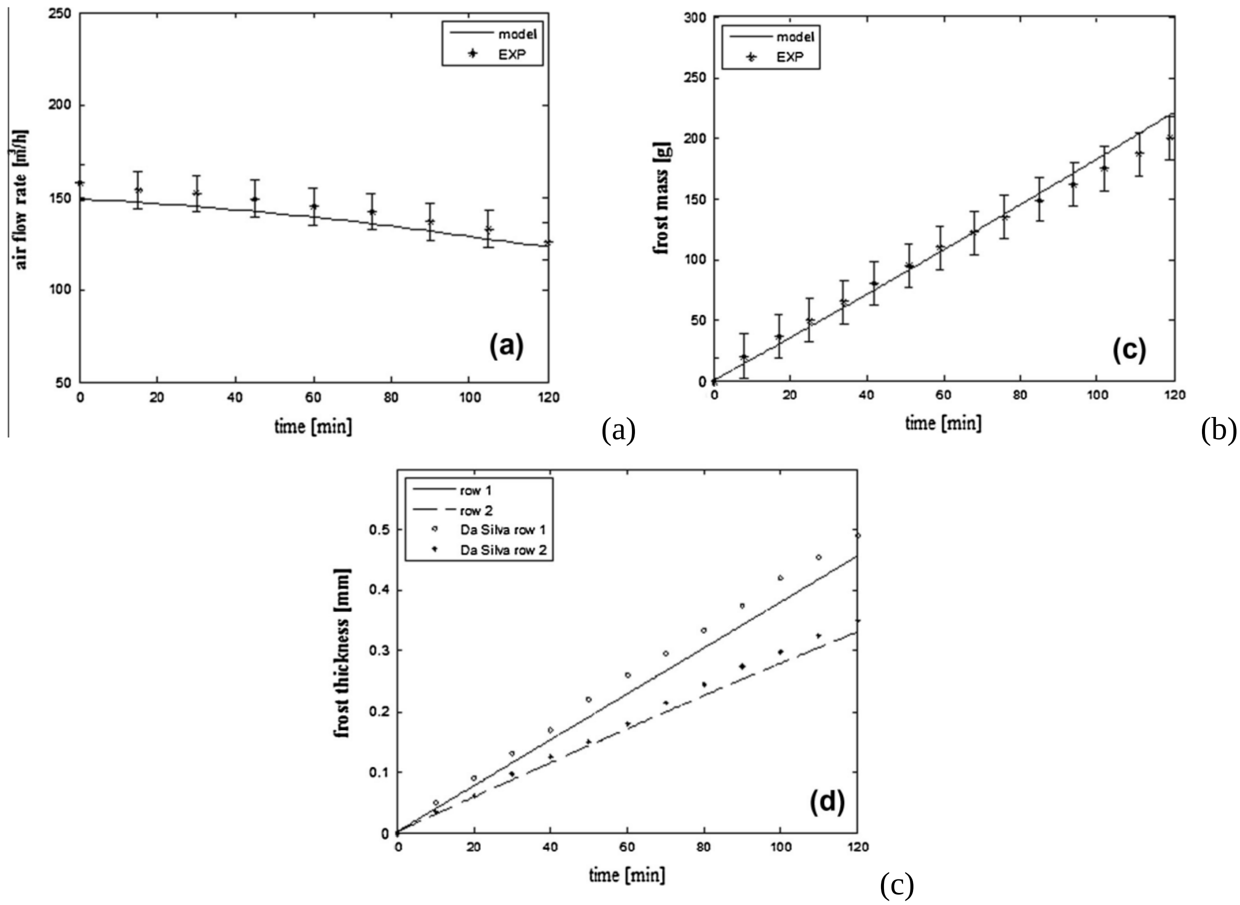

Figure 5.26 – Comparison of model results with experimental data of Da Silva et al. (2011) for evaporator air flow rate (a), frost mass amount (b) and frost thickness (c) as a function of time (Mastrullo et al., 2014)

The model agrees regarding the measured trends and values of temperatures (refrigerated space, evaporating, metal) and power consumption as shown in Figure 5.27. A decrease of metal temperature and evaporating temperature has been observed during the experiments and from the model. This is mainly due to the reduction of the air flow rate with less heat transferred and lower refrigerant outlet evaporator superheat, implying the closing of thermostatic expansion valve; this effect caused the reduction of evaporating pressure involving the decrease of power consumption (Figure 5.27d) until the defrost phase.

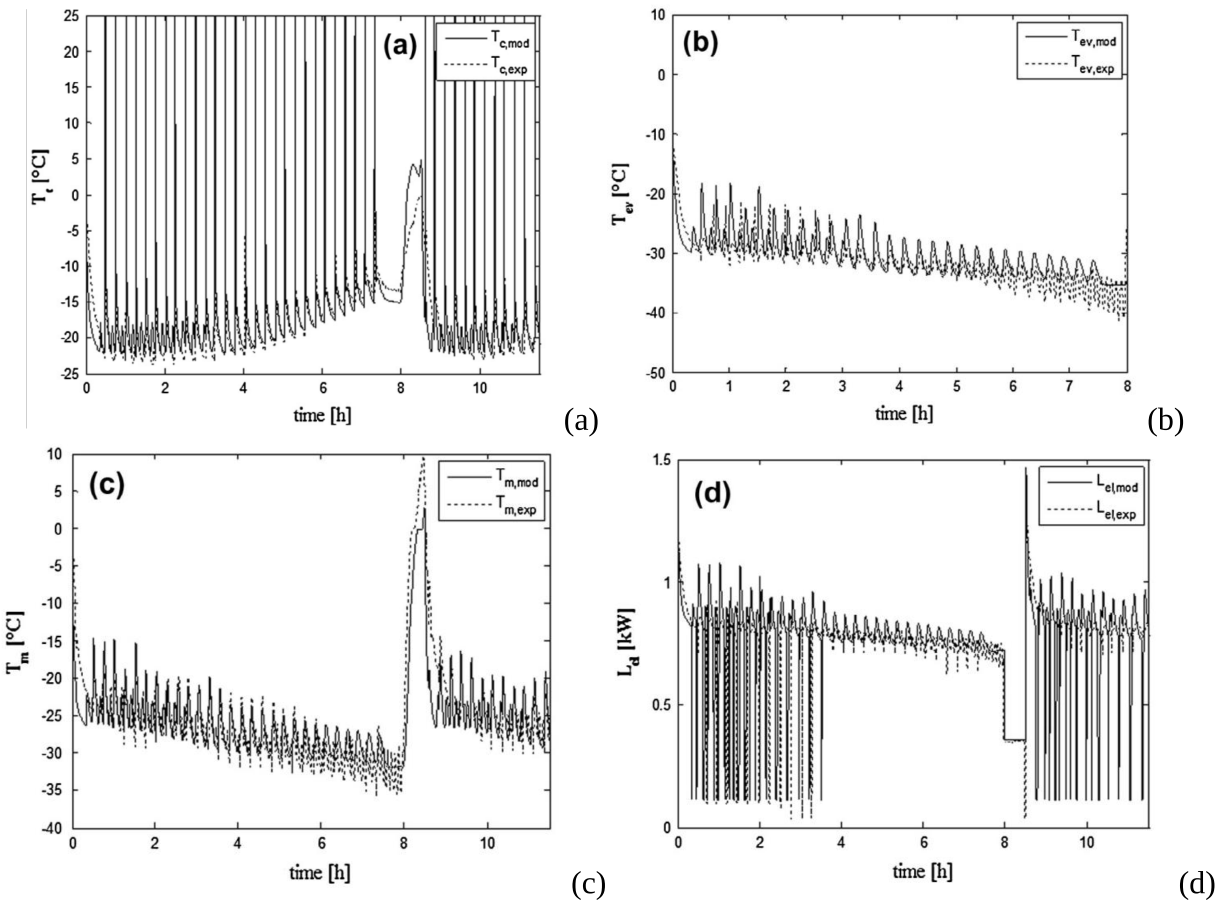

Figure 5.27 – Comparison between measured and simulated values of refrigerated space temperature (a), evaporating temperature (b), metal temperature (c) and power consumption (d) (Mastrullo et al., 2014)

The authors demonstrated, also, that the model can be a powerful tool for the design of the evaporator and the cabinets considering the effect of door opening, moist air infiltration and power faults occurrence on temperature variation inside the cabinet.

To sum up, in all mentioned works the frost formation is influenced mainly by air temperature, relative humidity and cold surface temperature rather than air velocity. In general, high value of air specific humidity and the difference with the corresponding value to cold surface temperature, leads to faster frost formation, with less dense structure and thermal conductivity. The rate of performance degradation is higher when the frost forms and grows fast. The predictive models on frost properties evaluation agree with experimental data up to 30%, instead, the ones predicting the system performances agrees up to 10%.

5.3 Defrost operation analysis and defrosting control logic optimization

As shown in previous paragraph, frost formation causes a reduction of the cooling capacity of refrigerators that will be not able to maintain the target temperatures with detrimental effect also in energy consumption (longer operation time). For these reasons, defrost operation is required to restore the initial capacity of the unit. Amer et Wang (2017) in their review on defrosting methods underline the importance of defrosting process. The authors defined two kinds of defrosting techniques:

- Active techniques, requiring additional energy consumption
- Passive techniques, not requiring additional energy

Surface treatments to avoid or delay frost formation belongs to passive methods. Conversely, hot-gas bypass, electric defrost, and on / off cycling are examples of active defrost systems. In hot-gas bypass defrost system the hot refrigerant coming from compressor flows into the evaporator heating up the metal and melting the ice; in electric defrost system, the evaporator is heated by means electric resistances. Finally, in on / off cycling the ice is melted due to the increase of evaporator temperature when the system is off, with the air having positive temperature. The defrost cycle ends when the temperature of heat exchanger reach a threshold value fixed during design and testing phase of the unit. Since there is a trade-off between the degradation of energy consumption and performances, during system operation, due to frost formation and the energy consumption during the defrost phase, the optimization of the defrosting control logic is required in refrigeration and air conditioning units. The time interval-based defrost control logic is the most used for its cheapness and simplicity than other methods such as on-demand defrost systems. These latter start the defrost cycle when the temperature difference between air and evaporator or air pressure drop differences are above a fixed threshold. The time interval-based systems bring unnecessary defrost cycles as stated by Datta et al. (1997) with impact on energy consumption and extra energy costs. The authors made a rough estimation of annual extra costs for defrost purpose of 500000£ for a large chain of retail food stores with 30000 display cases equipped with electrical heater, an average defrost time of 10 minutes and 4 defrost cycle in a day, without considering the energy expenditure to recover the temperature inside the cabinet after the defrost.

For this reason, defrost effectiveness, frost detection and on-demand defrosting control logic optimization are the most relevant topics of scientific and technical research about energy efficiency solutions in refrigeration and air-conditioning sector. A state of the art of research about these topics is presented in this paragraph.

Hoffenbecker et al. (2005) developed and validated a model of hot-gas bypass defrost system of an industrial air-cooling evaporator. The model predicts the time needed to melt completely the frost and the energy transferred to the refrigerated space (named parasitic energy) during the defrost period, starting from the space temperature and humidity, coil geometry, frost thickness, frost density and hot gas refrigerant inlet temperature. The model has been validated with experimental data collected in-situ in a fruit product storage, presented in Hoffenbecker (2004) with good agreement on defrost energy evaluation. The major finding of the analysis is that there is an optimum value of hot gas defrost temperature with the regards of mass and density frost on the evaporator. The parasitic energy was associated with the defrost dwell time; the limitation of this latter parameter plays a key role in minimizing the parasitic energy.

Cho et al. (2005) compared the on-off cycling defrost system with a hot-gas bypass one on a showcase refrigeration system with three evaporators. In Figure 5.28a the frosting and defrosting sequences are shown for on-off cycling and hot gas bypass defrost type; in case of hot-gas bypass system, the defrosting phases of each evaporator are separated of 80 minutes one from each other. The authors shown that with hot-gas bypass defrost, better temperature control can be achieved since less time to defrost is needed resulting in lower temperature fluctuations than the on-off cycling type, as shown in Figure 5.28b.

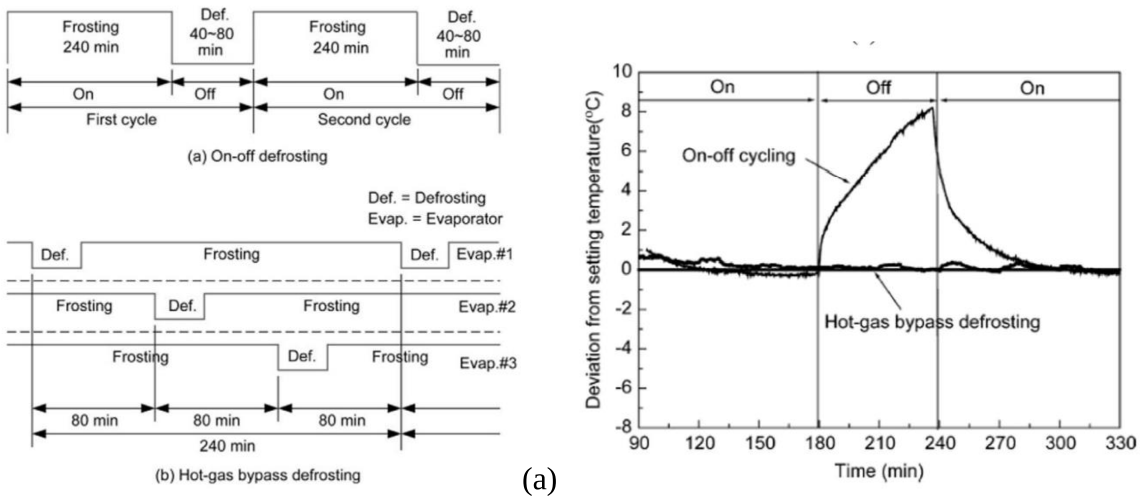

(a) (b)

Figure 5.28 – Frosting and defrosting phases for on-off cycling and hot-gas systems (a) and deviation from setting temperature in on / off operation phases for on / off cycling and hot-gas bypass defrost system (Cho et al., 2003)

The effect of frost distribution on evaporator surface and the downwards flowing melted frost on defrosting efficiency was studied by Song et al. (2018) that carried out an experimental campaign on an air source heat pump. Six experiments have been carried out and in three of these water collecting trays are installed on evaporator coil to keep away the melted frost water from the coil. From the experimental campaign emerged that higher FEV (frost evenness value) and collecting the melted frost during defrosting cycle are beneficial for defrost efficiency. Moreover, with the water trays the defrost reduction increases from 17 s to 22 s with the increase of FEV value from 79.4% to 96.6%; conversely, the defrost efficiency increase with FEV value is roughly the same comparing the case with (6.77%) and without (5.7%) the collecting trays.

Bansal et al. (2009) carried out a thermal analysis of heater defrost system in a household refrigerator. The aim of the work is to study the effectiveness of defrost mechanism on total energy consumption of refrigerator with an experimental campaign. A heat transfer model has been developed to estimate defrost duration. This latter is around 22 mins with the evaporator at -20°C. The major findings of experimental campaign are that with high rate of frost on evaporator the refrigerator absorbs less energy when the automatic defrost system is operated than the case without automatic defrost system; the second major conclusion is that the defrost mechanism has low efficiency since the heaters reaches unnecessary temperature levels, about 520°C and 560°C for minimal and heavy frost condition, respectively. Finally, two solutions have been proposed to increase the defrost efficiency, the first one is to install the heater inside the evaporator structure, and the second one is to use reverse cycle defrost as the heat pumps.

Knabben et al. (2011) developed a model of a fin and tube evaporator on household refrigerator to assess the impact of the design parameter on frost evaporator blockage effect and defrost efficiency. Sub models of air flow, heat exchanger and frost growth have been developed and validated with data collected with an experimental campaign. The model agrees with the measurement of pressure drop and mass of frost within a range of ± 10%. Then, an assessment of different geometries (reported in Table 5.1) of evaporators with different number of fins in each row has been carried out.

Table 5.1 – Analysed evaporator geometries in Knabben et al. (2011)

Setup	Rows 1 / 2	Rows 3 / 4	Rows 5 / 6	Rows 7 / 8	Rows 9 / 10
Original	26	34	67	67	67
Alternative #1	26	34	42	67	67
Alternative #2	26	34	42	42	67
Alternative #3	26	26	34	42	42

From the assessment, the authors found that removing 25 fins in rows 5 / 6 (Alternative #1) avoids the decrease of cooling capacity after 3.5 hours of operation than the case with original configuration but with a loss of 2.5% of cooling capacity during the entire operation, as shown in Figure 5.29. The reduction of fins in Alternatives #2 and #3 leads higher free flow area but less cooling capacity. The reduction of fin number causes a reduction of accumulated mass of frost.

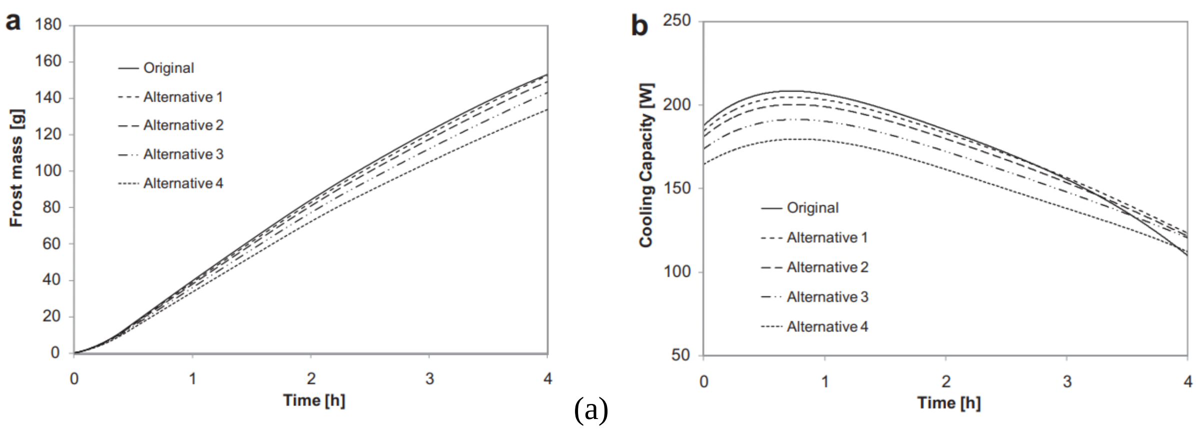

Figure 5.29 – Frost mass (a) and cooling capacity (b) as a function of time for different evaporator geometries (Knabben et al., 2011)

Moreover, the authors evaluated the needed amount of energy to defrost each row. Based on this evaluation, they proposed to split the total power of the defrost heater (235W) in two heaters, one of 175W to be placed in the first six rows and another of 60W for the last four rows.

Bejan et al. (1992), developed a model to find the optimal on / off sequence to minimize the power consumption on a household refrigerator. In the optimal on / off combination the refrigerator can maintain the temperature inside the refrigerated space and removes intermittently the ice layer. The model uses also empirical correlations of frost thickness as function of time.

In Datta et al. (1998) the authors proposed a method to predict the amount of frost using humidity as key parameter, to implement an on-demand defrost control logic. Since the humidity monitoring in each cabinet is not economically feasible, the authors used a parameter proportional to relative humidity, defined as follows:

$$\frac{T_{air,inlet}-T_{fin,ref,inlet}}{T_{air,inlet}-T_{coil,inlet}} \qquad \text{Eq. 5.1}$$

Where $T_{air,inlet}$ [°C] is the air temperature at evaporator inlet, $T_{fin,ref,inlet}$ [°C] is the fin temperature at refrigerant evaporator inlet point and $T_{coil,inlet}$ [°C] is the evaporator coil inlet temperature.

Another work dealing with the optimization of defrost control logic, instead of the use of pre-set interval time based, has been carried out by Datta et al. (1997). The authors carried out an experimental campaign on two display cabinets in laboratory, with controlled temperature and relative humidity conditions, collecting the condensate water at the end of each defrost; field tests data are added to the ones collected in laboratory. The amount of condensate water, obtained after 6 hours of cooling time, are reported as a function of temperature and relative humidity in Figure 5.30.

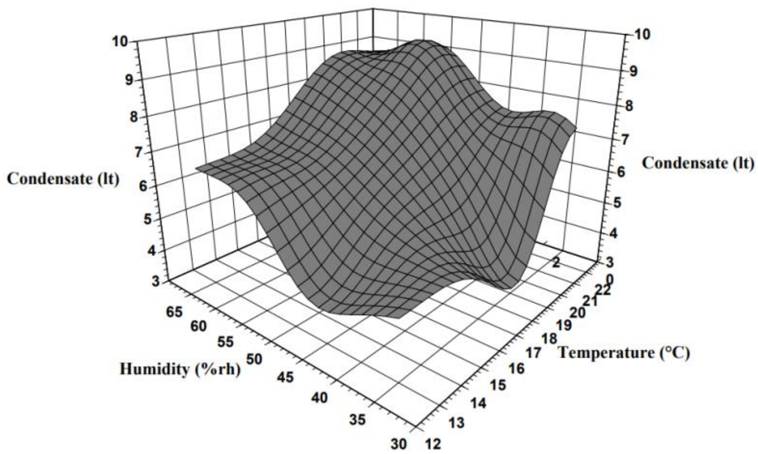

Figure 5.30 – Amount of condensate water as a function of temperature and humidity after 6 hours of cooling time (Datta et al., 1997)

The collected data are used to test and train an artificial neural network whose structure is depicted in Figure 5.31 whose strength is to overcome the use of the time-consuming correlations available in literature to evaluate the amount of frost.

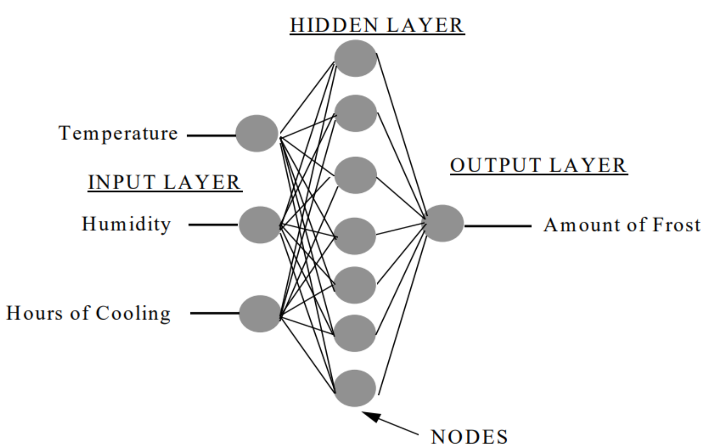

Figure 5.31 – Neural network modelled by Datta et al. (1997)

The measured temperature, humidity and hours of cooling are used in the input layer to predict the amount of frost; based on this information the controller can decide the right time to defrost. Good agreement has been found in training and testing phase between experimental and predicted data.
The results and conclusions of Datta et al. (1997) and Datta et al. (1998) are extended in the work of Tassou et al. (2001) where the authors declared and proved that the store humidity can be used as controlling parameter of defrost cycle, since the temperature does not vary considerably. Moreover, based on the measurements it is possible implement a defrost control logic varying the interval between defrosts and avoiding unnecessary defrost cycles, that are typical of the ones based on fixed time interval. According to the authors, the ideal defrost controller is the one that, starting from an initial programming, adapts its decision to start defrosting cycle to the variability of operating conditions of the refrigerator.
A machine learning algorithm called Support Vector Machine (SVM) has been used by Cao et al. (2013) to optimize the defrosting parameters on the control board of an open refrigerated display cabinets in supermarkets. The authors carried out an experimental campaign in laboratory with operating condition according to EN ISO 23953-2 standard. Using seven measured parameters (evaporator superheat, air supply temperature, ambient temperature, relative humidity, refrigeration time, defrosting time and air velocity), they trained and validated an artificial neural network to predict the ratio TEC / TDA (total energy consumption / total display area) and the M-packages temperature. The algorithm has been used to minimize the ratio TEC / TDA by varying the defrosting parameters (changeable on the controller) at the input of the neural network. Finally, after reloading the optimized values of the parameters on the display cabinet controller, tests have been carried out obtaining a reduction of the energy consumption and condensate water mass of 27% / 15.6% and 27.2% / 15.4% respectively, for climate class 3M / 0M according to EN ISO 23953-2 standard.
Frost detection systems are useful to improve on-demand defrost control logic, Buick et al. (1978) studied different kinds of frost detection systems based on the measurement of thermal resistance between the coil and the evaporator and others based on the capacitance variation in the space between two plates due to frost formation.
Xiao et al. (2009), studied the feasibility of the photoelectric technology to detect frost by means of an experimental campaign in laboratory. The effect of parameter of electric current, environment temperature, metal surface temperature, light intensity and sensor location on frost height and distribution on the test sample have been analysed. From the experimental campaign, it emerged that the novel technique could detect the frost height with good accuracy and it is suitable to be used for frost detection.
Xiao et al. (2010) carried out an experimental campaign to measure output voltage of a photoelectric system to correlate it to frost height. After that, a correlation to evaluate frost height from voltage has been developed and validated with data from literature with an agreement of 95% on the data sample within a relative deviation of ± 10%. This means that it is possible use voltage to detect and measure frost height with good accuracy. According to the authors further studies about the optimal disposition of the sensors and the drying-up time need to be carried out.
Despite the large number of works in literature, frost detection and defrost control logic optimization is still an open point in scientific and technical literature and there is lack of works on walk-in cold room types monoblock refrigeration about this matter.

Chapter 6 – Development of new method to define the optimal defrosting start time: experimental campaign, data analysis and assessment with commercial methods

In this chapter, the development of novel approach to determine the optimal defrost start time is presented. An experimental campaign on a prototype of monoblock refrigeration unit for walk-in cold rooms with different combinations of cold room temperature and relative humidity is carried out. Subsequently, a novel data reduction method to determine the optimal start defrost time is presented using the data collected in the first phase. Finally, the commercially available defrost control logics are assessed with the proposed method.

6.1 Commercial refrigeration unit prototype

The experimental campaign is carried out in Zanotti SpA in the same calorimetric chamber described in section 4.2.1., but with a smaller calibrated cold box which dimensions are listed in Table 6.1.

Table 6.1 –Calibrated box dimensions

Calibrated box			
	Length	**Width**	**Height**
	[mm]	*[mm]*	*[mm]*
External	1200	1200	2170
Internal	1000	1000	1970

The prototype used to carry out the experiments is a positive temperature commercial refrigeration monoblock unit manufactured by Zanotti SpA using R455A as refrigerant, equipped with microchannel condenser and tube and fins heat exchanger as evaporator, rotative compressor and thermostatic expansion valve. A commercial image and the photo took during the tests of the unit and its refrigeration schematic layout are shown in Figure 6.1. In Figure 6.1b the red-dotted lines refer to hot-gas bypass defrost line that is opened by means solenoid valve S, when the defrost is launched. The main characteristics of the prototype are listed in Table 6.2.

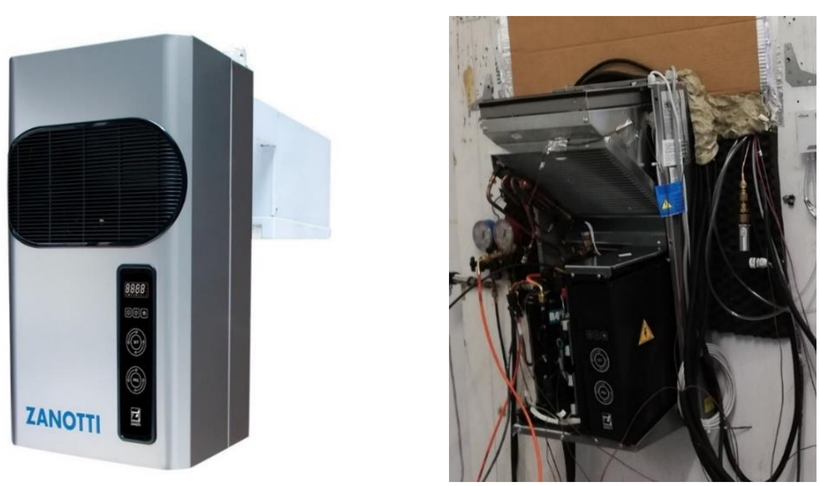

(a)

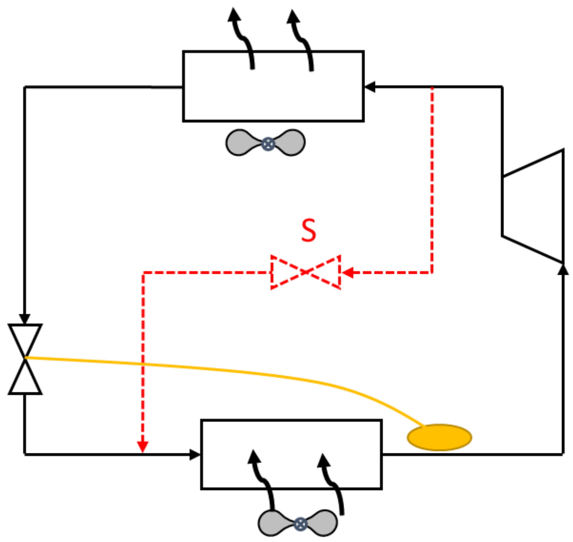

(b)

Figure 6.1 – Commercial image and photo during the test (a) refrigeration piping schematic layout (b) of the unit

Table 6.2 – Prototype characteristics

Compressor	
Type	Hermetic rotative
Displacement [cm^3]	16.4
Condenser	
Type and material	Microchannel /aluminium
Frontal area (Width × Height) [mm]	262 × 280
Fins (Height / Fin pitch) [mm]	8 / 2.8
Tube (Width × Height / Pitch) [mm]	21 × 2 / 10
Expansion device	
Thermostatic expansion valve	
Evaporator	
Type / material	Tube and fins / copper for tubes, aluminium for fins
Tube / Row pitch [mm]	25 / 25
Fin pitch [mm]	5
Tube external diameter [mm]	10
Row number	6
Tubes per row	10
Refrigerant	
Name	R455A
Refrigerant charge [kg]	0.5
Defrost type	Hot-gas bypass

6.2 Evaporator test section

As mentioned in the previous section, the evaporator of the prototype is a fin and coil heat exchanger, placed inside the calibrated box with 6 rows and 10 tubes per row having an external diameter of 10 mm. Its nominal capacity is 1.1 kW at 30 / 0°C ambient / cold room temperature.

The refrigerant and air flow paths on the evaporator form a cross-counter flow pattern, shown in schematic representation in Figure 6.2.

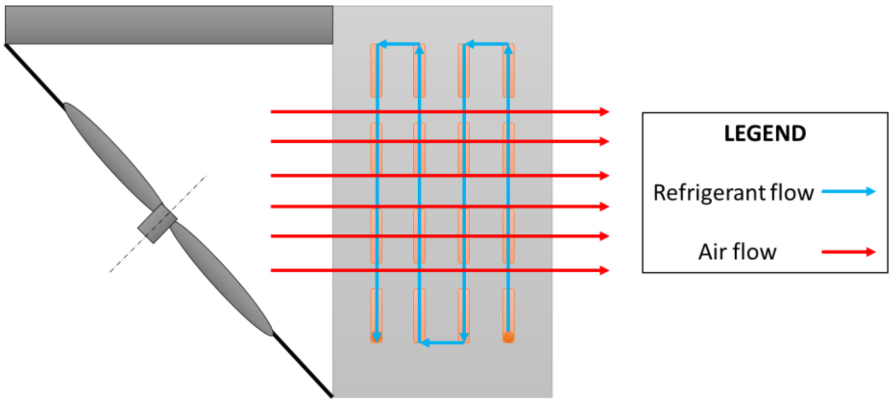

Figure 6.2 – Schematic representation of refrigerant (blue) and air flow (red) pattern

To visualize the frost formation in the air inlet section of evaporator surface during the tests, a hole is drilled and covered with Plexiglass and a camera is placed inside it as shown in Figure 6.3a. Moreover, to measure the air side pressure drops, small channels connected to a differential pressure transducer are installed as shown in Figure 6.3b. In addition, the air / frost temperature is measured in 12 points of the coil by means of two grids of 3 × 2 thermocouples placed according to the scheme represented in Figure 6.4; the first grid named “air inlet section” is placed at a depth of 14 cm, conversely, the second one “air outlet section” at a depth of 2 cm from the air outlet side.


(a)

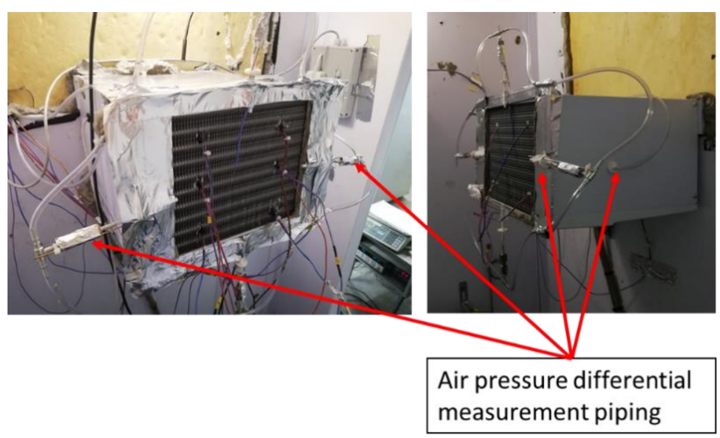

Figure 6.3 – Hole in evaporator side (a), channels to measure inlet and outlet air pressure (b)

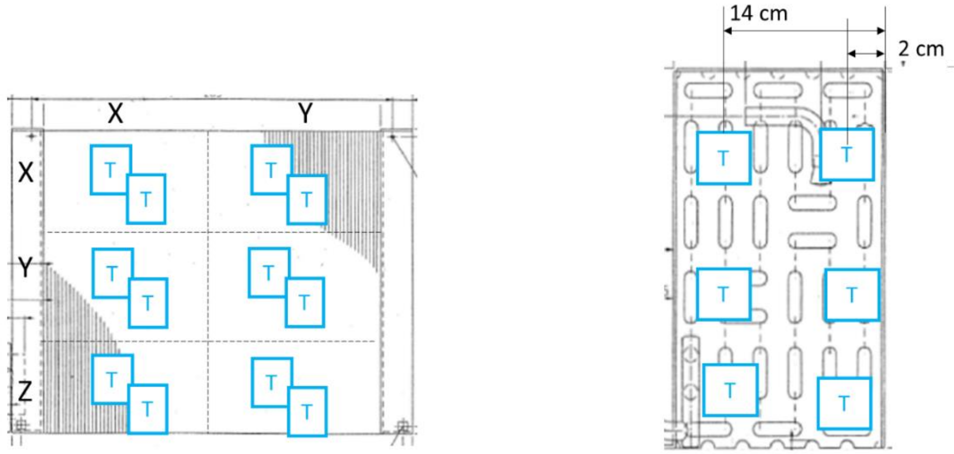

Figure 6.4 – Evaporator thermocouple grids layout

During a defrost cycle the solenoid valve S is opened and the refrigerant coming from compressor flows inside the evaporator heating the coil and melting the ice, then it returns to compressor.
The standard control board was substituted with another one equipped with on-demand defrost control logic from Ascon Technologic. The controller enables the defrost cycle basing on the increase of temperature difference between the calibrated box temperature and evaporator coil temperature (measured on the bottom side of evaporator surface $T_{zx,in}$ where the major amount of frost collects), compared to a reference value measured in the first on / off cycle. The defrost ends when a threshold of +15°C, measured with the same probe in $T_{zx,in}$ position, is reached. The on-demand defrost function is disabled during the tests where the prototype is operated until the evaporator is totally clogged by frost (round 1 tests).

6.3 Instrument and measurement uncertainties

In Figure 6.5, the schematic layout of sensors on the refrigeration piping and the installation scheme of the prototype inside the calibrated box. A humidifier constituted by an electrical heater immersed in demineralized water is used to keep and control humidity inside the calibrated box. Its capacity is regulated by means of solid-state relay connected to a PID and to the humidity sensor.
The air, refrigerant and coil temperatures are measured with the same T-type thermocouples used in the experimental campaign presented in the second part of Chapter 4, the pressures of the thermodynamic cycle are measured with 0 – 10 V pressure transducers having a calibration range of 0 – 30 bar for high pressure side and 0 – 10 bar for low pressure side. The air side pressure drop is measured with 0 – 10 V piezoresistive pressure transducer with calibration scale of 0 – 250 Pa. The electrical consumption of the whole prototype, the compressor and evaporator fan are measured with a power meter. The relative humidity is measured with 0 – 10 V output capacitive sensor. The temperature inside the calibrated cold box is regulated by the prototype itself during the tests. The thermocouples, pressure transducers, relative humidity and pressure differential sensors are connected to a datalogger connected to a PC where the data are visualised and saved. The water collected after the defrost cycle is weighed with a 0 - 30 kg scale. All the measurement instruments and its uncertainties are listed in Table 6.3.

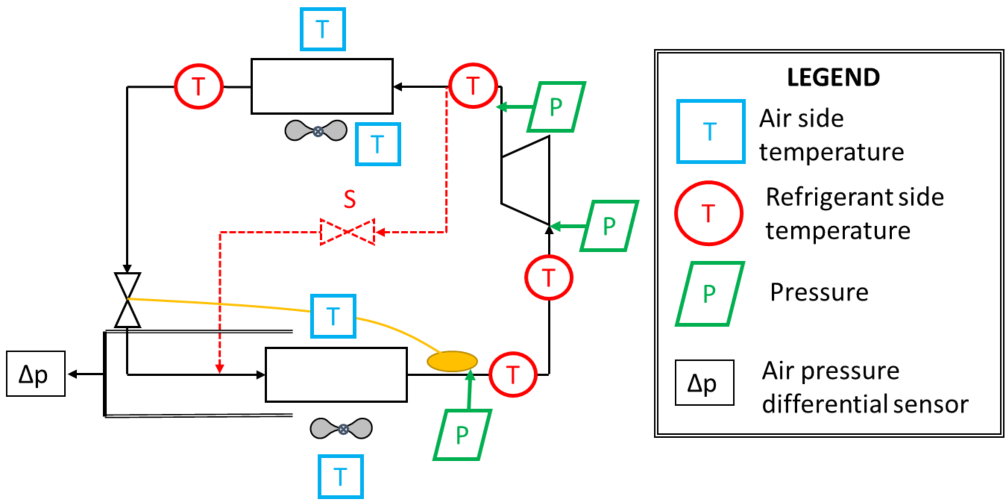

(a)

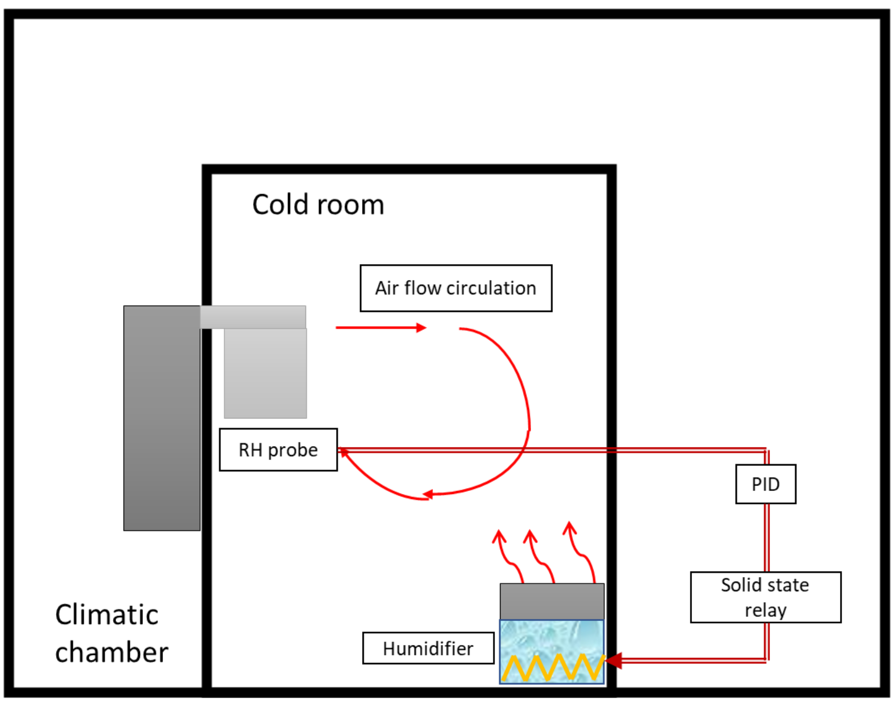

(b)

Figure 6.5 – Probe schematic layout (a), climatic chamber, calibrated box and humidifier control scheme (b)

Table 6.3 – Measurement instrument and uncertainties

Direct measurement	**Instrument**	**Calibration range**	**Uncertainty**
Temperature (air, refrigerant)	T-type thermocouple	-30°C to +90 °C	± 1.5K
Refrigerant high side pressure	0 – 10 V pressure transducer	0 – 30 bar	± 0.06 bar
Refrigerant low side pressure	0 – 10 V pressure transducer	0 – 10 bar	± 0.02 bar
Evaporator air side pressure drop	0 – 10 V piezoresistive transducer	0 – 250 Pa	1 % ±2 Pa
Total, compressor and evaporator fan power consumption	Power meter	0 – 975 V (voltage) 0 – 29 A (current)	0.5% W
Relative Humidity	0 – 10 V capacitive transducer	0 – 100 %	± (1.5+1.5% of the measure) % UR
Melted frost weight	Scale	0 – 30 kg	± 4 g

6.4 Test method

Two rounds of tests named “round 1” and “round 2” are carried out during the experimental campaign. In “round 1” tests the evaporator is fully frosted with a complete blockage of the airflow and the defrost is launched manually; instead, in “round 2” tests the on-demand defrost function is enabled according to the control logic.

The procedure employed in both rounds of tests is composed by three distinct phases:

1) Phase 1: preparation and stabilization
2) Phase 2: frost accumulation
3) Phase 3: defrosting

In Figure 6.6 ambient (inside calorimetric chamber) and calibrated box temperatures and relative humidity are shown together with the definition of the three phases of the test.

In phase 1, the calorimetric chamber is turned on with a set air temperature of 25°C, together with the prototype and the humidifier to reach the target temperature and relative humidity inside the calibrated box. The end of phase 1 depends on boundary conditions and it is judged when the ambient temperature fluctuations are within ± 0.5°C and the relative humidity fluctuations are within ± 5%. Then a manual defrost is operated to ensure that at the beginning of phase 2 the evaporator is free from frost; during manual defrost the humidifier and evaporator fan are off. After the defrost, the temperature inside the calibrated box is recovered with a smaller pulldown, then the phase 2 begins.

In the accumulation phase, the unit operates on / off cycles accumulating frost until the evaporator is stacked and the temperature at point $T_{ZX,\,in}$ of evaporator coil from Figure 6.4 is below -25°C. During this phase, the calorimetric chamber is on, the humidifier does on / off cycles depending on relative humidity value. During the off phase the relative humidity increases due to vapour stratification inside the calibrated box. Before operating the manual defrost a visual inspection of the outlet air section of the evaporator is carried out in each test.

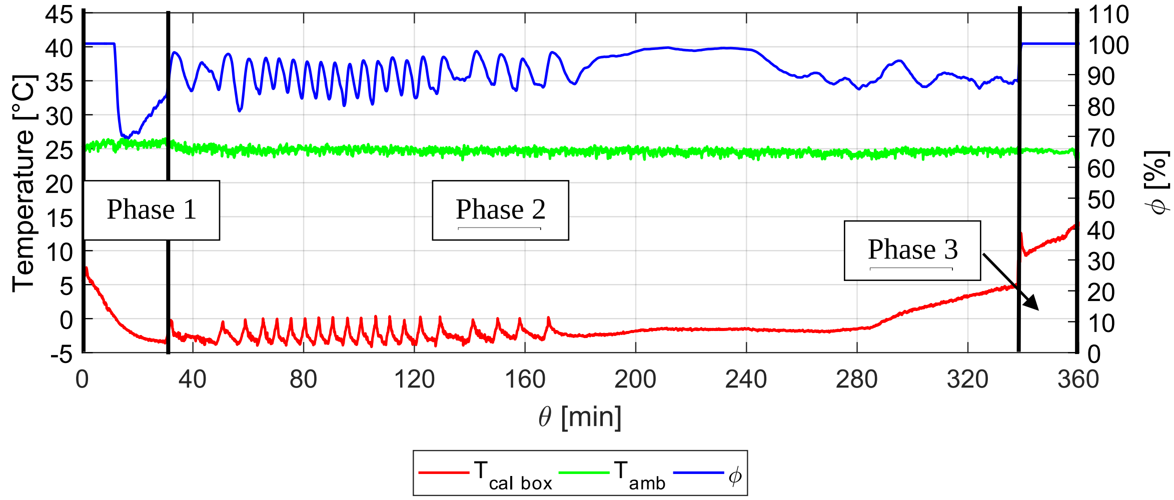

Figure 6.6 – Calorimetric chamber (T_{amb}), calorimeter box temperature ($T_{cal\ box}$) and relative humidity (ϕ) as a function of time for the different test phases in round 1 tests

In the last phase 3, the defrost is operated so the solenoid valve S opens, the evaporator fan and the humidifier are switched off; the defrost phase ends when the sensor placed at point $T_{ZX,\ in}$ of evaporator coil measures a temperature of +15°C. Subsequently, the acquisitions, the climatic chamber and the prototype are switched off and the defrost water is collected in a hermetically sealed tank that is weighed after 30 min and after 12h the test. Between the two weights a difference of less than 1% has been registered in all tests.

In the "round 2" tests the phase 1 is the same but phase 2 duration is smaller than in the first round since the controller operates an on-demand defrost when needed. This implies that more phases 2 and 3 are present in one test. The weighing of collected water is operated after 30 min of each defrost cycle as in the first round. In Figure 6.7, a trend of ambient, calibrated box temperatures and relative humidity are shown for the second round of tests during phases 2 and 3.

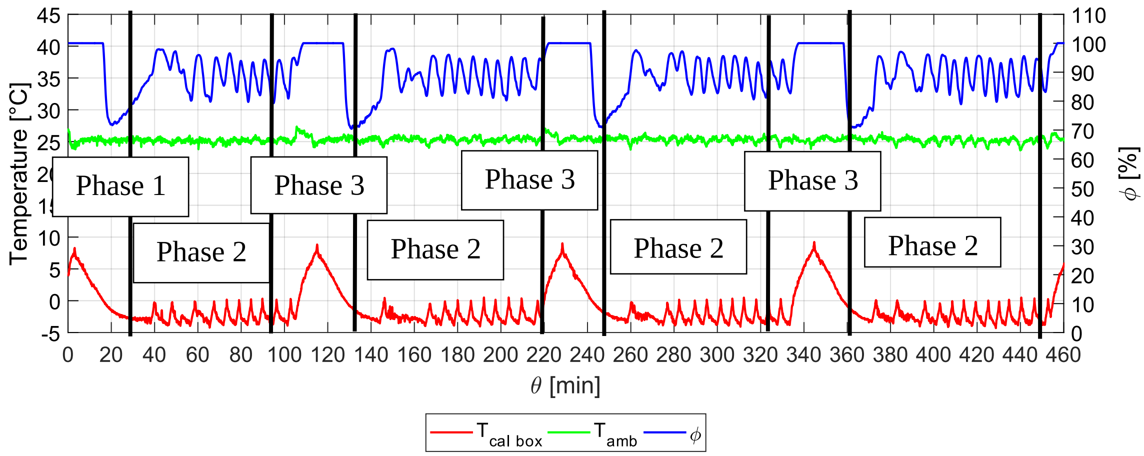

Figure 6.7 - Calorimetric chamber (T_{amb}), calorimeter box temperature ($T_{cal\ box}$) and relative humidity (ϕ) as a function of time for the different test phases in round 2 tests

In Table 6.4, a summary of operational state of each device during each phase of the test is presented.

Table 6.4 – Summary of operational state of devices in each phase of the tests (first round)

	Phase 1	**Phase 2**	**Phase 3**
Calorimetric chamber	*ON*	*ON*	*ON*
Compressor	*ON*	*ON / OFF*	*ON*
Evaporator fan	*ON*	*ON / OFF*	*OFF*
Humidifier	*ON*	*ON / OFF*	*OFF*

6.5 Test condition and results

During the experimental campaign, 9 combinations of calorimeter box temperature and relative humidity are tested in "round 1" and "round 2" tests while the calorimetric chamber temperature is set at 25°C in all tests. The tested combinations are listed in Table 6.5 in sense of increasing initial specific humidity difference $\Delta\omega$ [$g_w\ kg_a^{-1}$], defined in Eq. 6.1.

$$\Delta\omega = \omega_{cal\ box} - \omega_{ev} \qquad \text{Eq. 6.1}$$

It is the driving force of frost formation between the calorimetric box air stream ($\omega_{cal\ box}$) and the evaporator surface saturation (ω_{ev}) specific humidity.

Table 6.5 – Test condition summary

#	$T_{cal\ box}$	ϕ	$\Delta\omega$
	[°C]	[%]	[$g_w\ kg_a^{-1}$]
1	-2	70	0.60
2	2	70	0.81
3	-2	80	0.86
4	-4	80	0.86
5	0	80	0.91
6	-4	90	1.09
7	-2	90	1.17
8	2	90	1.19
9	0	90	1.27

$\omega_{cal\ box}$ and ω_{ev} are evaluated as follows:

$$\omega = 0.622\frac{\phi * p_{vs}}{p_t - \phi * p_{vs}} \qquad \text{Eq. 6.2}$$

$$\omega_{cal\ box} = f(T_{cal\ box}, \phi) \qquad \text{Eq. 6.3}$$

$$\omega_{ev} = f(T_{ev,dew}, \phi = 100\%) \qquad \text{Eq. 6.4}$$

In Eq. 6.2 p_t and p_{vs} are the total pressure equal to 101325 Pa and water saturation pressure at air temperature. In Eqs. 6.2, 6.3 and 6.4 ϕ is the measured relative humidity [%], $T_{ev,dew}$ [°C] is the refrigerant dew point saturation temperature at evaporator pressure. All the results will be presented in terms of $\Delta\omega$.

In Figure 6.8 calibrated box temperature and dew point evaporating temperature for tests with $\Delta\omega$ = 0.81 $g_w\ kg_a^{-1}$ and $\Delta\omega$ = 1.27 $g_w\ kg_a^{-1}$ are depicted.

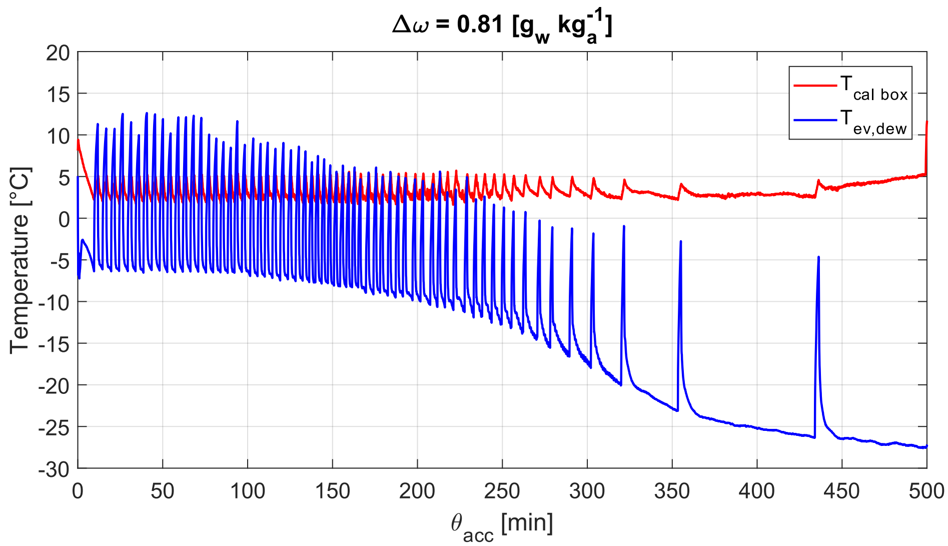

(a)

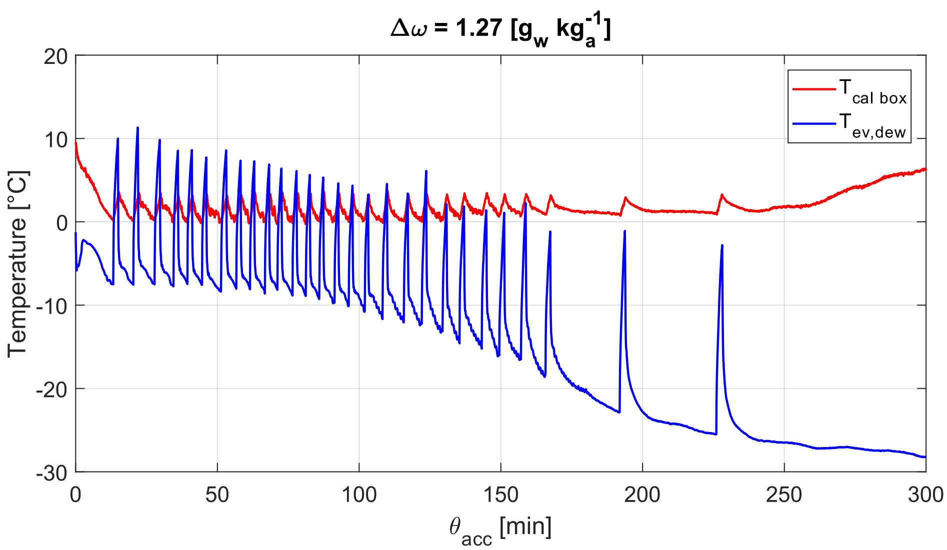

(b)

Figure 6.8 – Calibrated box and evaporating temperature as a function of time (phase 2) for tests at $\Delta\omega$ = 0.81 g_w kg_a^{-1} (a) and 1.27 g_w kg_a^{-1} (b)

In both tests the evaporating temperature decreases during the accumulation phase, this is due to the reduction of air flow rate across the evaporator with reduction of heat transferred with refrigerant. This effect leads a reduction of useful superheat and the subsequent valve closing to reach target value in the new operating condition. The rate of frost formation is directly related to the pushing force $\Delta\omega$; in fact, higher value of $\Delta\omega$ leads faster frost formation rate and evaporating temperature reduction as shown in Figure 6.8. In this latter, in case $\Delta\omega$ = 0.81 g_w kg_a^{-1} the evaporating temperature reaches -25°C after 400 min, instead, the same value is reached after 220 min in case $\Delta\omega$ = 1.27 g_w kg_a^{-1}.
The formation rate is also checked visually analysing the evolution of frost growth on air section inlet of evaporator frontal area represented in Figure 6.9.

θ [min]

$\Delta\omega = 0.81$ [$g_w\ kg_a^{-1}$]

$\Delta\omega = 1.27$ [$g_w\ kg_a^{-1}$]

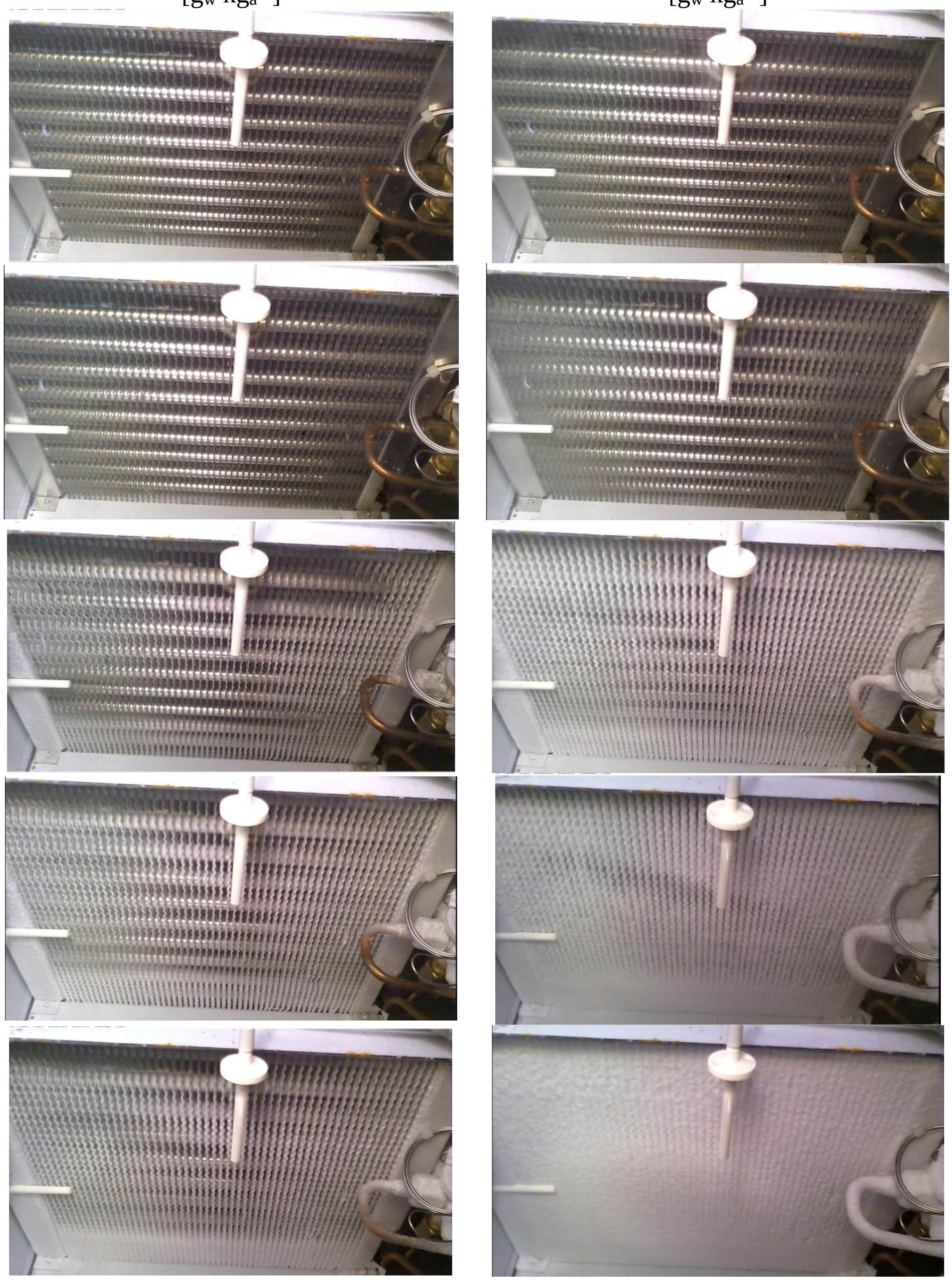

0

60

180

240

300

500	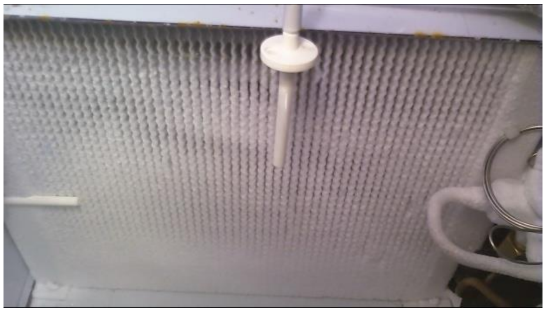	Phase 2 stopped

Figure 6.9 – Frost growth on air inlet section of evaporator frontal area for tests at $\Delta\omega$ = 0.81 g_w kg_a^{-1} and 1.27 g_w kg_a^{-1}

Zero minutes is referred to the beginning of phase 2, in this moment the evaporator surface is free from frost and clean; the unit works as it is in nominal condition. After 60 minutes, the evaporator begins to be covered by a high number of very small water droplets in test with $\Delta\omega$ = 1.27 g_w kg_a^{-1}, in fact the evaporator appears "whiter" than in the previous time step; conversely, in test with $\Delta\omega$ = 0.81 g_w kg_a^{-1}, the evaporator appears still clean. After 180 minutes, the evaporating temperatures is dropped for both tests respect to their initial value and the evaporator is covered by a higher amount of ice in test $\Delta\omega$ = 1.27 g_w kg_a^{-1} than the case with $\Delta\omega$ = 0.81 g_w kg_a^{-1}. In this latter, the frost is not homogeneous on evaporator surface, in fact portions free or poor of frost are visible; instead, for test with higher $\Delta\omega$, the frost covers all the surface with a higher amount on the bottom side. This distribution is caused by the deposition and falling of water droplets from the upper to the bottom side with frost densification and thickness growth in this region. The same behaviour is shown in the test with lower $\Delta\omega$ after 240 min. During the tests, the frost covers the entire surface of evaporator going from the bottom to the upper side with the blockage of air flow path after 500 min and 300 min for test at $\Delta\omega$ = 0.81 g_w kg_a^{-1} and 1.27 g_w kg_a^{-1}, respectively.

The evaporator coil temperatures measured in these two tests are shown in Figure 6.10.

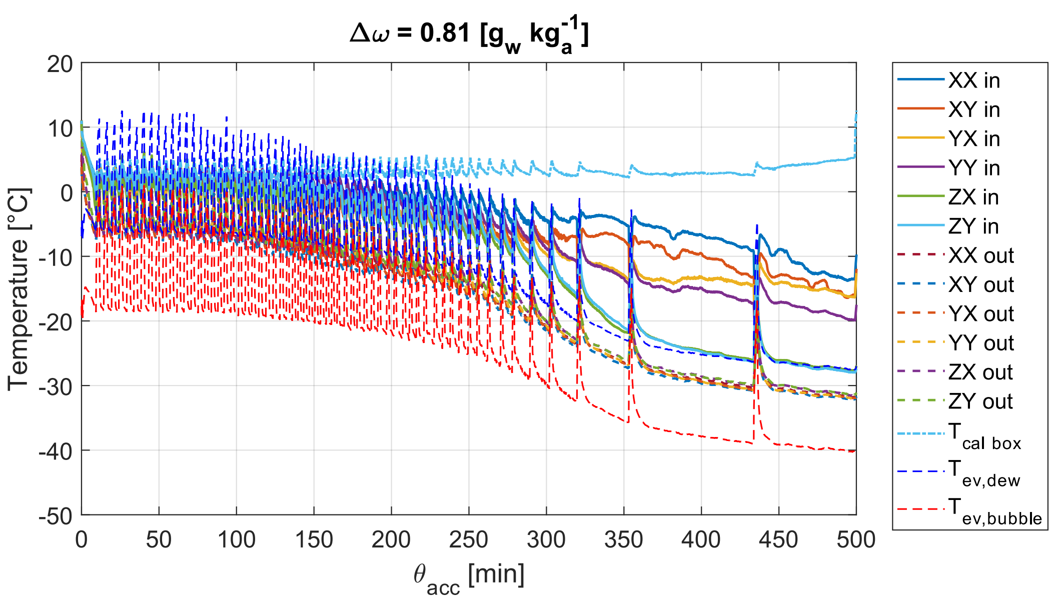

(a)

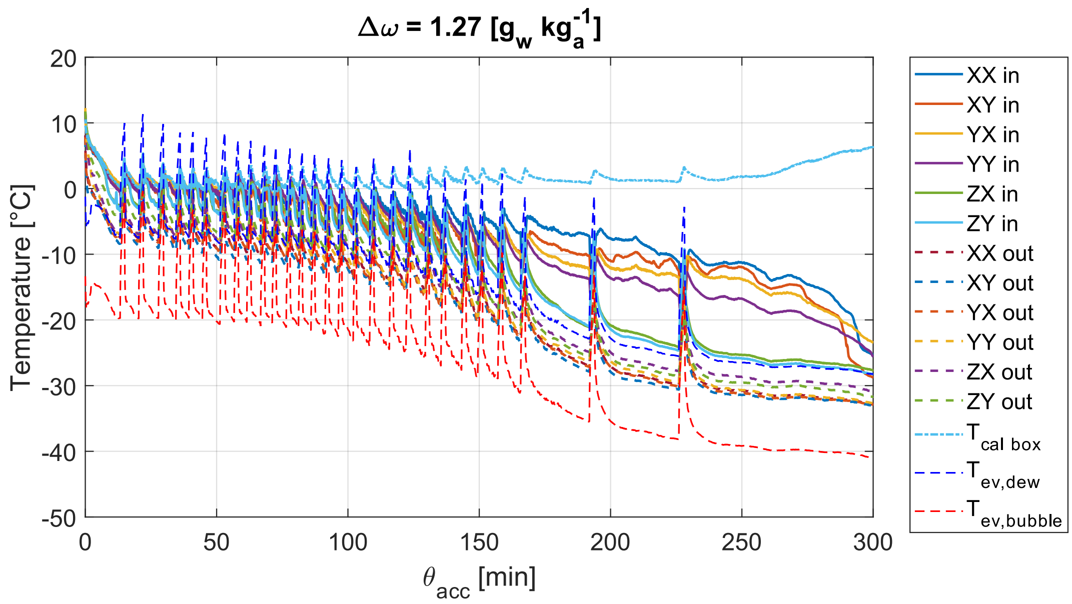

(b)

Figure 6.10 – Calibrated box, coils and evaporating temperature as a function of time (phase 2) for tests at $\Delta\omega$ = 0.81 g_w kg_a^{-1} (a) and 1.27 g_w kg_a^{-1} (b)

In both tests, the coil temperatures are measured at the inlet and outlet section; when the evaporator is free from frost, they measure the air temperature in six points at inlet (subscript "in") and outlet (subscript "out") side, for this reason the temperatures measured with the first six thermocouples are higher than the others. During the tests, the frost grows up covering the thermocouple and the measured temperatures are closer to the evaporator one due to heat conduction from thermocouple to fins through frost that probably has higher conductivity in the bottom side thanks to the densification phenomenon described above. In fact, the temperatures $T_{ZX,\,in}$ and $T_{ZY,\,in}$ are the closest to the dew point saturation temperature considering the inlet evaporator section.

In all tests, the reduction of evaporating pressure causes the reduction of condensing one with fixed calorimetric chamber temperature, this effect leads to a reduction of compressor power consumption as shown in Figure 6.11 for case at $\Delta\omega$ = 0.81 g_w kg_a^{-1}.

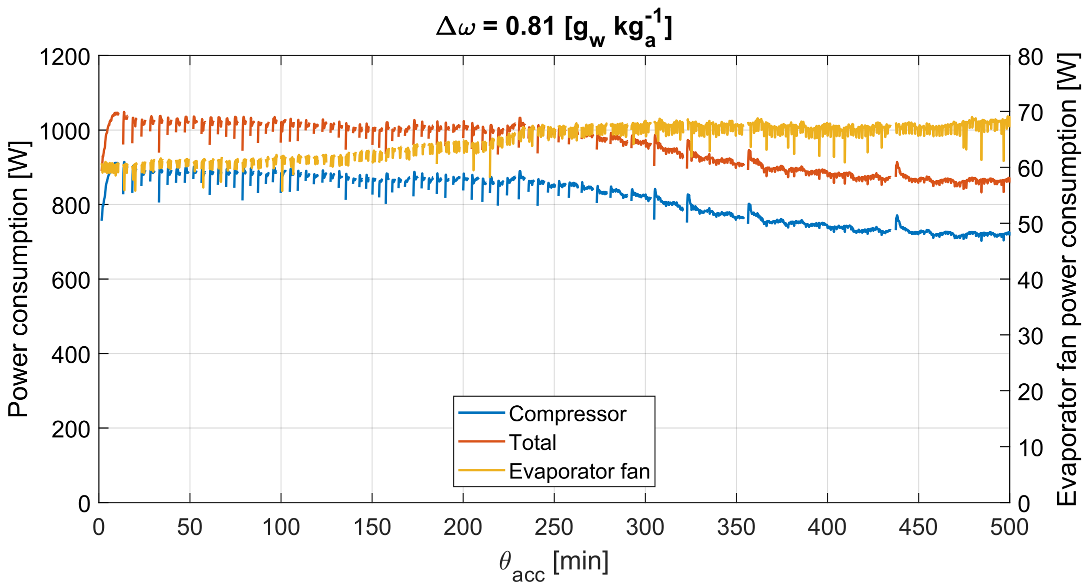

Figure 6.11 – Total, compressor and evaporator fan power consumption as a function of time for test at $\Delta\omega = 0.81\ g_w\ kg_a^{-1}$

The power consumption of evaporator fan has opposite trend than compressor one. This is mainly due to the increase of air side pressure drops through the evaporator which effect is predominant on volumetric air flow rate reduction. The same trends of evaporator fan power consumption and evaporator air side pressure drop, represented in Figure 6.12, corroborates this outcome.

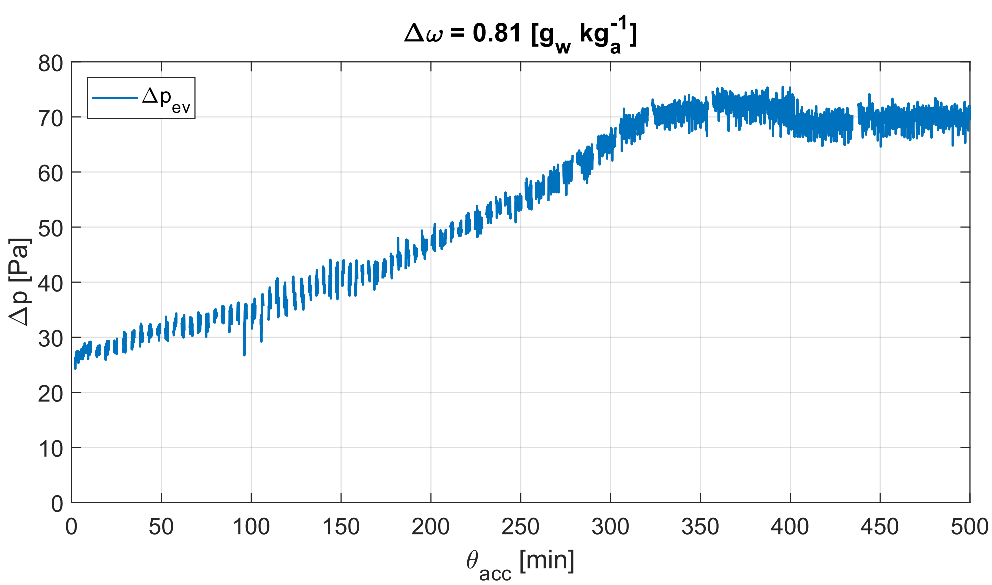

Figure 6.12 – Evaporator air pressure drop as a function of time for test at $\Delta\omega = 0.81\ g_w\ kg_a^{-1}$

The empty spaces in Figure 6.11 and Figure 6.12 refer to the off mode, in which the measurement for all parameters is 0.
The reduction of evaporating pressure causes a reduction of cooling capacity of the prototype that needs more operational time to maintain the calibrated cold box temperature at target value. This is shown in Figure 6.13 where the compressor on-time in each on / off cycle (τ_{ON}) is depicted as a function of accumulation time.

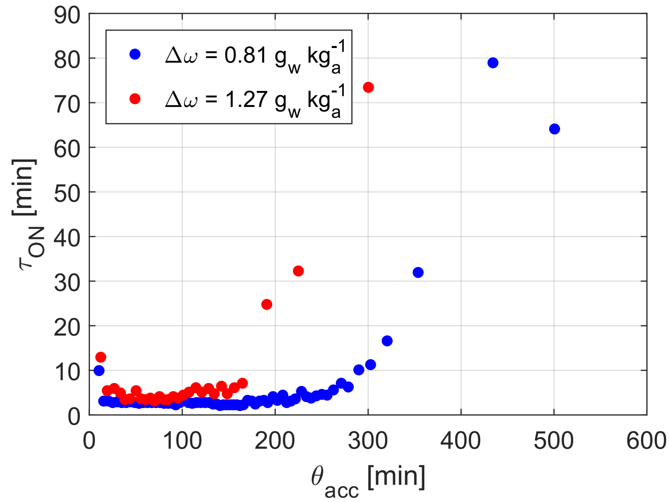

Figure 6.13 – Compressor on-time as a function of accumulation time for test at $\Delta\omega$ = 0.81 g_w kg_a^{-1}

The first red and blue points, refer to pulldown phase to recover the calibrated box temperature after phase 1. During the accumulation phase with the evaporator free from frost τ_{ON} is around 2.5 minutes with $\Delta\omega$ = 0.81 g_w kg_a^{-1} and around 5 minutes for $\Delta\omega$ = 1.27 g_w kg_a^{-1}. During the frost formation τ_{ON} increases up to 72 and 80 minutes at $\Delta\omega$ = 0.81 g_w kg_a^{-1} and $\Delta\omega$ = 1.27 g_w kg_a^{-1}, respectively. The last blue point at 500 min has lower compressor time than the previous time step due to the manual defrost activation.
In “round 1” tests the defrost is manually operated as described in section 6.4. During the defrost (phase 3) the hot refrigerant from compressor enters in the evaporator heating the metal and melting the ice. This phenomenon is shown in Figure 6.14, where the coil temperatures are depicted during the defrost phase for test with $\Delta\omega$ = 0.81 g_w kg_a^{-1}. The measurements are representative of the frost temperature since it completely covers the thermocouples during phase 2.

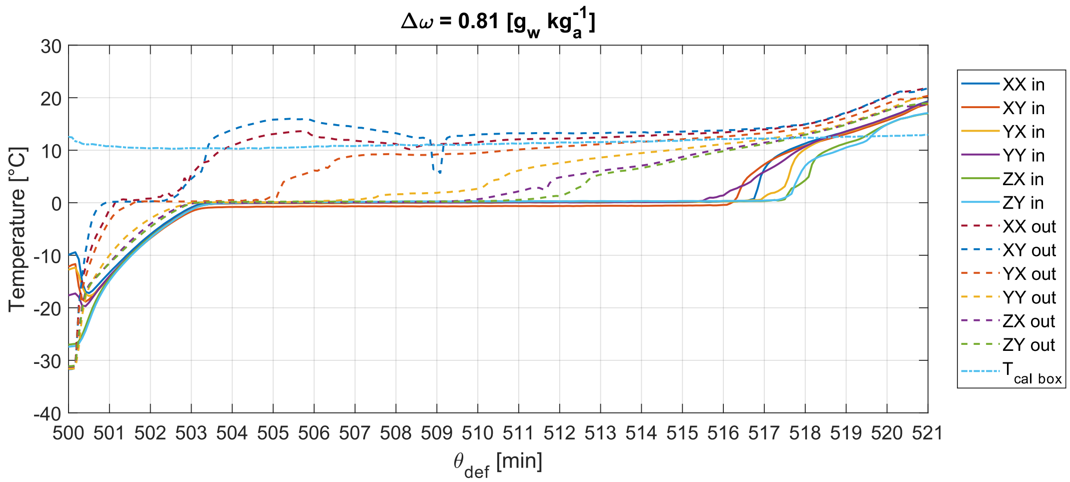

Figure 6.14 – Evaporator coil temperatures as a function of time during defrost (phase 3) for tests at $\Delta\omega = 0.81\ g_w\ kg_a^{-1}$

Initially, the frost temperature increases from negative values around -20°C / -30°C, up to melting point at 0°C. The length of melting phase depends on the amount and thermal conductivity of ice collected in the first layers, with higher amount of ice the duration of melting phase increases. For both air inlet and outlet section of evaporator, the highest amount of ice is collected on the bottom side and the duration of melting phase decreases going from bottom to upper side of surface. The highest amount of ice is collected in the evaporator air inlet section due to higher specific humidity of the air during phase 2.
In Figure 6.15, the power consumption of prototype is shown during the defrost phase. The small differences between the total and compressor power consumption are due to solenoid valve and electronic board power consumption, since evaporator and condenser fans are off.
During the defrost cycle, the power consumption is mainly constant approximately to 500W for the most part of defrost duration.

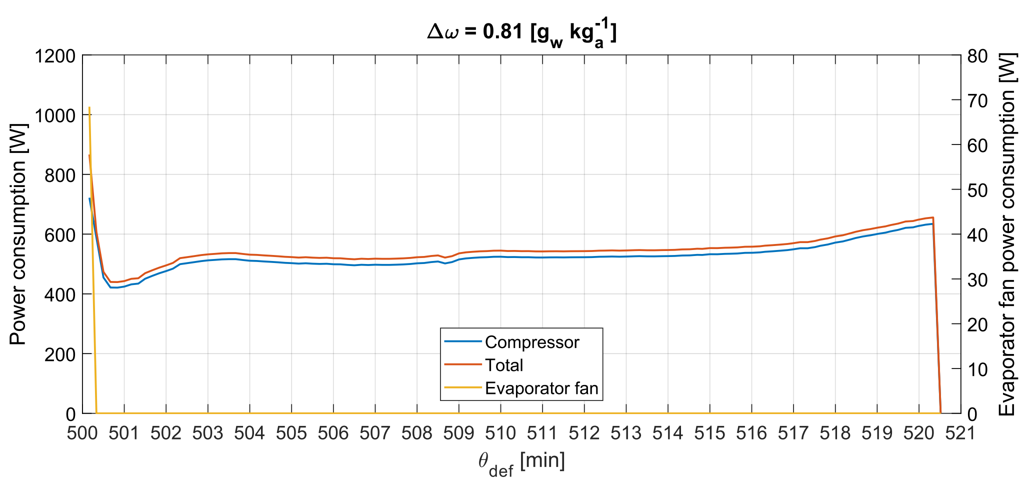

Figure 6.15 – Total, compressor and evaporator fan as a function of time during defrost (phase 3) for test at $\Delta\omega = 0.81\ g_w\ kg_a^{-1}$

At the end of each defrost cycle, in "round 1" and "round 2" tests, the melted ice is collected in a hermetically sealed tank and weighted following the procedure described above. In Figure 6.16 the measured mass of collected water is shown as a function of each respective accumulation time that goes from start to the end of phase 2 ($\Delta\theta_{acc}$).

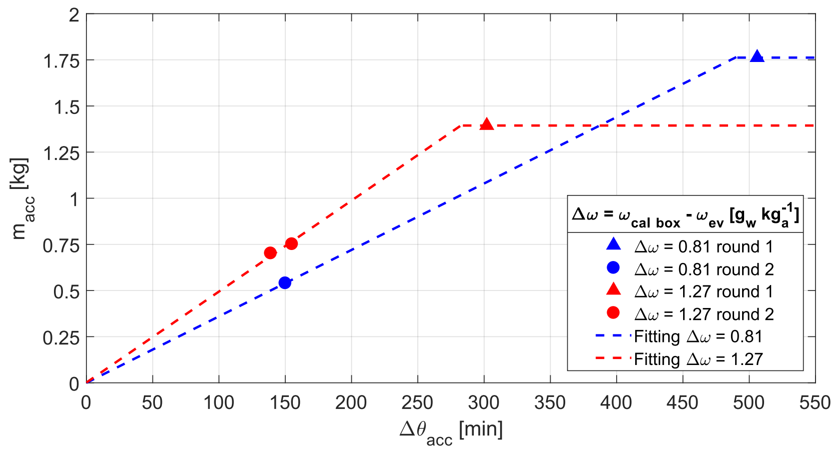

Figure 6.16 – Measured collected water mass as a function of accumulation time in tests at $\Delta\omega = 0.81$ $g_w\ kg_a^{-1}$ (a) and 1.27 $g_w\ kg_a^{-1}$ (b)

The triangles represent the water mass measured in "round 1" tests, the circles the ones measured in "round 2" tests and the dotted line the fitting of trends found with the measurements. The measurements form a linear trend with accumulation time up to a limit value, measured in "round 1" tests. The same behavior was also found by Da Silva et al. (2010) (2012), Guo et al. (2008) and Datta et al. (1998). The limit value of the weight is influenced by the geometry of evaporator and the boundary conditions of the tests that affect the frost growth rate and its geometry. Similar trends of measured parameters during phases 2 and 3 are found in all "round 1" and "round 2" tests.

In Table 6.6, the parameters of calibrated box temperature, relative humidity, initial specific humidity difference, weight of collected frost, number of compressor on / off cycles, duration of phase 2 ($\Delta\theta_{acc}$) and phase 3 ($\Delta\theta_{def}$) and average power consumption in accumulation and defrost phase are listed. Round 1 test are bolded and have asterisk on accumulation time.

Table 6.6 – Summary of principal parameters measured during the tests

$T_{cal\ box}$	ϕ	$\Delta\omega$	m_{acc}	N duty cycles	$\Delta\theta_{acc}$	$\Delta\theta_{def}$	$P_{avg,comp}$	$P_{avg,ev\ fan}$	$P_{avg,\ def}$
[°C]	*[%]*	*[$g_w\ kg_a^{-1}$]*	*[kg]*	*[-]*	*[min]*	*[min]*	*[W]*	*[W]*	*[W]*
-2	70	0.6	0.644	46	252	8	535	39	540
-2	70		0.902	60	310	10	587	42	544
-2	**70**		**1.402**	**72**	**568***	**19**	**554**	**43**	**531**
2	70	0.81	0.42	19	95	4	561	38	582
2	70		0.54	33	150	6	568	40	566
2	**70**		**1.76**	**52**	**502***	**20**	**575**	**42**	**543**
-2	80	0.86	0.66	21	147	9	616	44	501
-2	80		0.64	22	151	8	620	45	540
-2	80		0.7	24	160	8,6	614	44	543
-2	**80**		**1.258**	**38**	**393***	**15**	**580**	**44**	**502**
-4	80	0.86	0.48	8	100	6,5	688	49	556
-4	80		0.74	24	179	9	647	48	545
-4	80		0.81	29	213	10,5	642	48	543
-4	**80**		**1.32**	**41**	**433***	**17**	**607**	**47**	**545**
0	80	0.91	0.906	40	215	10	510	38	533
0	80		0.946	35	196	9	514	39	544
0	**80**		**1.474**	**52**	**427***	**18**	**564**	**43**	**531**
-4	90	1.09	0.62	10	100	7,5	712	52	548
-4	90		0.602	10	103	7,2	724	53	558
-4	90		0.602	11	104	7,8	693	50	544
-4	90		0.602	13	109	7,7	699	50	545
-4	**90**		**1.362**	**20**	**338***	**19**	**660**	**51**	**518**
-2	90	1.17	1.03	24	140	8	606	43	550
-2	90		0.872	34	190	12	600	45	540
-2	**90**		**1.258**	**43**	**340***	**19**	**580**	**46**	**519**
2	90	1.19	0.624	20	108	7,5	595	40	532
2	90		0.822	22	142	10	656	44	532
2	90		1.014	34	185	12	593	44	548
2	**90**		**1.68**	**41**	**350***	**20**	**610**	**43**	**515**
0	90	1.27	0.736	15	86	8	601	41	548
0	90		0.752	31	155	11	569	41	531
0	90		0.702	29	139	9	555	41	544
0	**90**		**1.394**	**28**	**305***	**18**	**691**	**51**	**518**

6.6 Optimization strategy and comparison with current technology

In this section, the results of "round 1" tests are analysed to define a procedure able to find the optimum accumulation time $\Delta\theta_{acc}$, phase 2 with the main targets of minimizing the total electric energy consumption and, at the same time, the number of hourly on / off compressor duty cycles to preserve its lifespan using the capacity ratio index, CR. This latter is constrained with the definition of a maximum value in order to guarantee that the refrigerator has enough capacity to cover the cooling demand in case of doors opening or other additional loads.
The total electric energy consumption is minimized by means the minimization of total average electric power consumption defined as follows:

$$\bar{P}_{tot\ avg} = \frac{\int_0^{\Delta\theta_{acc}} \bar{P}_{acc} \cdot d\theta + \bar{P}_{def} \cdot \Delta\theta_{def}}{\Delta\theta_{acc} + \Delta\theta_{def}} \qquad \text{Eq. 6.5}$$

Where $\bar{P}_{acc}$ [W] is the average value of total power consumption during on / off cycles in accumulation phase from the beginning of phase 2 to the actual value of accumulation time $\Delta\theta_{acc}$. This latter is the independent variable of the problem in the evaluation process. The power $\bar{P}_{def}$ is defined in the same way, it is evaluated from the beginning of phase 3 up to the total duration of defrost time $\Delta\theta_{def}$. $\bar{P}_{def}$ is considered constant during the whole phase 3 according to Figure 6.15, instead, $\Delta\theta_{def}$ is function of $\Delta\theta_{acc}$ through the amount of accumulated frost as shown in Figure 6.17.

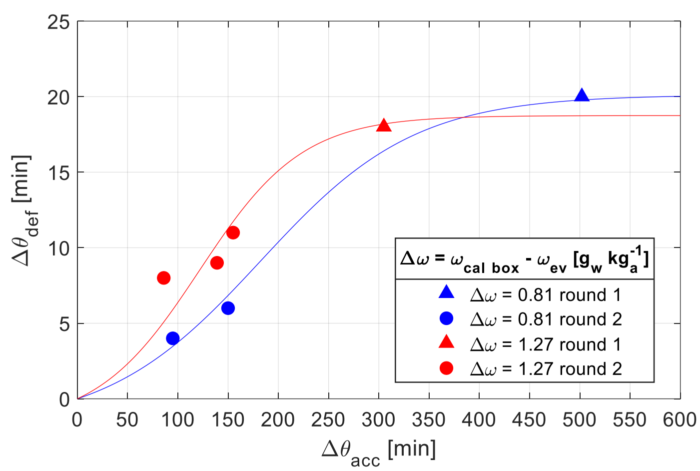

Figure 6.17 – Defrost duration $\Delta\theta_{def}$ as a function of accumulation time $\Delta\theta_{acc}$ at $\Delta\omega$ = 0.81 $g_w\ kg_a^{-1}$ (a) and 1.27 $g_w\ kg_a^{-1}$ (b)

The trends reflect the ones of measured water mass weight, with a limit value found in round 1 tests. To calculate the total average power consumption, a sigmoidal function that fits the experimental data points is used to calculate $\Delta\theta_{def}$ as a function of $\Delta\theta_{acc}$. The slope of the points and the fitted function increases with $\Delta\omega$ value since more mass of frost is accumulated on the evaporator surface at higher rate. After putting all the parameters as a function of accumulation time, the total average power consumption is evaluated for all values of $\Delta\omega$ and the trends are shown in Figure 6.18.

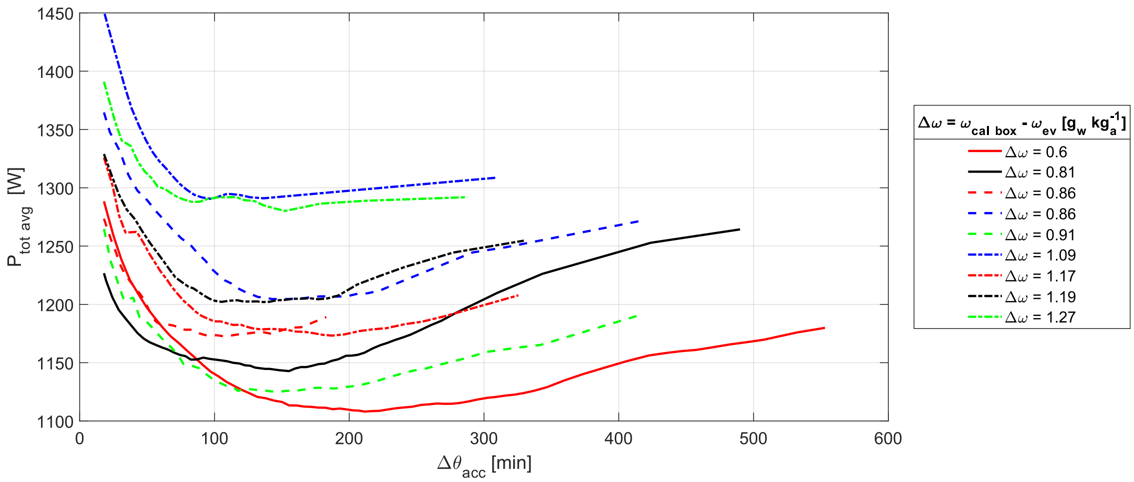

Figure 6.18 – Total average electric power consumption as a function of accumulation time for each operating condition Δω

Depending on the conditions, at the beginning of the phase 2 the total power consumption is high and then decreases; the whole trend can present a minimum value or a plateau. In all conditions, the difference between the maximum and minimum values of total average electric power consumption is relatively small, for instance in test with $\Delta\omega$ = 0.81 $g_w\ kg_a^{-1}$ this difference is less than 120 W (approximately 10% in this case). Since these little differences in power consumption trend, also the compressor on / off hourly duty cycles to be minimized are considered in the definition of optimal phase 2 duration.
This latter and the capacity ratio CR are defined as follows:

$$CR = \frac{\tau_{on}}{\tau_{on}+\tau_{off}} \qquad \text{Eq. 6.6}$$

$$\overline{N}_{duty-cycle/\,1h} = \frac{N_{duty-cycle}}{\sum_{i=1}^{N_{duty-cycle}}(\tau_{on}+\tau_{off})} \qquad \text{Eq. 6.7}$$

The CR index is evaluated by measuring the compressor on and off times τ_{on} and τ_{off}, respectively, instead the hourly on / off duty cycles, averaging the operation cycle time during phase 2. The trends of CR and average hourly on / off duty cycle number are reported in Figure 6.19 for the test with $\Delta\omega$ = 0.81 $g_w\ kg_a^{-1}$.
At the beginning of phase 2, the hourly on / off duty cycle number decreases sharply reaching a nearly constant value for a certain accumulation time interval, finally it continues to decrease as the frost builds up on the evaporator and the refrigerator requires more time to control the temperature. At the same time the CR increases during phase 2, up close to 1 since τ_{off} tends to 0. From one side, it is beneficial have the minimum value of hourly on / off cycles but on the other side the increase of CR has a negative effect since it means a reduction of cooling capacity and the impossibility for the refrigerator to cope with unexpected loads (e.g., frequent door opening, high food transpiration). For this reason, it should be sufficiently low and limited at a maximum threshold value decided basing on the application. Moreover, in Figure 6.19 the hourly on / off duty cycles are nearly constant in a large interval of accumulation time,

even the average power consumption shows less variations, conversely the CR vary significantly. In fact, considering an interval of accumulation time between 50 and 250 minutes, the total average power consumption ranges from 1143 to 1175 W, the number of hourly on / off cycles between 13 and 14, instead CR index vary from 0.57 and 0.75.

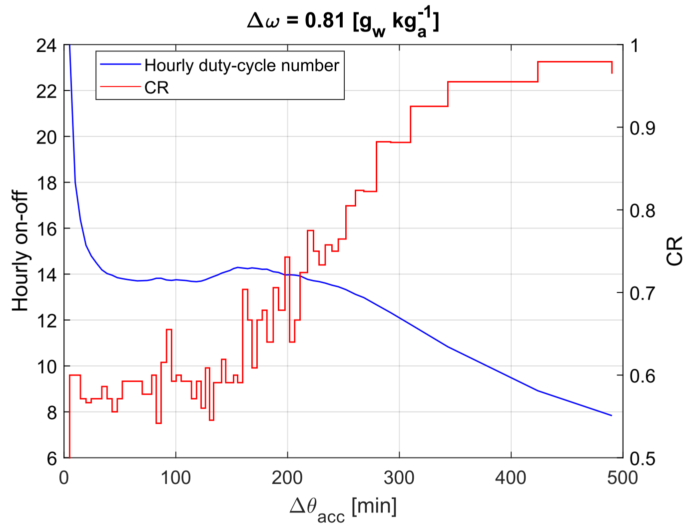

Figure 6.19 – Average hourly on / off duty cycle number and capacity ratio as a function of accumulation time for the test with $\Delta\omega$ = 0.81 $g_w\,kg_a^{-1}$

The same procedure is applied for all operating conditions, obtaining similar results that are listed in Table 6.7 where the ranges of hourly on / off cycles, total average power consumption, CR values, defrosting duration and accumulated frost are reported. In any operating condition the variation of average total power consumption and on / off cycles are limited and close to their minimum value even for accumulation interval higher than 3 hours. For this specific application it is possible assume a threshold value of CR index of 0.70. Reducing the CR value threshold, the determination of optimal accumulation time becomes difficult since the accumulation interval will be more restricted.

Table 6.7 - Ranges of hourly on / off cycles, total average energy consumption, CR index, defrosting period and accumulated frost mass for each operating condition within a wide range of accumulation time.

$T_{cal\ box}$	ϕ	Δω	Range $\Delta\theta_{acc}$	Range $\bar{N}_{duty-cycle/\,1h}$	Range $\bar{P}_{tot,avg}$	Range CR	Range $\Delta\theta_{def}$	Range m_{acc}
[°C]	[%]	[$g_w\ kg_a^{-1}$]	[min]	[1/h]	[W]	[%]	[min]	[kg]
-2	70	0.60	50 - 340	10 - 11	1127 - 1200	0.6 – 0.76	1.7 – 11.4	0.13 – 0.94
2	70	0.81	50 - 250	13 - 14	1143 - 1175	0.57 – 0.75	2 - 10	0.18 – 0.9
-2	80	0.86	50 - 113	17 – 18	1174 - 1200	0.625 – 0.75	2 – 4	0.22 – 0.5
-4	80	0.86	50 - 250	9 – 10	1226 - 1290	0.6 – 0.8	2 – 9.8	0.22 - 1
0	80	0.91	50 – 250	11 – 12	1144 - 1185	0.65 – 0.8	2.1 – 10.5	0.23 – 1.12
-4	90	1.09	50 – 200	7 - 9	1300 - 1340	0.68 – 0.85	2.8 – 11.2	0.29 – 1.16
-2	90	1.17	50 – 250	10 – 11	1185 - 1245	0.65 – 0.82	2.8 – 14	0.3 – 1.41
2	90	1.19	50 - 250	10 – 11	1235 - 1260	0.6 – 0.9	2.9 – 14.3	0.29 – 1.4
0	90	1.27	50 – 175	9 – 11	1287 - 1313	0.65 – 0.8	3 – 10.3	0.25 – 0.86

The average hourly on / off cycles don't not vary much with CR index as shown in Figure 6.20. Conversely, the length of error bars is not negligible and they depend by different operating conditions. For instance, for CR index equal to 0.70 the average hourly on / off cycles vary from 7 ($T_{cal\ box}$ = -4°C and ϕ = 90%) to 18 ($T_{cal\ box}$ = -2°C and ϕ = 80%).

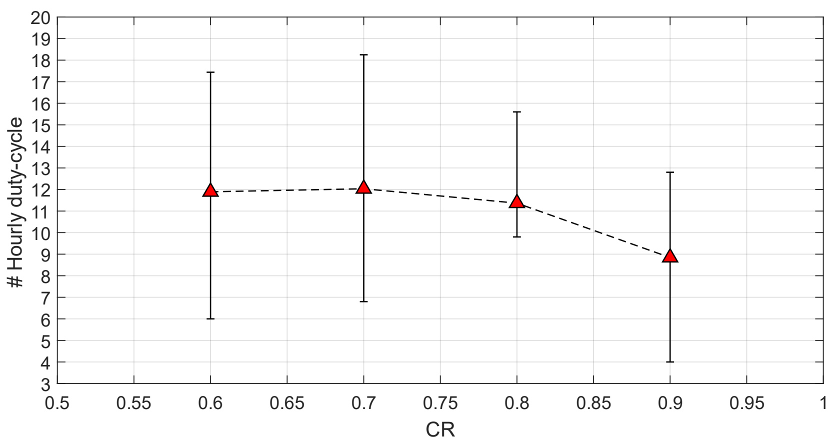

Figure 6.20 – Hourly duty-cycle numbers as a function of fixed threshold of CR index. The markers refer to average value, the error bands to on / off cycles variation within the tested conditions

Finally, the proposed evaluation method is used to assess the conventional system used to trigger the defrost phase. The operation principle of these systems is based on set time interval or on a threshold value of temperature difference between refrigerant and air, or on a threshold value of air pressure drop across the evaporator. In Figure 6.21 the CR index and hourly duty cycle trends for different value of temperature difference between air and refrigerant (a and b) and evaporator air pressure drop (c and d) are shown to evaluate the effectiveness of these systems with the regards of hourly on / off compressor cycles and CR index. In both cases, CR index increases with *ΔT* and *Δp* since the unit is left in operation and the frost accumulates on evaporator, leading a decrease of capacity that must balance the cooling demand in more time. For the same reason hourly duty cycles number decreases. Considering a fixed value *ΔT* or *Δp* (as threshold values for defrost triggering system) a not negligible variation of CR index and hourly duty cycle number, showed by the error bands, are noticed within the different tested operating conditions. This means that, the actual defrosting strategies could minimize the overall energy consumption, but they may not lead to an optimized CR value and hourly duty cycle. In fact, the first could overcome its design value or be too restrictive according to the cold room conditions of temperature and humidity values; instead, the second one would be too high in some operating conditions leading a reduction of compressor lifespan.

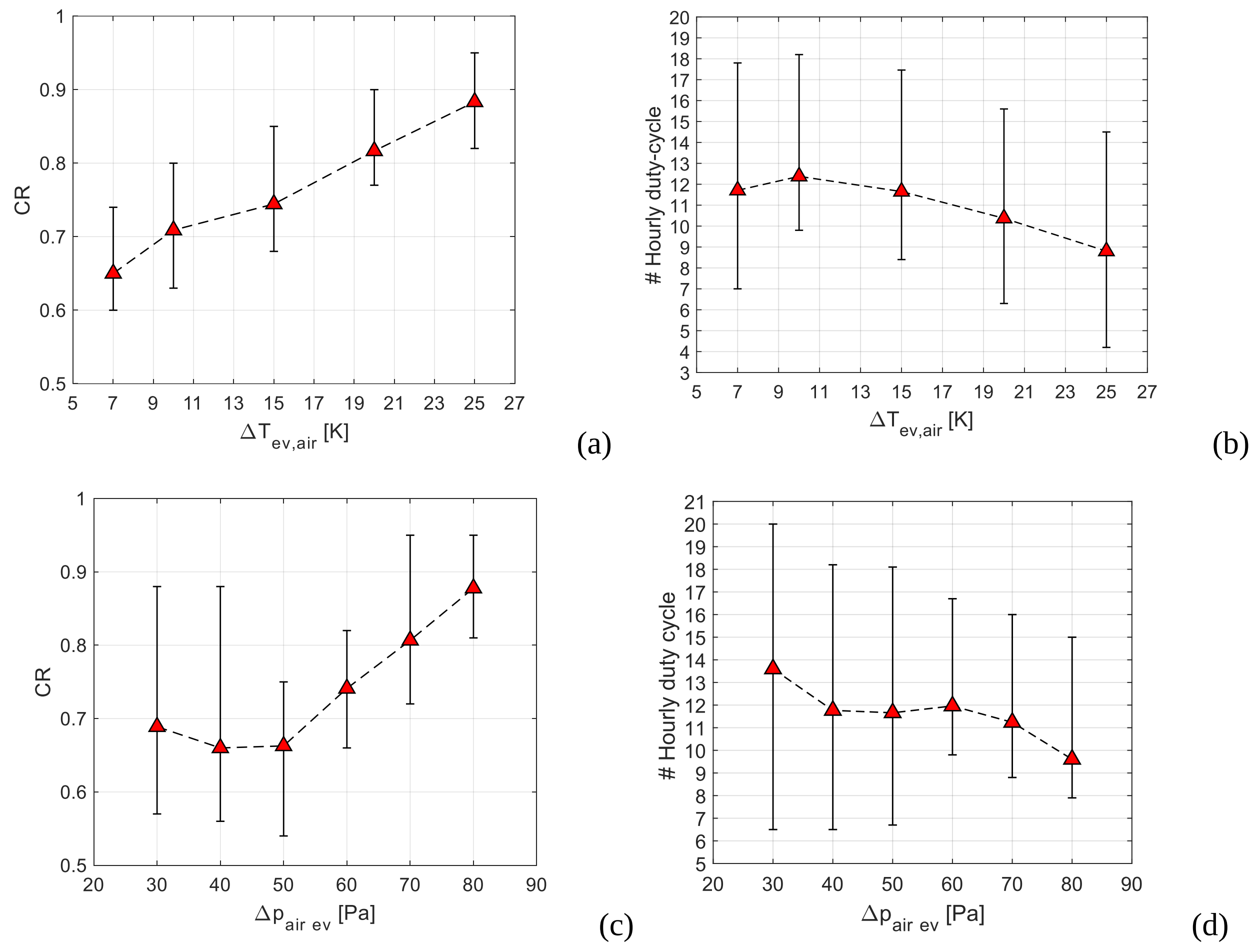

Figure 6.21 – CR trend and hourly compressor duty cycle as a function of evaporator temperature difference between air and refrigerant (a and b) and evaporator air-side pressure drop (c and d)

To highlight the improvements achieved with the new evaluation method in terms of CR value and hourly duty cycle number, the operational area delimited by the minimum and maximum values of both parameters are shown in Figure 6.22 for each value of temperature (a) or air side pressure (b) difference depending by the conventional system employed. The shape of the areas (delimited by dotted line) drawn in Figure 6.22 are affected by the actual test conditions, and they are not representative of the overall operating range of a commercial refrigeration unit.
In conventional systems for each value of threshold, the variation of hourly duty cycle number has the same order of magnitude than the one evaluated with new method fixed the CR. Moreover, the conventional systems operate on more restricted and not controlled CR ranges (e.g. a conventional system based on a temperature difference threshold of 7K launches the defrost within CR values ranging between 0.6 and 0.74). Conversely, a system based on new data reduction method is able to control and adjust the CR threshold value depending on operating condition on a wider range.

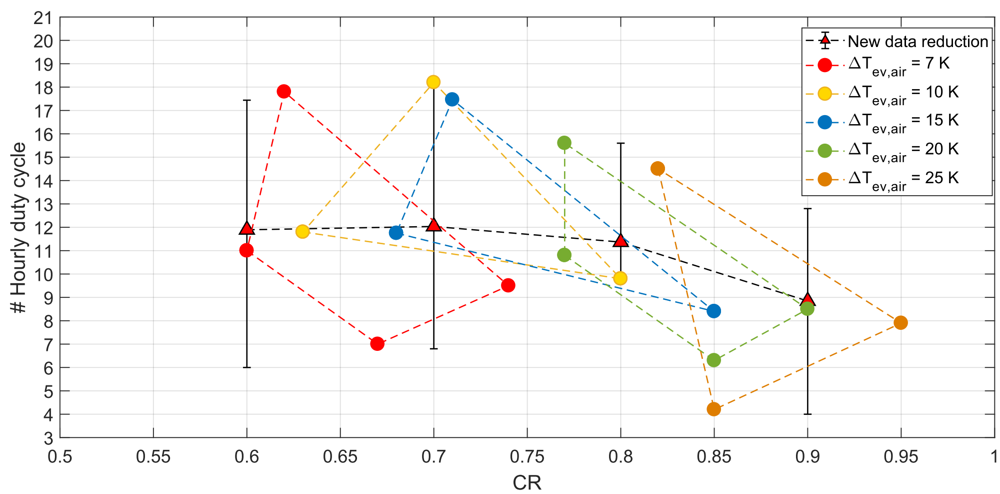

(a)

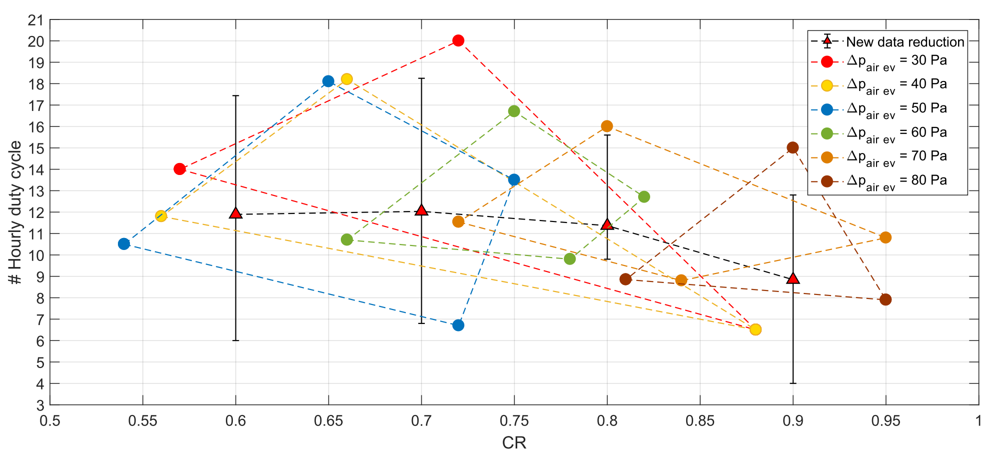

(b)

Figure 6.22 – Comparison between proposed method and conventional systems based on temperature difference threshold (a) and air-side pressure drop threshold (b). The circles refer to minimum and maximum value of CR and hourly duty cycle number for each value of imposed threshold.

Conclusions

In this thesis research activity work about low – GWP refrigerants and novel mathematical approach to determine the optimal start defrost time in commercial refrigeration applications is reported. The research activity and the PhD grant is funded by Zanotti SpA (member of Daikin group). The work is established in the framework of changes and technical challenges involving commercial refrigeration sector.

Conclusion and perspectives of part I of the thesis

In the first part of the thesis, low – GWP refrigerants research activity is presented firstly with theoretical approach about thermo-economic optimization and environmental analysis of low - GWP blends and propane in a 2.5 kW one-stage commercial refrigeration unit and in the second part with an experimental activity on a two-stage condensing unit using CO_2 as refrigerant.
The results of the first part of the work relating on the theoretical analysis of low – GWP blends and propane from thermodynamic, economic and environmental perspectives are:

- R449A represents a good compromise as mid-term R404A replacement since it has the lowest set-up costs among refrigerants and COP value similar than R404A and R452A.

- Considering the low - GWP blends (GWP < 150), R454C has the second highest COP value, equal to 2.49, and the lowest set-up costs.

- The dramatic reduction of feasible configurations on Pareto front together with the lower isentropic compressor efficiency disfavour propane among the refrigerants in terms of costs and performances; the improvement of compressor technology, the increase of refrigerant charge limit and the reduction of components costs can help to reduce this gap allowing propane to be an interesting long-term option for this sector.

- R454C is the refrigerant with the lowest environmental impact in France and share this outcome with R449A in Italy.

- R449A has the lowest environmental impact in Germany.

- The optimal configuration in terms of COP – set-up costs, for each refrigerant, has not always the lowest environmental impact.

The main outcomes regarding the experimental activity on the two-stage CO_2 condensing unit prototype are:

- The evaporating temperature effect on performances is more marked at higher temperature, in fact from -10°C to -20°C reductions up to 30% and 28% for cooling capacity and COP respectively at T_{amb} = 5°C are found; instead, they are 54% and 53% at T_{amb} = 43°C.

- The ambient temperature influences the performances with different behaviour, in fact for ambient temperatures below 25°C the thermodynamic cycle is subcritical and the cooling capacity trend has a flatter slope than the case at 32°C and 43°C where the thermodynamic cycle is transcritical and shows a sudden drop up to 40% and 20% of the maximum cooling capacity measured at T_{amb} = 5°C and T_{ev} = -10°C (reference value).

- The COP decreases with linear trend showing a reduction of 76% and 84% at T_{ev} = -10°C and -20°C, respectively, going from 5°C to 43°C than the reference value.

- The operation of intercooler has a beneficial effect on unit reliability since the refrigerant from the intercooler cools the electric motor preserving its lifespan at higher ambient temperatures; moreover, a reduction of receiver pressure is also encountered leading to higher volumetric efficiency in the first stage and lower quality at evaporator inlet, with the increase of cooling capacity and COP of 10% than the case without intercooler.

- The cooling effect of flash gas injection valve increases with ambient temperature, due to the increase of vapour mass flow rate coming from flash gas valve thanks to higher receiver quality.

- The SEPR value is 33% higher than the minimum value threshold imposed by EU Regulation 2015/1095 (European Commission, 2015); moreover, it is 2% higher than the one of a R449A unit of similar cooling capacity.

Finally, the presented method and results of theoretical study about low-GWP blends and propane could be helpful to address the design and business choices of the walk-in refrigerators manufacturers in design, manufacturing, and sales phases. The best compromise solution between set-up costs and performances and at the same time environmentally friendly and economic for the final user, could be achieved by means of a careful design.
Instead, the results achieved in the second part of low – GWP refrigerant topic had the intention to demonstrate the potential use of CO_2 on small scale plants to replace the high – GWP refrigerants; the higher complexity and costs of the plant than other refrigerants, required to overcome the thermodynamic peculiarities of CO_2, may be mitigated by the more longevity of using CO_2 as refrigerant. In future, the diffusion of components suitable to operate with higher pressure, increase of components efficiency and decrease of costs could further reduce the gap of the investment costs and performances with the other refrigerants.

Conclusion and perspectives of part II of the thesis

In the second part of the thesis, a novel mathematical data reduction to evaluate the optimal start defrost time is proposed; in the final part, the assessment of commercial methods used to trigger the defrost based on threshold value of temperature difference between air and refrigerant and air side pressure drop across the evaporator is presented. The main outcomes of the activity are:

- It is possible to define a method to calculate the minimum total average electric power consumption, including that of the accumulation phase and of the defrosting phase. The required time and power for defrosting are assumed to be already optimized by the control unit.

- For the analysed system, it is possible to define a wide range of operation time before defrosting in which the total power consumption and the number of hourly on / off cycles are close to their minimum value, with the capacity ratio CR index constrained below the value of 0.70. By changing the chosen CR, the $\Delta\theta_{acc}$ band will become more restrictive and difficult to determine.

- The proposed method can be implemented on new defrost control units by imposing the control of a threshold value of the capacity ratio index CR to calculate the optimum time before triggering the defrosting phase. The only limit is that the CR should be sufficiently high to have a low sensitivity on power consumption and compressor on / off cycles. The effect of door opening is ignored and this can replicate the situation where transpiring foods such as fruit and vegetables are stored for at least one day with less than 3 door openings.

- The commercial defrosting strategies may guarantee that the unit works close to its minimum value of total power consumption and compressor on / off cycles. Conversely, they are not able to guarantee the control of CR index since this parameter shows a large variation for a fixed value of ΔT or Δp and therefore is not optimized for the specific application.

References

2012. [Online]. Available: https://www.eea.europa.eu/data-and-maps/figures/co2-electricity-gperkwh/co2-per-electricity-kwh-fig-1_2010_qa.xls.

Amer, M., Wang, C. 2017. Review of defrosting methods, Renewable and Sustainable Energy Reviews, Volume 73, 2017, Pages 53-74, ISSN 1364-0321. Doi: https://doi.org/10.1016/j.rser.2017.01.120.

Bansal, P., Fothergill, D., Fernandes, R., 2010. Thermal analysis of the defrost cycle in a domestic freezer. International Journal of Refrigeration. 33. 589-599. 10.1016/j.ijrefrig.2009.11.012.

Bejan, A., Vargas, J.V.C., Lim, J.S.1995. When to defrost a refrigerator, and when to remove the scale from the heat exchanger of a power plant. International Journal of Heat and Mass Transfer, 37, 523

Blasius, P.R.K., Das Aehnlichkeitsgesetz bei Reibungsvorgangen in Flüssigkeiten. Forschungsheft 131 (1913), 1-41.

Boccardi, G., Calabrese, N., Celata, G. P., Mastrullo, R., Mauro, A.W., Perrone, A., Trinchieri, R., 2013. Experimental performance evaluation for a carbon dioxide light commercial cooling application under transcritical and subcritical conditions, Appl. Th. Eng. 54 (2013) 528-535

Buick, T.R., McMullan, J.T., Morgan, R. and Murray, R.B. 1978. Ice detection in heat pumps and coolers. Int. J. Energy Res., 2: 85-98. doi:https://doi.org/10.1002/er.4440020109

Cabello, R., Sánchez,D., Patiño, J.,Llopis,R., Torrella,E., Experimental analysis of energy performance of modified single-stage CO2 transcritical vapour compression cycles based on vapour injection in the suction line, Applied Thermal Engineering, Volume 47, 2012, Pages 86-94, ISSN 1359-4311.doi: https://doi.org/10.1016/j.applthermaleng.2012.02.031

Cao, Z.-K., Zhang, C.-X., Gu B., 2013. Application of a support vector machine algorithm for improving effects of defrosting of commercial refrigerated display cabinets in supermarkets. HVAC&R Research, 19:3, 230-241.

Cascini, A., Gamberi, M., Mora, C., Rosano, M., Bortolini, M., 2016. Comparative Carbon Footprint Assessment of commercial walk-in refrigeration systems under different use configurations. Journal of Cleaner Production 112, pp. 3998-4011, 2016

Catalán-Gil, J., Sánchez, D., Cabello, R., Llopis, R., Nebot-Andrés, L., Calleja-Anta, D., 2020. Experimental evaluation of the desuperheater influence in a CO2 booster refrigeration facility, Applied Thermal Engineering 168. doi: https://doi.org/10.1016/j.applthermaleng.2019.114785

Cecchinato, L., Chiarello, M., Corradi, M., Fornasieri, E., Minetto, S., Stringari, P., Zilio, C., 2009. Thermodynamic analysis of different two-stage transcritical carbon dioxide cycles. International Journal of Refrigeration-revue Internationale Du Froid - INT J REFRIG. 32. 1058-1067. 10.1016/j.ijrefrig.2008.10.001.

CEN (EUROPEAN COMMITTEE FOR STANDARDIZATION), 2016. EN13215:2016 Condensing units for refrigeration - Rating conditions, tolerances and presentation of manufacturer's performance data

CEN (EUROPEAN COMMITTEE FOR STANDARDIZATION) 2016. EN378-1:2016 Refrigerating systems and heat pumps - Safety and environmental requirements – Part I: Basic requirements, definitions, classification and selection criteria.

CEN (EUROPEAN COMMITTEE FOR STANDARDIZATION), 2017. EN13771-2:2017, Compressors and condensing units for refrigeration- Performance testing and test methods- Part 2: Condensing units.

Chen Y.G., Guo X.M., 2005. Numerical simulation on the performance of heat pumps under frost conditions. Proceedings of 5th International Conference on Compressor and Refrigeration, vol. 8, Dalian, China, 2005, pp. 373–381.

Cho, H., Kim, Y., Jang, I., 2005. Performance of a showcase refrigeration system with multi-evaporator during on–off cycling and hot-gas bypass defrost, Energy, Volume 30, Issue 10, 2005, Pages 1915-1930. Doi: https://doi.org/10.1016/j.energy.2004.11.006.

Citarella, B., Mastrullo, R., Mauro, A. W., Sfragara, M., Tammaro, M., 2019. Performance measurement of a two stage CO2 refrigerator and SEPR comparison with low-GWP alternative. Proceedings of the 25th IIR International Congress of Refrigeration: Montréal, Canada, August 24-30, 2019. Doi: http://dx.doi.org/10.18462/iir.icr.2019.1290

Citarella B., Mastrullo R., Mauro A.W., Sfragara M., Tammaro M., 2020. Performance assessment of a two stage CO2 small scale MT refrigerator. Int. J. Refrigeration. https://doi.org/10.1016/j.ijrefrig.2020.12.024

Citarella, B., Viscito, L., Mochizuki, K., Mauro, A.W., 2021. Multi-criteria (thermo-economic) optimization and environmental analysis of a food refrigeration system working with low environmental impact refrigerants. Energy Conversion and Management, Volume 253, 2022, 115-152, ISSN 0196-8904. https://doi.org/10.1016/j.enconman.2021.115152.

Clodic D., PAN X., Devin E., Michineau T., Barrault S., 2014. Alternatives to high GWP HFCs in refrigeration and air-conditioning applications. Final report, available online and visited on 10 December 2017. http://www.cemafroid.fr/doc_telechargement/Rapport_alternative_HFC_ENG.pdf

Council Decision (EU) 2016/1841 of 5 October 2016 on the conclusion, on behalf of the European Union, of the Paris Agreement adopted under the United Nations Framework Convention on Climate Change.

Da Silva, D. L., Hermes, C. J. L., Melo, C., 2011. Experimental study of frost accumulation on fan-supplied tube-fin evaporators, Applied Thermal Engineering, Volume 31, Issues 6–7, Pages 1013-1020. Doi: https://doi.org/10.1016/j.applthermaleng.2010.11.006.

Da Silva, D. L., 2012. Frost Formation on Fan-Supplied Tube-Fin Evaporators: A Visual and Numerical Analysis". International Refrigeration and Air Conditioning Conference. Paper 1164. http://docs.lib.purdue.edu/iracc/1164

Datta, D. Tassou, S., Marriott, D., 1997. Frost Prediction On Evaporator Coils Of Supermarket Display Cabinets Using Artificial Neural Networks.

Datta, D.; Tassou, S. A.; and Marriot, D., 1998. Experimental Investigations into Frost Formation on Display Cabinet Evaporators in Order to Implement Defrost on Demand. International Rerigeration and Air Conditioning Conference. http://docs.lib.purdue.edu/iracc/420

Deng, H., Rossato, M., Fernandino, M., Del Col D., 2019. A new simplified model for condensation heat transfer of zeotropic mixtures inside horizontal tubes, Appl. Th. Engin. 153 (2019) 779-790

Dittus, F. W., Boelter, L. M. K., 1930. Heat Transfer in Automobile Radiators of the Tubular Type. University of California Publications in Engineering, vol. 2, pp. 443-461, 1930.

Domanski, P. A., Brignoli, R., Brown, J. S, Kazakov A. F., McLinden, M. O. 2017. Low-GWP refrigerants for medium and high-pressure applications. International Journal of Refrigeration 84, pp. 198-209, 2017

EPA, Transitioning to low-gwp alternatives in Commercial Refrigeration, 2016. Available on-line and visited on 2 January 2018. https://www.epa.gov/sites/production/files/2016-12/documents/international_transitioning_to_low-gwp_alternatives_in_commercial_refrigeration.pdf

European Commission, Joint Research Centre, Institute for Prospective Technological Studies 2014. Ecodesign for Commercial Refrigeration, preparatory study update, final report. Available on-line and visited on 14 April 2018 http://www.eup-network.de/fileadmin/user_upload/COMM_REFRIG_FINAL_BKG_DOC_FINAL.pdf

European Parliament, 2009. Directive 2009/125/EC of the European Parliament and of the Council of 21 October 2009 establishing a framework for the setting of ecodesign requirements for energy-related products

European Parliament, 2014. Regulation (EU) No 517/2014 of the European Parliament and of the Council of 16 April 2014 on fluorinated greenhouse gases and repealing Regulation (EC) N° 842/2006

European Parliament, 2015. Commission Regulation (EU) 2015/1095 of 5 May 2015 implementing Directive 2009/125/EC of the European Parliament and of the Council with regard to ecodesign requirements for professional refrigerated storage cabinets, blast cabinets, condensing units and process chillers

European Parliament, 2017. Regulation (EU) 2017/1369 of the European Parliament and of the Council of 4 July 2017 setting a framework for energy labelling and repealing Directive 2010/30/EU

European Parliament, 2019. Commission Delegated Regulation (EU) 2019/2018 of 11 March 2019 supplementing Regulation (EU) 2017/1369 of the European Parliament and of the Council with regard to energy labelling of refrigerating appliances with a direct sales function

European Parliament, 2019. Commission Regulation (EU) 2019/2024 of 1 October 2019 laying down ecodesign requirements for refrigerating appliances with a direct sales function pursuant to Directive 2009/125/EC of the European Parliament and of the Council.

Europa: HFC, prezzi stabili ma leggero aumento della domanda nel quarto trimestre 2020 https://www.zerosottozero.it/2021/04/16/europa-hfc-prezzi-stabili-ma-leggero-aumento-della-domanda-nel-quarto-trimestre-2020/ visited on 15/12/2021

Eurostat, "Electricity price statistics," 2021. [Online]. Available: https://ec.europa.eu/eurostat/statisticsexplained/ index.php?title=Electricity_price_statistics#Electricity_prices_for_nonhousehold_consumers.

E.W. Lemmon, M.O. Mc Linden, M.L. Huber, REFPROP NIST Standard Reference Database, Version 10.0.

Getu, H.M., Bansal, P.K., 2007. Modeling and performance analyses of evaporators in frozen-food supermarket display cabinets at low temperatures, International Journal of Refrigeration, Volume 30, Issue 7, Pages 1227-1243. Doi: https://doi.org/10.1016/j.ijrefrig.2007.02.003.

Gullo, P., Cortella, G., 2016. Theoretical evaluation of supermarket refrigeration systems using R1234ze(E) as an alternative to high-global warming potential refrigerants. Science and Technology for the Built Environment, vol. 22, no. 8, pp. 1145-1155, 2016

Gullo, P., Elmegaard, B., Cortella, G., 2016. Energy and environmental performance assessment of R744 booster supermarket refrigeration systems operating in warm climates, International Journal of Refrigeration, 64 61-79. doi: https://doi.org/10.1016/j.ijrefrig.2015.12.016.

Gullo, P., Tsamos, K., Hafner, A., Ge, Y., Tassou, S. A. 2017. State-of-the-art technologies for transcritical R744 refrigeration systems - a theoretical assessment of energy advantages for European food retail industry. Energy Procedia, vol. 123, pp. 46-53, 2017

Gullo, P., Hafner, A., Cortella, G., 2017. Multi-ejector R744 booster refrigerating plant and air conditioning system integration – A theoretical evaluation of energy benefits for supermarket applications. International Journal of Refrigeration. 75. 164-176. 10.1016/j.ijrefrig.2016.12.009.

Gullo, P. 2019. Innovative fully integrated transcritical R744 refrigeration systems for a HFC-free future of supermarkets in warm and hot climates. International Journal of Refrigeration, 108, 283-310. https://doi.org/10.1016/j.ijrefrig.2019.09.001

Guo, X. & Wang, C. & Wang, W. & Chen, C., 2006. Numerical simulation and experimental verification on dynamic performance of air source heat pump under frosting conditions. 40. 544-548.

Guo, X.M., Chen, Y.G., Wang, W.H., Chen, C. Z., 2008. Experimental study on frost growth and dynamic performance of air source heat pump system, Applied Thermal Engineering, Volume

28, Issues 17–18, 2008, Pages 2267-2278. Doi: https://doi.org/10.1016/j.applthermaleng.2008.01.007.

Hayashi, Y., Aoki, A., Hori, K., 1977. Study of frost properties correlating with frost formation types. J. Heat Transfer 99, 239-245

Hermes, C. J. L., Piucco, R. O., Barbosa, J. R., Melo, C., 2009. A study of frost growth and densification on flat surfaces, Experimental Thermal and Fluid Science, Volume 33, Issue 2, 2009, 371-379. doi: https://doi.org/10.1016/j.expthermflusci.2008.10.006.

Heredia-Aricapa, Y., Belman-Flores, J. M., Mota-Babiloni, A., Serrano-Arellano J., Garcìa Pabon, J. J., 2020. Overview of low GWP mixtures for the replacement of HFC refrigerants: R134a, R404A and R410A. International Journal of Refrigeration, vol. 111, pp. 113-123, 2020

Hoffenbecker, N., 2004. Investigation of alternative defrost strategies. MS Thesis. University of Wisconsin—Madison; 2004.

Hoffenbecker, N., Klein, S.A., Reindl, D.T. 2005. Hot gas defrost model development and validation, International Journal of Refrigeration, Volume 28, Issue 4, 2005, Pages 605-615, ISSN 0140-7007, doi: https://doi.org/10.1016/j.ijrefrig.2004.08.016.

IEC, International Electrotechnical Commission, 2010. IEC60335-2-89:2010 Household and similar electrical appliances - Safety - Part 2-89: Particular requirements for commercial refrigerating appliances with an incorporated or remote refrigerant unit or compressor

IIR, "The role of refrigeration in worldwide nutrition - 5th Informatory note on refrigeration and food," Paris: International Institute of Refrigeration (IIR), 2009.

IIR, "The role of Refrigeration in the Global Economy, 29th Informatory note on Refrigeration Technologies," 2015.

Karampour, M., Sawalha, S., 2018. State-of-the-art integrated CO2 refrigeration system for supermarkets: A comparative analysis. International Journal of Refrigeration,86, 239-257 doi: https://doi.org/10.1016/j.ijrefrig.2017.11.006

Knabben, F. T., Hermes, C. J. L., Melo, C., 2011. In-situ study of frosting and defrosting processes in tube-fin evaporators of household refrigerating appliances, International Journal of Refrigeration, Volume 34, Issue 8, 2011, Pages 2031-2041. Doi: https://doi.org/10.1016/j.ijrefrig.2011.07.006.

Lemmon, E.W., Huber, M.L., McLinden, M.O., 2013. NIST Standard Reference Database 23: Reference Fluid Thermodynamic and Transport Properties-REFPROP, Version 9.1, Natl Std. Ref. Data Ser. (NIST NSRDS) -. (2013). https://www.nist.gov/publications/niststandard- reference-database-23-reference-fluid-thermodynamic-and-transport [accessed 25.03.2020].

Leoni, A., Mondot, M., Durier, F., Revellin, R., Haberschill, P., 2016. State-of-the-art review of frost deposition on flat surfaces. International Journal of Refrigeration, Volume 68, 2016, 198-217, doi: https://doi.org/10.1016/j.ijrefrig.2016.04.004

Leoni, A., Mondot, M., Durier, F., Revellin, R., Haberschill, P., 2017. Frost formation and development on flat plate: Experimental investigation and comparison to predictive methods. Experimental Thermal and Fluid Science. Volume 88, 2017, 220-233, doi: https://doi.org/10.1016/j.expthermflusci.2017.06.005.

Li, S.-M.; Yang, K.-S.; Wang, C.-C., 2021. A Semi-Empirical Model for Predicting Frost Properties. Processes 2021, 9, 412. https://doi.org/10.3390/pr9030412

Liao, S.M., Zhao, T.S., Jakobsen, A., 2000. A correlation of optimal heat rejection pressures in transcritical carbon dioxide cycles, Applied Thermal Engineering, Volume 20, Issue 9, 2000, Pages 831-841, ISSN 1359-4311, https://doi.org/10.1016/S1359-4311(99)00070-8.

Llopis, R., Sánchez, D., Cabello, R., Nebot-Andrés, L., Catalán-Gil, J., 2017. R-407H as drop-in of R-404A. Experimental analysis in a low temperature direct expansion commercial refrigeration system, International Journal of Refrigeration, Volume 80, 2017, Pages 11-23, ISSN 0140-7007, https://doi.org/10.1016/j.ijrefrig.2017.04.030

Llopis, R., Calleja-Anta, D., Sanchez, D., Nebot-Andres, L., Catalan-Gil J., Cabello, R., 2019. R-454C, R459B, R-457A and R-455A as low-GWP replacements of R-404A: Experimental evaluation and optimization. International Journal of Refrigeration, vol. 106, pp. 133-143, 2019

Llopis, R., Calleja-Anta, D., Maiorino, A., Nebot-Andrés, L., Sánchez, D., Cabello, R. 2020. TEWI analysis of a stand-alone refrigeration system using low-GWP fluids with leakage ratio consideration, International Journal of Refrigeration, Volume 118, 2020, Pages 279-289, ISSN 0140-7007, https://doi.org/10.1016/j.ijrefrig.2020.05.028.

Makhnatch, P., Mota-Babiloni, A., Rogstam J., Khodabandeh, R., 2017. Retrofit of lower GWP alternative R449A into an existing R404A indirect supermarket refrigeration system. International Journal of Refrigeration, vol. 76, pp. 184-192, 2017

Mastrullo, R., Mauro, A.W., Menna, L., Palma, A., Vanoli, G.P., 2014.Transient model of a vertical freezer with door openings and defrost effects, Applied Energy, Volume 121, 2014, Pages 38-50. Doi: https://doi.org/10.1016/j.apenergy.2014.01.069.

Mastrullo, R., Mauro, A.W., Menna, L., Vanoli, G.P., 2014. Replacement of R404A with propane in a light commercial vertical freezer: A parametric study of performances for different system architectures. Energy Conversion and Management 82 (2014) 54-60

Mastrullo R., Mauro A.W., Viscito L., 2019. Flow boiling of R452A: Heat transfer data, dry-out characteristics and a correlation, Exp. Th. Fluid Science 105 (2019) 247-260.

Mauro A.W., Napoli G., Pelella F., Viscito L., 2020. Flow boiling heat transfer and pressure drop data of nonazeotropic mixture R455A in a horizontal 6.0 mm stainless steel tube, Int. J. Refrigeration 119 (2020) 195-205.

McLinden, M. O., Lemmon, E. W., Jacobsen, R. T. 1998. Thermodynamic properties for the alternative refrigerants," International Journal of Refrigeration, vol. 21, no. 4, pp. 322-338, 1998

McLinden, M. O., Kazakov, A. F., Brown, J. S., Domanski, P. A. 2014. A thermodynamic analysis of refrigerants: Possibilities and tradeoffs for Low-GWP refrigerants. International Journal of Refrigeration, vol. 38, pp. 80-92, 2014

Md. Amirul Islam, K. Srinivasan, Kyaw Thu, Bidyut Baran Saha, Assessment of total equivalent warming impact (TEWI) of supermarket refrigeration systems, International Journal of Hydrogen Energy, Volume 42, Issue 43, 2017, Pages 26973-26983, ISSN 0360-3199. Doi: https://doi.org/10.1016/j.ijhydene.2017.07.035.

Mengjie, S., Cheng, F., Ning, M., Zhihua, W., Yudong, X., 2019. Experimental study on frost unevenly distributed and melted frost downwards flowing during defrosting for ASHPs, Energy Procedia, Volume 158, 2019, Pages 2826-2833, ISSN 1876-6102. Doi: https://doi.org/10.1016/j.egypro.2019.02.045.

Moallem, E., Hong, T., Cremaschi, L., Fisher, D., 2013. Experimental investigation of adverse effect of frost formation on microchannel evaporators, part 1: Effect of fin geometry and environmental effects. International Journal of Refrigeration. 36. 1762-1775. Doi: 10.1016/j.ijrefrig.2012.09.009

Montreal Protocol on substances that deplete the ozone layer - Declaration by the European Economic Community

Mota-Babiloni, A., Haro-Ortuno, J., Navarro-Esbri' J., Barragan-Cervera, A., 2018. Experimental drop-in replacement of R404A for warm countries using the low GWP mixtures R454C and R455A. International Journal of Refrigeration, vol. 91, pp. 136-145, 2018

Müller-Steinhagen, H., Heck, K., 1986. A simple friction pressure drop correlation for two-phase flow in pipes. Chemical Engineering and Processing: Process Intensification, pp. 297-308, 1986.

Na, B.; Webb, R.L. New model for frost growth rate. Int. J. Heat Mass Transf. 2004, 47, 925–936, doi: https://doi.org/10.1016/j.ijheatmasstransfer.2003.09.001

Nebot Andres, L., Doménech, R., Catalán Gil, J., Sánchez, D., Cabello, R., 2018. Energy evaluation of the mechanical subcooling impact on a CO2 DX-system in a commercial MT cabinet. 13th IIR Gustav Lorentzen Conference On Natural Refrigerants, Valencia, Spain. doi:10.18462/iir.gl.2018.1127

Persistence Market Research, 2014. Frozen food market to rise 30% by 2020. Available on-line and visited on 12 March 2020. https://www.coolingpost.com/world-news/frozen-food-market-to-rise-30-by-2020/

Pisano, A., Martínez-Ballester, S., Corberán, J.M., Mauro, A.W., 2015. Optimal design of a light commercial freezer through the analysis of the combined effects of capillary tube diameter and refrigerant charge on the performance, International Journal of Refrigeration, Volume 52, 2015, Pages 1-10, ISSN 0140-7007, https://doi.org/10.1016/j.ijrefrig.2014.12.023.

Rouhani, S. Z., Axelsson, E., 1970. Calculation of void volume fraction in the subcooled and quality boiling regions," International Journal of Heat and Mass Transfer, vol. 13, no. 2, pp. 383-393, 1970.

Şahin, A. 1994. An Experimental Study on The Initiation and Growth Of Frost Formation On A Horizontal Plate. Experimental Heat Transfer, 7:2, 101-119

Sawalha, S. Karampour, M., Rogstam, J., 2015. Field measurements of supermarket refrigeration systems. Part I: Analysis of CO2 trans-critical refrigeration systems. Applied Thermal Engineering. 87. 633-647. 10.1016/j.applthermaleng.2015.05.052.

Sawalha, S., Piscopiello, S., Karampour, M., Manickam, L., Rogstam, J. 2017. Field measurements of supermarket refrigeration systems. Part II: Analysis of HFC refrigeration systems and comparison to CO2 trans-critical, Applied Thermal Engineering, Volume 111, 2017, Pages 170-182, ISSN 1359-4311, https://doi.org/10.1016/j.applthermaleng.2016.09.073.

Seker, D., Karatas, H., Egrican, N., 2004. Frost formation on fin-and-tube heat exchangers. Part I— Modeling of frost formation on fin-and-tube heat exchangers. International Journal of Refrigeration, Volume 27, Issue 4, Pages 367-374. Doi: https://doi.org/10.1016/j.ijrefrig.2003.12.003

Sethi, A., Pottker, G., Motta, S. Y., 2016. Experimental evaluation and field trial of low global warming potential R404A replacements for commercial refrigeration Science and Technology for the Built Environment, vol. 22, no. 8, pp. 1175-1184, 2016

Tammaro, M., Mastrullo, R., Mauro A. W., Sfragara, M. 2018. Experimental comparison of cooling capacity and EER in a positive temperature monoblock after replacement of R404A with R407H and soft-optimization of components. International Conference on Cryogenics and Refrigeration, Shanghai, 2018

Tassou S., Datta D., Marriott D., 2001. Frost formation and defrost control parameters for open multideck refrigerated food display cabinets. Proceedings of the Institution of Mechanical Engineers, Part A: Journal of Power and Energy. 2001;215(2):213-222. doi:10.1243/0957650011538488

Troch, S., Hoseong, L., Hwang, Y., & Radermacher, R., 2016. Harmonization of Life Cycle Climate Performance (LCCP) Methodology. International Refrigeration and Air Conditioning Conference. http://docs.lib.purdue.edu/iracc/1724

UNEP, "2002 Report of the refrigeration, air conditioning and heat pumps technical options committee," Nairobi, 2002.

Wang, C.C., Lee, C.J., Chang, C.T., Lin, S.P., 1999. Heat transfer and friction correlation for compact louvered fin-and-tube heat exchangers, Int. J. Heat Mass Transfer 42 (1999) 1945-1956.

Wang, C.C., Lin, Y.T., Lee, C.J., 2000. An airside correlation for plain fin-and-tube heat exchangers in wet conditions. Int. J. Heat Mass Transfer 43 (2000) 1869-1872.

Wu, X., Dai, W., Xu, W., Tang, L., 2007. Mesoscale investigation of frost formation on a cold surface, Experimental Thermal and Fluid Science,Volume 31, Issue 8, 2007, Pages 1043-1048.

Xia, Y., Zhong, Y., Hrnjak, P.S., Jacobi, A.M., 2006. Frost, defrost, and refrost and its impact on the air-side thermal-hydraulic performance of louvered-fin, flat-tube heat exchangers, International Journal of Refrigeration, Volume 29, Issue 7, Pages 1066-1079, ISSN 0140-7007. Doi: https://doi.org/10.1016/j.ijrefrig.2006.03.005.

Xiao, J., Wang, W., Zhao, Y.H. & Zhang, F. R. 2009. An analysis of the feasibility of photoelectric technique applied in defrost-control. International Journal of Refrigeration. 32. 1350-1357. 10.1016/j.ijrefrig.2009.02.014.

Xiao, J., Wang, W., Guo, Q.C., Zhao, Y., 2010. An experimental study of the correlation for predicting the frost height in applying the photoelectric technology. International Journal of Refrigeration-revue Internationale Du Froid - INT J REFRIG. 33. 1006-1014. 10.1016/j.ijrefrig.2010.03.002.

Xu, B., Han, Q., Chen, J., Li, F., Wang, N., Li, D., Pan, X., 2013. Experimental investigation of frost and defrost performance of microchannel heat exchangers for heat pump systems, Applied Energy, Volume 103, Pages 180-188. Doi: https://doi.org/10.1016/j.apenergy.2012.09.026

Zeiger B. 2015. The EU HFC amendment proposal- Support for decision-making: Country-specific case studies. Öko-Recherche Institute. Available on-line and accessed on 10 december 2017. https://www.oekorecherche.de/sites/default/files/publikationen/european_union-case_study_summary2015.pdf

Zhili, S., Jiamei, L., Youcai, L., Huan, S., Shengchun, L., Lijie, Y., Caiyun, Y., 2020. Performance Assessment of CO2 supermarket refrigeration system in different climate zones of China. Energy Conversion and Management. 10.1016/j.enconman.2020.112572.